AFRL-RX-WP-JA-2017-0160

A CRITICAL REVIEW OF HIGH ENTROPY ALLOYS AND RELATED CONCEPTS (POSTPRINT)

O.N. Senkov
UES

D.B. Miracle
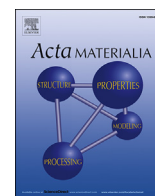**AFRL/RX**

2 May 2016
Interim Report

(STINFO COPY)

AIR FORCE RESEARCH LABORATORY
MATERIALS AND MANUFACTURING DIRECTORATE
WRIGHT-PATTERSON AIR FORCE BASE, OH 45433-7750
AIR FORCE MATERIEL COMMAND
UNITED STATES AIR FORCE

REPORT DOCUMENTATION PAGE

Form Approved
OMB No. 0704-0188

1. REPORT DATE *(DD-MM-YY)*	2. REPORT TYPE	3. DATES COVERED *(From - To)*
2 May 2016	Interim	22 September 2014 – 21 September 2015

4. TITLE AND SUBTITLE
A CRITICAL REVIEW OF HIGH ENTROPY ALLOYS AND RELATED CONCEPTS (POSTPRINT)

5a. CONTRACT NUMBER
FA8650-10-D-5226-0005

5b. GRANT NUMBER

5c. PROGRAM ELEMENT NUMBER
62102F

6. AUTHOR(S)
1) O.N. Senkov – UES
2) D.B. Miracle – AFRL/RX

5d. PROJECT NUMBER
4347

5e. TASK NUMBER

5f. WORK UNIT NUMBER
X0UP

7. PERFORMING ORGANIZATION NAME(S) AND ADDRESS(ES)
1) UES, Inc.
4401 Dayton-Xenia Road
Beavercreek, OH 4543

2) AFRL/RX
Wright-Patterson AFB, OH
45433

8. PERFORMING ORGANIZATION REPORT NUMBER

9. SPONSORING/MONITORING AGENCY NAME(S) AND ADDRESS(ES)
Air Force Research Laboratory
Materials and Manufacturing Directorate
Wright-Patterson Air Force Base, OH 45433-7750
Air Force Materiel Command
United States Air Force

10. SPONSORING/MONITORING AGENCY ACRONYM(S)
AFRL/RXCM

11. SPONSORING/MONITORING AGENCY REPORT NUMBER(S)
AFRL-RX-WP-JA-2017-0160

12. DISTRIBUTION/AVAILABILITY STATEMENT
Distribution Statement A. Approved for public release: distribution unlimited.

13. SUPPLEMENTARY NOTES

14. ABSTRACT *(Maximum 200 words)*

High entropy alloys (HEAs) are barely 12 years old. The field has stimulated new ideas and has inspired the exploration of the vast composition space offered by multi-principal element alloys (MPEAs). Here we present a critical review of this field, with the intent of summarizing key findings, uncovering major trends and providing guidance for future efforts. Major themes in this assessment include definition of terms; thermodynamic analysis of complex, concentrated alloys (CCAs); taxonomy of current alloy families; microstructures; mechanical properties; potential applications; and future efforts. Based on detailed analyses, the following major results emerge. Although classical thermodynamic concepts are unchanged, trends in MPEAs can be different than in simpler alloys. Common thermodynamic perceptions can be misleading and new trends are described. From a strong focus on 3d transition metal alloys, there are now seven distinct CCA families. A new theme of designing alloy families by selecting elements to achieve a specific, intended purpose is starting to emerge.

15. SUBJECT TERMS
High-entropy alloys; Microstructure; Mechanical properties; Thermodynamics; Multicomponent

16. SECURITY CLASSIFICATION OF:

a. REPORT	b. ABSTRACT	c. THIS PAGE	17. LIMITATION OF ABSTRACT:	18. NUMBER OF PAGES
Unclassified	Unclassified	Unclassified	SAR	66

19a. NAME OF RESPONSIBLE PERSON (Monitor)
Andrew Nauss

19b. TELEPHONE NUMBER *(Include Area Code)*
(937) 255-1150

Standard Form 298 (Rev. 8-98)
Prescribed by ANSI Std. Z39-18

By invitation only: overview article

A critical review of high entropy alloys and related concepts

D.B. Miracle [a, *], O.N. Senkov [a, b]

[a] AF Research Laboratory, Materials and Manufacturing Directorate, Wright-Patterson AFB, OH USA
[b] UES, Inc., 4401 Dayton-Xenia Road, Beavercreek, OH, USA

ABSTRACT

High entropy alloys (HEAs) are barely 12 years old. The field has stimulated new ideas and has inspired the exploration of the vast composition space offered by multi-principal element alloys (MPEAs). Here we present a critical review of this field, with the intent of summarizing key findings, uncovering major trends and providing guidance for future efforts. Major themes in this assessment include definition of terms; thermodynamic analysis of complex, concentrated alloys (CCAs); taxonomy of current alloy families; microstructures; mechanical properties; potential applications; and future efforts. Based on detailed analyses, the following major results emerge. Although classical thermodynamic concepts are unchanged, trends in MPEAs can be different than in simpler alloys. Common thermodynamic perceptions can be misleading and new trends are described. From a strong focus on 3d transition metal alloys, there are now seven distinct CCA families. A new theme of designing alloy families by selecting elements to achieve a specific, intended purpose is starting to emerge. A comprehensive microstructural assessment is performed using three datasets: experimental data drawn from 408 different alloys and two computational datasets generated using the CALculated PHAse Diagram (CALPHAD) method. Each dataset emphasizes different elements and shows different microstructural trends. Trends in these three datasets are all predicted by a 'structure in − structure out' (SISO) analysis developed here that uses the weighted fractions of the constituent element crystal structures in each dataset. A total of 13 distinct multi-principal element single-phase fields are found in this microstructural assessment. Relationships between composition, microstructure and properties are established for 3d transition metal MPEAs, including the roles of Al, Cr and Cu. Critical evaluation shows that commercial austenitic stainless steels and nickel alloys with 3 or more principal elements are MPEAs, as well as some established functional materials. Mechanical properties of 3d transition metal CCAs are equivalent to commercial austenitic stainless steels and nickel alloys, while some refractory metal CCAs show potential to extend the service strength and/or temperature of nickel superalloys. Detailed analyses of microstructures and properties allow two major HEA hypotheses to be resolved. Although the 'entropy effect' is not supported by the present data, it has nevertheless made an enduring contribution by inspiring a clearer understanding of the importance of configurational entropy on phase stability. The 'sluggish diffusion' hypothesis is also not supported by available data, but it motivates re-evaluation of a classical concept of metallic diffusion. Building on recent published work, the CCA field has expanded to include materials with metallic, ionic or covalent bonding. It also includes microstructures with any number of phases and any type of phases. Finally, the MPEA field is shown to include both structural and functional materials applications. A significant number of future efforts are recommended, with an emphasis on developing high-throughput experiments and computations for structural materials. The review concludes with a brief description of major accomplishments of the field and insights gained from the first 12 years of research. The field has lost none of its potency and continues to pose new questions and offer new possibilities. The vast range of complex compositions and microstructures remains the most compelling motivation for future studies.

Contents

1. Introduction

The first results on multi-component [1] and high entropy [2—6] crystalline alloys were published in 2004, about 12 years ago. The two major, new concepts of this approach include opening a vast, unexplored realm of alloy compositions and the potential to influence solid solution phase stability through control of configurational entropy. These two distinct ideas have captured the imagination and efforts of growing numbers in the materials science community. This field is characterized by many new findings, unexplained results, vigorous controversies and new fundamental questions. A large body of work has been published, including several compilations and viewpoint sets [7—15] and two books [16,17]. This extensive literature gives data against which the initial concepts can be evaluated and trends can be established, but a critical assessment of this rapidly evolving field is not yet available.

The purpose of this paper is to critically assess the major ideas and proposed characteristics of high entropy and multi-principal element alloys against published data and established materials science knowledge.

As much as possible, each section of this assessment is intended to be independent − each can be read separately and ends with a summary of main points. The hurried reader is referred to the summaries at the end of each major section for topical results and to Section 8 for a quick synopsis of major accomplishments and insights. Section 1 introduces the field of multi-principal element and high entropy alloys. A brief historical sketch (Section 1.1) is followed by definitions (Section 1.2). In many studies, definitions are woven together with motivations and expected outcomes, and so these are also discussed. The major ideas behind multi-principal element and high entropy alloys are described in Section 1.3. Attempts to visualize and describe hyper-dimensional composition space (Section 1.4) are followed by a brief summary (Section 1.5).

The remaining manuscript is organized into the following major topics. Section 2 discusses the application of classical thermodynamic concepts to complex, concentrated alloys. The taxonomy of high entropy and multicomponent alloys in Section 3 organizes reported alloys into common element groupings, illustrating biases and emerging trends. Microstructures (Section 4) and properties (Section 5) are analyzed to explore hypotheses regarding phase stability, strengthening and other major concepts in complex, concentrated alloys. This review closes with consideration of potential applications (Section 6), suggested future directions (Section 7) and concluding remarks of insights and major accomplishments (Section 8).

1.1. Historical sketch

The first results on crystalline multi-principal element alloys (MPEAs) [1] and high entropy alloys (HEAs) [2–6] were published in the same year, but background work began much earlier [17]. For MPEAs, initial studies began as an undergraduate thesis in the late 1970's and were followed by another undergraduate project in 1998. These studies were refined and expanded, presented at a conference in 2002 and subsequently published [1]. HEA work began as a series of theses in 1996, leading to five publications in 2004 [2–6]. The terms, 'high entropy alloys' and 'multi-principal element alloys' (MPEAs) were both introduced in this last group of publications.

In addition to these modern publications, three other early works are worth mentioning. A very early work reported the basic properties (hardness, density, etc) of mixtures of up to 7 metallic elements in equal mass fractions (see Section 1.4.1 in Ref. [17]). Drawn from 11 different elements, over 900 alloys were characterized. Well ahead of it's time, it seems to have been forgotten until re-introduced in 1963 [18]. In spite of this more modern exposure, this early work remained relatively obscure, and was re-introduced once again to put the modern HEA and MPEA concepts into historical perspective [17]. A second paper of historical note applied the MPEA concept to metallic glasses [19]. This paper used equimolar substitution of chemically similar elements in a known metallic glass alloy. This is the first modern publication to introduce the idea of the expansive range of composition space offered by MPEAs. This is also the first modern published paper to give experimental results on this topic. A paper published in 2003 is also important in the HEA field [20]. This paper gives no results, but provides an eloquent and evocative introduction to major HEA concepts, which were in press at the time and were published early the following year.

1.2. Definitions and motivations

The motivation in one of the founding papers is "to investigate the unexplored central region of multicomponent alloy phase space" [1]. Entropy is not mentioned and there is no stated intent to search for single-phase, disordered solid solution (SS) phases. On the other hand, HEA studies often appear to be motivated by the concept that high configurational entropy may favor single-phase SS phases over alloys with intermetallic (IM) phases [5,6]. Both motivations explore the interior regions of hyper-dimensional composition space, away from the vertices, edges and faces, but HEA studies additionally emphasize the search for single-phase solid solutions. No definition is given for 'multicomponent alloys' [1], while several HEA definitions exist. The number of HEA definitions gives some confusion, fueling controversies whether some alloys may be called HEAs. Commonly used definitions and controversies will be introduced and discussed.

1.2.1. Composition-based definition

One of the earliest papers defines HEAs as, "those composed of five or more principal elements in equimolar ratios" [6]. The requirement for equimolar concentrations is restrictive, and the following sentence in the same paper expands this definition to include, "principal elements with the concentration of each element being between 35 and 5 at.-%." Thus, HEAs need not be equimolar, increasing the number of HEAs significantly. HEAs may also contain minor elements to modify the properties of the base HEA, further expanding the number of HEAs [21]. This composition-based definition prescribes elemental concentrations only and places no bounds on the magnitude of entropy. This definition further places no requirement on the presence of a single-phase SS.

1.2.2. Entropy-based definition

The phrase, "high entropy" motivates a definition based on the magnitude of entropy. Thus, an alternate definition separates low ($S^{SS,ideal} < 0.69R$, where $S^{SS,ideal}$ is the total configurational molar entropy in an ideal SS and R is the gas constant), medium ($0.69R < S^{SS,ideal} < 1.61R$) and high ($S^{SS,ideal} > 1.61R$) entropy alloys [21]. The Boltzmann equation gives a simple approach to estimate $S^{SS,ideal}$ from alloy composition, but it requires that atoms occupy random lattice positions. This rarely occurs in metallic solutions (Section 2.1.1). This definition also implies that an alloy has a single value of configurational entropy. However, an alloy's entropy can change with temperature. The temperature effect can be mild, by giving small changes in short-range atomic ordering, or it can be dramatic, by chemical partitioning between parent and product phases at a first-order phase transformation. To address these issues, the entropy-based definition assumes the alloy can be represented by the "liquid solution and high-temperature solid solution states where the thermal energy is sufficiently high to cause different elements to have random positions within the structure" [21]. This characterizes an alloy by the maximum entropy possible, and implies that such a state is achieved at high temperature or in the liquid state. However, even binary metallic liquids typically do not have random atomic positions at the melting temperature (Section 2.1.1). This underscores earlier findings that metallic solutions are generally not ideal [22]. These issues represent challenges in the use of this definition.

1.2.3. Other definitions and interpretations

Beyond these primary HEA definitions, several other interpretations appear in the literature. Some papers introduce HEAs as equimolar alloys only and some use different values of $S^{SS,ideal}$ to specify HEAs. This is supported by ambiguity that comes from

combining composition-based and entropy-based definitions. Specifically, the maximum configurational entropy of a 5-element HEA is $1.61R$ (for the equimolar alloy), but the minimum value is $1.36R$ (for an alloy with 5% A, 5% B, 20% C, 35% D and 35% E). This latter alloy is considered to be an HEA by the composition-based definition but not by the entropy-based definition. Some have considered quaternary equimolar alloys with $S^{SS,ideal} = 1.39R$ as HEAs [23,24], since this is higher than the minimum value offered by the composition-based definition, even though these are excluded by the composition-based definition. As a compromise, some have suggested that any alloy with $S^{SS,ideal} \geq 1.5R$ may be considered HEAs [25]. This excludes a small number of alloys allowed by the composition-based definition and any alloy with fewer than 5 elements.

Perhaps the most common interpretation that differs from primary definitions is that an HEA must be a single-phase, SS (see for example comments in Ref. [9]). This emphasizes the widely-stated *motivation* of producing single-phase, SS microstructures, even though this is not required by either of the primary definitions. Rather than characterizing an alloy based on the maximum possible (i.e., ideal) value of configurational entropy, this interpretation emphasizes the actual configurational molar entropy of an alloy (S^{SS}), which can be much lower. This has a logical appeal, but nevertheless has conceptual challenges. This approach reasons that a SS phase that remains after nucleating a product phase may no longer meet composition-based or entropy-based HEA definitions, even though the parent SS phase satisfied the definitions. This confuses the configurational entropy of the alloy with entropy of individual phases within the alloy. Further, rejecting alloys that are multi-phase at *some* observation temperature implies that the alloy must be single-phase at *all* temperatures. Since the entropic energy is given by the product, $-TS^{SS}$, at $T = 0$ this interpretation reduces the number of alloys that could be considered as HEAs to a trivial few regardless of the magnitude of S^{SS} [26].

We acknowledge the right of the discoverer to name and define the discovery, and so here we emphasize definitions in the earliest works as long as there are no conceptual difficulties. There is no fundamental issue with the composition-based definition. The entropy-based definition has conceptual challenges, and further confusion results when composition- and entropy-based definitions are taken together. These challenges are deepened by mixing definitions with the intended outcome of producing single-phase SS alloys. Some studies tighten the definition (an HEA must be single-phase or must be equimolar) and in others the definition is broadened (to include 4 component systems and alloys with $S^{SS,ideal} > 1.36R$ or $S^{SS,ideal} > 1.5R$). Early definitions emphasize the maximum configurational entropy that *may* be possible in a system, whereas later interpretations favor actual (lower) values of configurational entropy. Initial definitions favor atom configurations at the highest temperatures including the liquid state, while later interpretations emphasize lower temperatures. There is no right or wrong answer, and the appropriate approach will depend on the intent of the work being performed.

1.2.4. Use of terms, HEA, MPEA and CCA in the present work

Whether initially intended or not, HEAs have become tightly associated with finding single-phase solid solutions by controlling configurational entropy. This causes controversy and distracts from the major objective of exploring the immense number of alloys in the central regions of hyper-dimensional composition space. There are several terms that evoke the vastness of composition space without any implications concerning the magnitude of entropy or the types of phases present. These terms include multi-principal element alloys (MPEAs), complex concentrated alloys (CCAs) and baseless alloys. In the present work we use these terms

interchangeably to describe the field broadly and to retain the motivation, "to investigate the unexplored central region of multicomponent alloy phase space" [1]. We use the term, HEA, when configurational entropy or the intent to produce single-phase SS microstructures are important. This careful use of terms is a practical approach to clarify discussion and to side-step an unproductive controversy, and is in no way intended to detract from the contributions of the pioneers in this field.

This review covers the field broadly. Thus, we include alloys that fit any of the definitions above, including concentrated ternary and quaternary alloys and other alloys that may not fit HEA definitions but nevertheless have features that contribute to the study or development of MPEAs. Multi-phase microstructures are specifically included here in the CCA concept.

1.3. Major concepts and proposed features

The HEA field introduces the major new ideas of intentionally exploring the vast realm of hyper-dimensional complex composition space and manipulating configurational entropy via alloy composition to favor SS alloys. The HEA field also proposes four characteristic HEA features. Each of these topics is briefly discussed below.

1.3.1. The vastness of new compositions and microstructures

The expansive range of new alloys and alloy systems offered by the interior regions of multi-principal element phase diagrams is a central idea in early MPEA publications [1,6,20]. This offers rich opportunities for the discovery of new alloys of scientific significance and practical benefit. Supporting this expectation, attractive structural and functional properties have already been reported, including one MPEA with a fracture toughness exceeding that of "virtually all pure metals and metallic alloys" [27]. A range of microstructures has also been produced that includes single-phase solid solutions, multi-phase alloys, nanocrystalline microstructures and amorphous structures (Section 4). Early HEA work shows attractive properties in multi-phase microstructures with boride [3] or nitride [2] phases, and many HEAs include compound-forming elements such as Al or Ti, producing unusual and attractive microstructures. In spite of the breadth of microstructures offered, the HEA field has come to strongly emphasize the search for single-phase solid solutions (Section 1.3.2). More recently, a call has been issued to embrace the development of multi-phase CCAs with microstructures that may give good high temperature structural properties [25,26]. Conventional alloy development strategies typically rely on microstructures with at least one SS phase, but recent work suggests that even microstructures consisting of two IM phases may give an attractive balance of structural properties if sufficient attention is paid to controlling the microstructure [28]. Broadening efforts to include the exploration of multi-phase microstructures in CCAs is an area of future emphasis (Section 4.1.5, Section 7.1.1).

1.3.2. Rationalizations for single-phase solid solutions

The search for single-phase SS alloys is sometimes rationalized by claiming that IM phases embrittle alloys and make processing difficult, while SS alloys are claimed to be strong and to retain ductility and damage tolerance (see for example, [6,21,29]). These generalizations are somewhat overstated. While IM formation often does embrittle alloys, this is not always the case. In fact, IM or ceramic phases are intentional, essential and major microstructural components in many of the most advanced structural alloys, including superalloys (for which the IM phase is often the largest constituent by volume), pearlitic steels and age-hardened aluminum alloys. Proper control of the size, shape, volume

fraction and distribution of IM or ceramic phases is responsible for an exceptional balance of strength and damage tolerance in such alloys.

Solid solution hardening is an important strengthening mechanism, but it is generally not as potent as precipitation-strengthening. Consider commercial solid solution and precipitation strengthened alloy families based on the same element: 3xxx or 5xxx series solid solution aluminum alloys vs 2xxx or 7xxx series age-hardened aluminum alloys; solid solution nickel alloys such as Alloy 400 (UNS No. N04400), Alloy 600 (UNS No. N06600) and Alloy 800 (UNS No. N08800) vs precipitation strengthened super-alloys; and solid solution austenitic steels vs pearlitic steels. In each of these examples, precipitate-strengthened alloys have superior strength relative to SS alloys while retaining useful ductility and damage tolerance [30]. Solid solution hardening may be more potent in MPEAs relative to conventional solution-strengthened alloys, but this hypothesis requires validation (Section 7.1.3). Finally, it is not always true that SS alloys are ductile. Well-known examples include β-titanium alloys, α-titanium alloys with small amounts of oxygen, and nickel alloys with small amounts of hydrogen. Many BCC metals also display a brittle-to-ductile transition temperature above which the alloy is ductile but below which it is intrinsically brittle.

The purpose of this discussion is not to contradict the generalizations used to support the search for single-phase SS alloys, but rather to give a more balanced view of the roles played by SS and IM phases in alloy properties. The general approach in alloy development is to establish properties required by an application, and then to develop compositions and microstructures that can provide all of the necessary properties [31]. The full range of applications and properties are open for consideration, and so the full range of microstructures should also be considered. Such an approach takes full advantage of the principal benefit of CCAs − the broad range of unexplored compositions *and microstructures*.

1.3.3. Four HEA 'core effects'

Four 'core effects' are often used to describe HEAs: the high entropy effect; the lattice distortion effect; sluggish diffusion; and the 'cocktail' effect [21]. Three of these are hypotheses and the 'cocktail' effect is a separate characterization of HEAs. These hypotheses were first proposed based on information available in the very earliest publications. A major objective of this assessment is to evaluate these hypotheses against the broader range of published data collected in the past 12 years. These hypotheses are briefly introduced below and are evaluated later in the manuscript.

1.3.3.1. The high entropy effect. The high entropy effect is the signature concept of HEAs, and proposes that increased configurational entropy in near-equimolar alloys with 5 or more elements may favor SS phases over competing IM compounds. Idealized configurational entropy is compared with the entropy of fusion for pure metals [6,17] or with formation enthalpies of selected IM compounds [6,25] to support this concept. Comparisons are generally qualitative (characterizing enthalpies and entropies as "high" or "low"), and are applied broadly by comparing all SS phases to all IM compounds, without considering specific systems and without acknowledging that a wide range of stabilities exists in SS and IM phases. These discussions only consider configurational entropy. While vibrational, electronic and magnetic terms are acknowledged [6,17], the configurational term is claimed to dominate [17]. We show that the vibrational entropy is much larger than $S^{SS,ideal}$ (Section 2.3.4), but the thermodynamic competition between SS and IM phases is rather complicated (Section 2.3.5) and much of the vibrational entropy cancels in parent and product phases. Finally, early observations supporting this effect emphasize

phases in as-cast product, complicating interpretation. The degree to which configurational entropy actually favors SS phases will be assessed against classical thermodynamic concepts (Section 2) and published microstructures (Section 4).

1.3.3.2. The lattice distortion effect. Severe lattice distortion comes from the different atom sizes that make up crystal lattices of complex, concentrated phases. The displacement at each lattice site depends on the atom occupying that site and the types of atoms in the local environment. These distortions are claimed to be more severe than in conventional alloys. Uncertainty in atom positions from these distortions contributes to the excess configurational entropy (Section 2.3.3), and is claimed to decrease the intensity of X-ray diffraction peaks [5,17,21], to increase hardness [17,21], to reduce electrical and thermal conductivity [17,21] and to reduce the temperature dependence of these properties [17,21]. These claims seem physically sensible, but systematic attempts to quantify most of these effects and to separate them from other contributions are still missing. For example, shear modulus mismatch between constituent atoms may also contribute to hardening, and electrical and thermal conductivities can be influenced by the electronic structures associated with variations in local bond states. Additional discussion is given in Section 4.4.4 and Section 7.1.8.

1.3.3.3. The sluggish diffusion effect. Diffusion is proposed to be sluggish in HEAs [6,21]. This claim is based on secondary observations that include formation of nanocrystals and amorphous phases upon solidification and on qualitative interpretations of microstructural stability upon cooling (Section 5.2). To further support this position, general comments relating to difficulty in substitutional diffusion and high activation energies are invoked [6]. One study has measured diffusion coefficients in complex alloys [32]. Analysis of this hypothesis is given in Section 5.2.

1.3.3.4. The 'cocktail' effect. The 'cocktail' effect is a colorful and evocative phrase first used by Prof. S. Ranganathan [20]. His initial intent was simply, "a pleasant, enjoyable mixture," but it later came to mean a synergistic mixture where the end result is unpredictable and greater than the sum of the parts [33]. This phrase was introduced to describe three distinct alloy classes: bulk metallic glasses; super-elastic and super-plastic metals (also called 'gum' metals [34]); and HEAs. Each of these alloy classes includes complex, concentrated alloy compositions. The 'cocktail' effect addresses the rather remarkable properties of fully amorphous bulk metallic glasses and the extreme structural and functional properties of 'gum' metals.

Unlike the other 'core effects', the 'cocktail' effect is not a hypothesis and requires no proof. The 'cocktail effect' reminds us that exceptional materials properties often result from unexpected synergies. Other materials responses could also be described as resulting from an unpredictable, synergistic response, including physical properties such as a near-zero coefficient of thermal expansion or catalytic responses; functional properties such as the thermo-electric response or photo-voltaic conversion; and an exceptional combination of structural properties such as ultra-high strength with good fracture toughness, fatigue resistance or ductility. In each of these cases, properties depend on material composition, microstructure, electronic structure and other features in complicated and sensitive ways. The 'cocktail' effect reminds us to remain open to non-linear, unexpected results that can come from unusual combinations of elements and microstructures in the vast composition space of MPEAs.

1.4. Visualization of hyper-dimensional composition space

Some concepts in this review require an ability to visualize hyper-dimensional composition space. Here we attempt to describe the main features, starting with ternary and quaternary phase diagrams and then moving to more complex phase diagrams. A ternary phase diagram has three constituents, N, and is shown in two spatial dimensions (2D) by an equilateral triangle at constant temperature, T, and pressure, P. Each vertex represents a pure, elemental constituent and each edge gives a binary phase diagram at the specified T, P. The three lines drawn from each vertex to the middle of the opposite edge intersect in the center of the diagram at the equimolar atom fraction, $1/N$. A quaternary phase diagram is shown at constant T, P in three dimensions (3D) by a regular tetrahedron. The 4 vertices represent the elemental constituents, the 4 faces are the bounding ternary diagrams, and the 6 edges are the bounding binary diagrams. Lines drawn from each vertex to the middle of the opposite face intersect at the equimolar atom fraction in the center of the tetrahedron. The bounding edges and faces of ternary and quaternary phase diagrams are straight lines and flat surfaces in 3D.

The same basic features hold for five component phase diagrams. $(N\text{-}1)$ spatial dimensions are needed to map quinary composition space at constant T,P, requiring 4 spatial dimensions (4D). This 4D phase diagram has 5 vertices, each with an opposite boundary that is a 3D tetrahedron of the remaining 4 elements. The 4D quinary phase diagram has ten 2D boundaries that are the constituent ternary diagrams and has ten 1D edges representing the bounding binary phase diagrams at the specified T,P. The boundaries of the quinary diagram are straight and flat in 4D but are curved in 3D in the same way that a line is straight in 2D but can be curved in 3D (consider a great circle on the surface of a sphere). The curvature is opposite that of the great circle example, so that the 3D 'shadow' of the 4D quinary phase diagram may be considered to be stellated — 'spiky' at the vertices and 'puckered' at the faces and edges.

Three illustrations aid this visualization. Fig. 1a represents a 4D quinary phase diagram. This shows all 5 vertices, all 10 binary diagrams, all 10 ternaries and all 5 quaternary diagrams. All edges are straight and all faces are flat in this visualization. The geometric compromise that allows this to be drawn as an isometric projection is that some of the features (the D-E binary; the A-B-C, A-D-E, B-D-E and C-D-E ternaries; and all of the quaternaries) are in the interior of the volume bounded by the 5 vertices. This unusual figure represents some key features but distorts others — it can be thought of as a 3D compromise representation of a 4D polytope. Graph theory provides a related visualization (Fig. 1b, redrawn from Ref. [35]). Phases are indicated by labeled points, and phases that co-exist with each other are connected by lines. Solid black lines show continuous solid solutions between the constituent elements, all other phase connections are shown by solid gray lines. Like Fig. 1a, positions are distorted and have no meaning. A sample is shown in Fig. 1b for the Co-Cr-Fe-Mn-Ni phase diagram. The calculations used to produce this diagram [36] are at low temperature and show IM phases in the Co-Fe, Co-Mn, Fe-Ni and Mn-Ni binary diagrams, so that a single-phase SS phase with Co, Cr, Fe, Mn and Ni is not shown.

Just as a 3D quaternary diagram can be constructed by a sequential stack of 2D pseudo-ternary diagrams, Fig. 1c illustrates a portion of the 4D, A-B-C-D-E quinary diagram by a series of 3D pseudo-quaternary diagrams. A line is drawn from the center (equimolar composition) of the quaternary ABCD 'hyper-face' to the element E vertex that is opposite. At one end of this line, 4D phase space is simply pure element E, and at the opposite end of this line the quinary phase diagram is the 3D quaternary A-B-C-D diagram. Between these end points, quinary phase space is shown by a series of pseudo-quaternary phase diagrams of compositions $(ABCD)_{1\text{-}x}E_x$, where $0 \leq x \leq 1$ is the fractional distance from the ABCD 'hyper-
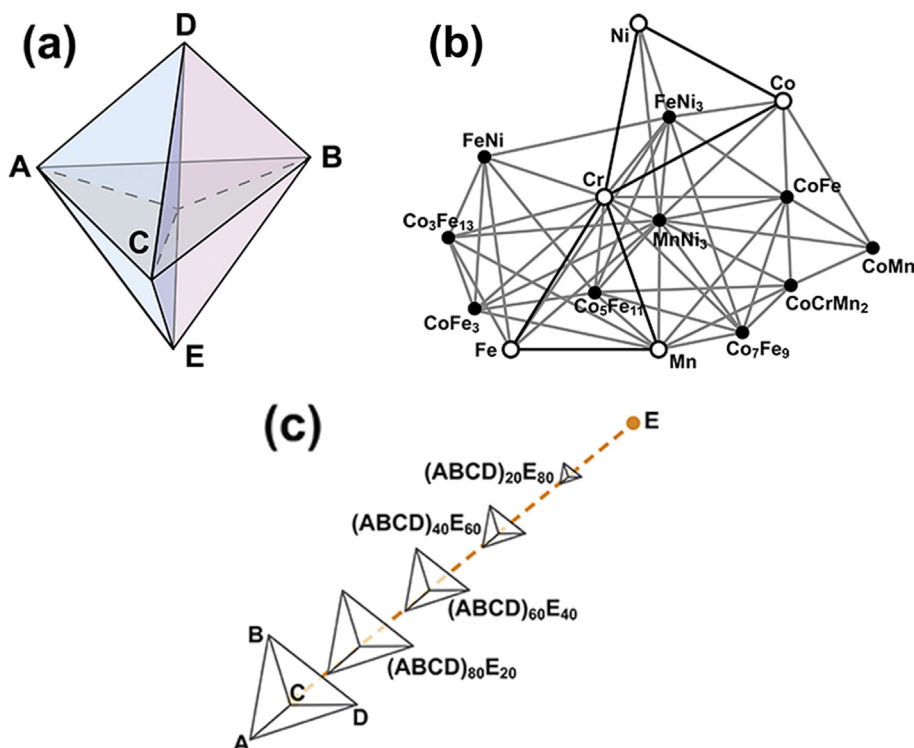

Fig. 1. Visual devices to illustrate 4D phase space in 2D. See text for descriptions.

face' to vertex E. A similar line can be drawn from any composition in the A-B-C-D system (that is, from any point in the quaternary diagram and not only from the equimolar composition) to vertex E, giving a new set of pseudo-quaternary phase diagrams along the new line. Five such quaternary − vertex lines exist in each quinary diagram, and they all intersect at the equimolar composition, ABCDE.

Isopleth diagrams at a fixed P are a more practical approach to map multi-dimensional phase diagrams in 2D. The effects of composition and T on the phases present can be mapped, but only one element can be varied independently at a time. For example, the effect of Al in Al$_x$CoCrFeNi is shown in Ref. [37]. These isopleth diagrams do not show phase compositions or volume fractions. Another practical approach is to plot the volume fractions of the phases present as a function of T at a fixed composition and P (see Fig. 11 in Ref. [38]). This approach does not show phase compositions. Other approaches to visualize 4D space, such as Schlegel diagrams and orthogonal projections, are well-known in the mathematics community and may also be used [39].

How close is the equimolar composition to phase diagram boundaries? The compositional distance from an N-component equimolar alloy to the center of a boundary with $n^* < N$ elements is

$$C = \frac{100(N - n^*)^{1/n^*}}{N} \tag{1.1}$$

The $n^* = 1$ boundaries (elemental vertices) are always farthest from the equimolar point, the $n^* = 2$ boundaries (binary edges) are always the next farthest, and the $n^* = (N - 1)$ boundaries are always closest. As N increases, the vertices become progressively farther from the equimolar point. Thus, vertices are 67%, 75% and 80% distant from equimolar ternary, quaternary and quinary alloys, respectively. The closest boundaries become progressively closer as N increases: binary edges are 33% distant from the ternary equimolar point; ternary faces are 25% away from the quaternary equimolar composition and quaternary boundaries are 20% away from the quinary equimolar alloy. For $N \leq 8$, binary edges are always within 33 ± 2% of equimolar alloys; ternary faces are within 23 ± 2%; and quaternary boundaries are at 19 ± 1% distance. This emphasizes the 'spiky' nature of complex phase diagrams − the midpoint of a ternary boundary is ~25% away from a 5-component equimolar alloy, the midpoint of a binary boundary is ~35% away, but the vertices are 80% away. This also illustrates the difficulty in visualizing the extension of binary and ternary terminal solid solution phase fields into hyper-dimensional composition space. Solid solutions that do not extend much beyond the elemental vertex are not likely to connect with the center of a 5-component phase diagram, but a binary or ternary system that is a solid solution at its midpoint is much closer to the equimolar composition.

1.5. Summary

The MPEA field is barely 12 years old. Many definitions are used to describe HEAs. A composition-based definition is clear, but entropy-based definitions have conceptual problems and a range of derivative definitions are also used. These definitions fuel an unproductive controversy and distract attention from the potential scientific and practical benefits offered by the vastness of hyper-dimensional composition space. As a practical approach, the term, high entropy alloy (HEA) is used when either the configurational entropy or the objective of producing a single-phase solid solution is important. Otherwise, the terms multi-principal element alloys (MPEAs) or complex, concentrated alloys (CCAs) are used to evoke the essential features of this field without any implications regarding the magnitude of configurational entropy or the types of

phases formed. This section also gives a brief historical sketch; introduces the major, new concepts and four 'core effects' provided by MPEAs; and discusses visualization of phase diagrams for multi-component alloys.

2. Thermodynamics of complex, concentrated alloys

Basic thermodynamic concepts are briefly reviewed to give a backdrop against which high entropy alloy (HEA) hypotheses can be discussed and evaluated. This review includes discussion of enthalpy, entropy and Gibbs energy of disordered solid solution (SS[1]) phases (Section 2.1) and ordered intermetallic (IM[1]) compounds (Section 2.2). The influence of multi-principal elements on the magnitudes of these terms is emphasized. Discussion of Gibbs phase rule, equilibrium, variation in atom sizes, total entropy, and the relative magnitudes of entropy and enthalpy appears in Section 2.3, followed by a brief summary (Section 2.4).

Minimizing Gibbs energy, G, is the standard method to predict the thermodynamically stable phases in an alloy. There are many competing phases in an alloy, and the phase or combination of phases with the lowest Gibbs energy is the equilibrium state. The integral molar Gibbs energy for phase $\varnothing$ is

$$G_m^\varnothing = \sum_i x_i(^\circ G_i^\varnothing) + {}^M G_m^{ideal} + {}^E G_m^\varnothing \tag{2.1a}$$

The summation term is the Gibbs energy of the i elemental constituents, ${}^M G_m^{ideal}$ is the ideal molar Gibbs energy of mixing, and ${}^E G_m^\varnothing$ is the excess molar Gibbs energy. This uses CALculated PHAse Diagram (CALPHAD) nomenclature with pre-superscripts $\circ$ (for pure components), M (for mixing) and E (for excess quantities); with superscripts indicating the phase of interest ($\varnothing$ and *ideal* in Eq. (2.1a)); and the subscript, m, for molar quantities [40,41].

To emphasize differences between enthalpy and entropy of SS and IM phases, we expand this equation and rearrange terms. In all cases, we use pure elements as the standard states, so the summation term is removed for expedience and we only discuss mixing and excess terms. Since ${}^M H_m^{ideal} = 0$, ${}^M G_m^{ideal}$ is given by the ideal molar configurational entropy of mixing, ${}^M S_m^{ideal} = -R \sum_i x_i ln(x_i)$ where R is the gas constant and x_i is the atom fraction of element i. ${}^E G_m^\varnothing$ includes the excess molar enthalpy, ${}^E H_m^\varnothing$, and an excess entropy term, ${}^E S_m^\varnothing$. We drop the enthalpy pre-superscript for simplicity and combine ideal and excess entropies into the total molar entropy of mixing, $S_m^\varnothing = {}^M S_m^\varnothing + {}^E S_m^\varnothing$. Finally, we consider only molar quantities and so the subscripts, m, are omitted. The final equation is the familiar result

$$G^\varnothing = H^\varnothing - T(S^\varnothing) \tag{2.1b}$$

where T is absolute temperature. $H^\varnothing$ includes only non-ideal interactions but $S^\varnothing$ includes ideal and excess terms. The phase, $\varnothing$, may be any solid or liquid phase, here we emphasize the distinction between SS and IM phases. SS and IM phases have distinct enthalpies and entropies that are described separately in the following sub-sections. Binary systems are used to illustrate key features, and these ideas can be extended to more complex systems with appropriate derivations. The classical concepts described here are developed more fully elsewhere [40–44]. The thermodynamic

---

[1] A more complete definition of solid solution and intermetallic phases is given in Section 4.1.5.

literature may use other notations and standard states, and so care is needed to ensure the appropriate quantities are being used.

2.1. Entropy and enthalpy of solid solution phases

2.1.1. General features of solid solutions

The Gibbs energy of a SS phase is

$$G^{SS} = H^{SS} - T\left(S^{SS}\right) \qquad (2.2)$$

In ideal solutions, the excess enthalpy of mixing, $H^{SS} = 0$ and the ideal configurational entropy of mixing is $S^{SS,ideal} = -R\sum_i x_i ln(x_i)$.

In regular solutions, $H^{SS} \neq 0$ but the deviation is small and S^{SS} is assumed to be the same as for ideal solutions. A negative deviation from ideal behavior occurs when $H^{SS} < 0$, and a positive deviation when $H^{SS} > 0$. Atoms are distributed randomly in ideal solutions and are assumed to be random in regular solutions (although any deviation from $H^{SS} = 0$ is generally associated with non-random atom arrangements), so that S^{SS} and H^{SS} are symmetric with respect the equimolar composition. Atoms are not randomly distributed in sub-regular solutions, so that S^{SS} or H^{SS} or both are asymmetric about the equimolar composition. This non-random distribution gives a tendency toward phase separation when $H^{SS} > 0$ or chemical short-range ordering (SRO) when $H^{SS} < 0$. The degree of phase separation or SRO can be small or it can be substantial. Both phase separation and SRO decrease the configurational entropy from ideal estimates.

Ideal and regular solutions are uncommon. Analysis of H^{SS} for 1176 binary metallic systems from Ref. [45] (atom pairs with H, B, C, N, O, P and S are excluded in the present analysis) shows that only 4% and 11% of the systems are ideal and regular solutions, respectively. The data in Ref. [45] are for mixing in the liquid state, and the percentages of ideal and regular solutions are expected to be even lower in the solid state. The basic features of solid solutions are summarized in Table 1.

From Eq. (2.2), disordered solid solutions become more stable (that is, have more negative values of G^{SS}) as S^{SS} becomes more positive and as H^{SS} becomes more negative. This does not seem to be widely appreciated in the HEA literature, and large, negative H^{SS} values have been suggested to destabilize disordered solid solutions *by competing with* S^{SS} [46–49]. In fact, large, negative H^{SS} values increase the stability of SS phases. A more likely interpretation of the trends observed in these studies is that systems with large, negative H^{SS} values are also likely to have H^{IM} values for IM phases that are slightly more negative than H^{SS} (Section 2.2.3). H^{SS} and H^{IM} are not independent, and H^{SS} may be a proxy for H^{IM} in these cases.

A common premise in the HEA literature is that the most stable solutions occur at the equimolar composition, but this is not necessarily true for sub-regular solutions [50]. Consider representative thermodynamic functions for regular (Fig. 2a) and sub-regular (Fig. 2b) solid solutions. The most stable composition in Fig. 2a is at the equimolar composition, but in Fig. 2b it is at $x_B = 0.55$. The degree of asymmetry in G^{SS} curves can be relatively mild or it can be more distinct. Analysis of data in Ref. [45] show

that the minimum in H^{SS} can occur anywhere within the range of $x_B = 0.50 \pm 0.10$. Since sub-regular solutions are by far the most common, the most stable solid solutions may generally be displaced from the equimolar composition.

Asymmetry in G^{SS} curves has an important influence on the stability of competing IM phases. The G^{SS} tangent is horizontal for the most stable solution at $G^{SS,min}$, so that an IM must have $G^{IM} < G^{SS,min}$ to co-exist with the SS at the composition of the most stable SS. For the sub-regular solution in Fig. 2b, the most stable SS is at $x_B = 0.55$ and the change in G^{SS} between the most stable solution and the equimolar alloy is small. However, the tangent is no longer horizontal for the equimolar alloy, significantly changing the stability of competing IM phases [50]. Thus, an IM with G^{IM} shown by the closed circle in Fig. 2b will be unstable against $G^{SS,min}$ for the SS at $x_B = 0.55$, but is stable compared to G^{SS} for the equimolar alloy. On the other hand, the IM with G^{IM} shown by the closed square in Fig. 2b will be stable relative to $G^{SS,min}$ for a SS with a composition at $x_B = 0.55$, but is unstable compared to G^{SS} at the equimolar composition.

Fig. 2 is intended to illustrate differences between the equimolar and most stable compositions in sub-regular solutions, and gives only part of the story regarding phase stability — curves for other phases must also be considered for the full picture, including other solid solutions, intermetallic compounds and the liquid phase.

2.1.2. Entropy of solid solutions

The HEA literature focuses almost exclusively on configurational entropy of ideal solutions, where atoms are distributed randomly. Early statements that atoms are randomly distributed [5] have not been verified — the large number of elements makes this a daunting experimental challenge [51]. The previous section shows that most binary solutions are sub-regular, so that atom arrangements are expected to be non-random. It is not clear to what extent this will influence the magnitude of configurational entropy or the shape of entropy curves. Other contributions to entropy include an excess configurational term resulting from different-sized atoms (Section 2.3.3), and non-configurational terms from vibrations, electronic and magnetic effects. The total influence of these terms can be significant (Section 2.3.4).

2.1.3. Enthalpy of solid solutions

Experimental H^{SS} data (see for example [52,53]) are difficult to obtain, so data are limited. H^{SS} can be estimated for binary solutions. A common approximation is the macroscopic atom model, often called the Miedema method [54]. This phenomenological model uses as input the electron density at the Wigner-Seitz cell boundary (estimated from the ratio of bulk modulus to molar volume) and the chemical potential of electronic charge (taken from the work function) of pure metals. This method can be applied to any system, but the accuracy is only fair. Comparison of several dozen predicted [45] and published [55] H^{SS} values in the liquid state give typical differences of the order of ±7 kJ-mol^{-1}. The median estimated H^{SS} is -5.1 kJ mol^{-1} so the percentage error is large, around $\pm50\%$. Even removing comparisons where $|H^{SS}|$ is small (<10 kJ-mol^{-1}) and the percentage error is very large ($>100\%$), the

Table 1
Features of solid solutions.

Type	H^{SS}	S^{SS}	Atom distribution	Curve shape	Frequency
Ideal	0	$-R\sum_i x_i ln(x_i)$	Random	Symmetric	Uncommon ($\approx 4\%$)
Regular	$\neq 0$	$-R\sum_i x_i ln(x_i)$	$\approx$ Random	Symmetric	Uncommon ($\approx 11\%$)
Sub-regular	$\neq 0$	No simple model	Non-random	Asymmetric	Common ($\approx 85\%$)

9
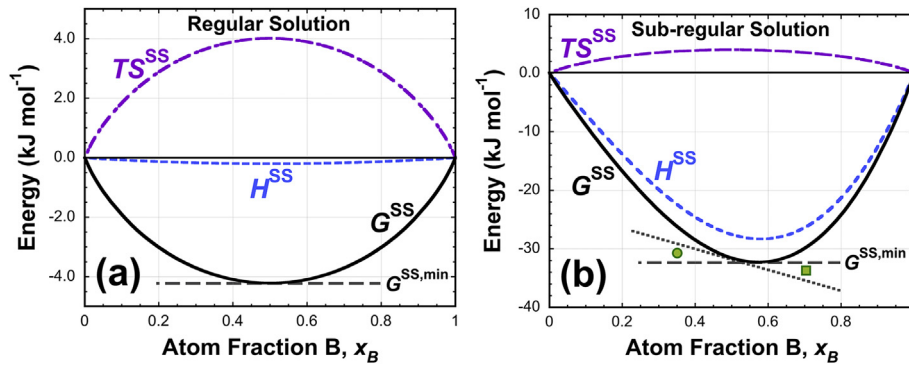
Fig. 2. The integral molar entropy, enthalpy and Gibbs energy (S^{SS}, H^{SS}, G^{SS}) at 700 K for negative deviations from ideal behavior ($H^{SS} < 0$) in (a) a regular solution, where atoms are distributed nearly randomly and H^{SS}, S^{SS} and G^{SS} are all symmetric about $x_B = 0.5$, and (b) a sub-regular solution, where atoms are not randomly distributed so that H^{SS} and G^{SS} are not symmetric. The areas between the dashed and dotted tangent lines in (b) show regions where phase stability is altered by asymmetry of the G^{SS} curve. Ideal S^{SS} is assumed and H^{SS} is taken from Ref. [45] for (a) Co-Ni and (b) Ce-Ni.
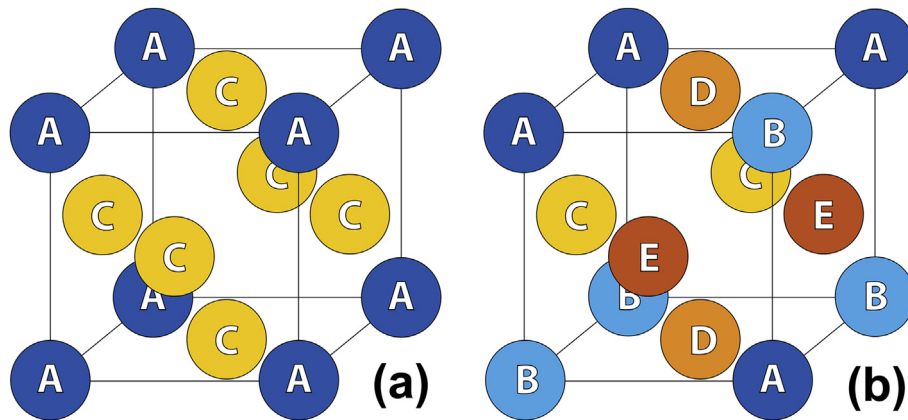
Fig. 3. Ordered crystals with (a) $S^{IM,ideal} = 0$ resulting from perfect order on A and C sub-lattices, and (b) a significant $S^{IM,ideal}$ due to disordered arrangements of A, B atoms on the A sub-lattice and of C, D, E atoms on the C sub-lattice.

typical error for remaining comparisons is still ±35%. This is larger than experimental errors, which can be as high as ±20% but are typically about ±5%. Variability in measured values for the same phase from different research groups is in the same range, roughly ±5% to ±15%. Nevertheless, the Miedema method gives quick and easy access to the general magnitudes of mixing enthalpies for all binary metallic systems.

H^{SS} values from binary solutions can be used to estimate the integral, molar enthalpy of mixing for N-component, complex solutions, $H^{SS,N}$ [45,56].

$$H^{SS,N} = \sum_{\substack{i=1 \\ i \neq j}}^{N_{ij}} 4c_i c_j \sum_{k=0}^{3} \Omega_k \left[(c_i - c_j)/(c_i + c_j) \right]^k = \sum_{i,j=1}^{N} 2c_i c_j \omega_{ij}$$

(2.3)

where N_{ij} is the number of i-j atom pairs, c_i and c_j are the i, j atom concentrations, Ω_k are parameters to fit H^{SS} in i-j solutions [45] and $\omega_{ij} = \sum_{k=0}^{3} \Omega_k [(c_i - c_j)/(c_i + c_j)]^k$ is an interaction parameter between elements i and j in a sub-regular solid solution [45]. Eq. (2.3) can accentuate the enthalpy of mixing in complex alloys when all binary H^{SS} values have the same sign (all positive or all negative). Like a parachute suspended from the corners of a room, the highest points will be in the corners, lower points occur along the walls, and the lowest point is near the middle of the room. Thus, when H^{SS}

< 0 for all atom pairs in an N-component solution, $H^{SS,N}$ can be more negative than any of the binary pairs. If $H^{SS} < 0$ for some atom pairs and $H^{SS} > 0$ for others, then the magnitude of $H^{SS,N}$ relative to the constituent H^{SS} values depends sensitively on composition.

2.2. Entropy and enthalpy of intermetallic phases

2.2.1. General features

Intermetallic compounds display long-range ordering (LRO) of atoms on two or more sub-lattices and so are structurally distinct from SS phases, see for example [57,58]. Atoms are randomly distributed in ideal and regular SS phases, so that the probability of finding an i atom on a given lattice site is equal to the atom fraction of that element, x_i. Atoms are not random in sub-regular solutions, but the probability of an i atom occupying a given site will not vary dramatically from x_i. Due to LRO, the probability of finding a particular atom on a given sub-lattice in a binary IM is not equal to x_i, and is typically very near 0 or 1. The probabilities may vary a small amount from 0 or 1, even in compounds that form only at a single composition (usually the stoichiometric composition). Variations from probabilities of 0 or 1 can also occur at non-stoichiometric compositions in the relatively small number of IM phases that are stable over a range of compositions. Probabilities may change more substantially as an IM approaches its dissolution or melting temperature, and some IMs display an order-disorder transformation temperature below which the structure has LRO

and above which it transforms to a SS. In spite of these exceptions, IMs are characterized by LRO on distinct sub-lattices with site occupancies that differ substantially from x_i, and so are fundamentally different from solid solutions. Some HEA papers include IM phases that vary from the stoichiometric composition as SS phases. Here we keep these separate and consider any phase with two or more sub-lattices to be an IM regardless of the range of compositions. Additional support for this distinction is given in Section 4.1.3.

The Gibbs energy for IM phases is

$$G^{IM} = H^{IM} - TS^{IM} \tag{2.4}$$

where H^{IM} and S^{IM} are the integral, molar formation enthalpy and entropy of IM phases.

2.2.2. Entropy of intermetallic phases

Given the important structural differences, SS and IM entropies are different, even in the same system and at the same composition. A classical binary IM is shown in Fig. 3a, where each sub-lattice is occupied by a single element. S^{IM} of such phases are typically very small and are reasonably approximated as zero [44]. However, IM phases in complex, concentrated alloys (CCAs) usually have more constituents than sub-lattices, so that two or more elements will usually occupy each sub-lattice. For example, an IM in alloy ABCDE may have a random distribution of elements A and B on one sub-lattice and a random distribution of elements C, D and E on the second sub-lattice (Fig. 3b). This is just one example, atoms may distribute on the sub-lattices in many different ways. This introduces disorder that increases the configurational entropy of IM compounds in CCAs. The ideal configurational entropy of such structures can be estimated from the sub-lattice model [40] as

$$S^{IM,ideal} = -R\left(\sum_{x=1}^{x} a^x \sum_{i=1}^{N} f_i^x \ln(f_i^x) \right) \bigg/ \sum_{x=1}^{x} a^x \tag{2.5a}$$

where a^x is the number of sites on the x sub-lattice and f_i^x is the fraction of element species i randomly distributed on the x sub-lattice. The total number of element species, i, is N.

For the $(A,B)_1(C,D,E)_3$ structure in Fig. 3b, there are two sub-lattices x,y; the number of sub-lattice sites are $a^x = 1$ and $a^y = 3$; and the fractions of element species i on each sub-lattice is the inverse of the number of atom species on each sub-lattice, n^x. There are two atom species (A,B) on sub-lattice x so that $n^x = 2$ and $f_A^x = f_B^x = 1/2$ and three atom species (C,D,E) on sub-lattice y so that $n^y = 3$ and $f_C^y = f_D^y = f_E^y = 1/3$. For the structure in Fig. 3b, Eq. (2.5a) becomes

$$S^{IM,ideal} = -R[a^x ln(1/n^x) + a^y ln(1/n^y)]/(a^x + a^y) \tag{2.5b}$$

This gives $S^{IM,ideal} = 0.997R$, which is over 60% of the configurational entropy of an ideal equimolar disordered SS with 5 constituents. Care is needed in applying this model, as the composition of the IM phase will generally be different from the alloy composition, and the composition on each sub-lattice may differ from stoichiometric ratios [56].

Unlike binary IM compounds, $S^{IM,ideal}$ may thus make an important contribution to G^{IM} in CCAs. Some commercial alloys with up to a dozen alloying elements are based on compounds, most notably Ni$_3$Al (L1$_2$, cP4, AuCu$_3$)[2] and NiAl (B2, cP2, ClCs)[2], but the concentrations of many elements are small and so this effect

may not be as important as in CCAs. It is difficult to determine experimentally when a particular sub-lattice is occupied by more than one element, and it is even more difficult to determine if those elements are randomly distributed on the sub-lattice [51,59]. As a result, the influence of sub-lattice disorder on $S^{IM,ideal}$ and the stability of IM compounds in CCAs may be important but is not yet established. The principles guiding elemental partitioning to different sub-lattices and the frequency with which this occurs remain unknown. It may therefore be inappropriate to assume that $S^{IM,ideal}$ contributions to G^{IM} can be ignored in CCAs.

2.2.3. Enthalpy of intermetallic phases

LRO leads to differences between H^{SS} and H^{IM}. To understand these differences, it is helpful to consider the bond enthalpies between i and j first-neighbor atoms, ε_{ij}, and the numbers and types of first-neighbor bonds per atom, n_{ij}[3]. Classical solution theory [42–44] gives the enthalpy of a condensed substance by summing ε_{ij} over all n_{ij} bonds in the structure,

$$H = \sum_{i,j} (n_{ij}\varepsilon_{ij}) \tag{2.6}$$

Intermetallic compounds and solid solutions of the same composition have essentially the same bond enthalpies ε_{ij}, but differences in ordering give different values of n_{ij}. For example, $n_{AA} = 0$ in the AC$_3$, L1$_2$ structure (cP4, AuCu$_3$ prototype, see Fig. 3a) since each A atom is surrounded only by C atoms, but $n_{AA} > 0$ for random solid solutions. Table 2 compares n_{ij} values in L1$_2$ and B2 (cP2, ClCs prototype) compounds against disordered FCC, HCP and BCC solutions of the same compositions. n_{ij} values for Al-Ni compounds are taken from Ref. [60] and the numbers of bonds in ideal and regular solutions are $n_{ii} = n_{tot}x_i^2$ and $n_{ij} = 2(n_{tot}x_ix_j)$ where n_{tot} is the number of bonds per atom. Table 2 shows that the numbers of unlike bonds, n_{AB}, are higher in IM compounds than in SS phases of the same composition and base crystal structure. n_{AA} and n_{BB} are both smaller than (in the L1$_2$ structure) or equal to (in the B2 compound) n_{ii} values in the solution.

Table 2 gives ε_{ij} for L1$_2$ and B2 compounds in the Al−Ni system and for solid solutions of the same compositions [60]. Since compounds generally have more of the most stable bonds (bonds between unlike atoms) relative to disordered solutions of the same composition, it is expected that $H^{IM} < H^{SS}$. Estimating H^{IM} and H^{SS} from the data in Table 2 and Eq. (2.6) confirms this result (see the seventh column in Table 2). The bond enthalpies are the same in these SS and IM phases and the differences in bond numbers are small, reinforcing the expectation that H^{IM} and H^{SS} are related (Section 2.1.1). The L1$_2$ and FCC/HCP structures have a total of 6 bonds per atom ($n_{tot} = 6$) and the BCC structure has $n_{tot} = 7$. The B2 structure also has 7 bonds per atom even though the elements that make up the B2 structure almost always have FCC or HCP crystal structures with $n_{tot} = 6$. This 'extra' bond may contribute to the stability of B2 compounds. The pairwise bonding framework described above is a substantial simplification aiming to show the origin of differences between H^{SS} and H^{IM}. More precise calculations of these quantities generally use multibody potentials.

Histograms of H^{IM} and H^{SS} are shown in Fig. 4 for binary systems. Data are taken from Refs. [52,54,55,61–65]. H^{IM} is essentially always negative, in agreement with the classical concept that IM phases only form in systems with a negative deviation from ideal

---

[2] Structures are described by Strukturbericht notation, Pearson symbols and the prototype phase.

[3] First neighbors in this analysis are determined by Voronoi tessellation, and so may have different bond lengths. Voronoi tessellation is an accepted approach that overcomes the arbitrary assignment of cut-off distance between first and second neighbor atoms.

Table 2
Numbers of bonds per atom and estimated formation enthalpies in different structures.

x_A	Structure	n_{AA}	n_{AB}	n_{BB}	n_{tot}	$\sum_{ij}(n_{ij}\varepsilon_{ij})$[b]	ε_{AlAl} (eV)[b,c]	ε_{AlNi} (eV)[b,c]	ε_{NiNi} (eV)[b,c]
0.25	L1$_2$, cP4, AuCu$_3$[a]	0	3	3	6	−4.62	−0.57 ± 0.01	−0.80 ± 0.02	−0.74 ± 0.02
	FCC, HCP	0.375	2.250	3.375	6	−4.51			
0.50	B2, cP2, ClCs[a]	1.5	4	1.5	7	−4.62	−0.49 ± 0.01	−0.73 ± 0.02	−0.64 ± 0.02
	BCC	1.75	3.5	1.75	7	−4.53			
	FCC, HCP	1.5	3	1.5	6	−3.89			

[a] Strukturbericht notation, Pearson symbol, prototype.
[b] Values given as eV/atom.
[c] Condensed bond enthalpies are taken from Ref. [60].
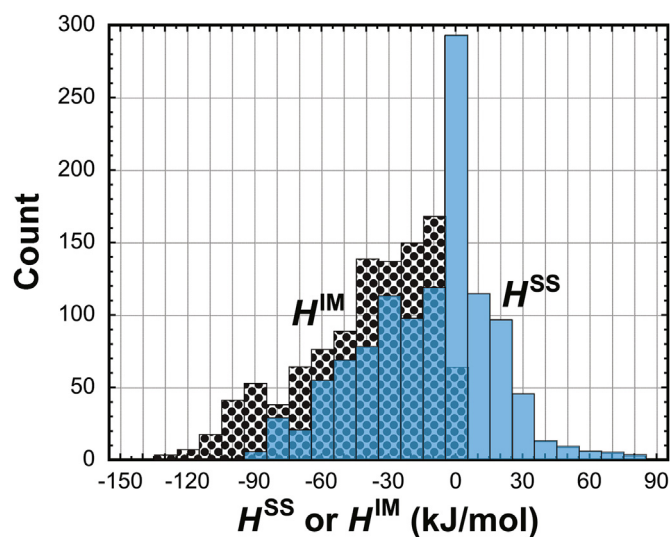
Fig. 4. Histograms of 1176 H^{SS} values estimated by the Miedema method from Ref. [45] (solutions with H, B, C, N, O, P and S are excluded in this analysis), and 1055 H^{IM} values for metal-metal and metal-semimetal compounds from Refs. [52,54,55,61–65] and assessed for accuracy in Ref. [25]. H^{SS} values are both positive and negative, while H^{IM} values are essentially always negative. H^{IM} values are generally slightly more negative than the dataset of negative H^{SS} values.

behavior. However, H^{SS} can be positive or negative, and so H^{IM} values are best compared with negative H^{SS} values. The median of negative H^{SS} values is −29 kJ/mol and the average is −30 kJ/mol. These are less negative than H^{IM}, where the median is −36 kJ/mol and the average is −42 kJ/mol. It is tempting to generalize that $H^{IM} < H^{SS}$, but there are issues with this approach. Comparison must be made between H^{IM} and H^{SS} for the same binary system at the same temperature. H^{SS} and H^{IM} values in Fig. 4 represent minimum values that occur at fixed compositions (usually near $x_B = 0.5$ for H^{SS} and at the stoichiometric composition for H^{IM}). However, rather than predicting one phase or the other to be stable at a given composition, the common tangent construct shows that *both* phases can co-exist over a range of compositions where neither G^{SS} nor G^{IM} are at the minimum value (Section 2.3.5).

Occupancy of multiple atom species on sub-lattices as illustrated in Fig. 3b is likely to give formation enthalpies of IM phases in N-component, complex alloys, $H^{IM,N}$, that differ from H^{IM} for the related binary compounds. There is no simple approach for estimating $H^{IM,N}$ from H^{IM}.

2.3. Discussion

2.3.1. Gibbs phase rule

Gibbs phase rule relates the number of phases in thermodynamic equilibrium, P, to the degrees of freedom, F, (the number of

intensive variables that can be changed arbitrarily and independently without changing equilibrium) and the number of components, N. At constant pressure, Gibbs phase rule is $P = N - F + 1$. There are $(N-1)$ compositional degrees of freedom and 1 degree of freedom for temperature, so that the maximum value of F is N. The minimum value of F is 0, which indicates a discrete point in a phase diagram with the maximum number of phases $(N+1)$. Any deviation in composition and/or temperature from this point decreases the number of equilibrium phases. The minimum number of phases is 1 when $F = N$. Gibbs phase rule bounds the number of phases possible and specifies the number of degrees of freedom that must exist for a given number of phases and components, but it gives no comment on the expectation of how many phases are actually present in any given alloy or system at a given temperature and pressure. Any number of phases can exist in an N-component system, from the minimum (1) to the maximum $(N+1)$, without violating Gibbs phase rule. There is no requirement that the maximum number of phases must be produced.

Some express surprise when the number of phases is less than the maximum value [11,66], and others claim that HEAs violate Gibbs phase rule [67]. The fact that HEAs have fewer than the maximum number of phases has also been used to support the entropy effect [17,68–71]. Analysis of binary phase diagrams gives a simple, visual approach to put this observation in perspective. The maximum number of phases in binary systems occurs when $F = 0$, at a discrete composition and temperature of a three-phase, invariant reaction. One of the three phases is often a liquid, making experimental observation by standard techniques very difficult. Even when all three phases are solid (eutectoid or peritectoid reactions), one or two of the phases are consumed by the reaction so that fewer phases are left below the reaction temperature. To experimentally observe three phases, a binary alloy must be equilibrated *and observed* at the discrete composition and temperature of the reaction. All of the studies cited above make observations at room temperature.

Some binary diagrams have several three-phase reactions, but some have no three-phase reactions at all. Given their infrequent occurrence and the requirement of observing the microstructure at a discrete composition and elevated temperature, the likelihood of seeing three phases in binary alloys is very small. Finding the minimum number of phases is more likely, as every binary phase diagram has at least one (and far more often, two or more) single-phase region. Single-phase fields exist over a range of temperatures and often extend over a composition range, so that the area of binary phase diagrams occupied by single-phase fields is far larger than the 'area' associated with discrete points of 3-phase invariant reactions. Many IM phases occur as line compounds at a discrete composition, while most SS phases occur over a range of compositions. This supports an expectation that single-phase SS alloys may be more common than single-phase IM alloys. This is shown by both experiment (Section 4.2.1) and calculations (Section

4.3.2.4). Finally, areas associated with 2-phase regions dominate many binary phase diagrams. This simple area fraction analysis shows that observing 1 or 2 phases is far more likely in binary phase diagrams than the maximum number allowed by Gibbs phase rule. Extending this simple analysis to more complex alloys supports the expectation that chancing upon exactly the right composition and temperature to produce the maximum number of phases in hyper-dimensional composition space may be a rare event. We conclude that the most likely result is that the number of observed phases will range from the minimum value to a number less than the maximum number.

2.3.2. Equilibrium

The concepts described in Section 2 apply to systems at thermodynamic equilibrium, but most CCA studies to date have been conducted on as-cast material (Section 4.4.1.1). Equilibrium phases may be found in as-cast material, but metastable or non-equilibrium phases are also commonly produced. The presence of microscopic (i.e., inter-dendritic) or macroscopic composition gradients give clear signs that equilibrium has not been reached, but it is not easy to verify that equilibrium has been achieved, since there is no guaranteed approach to produce thermodynamic equilibrium. Homogenization or annealing at temperatures above half the absolute melting temperatures is usually used, but there is no standard temperature or annealing time. Coarse phases formed at grain boundaries during annealing approach equilibrium more rapidly than the bulk of the microstructure due to accelerated diffusion along grain boundaries. Deformation processing can accelerate equilibration, since large deformation strains redistribute material much faster than diffusion. The use of such techniques is becoming more common in CCA studies, but it is prudent to consider claims regarding the number and types of phases in as-cast alloys with caution. This is discussed in more detail in Section 4.4.1.1.

2.3.3. Thermodynamics of systems with different-sized atoms

Classical thermodynamic solution theories assume that mixtures consist of equal-sized atoms, but real solutions usually have atoms of different sizes. This has important thermodynamic implications. Ideal configurational entropy is based on populating identical lattice sites with chemically different but equal-sized atoms. Atoms with different sizes can bring some uncertainty in atom location, thus giving an excess configurational entropy term. This effect may be small in dilute solutions, where the location of the minority atom is constrained by the surrounding majority atoms (Fig. 5a). The uncertainty in atom location increases with increasing size differences and concentrations. In multi-principal

element alloys (MPEAs) the lattice is expected to be highly strained, so that atoms are usually displaced from the average lattice sites (Fig. 5b), and this effect can become important. Equations describing the influence of atom size difference and concentration on excess entropy [72] have been applied to metallic glasses [73], but have not yet been applied to MPEAs. It has been suggested that atomic-level strains in may be a separate contribution to thermodynamic stability [25]. This is incorrect, since these contributions are already included measured values (see for example, [52–54,63–65]) and semi-empirical databases available with commercial CALPHAD packages.

With respect to enthalpy, the coordination numbers of elemental metals are typically 12 (for FCC or HCP crystals) or 14 (for BCC crystals). Coordination numbers in systems of different-sized atoms can differ from these values significantly. For example, co-ordination polyhedra in IM compounds often have 8 to 17 first neighbors [74], and measured total coordination numbers in metallic glasses range from 8.3 to 17.4 [75]. Since the enthalpy of a system depends on the number and the energy of atomic bonds, this change in coordination number may be important. Coordination numbers <12 are common around smaller atoms and coordination numbers >12 are common around larger atoms. Both smaller and larger atoms co-exist in systems of unequal atom sizes, so the average coordination number will fall somewhere between the extremes. Analysis of 238 binary IM structures containing metal or semi-metal atoms shows that most (162) have an average co-ordination number between 12 and 14. None of these structures have an average coordination number >14, and those with average coordination numbers <12 are dominated by compounds that contain a semi-metal element. Finally, it has been suggested that the condensed bond enthalpy for a given atom species adjusts in response to the number of bonds formed, so that the bond enthalpy decreases when the number of bonds increases and vice versa [60]. These considerations suggest that the enthalpy of unequal-sized systems may not differ dramatically from classical thermodynamic models.

2.3.4. Magnitudes of excess entropy terms relative to $S^{\varnothing,ideal}$

Several terms contribute to the total molar entropy of phase $\varnothing$, $S^\varnothing$. Atomic configurations give an ideal component for SS phases via the Boltzmann equation ($S^{SS,ideal}$, Section 2.1.1) and for IM phases with the sub-lattice model ($S^{IM,ideal}$, Section 2.2.2). An excess configurational term, $^{conf}S^\varnothing$, can result from SRO (Section 2.1.1) or differences in atom sizes (Section 2.3.3). Other excess entropy terms come from atomic vibrations ($^{vib}S^\varnothing$), magnetic moments
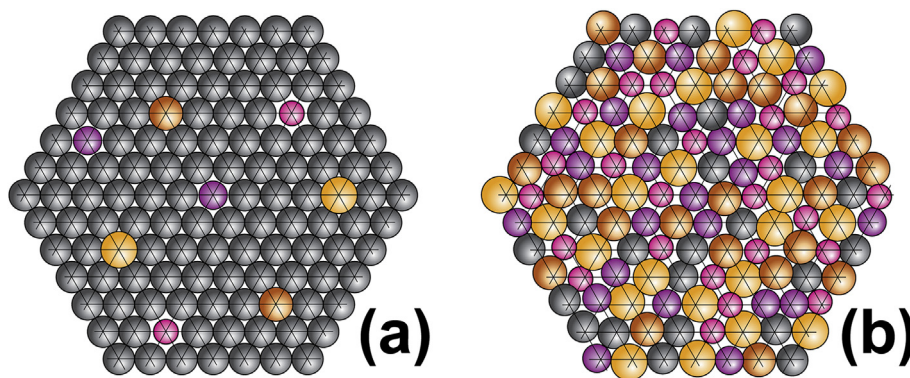
Fig. 5. The effect of atom size difference on atom positions in (a) a dilute solution, where solute atoms are constrained to occupy lattice sites by surrounding solvent atoms and (b) a complex, concentrated solution, where there is no dominant atom species and atom positions usually deviate from mean lattice positions. The variability in atom positions in (b) contributes to an excess configurational entropy.

($^{mag}S^{\varnothing}$), and electronic effects ($^{elec}S^{\varnothing}$). Excess terms occur in both SS and IM phases. Much has been written on the magnitude of $S^{\varnothing,ideal}$, but it is difficult to find a discussion of the magnitudes of excess entropy terms relative to $S^{\varnothing,ideal}$ and their importance in phase selection for MPEAs. We attempt a simple comparison of these terms here.

Adding the ideal and excess terms above gives the total molar entropy of phase $\varnothing$, $S^{\varnothing}$, as

$$S^{\varnothing} = S^{\varnothing,ideal} + {}^{conf}S^{\varnothing} + {}^{vib}S^{\varnothing} + {}^{elec}S^{\varnothing} + {}^{mag}S^{\varnothing} \tag{2.7a}$$

We are interested in the relative contributions of ideal and excess entropies to the total entropy change in a reaction, such as the competition between SS and IM phases. The difference in total molar entropies of SS and IM phases is $\Delta S^{SS-IM} = S^{SS} - S^{IM}$. Expanding and rearranging gives

$$\Delta S^{SS-IM} = \left(S^{SS,ideal} - S^{IM,ideal}\right) + \left({}^{conf}S^{SS} - {}^{conf}S^{IM}\right)$$
$$+ \left({}^{vib}S^{SS} - {}^{vib}S^{IM}\right) + \left({}^{elec}S^{SS} - {}^{elec}S^{IM}\right) + \left({}^{mag}S^{SS} - {}^{mag}S^{IM}\right) \tag{2.7b}$$

Total entropy curves of binary liquid alloys are given in compilations that use pure elements as the standard state [55]. To transform from this standard state to actual total entropies, we add the total entropies of the pure elements, $^{\circ}S^{\varnothing}$. Both $S^{\varnothing,ideal}$ and $^{conf}S^{\varnothing}$ in Eq. (2.7a) are zero for pure elements, and of the three remaining terms, $^{vib}S^{\varnothing}$ is usually by far the largest. We thus use $^{vib}S^{\varnothing}$ as a proxy for $^{\circ}S^{\varnothing}$. The actual $^{\circ}S^{\varnothing}$ will be slightly larger due to contributions from $^{elec}S^{\varnothing}$ and $^{mag}S^{\varnothing}$, but this approximation is adequate for the broad comparisons intended here.

Vibrational entropy increases with temperature and is given by $^{vib}S^{\varnothing} = \int_0^T \frac{C_v^{\varnothing}}{T} dT$, where $C_v^{\varnothing}$ is the molar heat capacity of element $\varnothing$ at constant volume. Standard equations give $C_v^{\varnothing}$ as a function of absolute temperature and the Debye temperature, T_{Θ} [42,43]. $C_v^{\varnothing}$ slightly underestimates $^{vib}S^{\varnothing}$, since $C_p^{\varnothing}$ should be used instead of $C_v^{\varnothing}$ and $C_p^{\varnothing}$ is slightly larger than $C_v^{\varnothing}$. $^{vib}S^{\varnothing}$ is calculated for Ni, Cu, Pd, Y and La from the equation above at 1800 K. These elements have different values of T_{Θ}, so the total entropies are different. Kopp's rule is used to approximate the alloy entropies as a linear average of the elemental entropies [43]. These total alloy entropies are added to data for four liquid binary systems from Ref. [55]. The results are shown in Fig. 6a.

The total molar liquid entropies, S^{liquid}, are over an order of magnitude larger than $S^{\varnothing,ideal}$. By far the largest contribution in Fig. 6a is the vibrational entropies of the pure elements. However, even though vibrational entropies of the elements are much larger than $S^{\varnothing,ideal}$, they do not necessarily dominate the entropy change of a reaction. The vibrational entropies of parent and product phases are roughly equivalent and generally cancel each other in the difference ($^{vib}S^{SS} - {}^{vib}S^{IM}$) in Eq. (2.7b). For example, the vibrational entropy difference was measured between a SS and IM phase with the same composition and was found to be about 0.1R [76]. Another study shows that the magnitude of $\left(S_{vib}{}^{SS} - S_{vib}{}^{IM}\right)$ is roughly the same magnitude as the difference in configurational entropy, ($S^{SS,ideal} - S^{IM,ideal}$) [77].

How significant are the remaining excess entropy terms relative to $S^{\varnothing,ideal}$? A closer look at the remaining terms is plotted in Fig. 6b,c for several binary systems, including those in Fig. 6a. The vibrational contributions from pure elements are removed to better
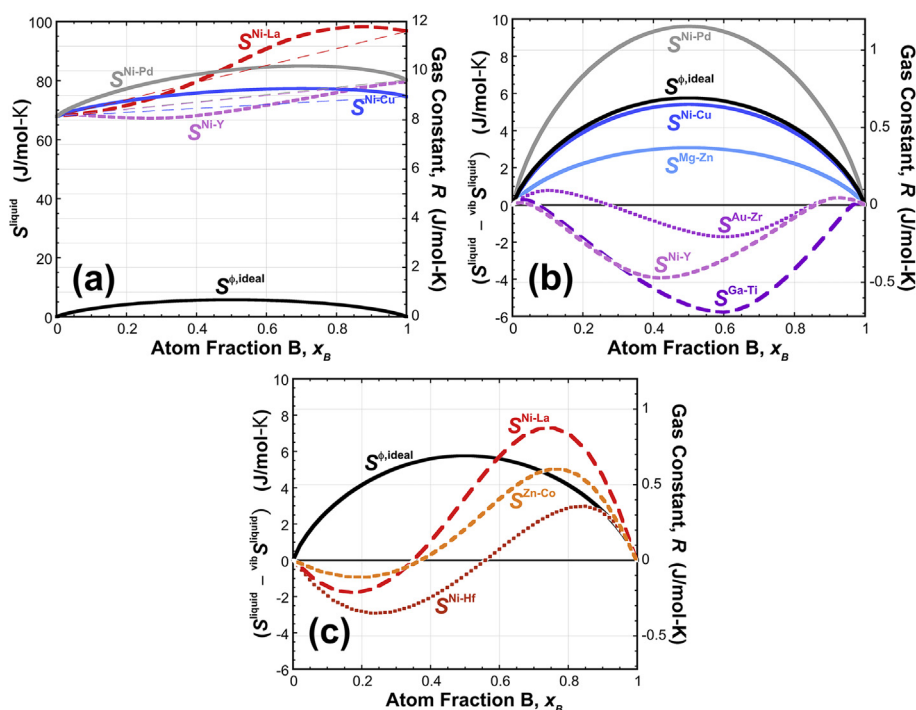
Fig. 6. (a) The total molar entropies of binary liquid alloys, S^{liquid}, including all of the terms in Eq. (2.7a). The vibrational entropies of constituent elements are the largest terms. The straight, dashed lines are linear averages of the elemental vibrational entropies. (b, c) S^{liquid}, after subtracting the vibrational entropy of the pure elements, in systems where entropy curves (b) are symmetric or modestly asymmetric, and (c) are highly asymmetric. (b, c) better illustrate the magnitude of the remaining excess entropy terms relative to $S^{\varnothing,ideal}$, which is shown for reference. Although some terms appear to be negative, this is an artifact of subtracting the much larger vibrational entropy of the pure elements, and the total entropies are always positive. Note the change in scale for (a). The curves in (b, c) are replotted from Ref. [55].

illustrate the relative magnitudes, so the curves in Fig. 6b,c shows

$$\left(S^{\varnothing} - {}^{vib}S^{\varnothing}\right) = S^{\varnothing,\text{ideal}} + {}^{conf}S^{\varnothing} + {}^{vib}S^{\varnothing,\text{remnt}} + {}^{elec}S^{\varnothing} + {}^{mag}S^{\varnothing}$$

(2.8)

A remnant vibrational entropy, ${}^{vib}S^{\varnothing,\text{remnt}}$, is included in Eq. (2.8), since Kopp's rule is not precise, and phonons in an alloy may be excited or damped that are not captured by averaging elemental vibrations. For example, bonds between unlike atoms with a co-valent component are often stiffer and shorter than bonds between like atoms, reducing vibrational entropy relative to pure elements [78]. For Ni-Pd, the excess terms on the right-hand side of Eq. (2.8) increase the entropy relative to $S^{\varnothing,\text{ideal}}$ (Fig. 6b). At the equimolar composition, the excess entropy terms are 67% of $S^{\varnothing,\text{ideal}}$. The excess entropy terms for Ni-Cu are nearly zero, so that the right-hand side of Eq. (2.8) is essentially identical to $S^{\varnothing,\text{ideal}}$. In the other systems in Fig. 6b, the excess terms on right-hand side of Eq. (2.8) decrease the entropy relative to $S^{\varnothing,\text{ideal}}$. The reduction is small for Mg-Zn (about $S^{\varnothing,\text{ideal}}/2$) and is as large as $2S^{\varnothing,\text{ideal}}$ for Ga-Ti. The excess entropies of alloys in Fig. 6c are positive over a narrow composition range and decrease the entropy over most of the alloy compositions. Again, the additions are relatively small (less than $S^{\varnothing,\text{ideal}}$), while the reductions are often greater than $S^{\varnothing,\text{ideal}}$. Some of the entropies in Fig. 6b,c appear to be negative, but this is only because ${}^{vib}S^{\varnothing}$ has been subtracted from these figures. The total entropies are always positive when this term is included, as illustrated in Fig. 6a.

This analysis suggests that excess entropy terms can make important contributions to the total entropy in the competition between phases. The shapes and values of the curves in Fig. 6 can alter entropy profiles from estimates based on configuration alone. Caution is therefore urged against using ideal estimates to represent total entropy, especially for sub-regular solutions. Unfortunately, there is no simple, analytic estimate of S^{SS} for the majority of solutions where atoms are not distributed randomly. The CALPHAD method gives an approach to estimate H^{SS} and S^{SS} from measured thermodynamic properties and phase equilibria (Section 4.3.2.4).

We have tried to show a representative range of behaviors in these comparisons, and the curves in Fig. 6 are by no means uncommon. Nevertheless, only a few systems are shown here, and no claims are made regarding typical entropy profiles. The estimates are rather simple, and more detailed comparisons may provide further insights.

2.3.5. Relative magnitudes of enthalpies and entropies

Of the four terms that contribute to Gibbs energy, no single term or pair of terms consistently dominates. It's tempting to compare the magnitude of $S^{SS,\text{ideal}}$ with H^{IM}. For example, $S^{SS,\text{ideal}}$ for an equimolar 11 component alloy is 20 J/(mol-K), and at 2000 K this gives an upper bound to the entropic energy, $-T(S^{SS,\text{ideal}})$, of 40 kJ/mol. Comparing this with Fig. 4, it might seem that compounds with H^{IM} more negative than 40 kJ/mol will not form solid solutions. However, the actual configurational entropy is likely to be less than the upper bound, since most solutions are not ideal. The excess entropy from atom size mismatch may increase S^{SS} while excess entropy terms may decrease S^{SS} (Section 2.3.4) Finally, $H^{SS,N}$ must be added to $-T(S^{SS,\text{ideal}})$ in this comparison, including contributions from all of the 55 different pairs of atoms that contribute to $H^{SS,N}$ in an 11 component alloy. Since $H^{SS,N}$ can be negative or positive, this can either stabilize or destabilize the solid solution. All of these adjustments can make significant contributions to the Gibbs energy of the solid solution, drastically complicating this 'simple' comparison.

Further, this approach only considers H^{IM} from binary compounds, and H^{IM} for phases in the 11 component alloy can be different than for the binaries. The configurational entropy of ordered compounds in an 11 component alloy can be a significant fraction of $S^{SS,\text{ideal}}$, stabilizing the compound relative to the solid solution. Finally, the simple comparison outlined here can only suggest the likelihood that a solid solution may or may not be stable by indicating what fraction of intermetallic compounds have H^{IM} that exceed the ideal entropic energy of solid solutions, $-T(S^{SS,\text{ideal}})$. A more rigorous assessment needs to compare against H^{IM} values for the specific alloy being considered. This discussion thus brings us back to the Gibbs energy equations that include all four thermodynamic terms for the specific CCA of interest.

As an added complexity, composition is often considered to adjust $S^{SS,\text{ideal}}$ independently without changing the other three terms. However, all four terms depend on composition and so changing composition will change all four terms. The composition dependences of S^{SS}, S^{IM}, H^{SS} and H^{IM} are sometimes complicated, so that one or more of these four curves can have more than one minima or maxima. The resulting G^{SS} and G^{IM} curves can also have more than one minima or maxima at compositions that may not line up. G^{SS} and G^{IM} are often compared at the same composition — usually the composition of the alloy or the ordered phase (where G^{IM} is usually a minimum). However, the common tangent construct [40,42,43] shows that co-existing stable phases have compositions that are different from each other and also different from the alloy composition, so that Gibbs energies must be considered over a range of compositions. This is especially important when the alloy composition is different from the most stable composition of the IM. G^{IM} often depends very strongly on composition, so that even small composition shifts from the stoichiometric composition can significantly increase G^{IM} (*i.e.*, reduce the IM stability). Nevertheless, the IM phase may remain stable over a wide range of alloy compositions as part of a SS + IM microstructure, even when $G^{IM} > G^{SS}$, due to the common tangent construct.

This discussion is not intended to discourage comparison between different combinations of enthalpies and entropies of CCAs. Rather, the purpose is to emphasize the complexity of the problem and to inspire new approaches. For example, the four separate terms may not be totally independent, and some connection may exist, such as a possible link between H^{SS} and H^{IM} (Section 2.1.1, Section 2.2.3). This relationship has recently been used to predict the boundary between SS and IM phases in MPEAs [79]. Further, systems with large $|H^{SS}|$ values are likely to have S^{SS} values below ideal estimates due to short-range ordering when $H^{SS} < 0$ or due to phase separation when $H^{SS} > 0$. Correlations between these four basic thermodynamic terms, if found, may give new approaches for estimating the types of phases produced in complex alloys.

Here we give a different way to consider the competition between thermodynamic terms. Current discussions seem to emphasize comparisons between different thermodynamic quantities such as entropy (for example, $S^{SS,\text{ideal}}$) and enthalpy (for example, H^{IM}). The challenges with such an approach are discussed above. In this section, we discuss the relative magnitudes of four primary terms, H^{SS}, S^{SS}, H^{IM} and S^{IM}, and in Section 2.3.4 we discuss the relative magnitudes of the various entropy terms. This gives a framework to compare the magnitudes of similar terms in different phases, as illustrated in Eq. (2.7b) for the competition, or reaction, between an IM and a SS phase. This comparison shows that the dominant entropy term, ${}^{vib}S^{\varnothing}$, becomes relatively unimportant since it has nearly the same magnitude in both SS and IM phases and the difference between these two values, $\left({}^{vib}S^{SS} - {}^{vib}S^{IM}\right)$, matters more than the magnitude of the individual terms. In the same way, the difference $\left(S^{SS,\text{ideal}} - S^{IM,\text{ideal}}\right)$ can be less than half

the value of $S^{SS,ideal}$ in CCAs due to atom mixing on sub-lattices (Section 2.2.2). Discussion in Section 2.1.1 and Section 2.2.3 lead to a similar conclusion for the difference, $(H^{SS} - H^{IM})$. Thus, we observe that phase selection in MPEAs *is often ultimately determined by comparing relatively small differences between larger pairs of values*.

2.4. Summary

Ideal configurational entropy of disordered solid solutions ($S^{SS,ideal}$) is often a poor estimate of total entropy (S^{SS}) (Section 2.3.4) Sub-regular solutions are by far the most common type of solution, leading to chemical short-range ordering or phase separation that reduces S^{SS} (Section 2.1.1). An excess configurational term due to atom size differences is available but has not been used in MPEAs (Section 2.3.3). Data for total entropies of binary liquid alloys suggest that excess entropy terms can be up to twice the value of $S^{SS,ideal}$, reducing the total entropy by important amounts. Total entropy curves can be highly asymmetric with respect to composition.

The enthalpy of mixing for disordered solid solutions (H^{SS}) in complex alloys depends sensitively on the enthalpies of mixing of all the constituent binary systems (Section 2.1.3). The enthalpy of mixing works together with, rather than against, entropy to stabilize solid solutions (Section 2.1.1). Together, these two terms compete with formation enthalpies and entropies of ordered compounds.

The configurational entropy of ordered phases (S^{IM}) may be significant when the number of elements is larger than the number of sub-lattices in an ordered compound (Section 2.2.2). As with solutions, excess configurational terms and non-configurational contributions to entropy may also be important.

The formation enthalpy of ordered, intermetallic compounds (H^{IM}) may be different than binary alloys, but it is difficult to assess the magnitude of this effect (Section 2.2.3). Neither experimental data nor calculated results are yet available.

The vibrational entropy, $^{vib}S^{\varnothing}$, is much larger than the ideal, configurational entropy, $S^{\varnothing,ideal}$, often by an order of magnitude or more (Section 2.3.4). However, $^{vib}S^{\varnothing}$ in the parent and product phases of a reaction have roughly equivalent magnitudes, so that this contribution is largely cancelled out.

Of the four major terms (H^{SS}, S^{SS}, H^{IM}, S^{IM}), no single term or pair of terms consistently dominates phase selection (Section 2.3.5). Phase selection is ultimately decided by relatively small differences between these four larger numbers, challenging the development of simplifying models that focus on individual terms. Relationships between pairs of terms, for example between H^{SS} and H^{IM} or between S^{SS} and S^{IM}, may give new approaches for estimating phase selection in CCAs.

Gibbs phase rule gives the maximum number of phases that can exist in an alloy as a function of the number of components and independent variables such as pressure and temperature (Section 2.3.1). It does not give probabilities or expectations of the number of phases that actually exist in any given alloy, and cannot be used to support the 'high entropy' hypothesis. Observing the maximum number of equilibrium phases is expected to be uncommon in all simple and complex alloys, including CCAs.

The thermodynamic arguments in the HEA literature are generally based on equilibrium. Therefore, when comparing experimental observations with these concepts it is important that some effort is made to observe systems that have the opportunity to approach equilibrium (Section 2.3.2). Results on as-cast material should be viewed with caution.

3. Taxonomy of complex, concentrated alloys

Here we describe the extent of composition space that has thus far been explored and the degree to which it has been studied. We characterize multi-principal element alloys (MPEAs) based on the frequency of the elements used and on common groupings of elements (Section 3.1). We identify seven distinct MPEA families in Section 3.2 and discuss the concept of alloy families more broadly in Section 3.3. We close this section with a brief summary (Section 3.4) Throughout this review, elements within an alloy are listed in alphabetic order. Thus, we report CoCrMnFeNi rather than NiFeCrCoMn or NiCoFeMnCr. This gives a simple, consistent approach for reporting data that otherwise can be confusing. Subscripts for each element indicate composition in molar ratios, if none is given then a subscript of 1 is implied.

3.1. Principal elemental constituents

Four hundred and eight distinct alloys are considered in this review. The list of the alloys used in this assessment is given in Supplementary data (see Appendix A.). This is not a comprehensive list, and emphasizes alloys published by mid-2015. These 408 alloys use 37 elements (Table 3, Fig. 7), including 1 alkali metal (Li); 2 alkaline earth metals (Be, Mg); 22 transition metals (Ag, Au, Co, Cr, Cu, Fe, Hf, Mn, Mo, Nb, Ni, Pd, Rh, Ru, Sc, Ta, Ti, V, W, Y, Zn, Zr); 2 basic metals (Al, Sn); 6 lanthanides (Dy, Gd, Lu, Nd, Tb, Tm); 3 metalloids (B, Ge, Si) and 1 non-metal (C). Some elements are exceptionally common in MPEAs. Al, Co, Cr, Cu, Fe, Mn, Ni, and Ti each appear in more than 100 alloys, and four of these elements (Co, Cr, Fe, Ni) are each in over 70% of the complex, concentrated alloys (CCAs) made to date. Refractory elements (Mo, Nb, V, Zr) are also often used. The average alloy in this review has 5.6 constituent elements.

Barely half of the 72 elements that are not radioactive, noble gases or halogens have been used in MPEAs, and a significant majority of the elements that have been used are used infrequently (Table 3). Over one third of the elements used appear in only 1 or 2 alloys, more than half of the elements used are found in fewer than 10 different alloys, and over 2/3 of the elements used occur in fewer than 5% of the alloys made to date. Fig. 7 emphasizes visually that the elements used in CCAs are highly skewed toward a favored few, and that the majority of elements are unused or only rarely used. Candidate and used elements are shown in Table 3, along with selected elemental properties [74,80,81].

3.2. Major alloy families

The 408 MPEAs described in this review can be classified into seven alloy families. These families include 3d transition metal CCAs, refractory metal CCAs, light metal CCAs, lanthanide (4f) transition metal CCAs, CCA brasses and bronzes, precious metal CCAs and interstitial compound (boride, carbide and nitride) CCAs. The alloy families are illustrated in Fig. 8 and are briefly introduced below.

3.2.1. 3d transition metal CCAs

By far the most widely studied alloy family contains at least 4 of the 9 following elements: Al, Co, Cr, Cu, Fe, Mn, Ni, Ti and V [1,5,6,11,17,21,68,82–84]. About 85% of the MPEAs in this review (345 out of 408) fall in this family. Five of these 9 elements are in the 'Cantor alloy' (CoCrFeMnNi) first reported in 2004 [1]. In addition to being one of the first MPEAs reported, this is also a prototypical single-phase disordered solid solution (SS) alloy, contributing to its popularity. About 96% of the 3d transition metal MPEAs use Fe (331 out of 345). About 29% of the MPEAs in this

Table 3
Element properties and the number of alloys that use the indicated elements.

Element	Atomic number	Used in # of alloys	Structure at RT[a]	Structure at T_m[a]	Atom radius (pm)[d]	T_m (K)[e]	Density (g cm^{-3})[e]	Young's Modulus (GPa)[e]	Pauling EN[e]	VEC[e,f]
H	1				25					
Li	3	7	A2 (BCC)	b	151.94	454	0.53	4.9	0.98	1
Be	4	1	A3 (HCP)	A2 (BCC)	112.8	1560	1.86	287	1.57	2
B	5	3	A10 (hR105)	b	82	2348	2.46		2.04	3
C	6	7	A3 (HCP)	b	77.3	4742	2.27		2.55	4
N	7				75	63	1.03		3.04	5
O	8				73	54	0.92		3.44	6
Na	11		A2 (BCC)	b	185.7	371	0.97	10	0.93	1
Mg	12	7	A3 (HCP)	b	160.13	923	1.74	45	1.31	2
Al	13	274	A1 (FCC)	b	143.17	933	2.70	70	1.61	3
Si	14	19	A4 (cubic)[c]	b	115.3	1687	2.33	47	1.90	4
P	15		A17 (oC8)	b	106	317	1.82		2.19	5
S	16		A16 (oF128)	b	102	388	2.06		2.58	6
K	19		A2 (BCC)	b	231	337	0.85		0.82	1
Ca	20		A1 (FCC)	A2 (BCC)	197.6	1115	1.53	20	1.00	2
Sc	21	1	A3 (HCP)	A2 (BCC)	164.1	1814	3.00	74	1.36	3
Ti	22	121	A3 (HCP)	A2 (BCC)	146.15	1941	4.50	116	1.54	4
V	23	70	A2 (BCC)	b	131.6	2183	6.12	128	1.63	5
Cr	24	301	A2 (BCC)	b	124.91	2180	7.19	279	1.66	6
Mn	25	101	A12 (cI58)	A2 (BCC)	135	1519	7.47	198	1.55	7
Fe	26	348	A2 (BCC)	A2 (BCC)	124.12	1811	7.88	211	1.83	8
Co	27	301	A3 (HCP)	A1 (FCC)	125.10	1768	8.84	209	1.88	9
Ni	28	341	A1 (FCC)	b	124.59	1728	8.91	200	1.91	10
Cu	29	186	A1 (FCC)	b	127.8	1358	8.94	130	1.90	11
Zn	30	6	A3 (HCP)	b	139.45	693	7.14	108	1.65	12
Ga	31		A11 (oC8)	b	139.2	303	5.91		1.81	3
Ge	32	1	A4 (cubic)[c]	b	124	1211	5.33		2.01	4
As	33		A7 (hR2)	b	115	1090	5.79	8	2.18	5
Se	34		A8 (hP3)	b	140	494	4.81	10	2.55	6
Rb	37		A2 (BCC)	b	244	312	1.53	2.4	0.82	1
Sr	38		A1 (FCC)	A2 (BCC)	215.2	1050	2.58		0.95	2
Y	39	5	A3 (HCP)	A2 (BCC)	180.15	1795	4.47	64	1.22	3
Zr	40	48	A3 (HCP)	A2 (BCC)	160.25	2128	6.51	68	1.33	4
Nb	41	37	A2 (BCC)	b	142.9	2750	8.58	105	1.60	5
Mo	42	47	A2 (BCC)	b	136.26	2896	10.23	329	2.16	6
Ru	44	2	A3 (HCP)	b	133.84	2607	12.37	447	2.20	8
Rh	45	2	A1 (FCC)	b	134.5	2237	12.43	275	2.28	9
Pd	46	3	A1 (FCC)	b	137.54	1828	12.43	121	2.20	10
Ag	47	1	A1 (FCC)	b	144.47	1235	10.50	83	1.93	11
Cd	48		A3 (HCP)	b	156.83	594	8.65	50	1.69	12
In	49		A6 (tI2)	b	165.9	430	7.29	11	1.78	3
Sn	50	11	A5 (tI4)	b	162	505	7.29	50	1.96	4
Sb	51		A7 (hR2)	b	145	904	6.69	55	2.05	5
Te	52		A8 (hP3)	b	145.2	723	6.24	43	2.10	6
Cs	55		A2 (BCC)	b	265	302	1.87	1.7	0.79	1
Ba	56		A2 (BCC)	b	217.6	1000	3.60	13	0.89	2
La	57		A3 (DHCP)	A1 (FCC)	187.9	1193	6.20	37	1.10	3
Ce	58		A3 (HCP)	A2 (BCC)	182.47	1072	6.77	34	1.12	3
Pr	59		A3 (DHCP)	A2 (BCC)	165	1204	6.77	37	1.13	3
Nd	60	1	A3 (DHCP)	A2 (BCC)	164	1289	7.01	41	1.14	3
Sm	62		C19 (hR3)	A2 (BCC)	181	1345	7.53	50	1.17	3
Eu	63		A2 (BCC)	b	198.44	1095	5.25	18	1.20	3
Gd	64	2	A3 (HCP)	A2 (BCC)	180.13	1586	7.90	55	1.20	3
Tb	65	2	A3 (HCP)	A2 (BCC)	178.14	1632	8.23	56	1.10	3
Dy	66	2	A3 (HCP)	A2 (BCC)	177.4	1685	8.55	61	1.22	3
Ho	67		A3 (HCP)	b	176.61	1745	8.80	65	1.23	3
Er	68		A3 (HCP)	b	175.58	1802	9.06	70	1.24	3
Tm	69	1	A3 (HCP)	b	156	1818	8.84	74	1.25	3
Yb	70		A1 (FCC)	A2 (BCC)	170	1097	6.97	24	1.10	3
Lu	71	2	A3 (HCP)	b	173.49	1936	9.84	69	1.27	3
Hf	72	6	A3 (HCP)	A2 (BCC)	157.75	2506	13.28	78	1.30	4
Ta	73	14	A2 (BCC)	b	143	3290	16.68	186	1.50	5
W	74	2	A2 (BCC)	b	136.7	3695	19.41	411	2.36	6
Re	75		A3 (HCP)	b	137.5	3458	21.02	463	1.90	7
Os	76		A3 (HCP)	b	135.23	3306	22.59		2.20	8
Ir	77		A1 (FCC)	b	135.73	2719	22.56	528	2.20	9
Pt	78		A1 (FCC)	b	138.7	2041	21.46	168	2.28	10
Au	79	1	A1 (FCC)	b	144.2	1337	19.29	78	2.54	11
Hg	80		A10 (hR1)	b	150	234	14.24		2.00	2
Tl	81		A3 (HCP)	A2 (BCC)	171.6	577	11.87	8	1.62	3
Pb	82		A1 (FCC)	b	174.97	600	11.35	16	2.33	4
Bi	83		A7 (mC4)	b	160	544	9.81	32	2.02	5

[a] Given by Strukturbericht notation and (crystal structure or Pearson Symbol).
[b] The crystal structure at the melting temperature, T_m, is the same as at room temperature (RT).
[c] Diamond cubic.
[d] Values taken from Refs. [74,80,81].
[e] Values taken from Ref. [81].
[f] Valence Electron Concentration.
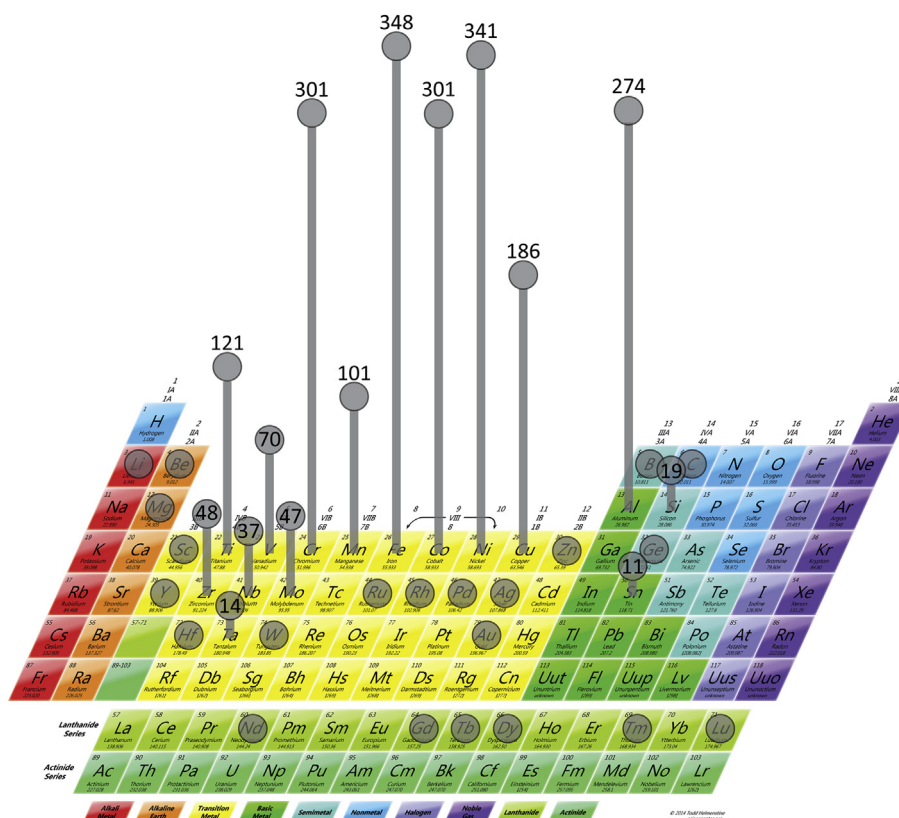
Fig. 7. The frequency with which elements are used in the 408 multi-principal element alloys (MPEAs) of this assessment. The vertical lines are proportional to the number of alloys that use the indicated element, which is also shown by the associated numbers. No number is given when an element is used in fewer than 10 alloys. Al, Co, Cr, Cu, Fe, Mn, Ni and Ti are by far the most commonly used elements. The periodic table image is provided courtesy of Sciencenotes.org at http://sciencenotes.org/printable-periodic-table/.

family contain Mn and only ~15% use V as principal elements. Other elements can also be added to this group as principal elements or as minor additions. Additions of B, C or N are considered separately (Section 3.2.3).

The branches of an alloy family tree can be characterized by element groupings. This family has 9 elements and so there are 126 possible 4-element branches[4]. Here we analyze the frequency of the 15 4-element branches taken from the 6 most common elements in 3d transition metal CCAs (Table 4). A significant majority of the alloys in this family (91%) have at least one of these 15 branches. The element groupings AlCrFeNi, CoCrFeNi, AlCoFeNi, AlCoCrNi and AlCoCrFe are the most common, and each of these occur in over half the transition metal CCAs. Each MPEA with 5 or more elements has multiple 4-element branches. For example, AlCoCrFeNi has five 4-element branches, including all 5 of the most common branches.

Alloys in the 3d transition metal family can be considered extensions of stainless steels and superalloys. Austenitic (FCC), duplex (FCC + BCC) and precipitation hardened stainless steels all have Fe-Cr-Ni as principal elements [30]. Mn is a principal element in some austenitic stainless steels, and compound forming elements such as Al, Cu, Nb and Ti are added in small amounts to precipitation hardened stainless steels. Austenitic nickel alloys have Ni-Cr-Fe or Ni-Cr-Mo as principal elements, with additions of Co, Fe or Mo and smaller additions of Al, Ni or Ti. Nickel superalloys are complex,

concentrated alloys based on Ni-Cr-Co-Fe-Mo with sufficient Al, Nb or Ti to form a significant volume fraction of the $Ni_3(Al,Nb,Ti)$ intermetallic phase. These are all concentrated alloys with 3, 4 or 5 principal elements. As examples, INCOLOY® 800 is nearly an equimolar ternary alloy ($Cr_{23}Fe_{46}Ni_{31}$) and Haynes® 556® is nearly an equimolar quaternary ($Co_{20}Cr_{25}Fe_{31}Ni_{21}(Mo,Ta,W)_3$). The commonality between 3d transition metal MPEAs and commercial alloys is discussed in more detail elsewhere (Section 5.5.2, Section 6.2.1.1).

3.2.2. Refractory metal CCAs

The refractory metal CCA family consists of alloys containing at least 4 of the 9 refractory elements: Cr, Hf, Mo, Nb, Ta, Ti, V, W, and Zr, plus Al [23,24,85—108]. This family is studied much less frequently than the 3d transition metal family of alloys. Only 29 refractory CCAs were reported by mid-2015, about 7% of the alloys covered in this assessment (see Supplementary data in Appendix A). They are often based on MoNbTaW, HfNbTaZr, CrMoNbTa or CrNbVZr element groupings. The alloys can also contain non-refractory elements such as Al or Si to decrease alloy density and improve properties [92—95,106—108]. Other refractory elements (Ir, Os, Re, Rh, Ru) have not been used to date in refractory metal CCAs and offer new possibilities.

Refractory metal CCAs were inspired by the objective to develop new high temperature structural metals. This represents perhaps the first attempt to devise a completely new CCA family to achieve a specific set of requirements. The refractory palette offers very wide ranges in elemental properties such as melting temperature, T_m, (2128—3695 K), density (4.5—19.4 g/cm^3) and elastic moduli (68—411 GPa for Young's modulus). This gives significant flexibility

---

[4] This uses the 'N-choose-r' equation (also known as the binomial coefficient) for determining the number of unique ways r elements can be chosen from a set of N elements when the order doesn't matter and repetition isn't allowed. The equation is $C(N, r) = N!/[r!(N-r)!]$.
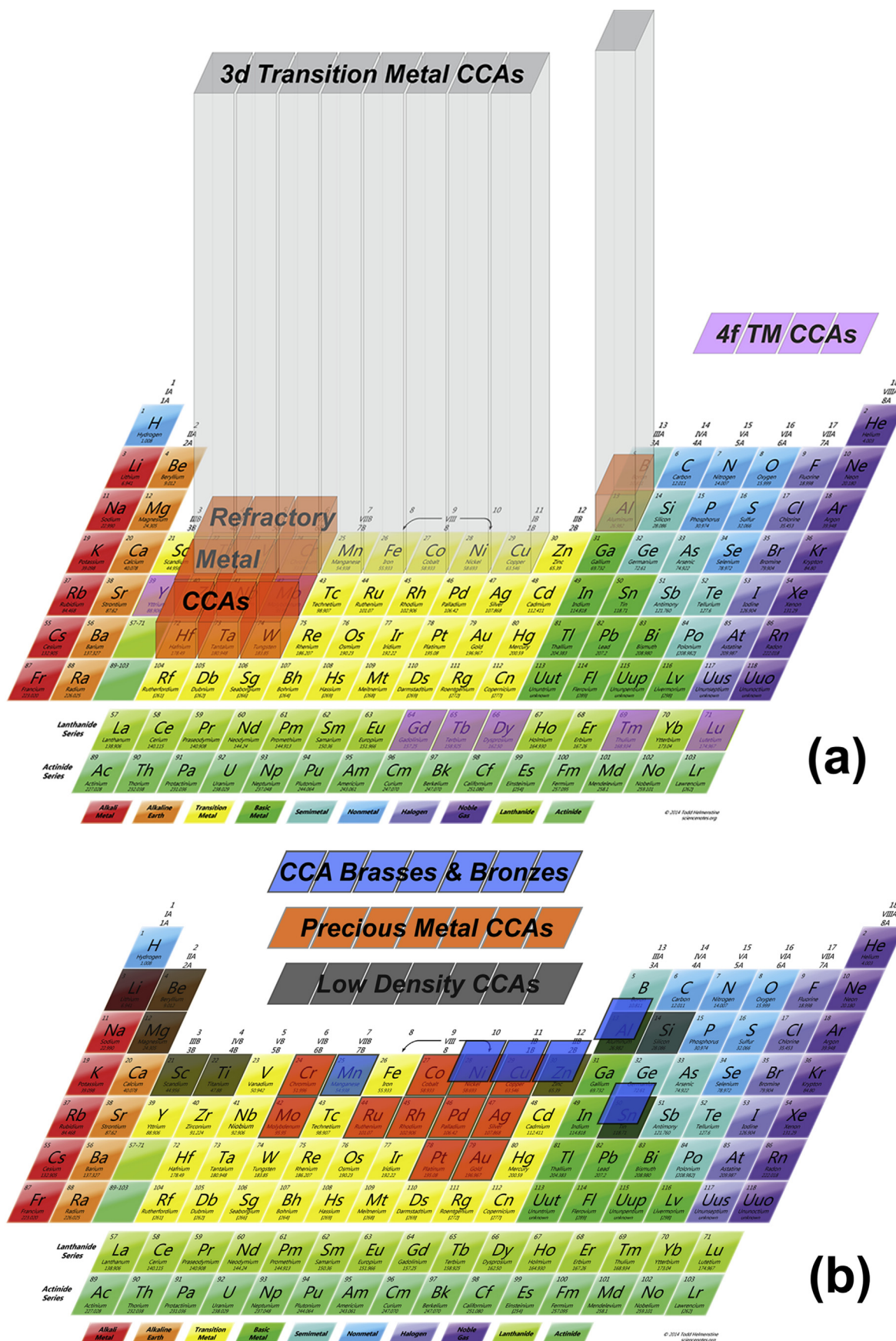
Fig. 8. Six of the seven CCA families illustrated by element groupings. (a) 345 3d transition metal CCAs, 29 refractory metal CCAs and 2 lanthanide (4f) transition metal CCAs. (b) 7 light metal CCAs, as well as precious metal CCAs and CCA brasses and bronzes. The heights of boxes in (a) are proportional to the number of alloys in the two major families. Alloys containing B, C and N are not shown. The periodic table image is provided courtesy of Sciencenotes.org at http://sciencenotes.org/printable-periodic-table/.

in tailoring alloys to achieve a particular property. For example, refractory metal CCAs with low density may favor Cr, Nb, V and Zr, while alloys with Mo, Nb, Ta and W may give the highest T_m. Both the high T_m and the range of T_m between elements give unique challenges in producing refractory metal MPEAs. Careful selection of master alloys can aid in the melting of refractory metal MPEAs.

3.2.3. Other alloy families

The initiative to design entirely new families came with the introduction of refractory metal CCAs in 2010. Since then, several new alloy families have been introduced. In fact, most of these new families were first reported in the past 2 years – with the exception of carbide and nitride films, none of the alloy families described in this subsection appeared in a recent book [17]. These new alloy families represent fledgling efforts and are briefly mentioned here.

A third family of MPEAs is motivated by the need to develop new structural metals with low density for aerospace and transportation applications. This alloy family is based on elements such as Al, Be, Li, Mg, Sc, Si, Sn, Ti and Zn. Seven alloys have been reported in the low-density CCA family [109–111]. A broad range of elemental melting and boiling points in this family make processing difficult, so that mechanical alloying [109,111] or careful selection of master alloys [110] is needed in primary processing.

The fourth family of alloys contains at least 4 of the lanthanide (4f) elements Dy, Gd, Lu, Tb and Tm, plus the element Y. Motivated by scientific curiosity, this family seeks to discover single-phase, SS high entropy alloys (HEAs) with the HCP crystal structure [67]. The two alloys in this family are DyGdLuTbY and DyGdLuTbTm.

Complex, concentrated brasses and bronzes have recently been introduced [112]. The motivation behind these alloys is to expand the already broad range of brasses and bronzes, and to achieve higher levels of strength via concentrated solid solutions. The elements in this family are Al, Cu, Mn, Ni, Sn and Zn. The alloys use the equi-atomic alloy substitution method [19], so that alloys are represented by the formula, $Al_xSn_yZn_z[CuMnNi]_{(1-x-y-z)}$.

The most recent CCA family uses precious metals for catalysis applications [113]. These alloys contain at least 4 elements from the palette of Ag, Au, Co, Cr, Cu, Ni, Pd, Pt, Rh and Ru. An earlier phase diagram study identified a single-phase HCP MoPdRhRu alloy [114], and this is included in the precious metal CCA family. At the time of this writing, alloys in Refs. [112,113] have not yet been published and are not included in Supplementary data (see Appendix A). They are mentioned here for completeness.

Special mention is made of MPEAs that contain B, C or N. Nearly all have elements drawn from the 3d transition metal or refractory metal CCA families. They are listed here as a separate family due to the dramatic effect of B, C or N on the phases and microstructures produced, on the distinct processing required, and properties. Most of the alloys include N [2,17,115–124], with only limited reports of alloys with C [17,124] or B [3]. Most of the alloys are produced as thin films, and alloys often contain several atom percent of O [2]. Due to their distinctly different nature and the non-bulk product form, alloys in this family are mentioned briefly in this review but are not covered comprehensively.

3.3. Discussion

Alloy families are presented here as groupings of elements with a common characteristic, or that are likely to produce a particular set of properties. Alloy families described here have a relatively small number of elements that are logically grouped by location in the periodic table or by properties such as high melting temperature, T_m, or low density. However, the desired alloy property can sometimes result from a non-intuitive interaction between two or more elements, so that the reason for selecting each element in a

family may not be obvious. For example, Al has a low T_m but it can form high T_m intermetallic phases that are essential in structural metals, so Al is often included as a candidate high temperature structural element. Identifying these non-intuitive interactions between atoms can be aided by computational methods, by theory, or by experimental data. The numbers of elements that may contribute to a particular property goal can expand significantly through the use of these tools. For example, phase diagram calculations of nearly 135,000 equimolar alloys (Section 4.3.2.4) show that as many as 21 elements are needed to build high temperature structural CCAs with the HCP crystal structure (see Table 12 and Table 13 in Ref. [56]). These include 5 elements from the 3d transition metal family of CCAs, 7 from the refractory metal family, 4 from the 4f transition metal family and 2 from the precious metal family.

New alloy families are being devised at a rapid pace, and the current approach for defining alloy families as a small number of elements with a common feature may continue to be useful. However, as the field continues to expand and mature, the definition of an alloy family by the constituent elements may become less useful, and alloy families based on intended properties or applications may become more useful. For example, Table S1 in Supplementary data (see Appendix A) includes 15 alloys whose grouping of elements do not fit into any of the alloy families discussed here. Increasing the number of elements needed to pursue a particular application will also challenge high-throughput techniques to rapidly evaluate alloy space (Section 7.1.2).

3.4. Summary

Fewer than half of 72 candidate elements (noble gases, halogens and radioactive elements are excluded) have been used to date in MPEAs. Most of the 37 elements used are used infrequently. Early work shows a startling focus on 9 elements (Al, Co, Cr, Cu, Fe, Mn, Ni, Ti and V) that define the 3d transition metal family of CCAs. The idea of developing new alloy families to achieve a specific design objective is still relatively new. Inspirations for new alloys families are based on intended applications or scientific curiosity. The seven alloy families described in this review are: 3d transition metal CCAs; refractory metal CCAs; light metal CCAs; lanthanide (4f) transition metal CCAs; brass and bronze CCAs; precious metal CCAs; and interstitial compound CCAs. Of these seven families, four were introduced in the last two years.

A 'family tree' analogy is introduced to describe alloy families. An alloy 'family tree' using *N* elements is characterized by branches containing fewer than *N* elements. This gives a simple way to identify element groupings that may dominate an alloy family. Five 4-element branches (AlCrFeNi, CoCrFeNi, AlCoFeNi, AlCoCrNi and AlCoCrFe) each occur in over half the 3d transition metal CCAs, and 91% of the 3d transition metal CCAs contain at least one of the 15 4-element branches drawn from the 6 most frequently used elements.

4. Microstructures

A wide range of microstructures has been produced in complex, concentrated alloys (CCAs), including amorphous, nanocrystalline, single-phase and multi-phase conditions. This section begins with a discussion of phase classifications and definitions in high entropy alloys (HEAs) (Section 4.1). Observed phases and microstructures (Section 4.2) and approaches for predicting phases (Section 4.3) are reviewed. Discussions of important topics are given in Section 4.4, including features biasing current observations, comparison of observed and predicted microstructures, and a detailed consideration of the high entropy effect. This section concludes with a

Table 4
Common 4-element branches in the 3d transition metal family of CCAs.

4-Element branches	Percentage of 3d transition metal CCAs that use each branch	Percentage of branch binaries that are ideal or regular solutions
AlCrFeNi	65%	33%
CoCrFeNi	63%	83%
AlCoFeNi	55%	50%
AlCoCrNi	53%	33%
AlCoCrFe	51%	50%
CrCuFeNi	40%	17%
AlCuFeNi	39%	17%
AlCrCuNi	38%	0%
AlCrCuFe	36%	17%
CoCuFeNi	35%	50%
AlCoCuNi	31%	17%
CoCrCuNi	30%	33%
AlCoCuFe	29%	17%
CoCrCuFe	28%	50%
AlCoCrCu	28%	17%

summary of major points (Section 4.5).

4.1. Definitions and classifications of phases

The materials science community sometimes uses the same term to mean different things. Several terms in the multi-principal element alloy (MPEA) field have such double meanings, leading to some confusion. Here we discuss these terms and prescribe the definitions used in the present work. We do not create any new definitions here, but rather specify which meaning is used to avoid confusion.

4.1.1. Overview of current classification schemes

Configurational entropy of HEAs is suggested to favor disordered solid solutions (SS) with simple crystal structures over ordered intermetallic (IM) phases. HEA phase classification must therefore address whether a phase is (i) ordered or disordered, (ii) if it is a SS, and (iii) whether it is simple or complex. A recent review discusses three HEA classification schemes [82]. The first gives *terminal solid solutions* where one element dominates, *intermetallic compounds* that are restricted to a fixed, stoichiometric ratio of constituent atoms, and *intermediate solutions*. The second taxonomy gives *random solid solutions*, *ordered solid solutions* and *intermetallic phases*. The third scheme characterizes structures as simple or complex and as ordered or disordered. Simple phases are defined as identical to or derived from face-centered cubic (FCC), body-centered cubic (BCC) or hexagonal close-packed (HCP) structures. According to this classification, structures such as B2 (cP2, ClCs)[2], L1$_2$ (cP4, AuCu$_3$) and B4 (hP4, ZnS) are simple structures. If atom positions in a crystal lattice are different from simple structures, the phase is considered to be complex. Sigma and Laves phases are examples of complex phases. This classification gives three types of HEA phases: simple disordered phases (SDPs), simple ordered phases (SOPs), and complex ordered phases (COPs) [82].

Confusion remains with these classifications. Restricting IM phases to stoichiometric compounds is inconsistent with the vast IM literature, which includes all structures with two or more sub-lattices, including compounds that exist over a range of compositions (see for example [57,58]). Complex, disordered phases (CDPs) are omitted, and a detailed discussion of order and disorder is needed to resolve an apparent inconsistency in the treatment of SS phases. We discuss the issues by addressing each of the three classification characteristics above.

4.1.2. Order and disorder

At least three distinct forms of order are described in materials science. Amorphous structures are sometimes referred to as disordered and crystalline phases as ordered. In this context, order and disorder refer to the presence or absence of a crystal lattice (*i.e.* translational symmetry), respectively. Disorder can also refer to the lack of chemical ordering of atom species in an amorphous structure. While amorphous phases have certainly been produced in HEAs, to reduce confusion we do not use the term disorder to refer to the absence of a crystalline lattice — such structures are labeled as amorphous or non-crystalline or glassy.

The term, 'long-range order', can refer to translational and/or rotational symmetry of crystalline structures. However, it is also commonly used in the intermetallics community to describe phases with chemically distinct sub-lattices (see for example, [57,58] and Section 2.2.1). We use this latter definition throughout this work to distinguish between SS and IM phases. Structures with chemical long-range order (LRO) of alloying elements are referred to here as ordered or intermetallic or compounds, while phases with only one lattice are commonly referred to as disordered. Perfect order occurs when the probability of a given atom species occupying a particular sub-lattice is 0 or 1 — these are called stoichiometric compounds. Some disorder occurs when the site occupancy is between 0 and 1. This disorder can become significant in multi-principal element alloys (MPEAs) when the number of atom species in a phase is greater than the number of sub-lattices, contributing significantly to configurational entropy (Section 2.2.2). Intermetallic compounds with some degree of disorder on one or more sub-lattice may exist over a composition range and can be considered as ordered solid solutions. However, such phases are not considered solid solutions in the present work (Section 4.1.3).

The terms order and disorder are also used to describe local chemistry. Chemical short-range order (SRO) is absent in ideal solutions, where atom species occupy lattice sites randomly (Section 2.1). SRO exists in structures that show a preference for a particular pair of atoms to occur as first neighbors. These phases are regular (for a small preference) or sub-regular solutions. The Boltzmann model for configurational entropy is not valid when the degree of SRO is non-trivial. It is not simple to quantify SRO experimentally.

The first type of order discussed here (amorphous *v.* crystalline) is an all-or-nothing feature — there is no such thing as a 'mostly crystalline' phase. However, phases may display LRO or SRO that is complete, or incomplete, or completely absent. Partial states of order add to confusion when describing HEA phases simply as disordered or ordered.

4.1.3. Solid solutions

Disordered solid solution phases have a single crystal lattice and do not possess LRO. They may or may not display SRO. Disordered SS phase fields are usually contiguous with at least one pure

21

element, such phases are called terminal solid solutions. However, a single element need not dominate as has been suggested [82]. This is demonstrated by alloys such as the single-phase CoCr-FeMnNi MPEA. This is a terminal SS, since it is contiguous with all five elemental solid solutions, and yet no single element dominates.

Non-stoichiometric IM phases are another type of SS phases. In a broad sense it is certainly correct to call these SS phases, but it is judged to be inappropriate in the present context. Configurational entropy is proposed to favor SS phases in HEAs, and the Boltzmann model is used to estimate configurational entropy to support this hypothesis. But the Boltzmann model is only appropriate for disordered solutions — a different model is needed to estimate the configurational entropy of structures with two or more sub-lattices (Section 2.2.2). To be consistent with the models used to explore the high entropy hypothesis, it is recommended that phases with two or more sub-lattices are not counted as SS phases in the HEA field. This approach is taken here.

4.1.4. Simple and complex phases

Previous discussions of simple or complex phases omit amorphous structures and complex, disordered phases (CDPs) such as A4 (cF8, C (diamond)), A5 (tI4, β-Sn), A8 (hP3, γ-Se) A12 (cI58, α-Mn) and A13 (cP20, β-Mn). These issues are easily fixed, but a more basic concern is that the HEA literature often assigns properties to simple and complex phases. Specifically, complex phases are stereotyped as brittle with little practical use and SS phases are characterized as strong and ductile. These generalizations have many very important exceptions. For example, simple structures (most HCP and some BCC) are often brittle, and SS alloys are rarely as strong as precipitation-strengthened alloys (Section 1.3.2 and [26]). More important, many functional materials have complex, ordered crystal structures but are nevertheless extremely useful. These stereotypes over-emphasize structural materials, ignore the dominant role of microstructure design and control, and have the negative effect of discouraging work in important directions. In the present paper we avoid these difficulties by making no assumptions regarding materials properties or utility based on crystal structure. We include simple and complex structures and pursue both structural and functional materials in CCAs.

4.1.5. Definitions for phases and microstructures in complex, concentrated alloys

The previous discussion supports the following definitions in the present work. A phase with no crystal structure is called non-crystalline or amorphous (AM) or glassy. Even though atoms are disordered in an amorphous structure, it is not called disordered in the present work to avoid confusion with disordered crystalline solid solution phases. A phase with two or more chemically distinct sub-lattices, and therefore possessing chemical LRO, is defined as ordered or intermetallic (IM) or compound, even if it exists over a range of compositions. In this work, LRO refers only to chemical ordering on sub-lattices, and not to translational and/or rotational symmetry. IM phases are specified by common A_xB_y notation, and also by Strukturbericht notation, Pearson symbol or common name (such as Laves or sigma), and prototype compound. A phase with alloying elements occupying a single crystal lattice (no sub-lattices) is described as a disordered solid solution (SS). SRO may be present or absent in SS phases. The specific type of SS phase is described by the atom packing scheme (FCC, BCC, HCP) or by Strukturbericht notation for more complex structures. The distinction between simple and complex phases is limited to crystal structure, and there are no implications regarding properties or utility.

A recent scheme to classify microstructures is consistent with these definitions [56,125]. Microstructures with one or more disordered solid solutions are referred to as SS microstructures or alloys; microstructures with one or more intermetallic phase are called IM microstructures or alloys; and microstructures with a mixture of both disordered solid solution and intermetallic phases are called (SS + IM) microstructures or alloys. CCAs are not limited to SS phases or single-phase microstructures, and can have any number of SS or IM phases, or a mixture of both SS and IM phases. The acronyms SS and IM can refer to a phase, a microstructure or an alloy — the intended meaning will be made clear by context. An additional class of HEAs — metallic glasses — has a metastable amorphous structure that can be produced by rapid solidification or mechanical alloying [46,83,126,127]. Amorphous HEAs are not emphasized in this review.

4.2. Observed phases

This review includes 408 unique alloys. Some alloys are evaluated in more than one paper and/or with more than one process condition, giving a total of 648 unique microstructure reports. A microstructure report gives alloy composition, processing and post-processing methods, and the number and types of phases. In the analyses performed here, results from each report are counted with equal weight. This is an imperfect approach, since alloys, microstructures and phases that are studied more frequently will seem to be more common. For example, CoCrFeMnNi is studied in 15 different reports and CoCrFeNi appears in 16 reports, giving an apparent bias to the single-phase, FCC microstructures in these alloys. Also, this approach counts erroneous results. For example, non-equilibrium phases in an as-cast alloy are counted with equal merit as are equilibrium phases in the same alloy that has been homogenized. However, different assessment approaches also have issues. One alternative approach could assign a single microstructure to each unique alloy after assessing all data for that alloy. In this case, the assessed microstructure may be rather subjective and can also give erroneous results, especially when data are conflicting or incomplete. This alternative approach is also vulnerable to oversampling, since it is not always clear when two different alloys belong to the same phase field (Section 4.4.1.4). For example, do CoCrFeNi and CoCrFeMnNi belong to the same FCC phase field? Data needed to answer such questions are generally not yet available in the HEA literature. There are many opportunities for such evaluations to be subjective, and none of the approaches give a clear, unambiguous counting of microstructures and phases. The rules for counting alloys, microstructures and phases are clearest (that is, the least subjective) in the present approach, and the most significant issue (oversampling) can be accounted for (Section 4.3.1.3).

Section 4.2.1 and 4.2.2 thus report the percentages of total microstructure reports that display particular phases or microstructures in the alloys selected for study (see Table S1 in the Supplementary data, Appendix A). Issues biasing the current data and the effects of these biases are discussed extensively in Section 4.4.1. As a result of these biases, these results do not necessarily represent the probability with which any particular phase or microstructure may occur in a randomly selected alloy.

4.2.1. Number and types of observed phases

Twenty-three different crystalline phases are found in this assessment (see Table S1 of the Supplementary data in Appendix A). Crystal structures are listed in this work primarily by Strukturbericht notation. Exceptions are the A1 structure (Pearson symbol cF4, Cu prototype), which is listed as FCC; the A2 structure (Pearson symbol cI2, W prototype), which is labeled as BCC; the A3 structure (Pearson symbol hP2, Mg prototype), given as HCP; and σ is used to indicate the $D8_b$ crystal structure (Pearson symbol tP30, σ-CrFe prototype). Other crystal structures reported for CCAs are: A5 (tI4,

β-Sn); A9 (hP4, graphite); A12 (cI58, α-Mn); B2 (cP2, ClCs, *AlNi*); C14 (the hexagonal Laves phase) (hP12, MgZn$_2$, *Fe$_2$Ti*); C15 (the cubic Laves phase) (cF24, Cu$_2$Mg); C16 (tI12, Al$_2$Cu); DO$_2$ (cF16, BiF$_3$, *Li$_2$MgSn*); DO$_{11}$ (oP16, Ni$_3$Si); DO$_{22}$ (tI8, Al$_3$Ti); DO$_{24}$ (hP16, Ni$_3$Ti); D2$_b$ (tI26, Mn$_{12}$Th, *AlFe$_3$Zr*); D8$_5$ (hR13, Fe$_7$W$_6$, *Co-Mo* and *Fe-Mo*); D8$_m$ (tI32, W$_5$Si$_3$, *Mo$_5$Si$_3$*); E9$_3$ (cF96, Fe$_3$W$_3$C, *Fe-Ti*); L1$_0$ (tP2, AuCu); L1$_2$ (cP4, AuCu$_3$); and L2$_1$ (Heusler) (cF16, AlCu$_2$Mn). Strukturbericht notation could not be found for NiTi$_2$ (cF96). The phase immediately following the Pearson symbol in the list above is the prototype phase and italicized compounds indicate reported phases when different from the prototype. Phases that display at least one superlattice peak but that are otherwise undetermined are listed as IM and phases for which no identification is offered are listed as Unk (unknown). This list includes 6 disordered crystal structures (BCC FCC, HCP, A5, A9, A12).

SS microstructures are the most commonly reported (309 reports, 48% of the total reported microstructures), but (SS + IM) alloys are nearly as common (268 reports, 42% of the total) and 66 alloys (10%) have only IM phases (Fig. 9a). SS alloys are most often single-phase (163 reports, 25% of reported microstructures and 53% of the SS alloys), with fewer 2-phase alloys (113 reports, 17% of reported microstructures) and 33 3-phase SS alloys (5% of reported microstructures). These sub-classifications are shown for SS, IM and (SS + IM) alloys in Fig. 9a.

The 648 reports include 213 single-phase alloys (33%), 294 2-phase alloys (45%), 105 3-phase alloys (16%), 21 4-phase alloys, 8 5-phase alloys and 2 6-phase alloys (Fig. 9b). Of the 213 single-phase alloys, 163 are SS and 50 are IM (see the sub-classifications in Fig. 9b).

By far the most common phases are disordered FCC (found 465 times in 410 alloys) and BCC (found 357 times in 306 alloys), followed by the ordered IM phases B2 (177 occurrences in 175 alloys), σ (60 occurrences in 60 alloys) and the hexagonal Laves phase C14 (found 50 times in 50 alloys) (Fig. 10). The HCP phase occurs in only 7 alloys. The total number of times an FCC phase appears in a microstructure, normalized by the number of times BCC, FCC or HCP phases appear, is 56%. BCC phases are slightly less common (43%), and HCP phases make up 1% of the times a BCC, FCC or HCP phase is reported (Table 5). Six of the 7 HCP phases come from three different alloy families (light metal, 4f transition metal and 'other' CCAs). There are no common elements between these alloy families, suggesting that there are still many opportunities to discover new CCAs with the HCP crystal structure.

All but one single-phase FCC SS alloy belong to the 3d transition metal MPEA family and ternary alloys of 3d transition metals (the exception is AlLiMg$_{0.5}$ScTi$_{1.5}$). Typical single-phase FCC SS alloys are CoCrFeMnNi [1,128,129], CoCr$_x$FeNi ($0.5 \leq x \leq 1.15$) [129,130],
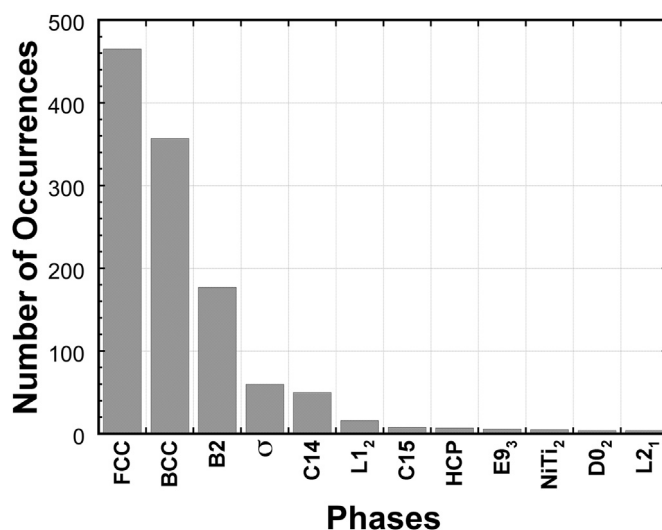
Fig. 10. The number of times each phase is found in the 648 microstructure reports in this review. If a phase occurs more than once in the same alloy then that phase is counted for each occurrence. IM denotes phases identified as intermetallic compounds without specifying the particular crystal structure. Phases that occur fewer than 4 times are not shown, and include A5, A9, A12, C16, DO$_{22}$, DO$_{24}$, D2$_b$, D8$_5$, D8$_m$, L1$_0$ and Ni$_3$Si. Unidentified phases and amorphous phases are also not shown.

Al$_x$CoCrFeNi ($x \leq 0.3$) [131–133], CoCrCuFeNi [134–136] and CoCrCuFeMnNi [6,49,137]. A glimpse of this phase field comes from previous experience on austenitic stainless steels and nickel alloys, but the present work shows that it extends much farther in hyper-dimensional composition space. Using CoCrFeNi as a base, alloys that additionally contain Cu, Mn, Mo, Pd and V have now been studied. Both equimolar and non-equimolar concentrations of these elements have been considered. The compound-forming elements Al, Si, Sn and Ti have also been added. The limits of the FCC single-phase field have been determined for most of these elements. The extent of this phase field is remarkable, and includes a six-component equimolar alloy (CoCrCuFeMnNi) and non-equimolar seven-element alloys. The frequency and extent of this phase field has been used to support the high entropy effect hypothesis. However, the constituent elements in this alloy system typically have unusually low mixing enthalpies, H^{SS}, (Section 4.4.1.3). The FCC crystal structure in these alloys also appears to be influenced by high atomic fractions of FCC-stabilizing elements such as Co, Cu, Mn and Ni (see Section 4.3.1.3), as well as small atomic size difference between the alloying elements. Thus other
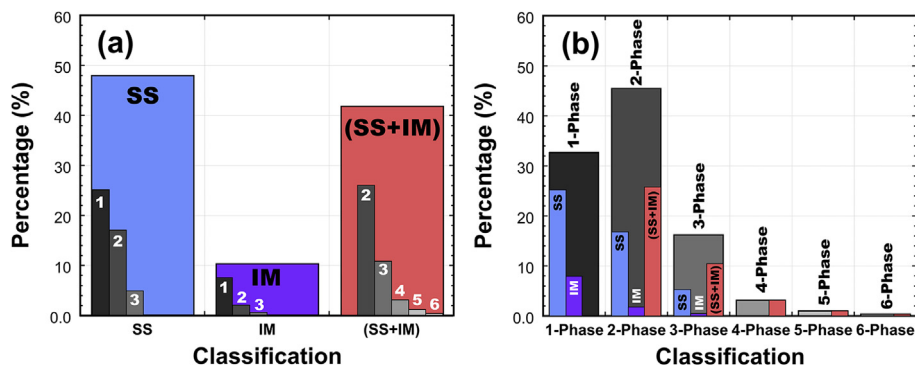
Fig. 9. (a) Microstructure classification by phase type (SS, IM, SS + IM) with sub-classifications by the number of phases, and (b) classification by number of phases with sub-classification by the phase types. The vertical axis is the percentage of the 648 microstructure reports that give the indicated type or number of phases. A SS microstructure contains one or more SS phases, an IM microstructure has one or more IM phases, and a (SS + IM) microstructure has at least one SS phase and at least one IM phase.

Table 5
BCC, FCC and HCP phases as percentages of the total number of times these phases occur in experimental and CALPHAD microstructures.

Structure	Experiment	Experiment SISO[a]	CALPHAD ($f_{AB} = 1$)	CALPHAD ($f_{AB} = 1$) SISO[a]	CALPHAD ($f_{AB} = $ All)	CALPHAD ($f_{AB} = $ All) SISO[a]
BCC	43%	50%	65%	64%	62%	63%
FCC	56%	49%	29%	32%	12%	26%
HCP	1%	1%	6%	4%	26%	11%

[a] 'Structure in − structure out' analysis (Section 4.3.1.3).

factors are likely to be important and this result cannot be credited to configurational entropy alone.

Although CoCrFeMnNi is widely considered a prototype single-phase FCC SS alloy, three additional phases are found when annealing at 723 K after severe plastic deformation [138]. The new phases observed using transmission electron microscopy (TEM) and 3D atom probe tomography (3D-APT) are FeCo, MnNi and a Cr-rich phase. For comparison, the low-temperature Co-Cr-Fe-Mn-Ni phase diagram in Fig. 1b shows FeCo, MnNi$_3$ and CoCrMn$_2$.

About 45% of reported single-phase BCC alloys belong to refractory metal CCAs, even though this alloy family comprises only 7% of the alloys in this assessment. The remaining 55% of single-phase BCC alloys are 3d transition metal MPEAs. All the BCC alloys from the 3d transition metal alloys contain Al, Cr and Fe and some also contain Si, Ti and BCC refractory elements [9,17,48,108]. All these elements are BCC stabilizers in steels. Single-phase BCC refractory CCAs consist of BCC refractory elements, excluding Cr, and some of them also contain Al, Ti, Hf and Zr [23,38,100,104,107,139,140].

All duplex (BCC + FCC) MPEAs belong to the 3d transition metal family. The duplex structure in these alloys is formed at certain combinations of FCC and BCC stabilizing elements. Almost all the duplex alloys contain more than 10 at.%Al. Those with smaller amounts of Al or without it are enriched with Cr, Ti and/or V.

Common IM phases include B2 (cP2, ClCs prototype, in 175 alloys), σ (D8$_b$, tP30, CrFe prototype, 60 alloys) and C14 hexagonal Laves (C14, hP12, MgZn$_2$ prototype, 50 alloys). Laves phases also have a cubic form (C15, cF24, Cu$_2$Mg prototype) that is less common in this dataset (Fig. 10). The B2 phase generally appears in microstructures with a BCC phase, and the L1$_2$ phase is generally seen with an FCC phase. All B2 and L1$_2$ phases are in alloys that contain Al. The σ phase always forms in 3d transition metal alloys that generally contain Co, Cr and/or V, Fe and Ni. The Laves phase forms mostly in the 3d transition metal family with a few in the refractory metal family. Alloys with the Laves phase always have Cr and (Nb or Ti), and usually have Co, Fe and Ni. Its formation is supported by a large atomic size difference. Specific structures are not given for 49 IM phases. A histogram of phases in the 648 reports is shown in Fig. 10. Microstructures often have more than one phase, so the histogram bars in Fig. 10 sum to more than 648.

These results suggest that SS phases (Fig. 9a), single-phase microstructures (Fig. 9b) and FCC phases (Fig. 10) are all rather common, and such observations have been used to support the high entropy effect. However, detailed analysis shows that six major concerns bias these results and limit the degree to which the data give a statistically representative sampling of the broad field of CCAs (Section 4.4.1). An in-depth analysis of the current evidence regarding the high entropy effect is given in Section 4.4.3.

4.2.2. Phase morphologies and distributions

Microstructure is of fundamental importance in controlling materials properties. Most early MPEA studies characterize microstructures in the as-cast condition (Section 4.4.1.1), and a growing number report homogenized microstructures. Dendrites and compositional coring are common. Eutectic microstructures and spinodal decompositions are also indicated. In many cases, phases

are produced with sub-micron and even nanometer dimensions, and amorphous phases can be produced. Some rather remarkable 2-phase microstructures have been studied [141−144]. In short, a broad range of microstructures has been observed in MPEAs. However, very few HEA studies have undertaken to intentionally design and manipulate microstructure. The motivation in the HEA community to explore single-phase SS alloys may contribute to this state. Recent papers emphasize the importance of microstructural design [25,26], supporting the growing interest in precipitation in MPEAs. Some recent efforts are briefly described here.

Precipitation hardening is an effective strengthening mechanism for CCAs [145−147], but few publications report precipitate formation, morphology, phase and structure. Several papers focus on precipitation in the Al-Co-Cr-Cu-Fe-Ni system [59,148−152]. Al and Cu are the most influential elements to phase formation in this system. For example, Al$_x$CoCrCuFeNi with $x \geq 1.0$ have BCC/B2 structures, with $0.8 \leq x < 1.0$ have BCC/B2+FCC structures and with $x < 0.8$ have FCC structures [149]. Plate-like, spherical and rhombohedral precipitates are found in the BCC phase of AlCoCrCuFeNi [148]. Needle-like Widmanstätten and small spherical precipitates, both enriched with Cu, are found in the FCC phase of Al$_{0.5}$CoCr-CuFeNi after annealing at 900 °C for 5 h [150]. Plate-like and spherical FCC precipitates are seen in Al$_{0.3}$CoCrCu$_{0.5}$FeNi after homogenization at 1100 °C for 24 h and furnace cooling [151]. The plate-like precipitates are roughly rectangular, with habit planes parallel to {100} and edges along <100> of the FCC parent phase. Two phases are found in the plates: a Cu-rich phase with an FCC structure and a (Ni,Cu)$_3$Al phase with an L1$_2$ structure. Both phases are coherent with the matrix. Spherical precipitates rich in Al, Ni, and Cu are also coherent and have an L1$_2$ structure. During cooling, Cu-Ni-Al-rich plates are suggested to precipitate first. These plates subsequently separate into Cu-rich and (Ni,Cu)$_3$Al phases when the temperature falls below 930-900 °C during furnace cooling. At still lower temperature, spherical precipitates form in the inter-plate region due to further reduction in solubility.

Precipitation kinetics are studied in cast and homogenized Al$_{0.3}$CrFe$_{1.5}$MnNi$_{0.5}$ [153]. In the homogenized condition, the alloy has a 2-phase, BCC + FCC structure. Subsequent aging in the range of 500−700 °C results in IM precipitation and age hardening. Hardening occurs much faster at the surface than in the bulk. The time dependence of the thickness of the hardened surface layer does not follow long-distance diffusion kinetics but occurs similar to a self-induced or reaction-accelerated short-range decomposition with the thickness increasing with the cube of aging time. The rapid formation and growth of surface precipitates is concluded to come from a lower total nucleation energy and strain energy on the surface (55 kJ/mol) relative to the nucleation energy in the bulk (78 kJ/mol).

4.3. Calculated phases

Many attempts have been made to predict alloys that favor SS phases, but more recent approaches explore systems that may enable precipitation strengthening. The largest effort is on empirical approaches, but growing efforts are apparent in thermodynamic modeling and the use of atomistic models. These efforts are

briefly reviewed here.

4.3.1. Empirical approaches

4.3.1.1. Hume-Rothery rules and thermodynamic parameters for HEAs. Hume-Rothery rules are perhaps the earliest guide to the formation of SS alloys [154–156]. These rules state that extended solid solutions are favored in alloys whose elements have similar atom sizes, crystal structures, electronegativities and valencies. To apply these concepts to predict SS phase formation in complex alloys, the HEA community has developed composition-weighted terms for differences in atom radii (δr) and electronegativity ($\delta \chi$), and for an average valence electron concentration (VEC) [29,46–49]. Thermodynamic considerations are reflected through the enthalpy of mixing (H^{SS})[5] and through an Ω term that combines H^{SS}, entropy of mixing (S^{SS})[5] and melting temperature, T_m [157]. Equations for these terms are

$$\delta r = \sqrt{\Sigma c_i (1 - r_i / \bar{r})^2} \tag{4.1}$$

$$\delta \chi = \sqrt{\Sigma c_i (1 - \chi_i / \bar{\chi})^2} \tag{4.2}$$

$$VEC = \Sigma c_i VEC_i \tag{4.3}$$

$$H^{SS} = \sum_{i<j} 4 H_{ij} c_i c_j \tag{4.4}$$

$$\Omega = \left(\Sigma c_i T_{m,i} \right) \left(S^{SS} \right) / \left| H^{SS} \right| \tag{4.5}$$

Here r_i, χ_i, VEC_i and $T_{m,i}$ are atomic radius, electronegativity, valence electron concentration and melting temperature of element i; c_i and c_j are the atom fractions of atoms i and j; $\bar{r} = \sum c_i r_i$ and $\bar{\chi} = \sum c_i \chi_i$ are the average atomic radius and electronegativity; and H_{ij} is the enthalpy of mixing of elements i and j at the equimolar concentration in regular binary solutions [158]. The terms δr and $\delta \chi$ are often reported as percentages — Eqs. (4.1) and (4.2) are multiplied by 100 accordingly.

4.3.1.2. Correlations using δr, $\delta \chi$, VEC, H^{SS} and Ω. No correlations are found between phases formed and $\delta \chi$ or VEC when a large number of alloys and a range of alloy families are considered — SS, IM and (SS + IM) MPEAs all have similar ranges in $\delta \chi$ and VEC values [46,56]. However, VEC can separate phases when a limited number of alloys are considered within a given alloy family. Compositions for BCC and FCC phases are separated in as-cast $Al_x CoCrCuFeNi$ and $Al_x CoCrFeNi_2$ alloys ($0 \leq x \leq 2$) [29], and σ phase formation is predicted in annealed alloys containing Cr and Fe along with Al, Co, Mn, Ni, Ti and/or V [159]. These correlations become unreliable as more elements are added, for example the same VEC range predicts BCC + FCC in Ref. [29] but predicts σ phase formation in Ref. [159]. The addition of Mn is suggested to make these predictions unreliable [29].

Most empirical approaches to predict SS or IM phases in HEAs use δr and H^{SS} or Ω [48,49,157,160–164]. Atom size mismatch and H^{SS} are well-known empirical criteria for amorphous (AM) alloys [165]. These parameters separate SS and AM phases in HEAs, but IM phases overlap with both of these fields [49,162] (Fig. 11a). A later attempt to separate SS and IM domains combines H^{SS}, S^{SS} and T_m in the Ω parameter [48]. The results are a little better than δr vs. H^{SS}

correlations but overlap is still seen (Fig. 11b). The ability to separate SS and AM phases can be understood, since H^{SS} is a property of disordered solution phases, to which SS and AM phases belong. In all of these analyses, negative H^{SS} values are claimed to stabilize IM phases or to destabilize SS phases by competing with S^{SS} [48,49,157,160]. These statements are incorrect, since negative H^{SS} values work together with S^{SS} to stabilize solid solutions (Section 2.1.1). Large, negative values of H^{IM} will destabilize SS phases by competing with S^{SS}. H^{SS} may be a proxy for H^{IM} — systems with large, negative H^{SS} will generally have even more negative values of H^{IM} and thus be prone to IM phase formation (Section 2.2.3). This idea has recently inspired new approaches to improve SS and IM phase prediction by explicitly considering H^{IM} (Section 4.3.2.2, Section 4.3.2.3), giving an improved ability to separate IM and SS phases.

As-cast microstructures are usually used to support these criteria, limiting their predictive capability to near-solidus temperatures [32,166]. This approach may also be acceptable for the limited number of alloys with no phase transformations below the solidus temperature, but caution is required for most alloys since the microstructures produced do not represent the equilibrium state and will depend on casting conditions. It is therefore not surprising to find that different phases and different levels of decomposition and inhomogeneity are found in the same HEAs by different authors [11,17,82]. As-cast observations overestimate the extent of SS microstructures, and annealing 27 alloys significantly narrows the range of SS phases in the H^{SS} *vs.* δr plot [167]. This appears to improve separation between SS and IM domains (Fig. 11a), but some overlap may remain due to issues regarding the ability to correctly identify IM phases (Section 4.4.1.5) [167]. More recent work compares 45 annealed microstructures against the empirical models in Fig. 11, and much poorer separation between SS and IM phases is found [79]. Combining annealed data with thermodynamic models that correctly account for H^{IM} gives improved results (Section 4.3.2.3).

4.3.1.3. 'Structure in — structure out' (SISO) correlations. Surprise is sometimes reported at the frequency with which microstructures are single-phase, or SS, or contain simple (FCC, BCC or HCP) crystal structures (see for example [6,82]), and these comments are used to support the high entropy effect. Here we suggest that HEA solid solutions have simple crystal structures simply because the elements used in HEAs almost always have simple structures. Of the 37 elements in the 408 alloys analyzed here, 33 have BCC, FCC or HCP crystal structures at their melting temperature, T_m (Table 3). The 4 elements with complex crystal structures at T_m (B, Ge, Si, Sn) are used infrequently, and no HEA contains more than one complex element, so that HEAs are always dominated by simple elements. If we normalize the number of times these 4 elements are used (34, see the 3rd column in Table 3) by the total number of alloy-elements (2284, sum the 3rd column in Table 3), we estimate that < 2% of SS phases are expected to have complex structures. None are reported. We conclude that it is not surprising that most HEA SS phases have simple crystal structures.

Further, we estimate the fractions of observed BCC, FCC and HCP phases by considering how often these crystal structures are used. From Table 3, we sum the number of times elements are used with BCC, FCC or HCP crystal structures at T_m. We normalize these three sums by the total number of times that BCC, FCC and HCP elements are used in alloys (2250). For the 408 alloys analyzed here, this approach estimates that 50% of observed SS phases will be BCC, 49% will be FCC and 1% will have the HCP structure. This gives good agreement with experimental data (Table 5) and is shown graphically in Fig. 12.

Elements in CALculated PHAse Diagram (CALPHAD) calculations

---

[5] The terms H^{SS} and S^{SS} are used here to maintain consistency with notation in the present work. These terms are equivalent to ΔH_{mix} and ΔS_{mix}, respectively, in the cited papers.
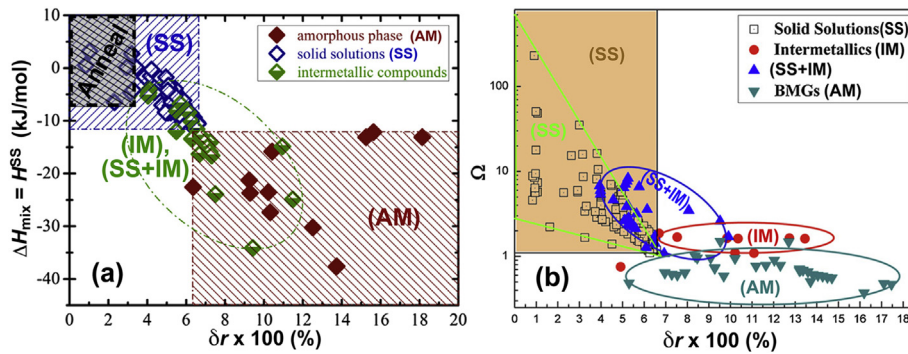
Fig. 11. Empirical correlations to separate SS, IM, (SS + IM) and amorphous (AM) phase regions using (a) δr vs. H^SS [160] and (b) δr vs. Ω [48]. Both correlations separate SS and AM, but IM and (SS + IM) overlap these two regions in (a) and (SS + IM) overlaps in (b). As-cast data are typically used to support these correlations. Annealing reduces the extent of the SS region [167], as shown in (a). Figures are redrawn from Refs. [48,160] for consistency with current terms.

(Section 4.3.2.4) show different biases than the experimental dataset, but the fractions of BCC, FCC and HCP phases from CAL-PHAD calculations can nevertheless be estimated with the same 'structure in − structure out' analysis demonstrated above for experimental alloys. The estimates sum of the number of times BCC or FCC or HCP elements are used in CALPHAD alloys divided by the total number of times BCC and FCC and HCP elements are used. This analysis agrees well with CALPHAD results for two different data-sets (Table 5 and Fig. 12), one with only the most reliable results ($f_{AB} = 1$) and another for the full dataset ($f_{AB} = $ All) (see Section 4.3.2.4 for discussion of these datasets). A similar analysis also gives good agreement by calculating the fractions of N-component alloys where all elements in the alloy have the indicated crystal structure [56,125]. These simple estimates apply the Hume-Rothery criterion of crystal structure to CCAs for the first time, and can be viewed as a 'structure in − structure out' (SISO) analysis. It is recommended by its simplicity, intuitive physical foundation and ability to predict the fractions of simple crystal structures.

We apply a similar approach to estimate the fraction of SS

Fig. 12. Comparison of observed (experimental measurements or CALPHAD calculations) and estimated (by a 'structure in − structure out' analysis) phase content. Observed content is the number of times a phase (BCC, FCC or HCP) or microstructure (SS) is reported, normalized by the total number of observations (BCC + FCC + HCP for phase analysis and SS + IM + (SS + IM) for microstructure analysis). The 'structure in − structure out' analysis is based on the crystal structure of constituent elements at T_m (for phase estimates) or on the percentage of binary systems in a collection of alloys that are ideal or regular solutions. The data are given in Table 5.

microstructures. The 3d transition metal family of alloys represents 85% of all MPEAs in this assessment, 63% of these alloys have the CoCrFeNi 4-element branch, and 83% of the 6 binary systems in this 4-element branch are either ideal or regular SS alloys (Table 4). We estimate the fraction of SS alloys in the full dataset as the product of these percentages, (85%)(63%)(83%) = 44%. This is close to the value from the full dataset of 408 alloys (48%). Of course the problem is more complicated, but this zero-order estimate suggests that the current results are not so surprising, given the experimental bias for alloys that contain a significant fraction of ideal or regular binary solutions (Section 4.4.1.2).

The 'structure in − structure out' analysis is based on Hume-Rothery principles and formalizes our intuition − we are not surprised that BCC solid solutions dominate refractory metal CCAs (whose constituent elements are dominated by BCC elements) and that FCC solid solutions occur more commonly in 3d transition metal CCAs, where FCC constituent elements are more frequently used. This analysis correctly predicts the fractions of BCC, FCC or HCP SS phases in three different datasets from experiments and calculations. It does this by calculating the fractions of elements used with BCC, FCC or HCP crystal structures at T_m in each dataset. The only significant disagreement is for FCC and HCP phases of the least reliable calculations ($f_{AB} = $ All). FCC and HCP structures can be difficult to separate energetically, since both have the same 1st neighbor environment and differ only in the 2nd neighbor shell and beyond. The 'structure in − structure out' analysis also predicts the frequency with which SS microstructures are found relative to all microstructure types (SS, IM and (SS + IM)). This approach assumes that each element has an equal influence, but a casual analysis shows that this is not always true. The CoCrFeMnNi alloy is single-phase FCC, even though 3 of the constituent elements are BCC at T_m (Cr, Mn, Fe) and only 2 are FCC (Co, Ni). Thus, this approach does not always correctly predict which alloy will have a particular crystal structure. It may be able to estimate the probability with which an alloy will have a particular crystal structure, and when considered over a large number of alloys the 'structure in − structure out' analysis seems to give reliable results.

4.3.2. Thermodynamic models

Several thermodynamic models have been used to estimate the phases in HEAs. These are described below, starting with the simplest model and progressing to the most detailed thermodynamic description.

4.3.2.1. Ideal configurational entropy only (the high entropy effect).

The high entropy effect hypothesizes that configurational entropy alone may favor single-phase, SS microstructures [6,21]. This
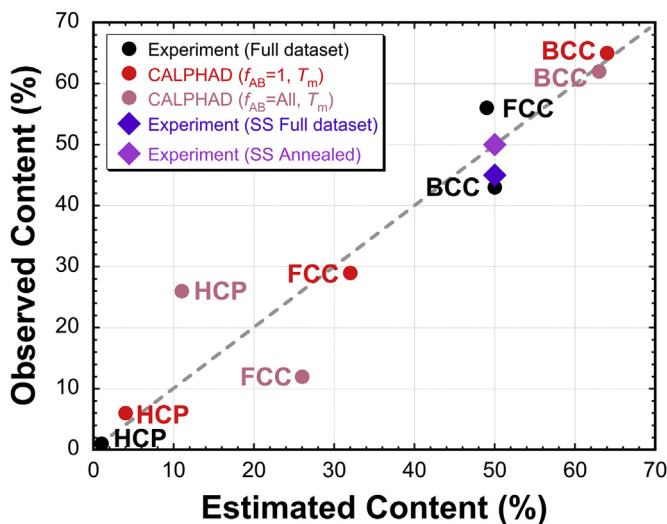
models alloys as ideal solutions where configurational entropy dominates the Gibbs energy. Eq. (2.2) for ideal solid solutions gives

$$G^{\text{SS,ideal}} = -T\left(S^{\text{SS,ideal}}\right) = -RT\sum_i x_i ln(x_i) \qquad (4.6a)$$

where R is the gas constant, T is absolute temperature and x_i is the atom fraction of element i. For equimolar alloys with N components, this reduces to

$$G^{\text{SS,ideal}} = RTln(N) \qquad (4.6b)$$

In this approach, the Gibbs energy is adjusted by varying the number and concentrations of alloy elements in Eq. (4.6a). The Gibbs energies of competing IM phases are not considered directly. The simplicity of this model is perhaps its most attractive feature. A critical assessment of this hypothesis is a major objective of this paper, and is given in Section 4.4.3.

4.3.2.2. Ideal configurational entropy and intermetallic formation enthalpy only. The stability of competing SS and IM phases is analyzed by comparing contributions to Gibbs energy from ideal configurational entropies of SS alloys ($S^{\text{SS,ideal}}$) and formation enthalpies of binary IM compounds ($H^{\text{IM,binary}}$) [168]. $H^{\text{IM,binary}}$ values are calculated using high throughput density functional methods [6], and differences between $H^{\text{IM,binary}}$ and formation enthalpies of IM phases in N-component, complex alloys, $H^{\text{IM,N}}$, (Section 2.2.3) are neglected. The annealing temperature, T_{ann}, is taken to be at least 55% of the absolute melting temperature, T_m. The Gibbs energy difference between IM and SS phases is thus

$$\Delta G^{\text{IM}-\text{SS}} = \left(H^{\text{IM,binary}} - H^{\text{SS}}\right) - T_{\text{ann}}\left(S^{\text{IM}} - S^{\text{SS,ideal}}\right)$$
$$= \left[H^{\text{IM,binary}} + T_{\text{ann}}\left(S^{\text{SS,ideal}}\right)\right] - \left[H^{\text{SS}} + T_{\text{ann}}\left(S^{\text{IM}}\right)\right] \qquad (4.7)$$

As simplifications, SS enthalpies and IM entropies are assumed to be zero, $H^{\text{SS}} = S^{\text{IM}} = 0$. Both H^{SS} (Section 2.1.3, Section 2.2.3) and S^{IM} (Section 2.2.2) may be significant in CCAs, but generally $H^{\text{SS}} < 0$ in alloys that form IM phases and $S^{\text{IM}} > 0$ in CCAs with more elements than sub-lattices in the IM structure. These two terms will therefore generally offset each other (see the last two terms in Eq. (4.7)), supporting the approximation that $H^{\text{SS}} = S^{\text{IM}} = 0$ in this approach. Unlike phenomenological methods that incorrectly assume that H^{SS} destabilizes SS phases by competing with S^{SS}, this approach correctly represents the competition between H^{IM} and $S^{\text{SS,ideal}}$. Single phase alloys are proposed to result if all $H^{\text{IM,binary}}$ values in a given MPEA fall between the entropic energy $-T_{\text{ann}}S^{\text{SS}}$ and an enthalpy empirically determined as the limit for phase separation (37 meV/atom or 3.6 kJ/mol).

This model does a good job of distinguishing between alloys determined experimentally to be single-phase SS and microstructures that contain IM phases. The model reinforces the earlier experimental result that both configurational entropy and H^{IM} must be considered to understand phase formation in HEAs [169]. A list of 30 predicted, new single phase SS HEAs is provided to stimulate future experimental studies. In addition to Co, Cr, Fe, Mn and Ni, these alloys contain elements such as Ir, Os, Pd, Pt, Re, Rh and Ru. This approach predicts that the fraction of single-phase, SS alloys decreases as the number of components increase, supporting
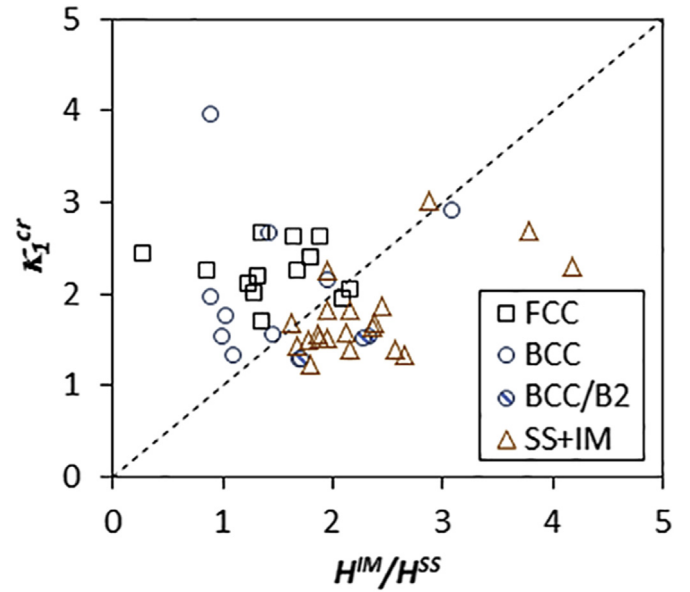
Fig. 13. A plot of the critical value κ_1^{cr} *vs.* $H^{\text{IM}}/H^{\text{SS}}$ for annealed MPEAs. κ_1^{cr} is evaluated at the annealing temperature, T_A. Good separation of SS alloys from IM-containing alloys is shown. All SS alloys, except two with an FCC structure and one with a BCC structure, fall above the dashed line and all but two of the IM-containing HEAs fall below this line. The figure is replotted from Ref. [79] to maintain consistency with current nomenclature.

earlier predictions of the same result [56,125].

All predictions are made for equimolar alloys, and some adjustment may be needed for non-equimolar alloys. The entropy can be easily adjusted to include non-equimolar alloys. However, the current model uses the most negative value of $H^{\text{IM,binary}}$ in a binary system, but this IM phase may not occur in non-equimolar alloys. For example, experimental results on annealed alloys show that the B2 phase often occurs in alloys containing Al, but SS microstructures are reported when the Al concentration falls below a critical level.

4.3.2.3. Linear relationships between enthalpies and between entropies. S^{IM} of compounds with more elements than sub-lattices can be a significant fraction of $S^{\text{SS,ideal}}$ for the same composition (Section 2.2.2), and it's likely that H^{IM} and H^{SS} are related (Section 2.2.3). These ideas have inspired an approach that assumes linear relationships between H^{IM} and H^{SS} and between S^{IM} and S^{SS} for a given alloy [79].

$$H^{\text{IM}}\big/H^{\text{SS}} = \kappa_1 \quad and \quad S^{\text{IM}}\big/S^{\text{SS}} = \kappa_2 \qquad (4.8a)$$

where $\kappa_1 > 1$, $0 \leq \kappa_2 < 1$, and it is assumed that $S^{\text{SS}} = S^{\text{SS,ideal}}$. Comparing H_{ij}^{IM}(from Refs. [170,171]) and H_{ij}^{SS} (from Ref. [45]) for 456 binary i,j alloys gives $H_{ij}^{\text{IM}} = 1.08H_{ij}^{\text{SS}} - 7.95(kJ/mol - atom)$, supporting this approach. κ_2 increases with a decrease in the level of ordering of the IM phase, which can be estimated using the sublattice model [40] and assigning the site occupancy. For multi-component IM phases with L1$_2$ or B2 crystal symmetry, κ_2 can vary from 0.4 to 0.8. Substituting Eq. (4.8a) in Gibbs energy equations for SS and IM phases, a critical value of κ_1 is calculated as

$$\kappa_1^{cr} = \frac{TS^{\text{SS}}}{H^{\text{SS}}}(1 - \kappa_2) + 1 \qquad (4.8b)$$

SS phases are predicted when $\kappa_1^{cr} > (H^{\text{IM}}/H^{\text{SS}})$ and IM phases are

---

[6] The twenty-nine most negative values in Table 1 of Troparevsky et al. appear to give enthalpies for the structural unit rather than per atom. These values may need to be divided by the number of atoms in the structural formula to give the enthalpy in eV/atom.

expected when $\kappa_1^{cr} < (H^{IM}/H^{SS})$. Comparing this model against the 45 annealed microstructures available shows an improved ability to separate SS and IM phases compared to empirical models, with only a minor degree of remaining overlap (Fig. 13).

This model assumes that κ_1 and κ_2 are independent, but some relationship may link these terms. Specifically, the larger is H^{IM}, the larger is the deviation from ideal behavior and the less likely it becomes that atoms are randomly distributed in competing solid solutions. As a broad generalization, this condition gives $S^{SS} < S^{SS,ideal}$, so that κ_2 increases as κ_1 increases. Further, κ_1^{cr} may decrease as κ_1 increases, producing a non-linear refinement. At present there is no rationale for estimating the effect of increasing H^{IM} on S^{SS}.

4.3.2.4. CALculated PHAse diagram (CALPHAD) modeling.

Phase diagrams are roadmaps for materials design. They give essential information for a given alloy composition and temperature, including the phases present, their compositions, volume fractions and transformation temperatures. Most binary and some ternary phase diagrams have been measured experimentally, but multi-component systems remain mostly unexplored. Experimental definition of multi-component phase diagrams is impractical due to the tremendous amount of work involved. In recent years, integration of the CALPHAD approach with key experiments has been demonstrated as an effective approach to determine complicated multi-component phase diagrams [37,50,56,125,172,173].

The essence of the CALPHAD approach is to develop thermodynamic functions that are empirically fit to experimental data from binary and ternary phase diagrams. Quaternary and higher order systems are not used because higher order interactions become negligibly weak [174], and a reliable account of more complex alloys is possible via combination and extrapolation of binary and ternary data [175]. Thermodynamic functions are grouped for a particular collection of elements into a thermodynamic database for a specific alloy family. These databases are intended not only to reproduce known data, but also to predict phase equilibria for alloys where data are not available. Most databases have been developed for alloy systems that are based on one principal element. A detailed account of the CALPHAD approach can be found elsewhere [41,176]. Here we discuss those features that are important for MPEAs.

The CALPHAD method is most reliable when interpolating between compositions used to build the database. Since databases usually use binary and ternary data, extrapolation is generally required for MPEAs, potentially reducing the accuracy of CALPHAD predictions. Nevertheless, extrapolation can give a good predictive capability. As an example, a thermodynamic database for the Al–Co–Cr–Fe–Ni system was developed by extrapolating binary and ternary systems to wider composition ranges, and phase diagrams predicted with this database agree well with experimental results [37]. Calculated multicomponent phase diagrams may also have reasonable accuracy without developing new databases. For example, a Ni-based database successfully predicted equilibrium phases and phase fractions in Al-Co-Cr-Cu-Fe-Ni alloys [166,177].

An approach is being developed to quantify the credibility of CALPHAD calculations [56,125]. Each database is constructed using some number of binary and ternary phase diagrams, and each alloy modeled by that database samples these binary and ternary diagrams differently. Consider a database for elements A−H that includes A-B, A-C, A-D, B-C and B-D binary diagrams and A-B-C and A-B-D ternary diagrams. Alloy ABCD has 6 binary and 4 ternary systems, but only 5 of the binary and 2 of the ternary diagrams are included in the A-H database. Thus, the fraction of assessed binary systems (f_{AB}) for alloy ABCD is 5/6 and the fraction of assessed ternary systems (f_{AT}) is 2/4. Alloy ACDE uses only 2 of the binary and none of the ternary diagrams in the A-H database, so that f_{AB} is 2/6 and f_{AT} is 0 for this alloy. Different alloys can have different f_{AB} and f_{AT} values when using the same database, and the same alloy can have different f_{AB} and f_{AT} values when modeled with different databases. The basic premise of this approach is that the credibility of CALPHAD calculations is related to the magnitude of f_{AB} and f_{AT} — the larger are these values, the more credible are the calculations. It is not yet known what f_{AB} and f_{AT} values are needed to produce phase diagram predictions with acceptable reliability. Good agreement is found when $f_{AB} = 1$ [56,125], and nominal agreement for the types and numbers of phases is still achieved when f_{AB} is as low as 0.6, especially near the solidus temperature [56,125].

Phase diagrams of over 130,000 different equimolar alloys containing from 3 to 6 elements, produced by high-throughput CALDPHAD calculations, have been analyzed to assess trends in phases present [56,125]. These analyses show that the likelihood of forming SS alloys decreases as the number of alloy constituents, N, increases. The same trend is found for the most credible calculations ($f_{AB} = 1$), for calculations with any f_{AB} value, and at both T_m and at 600 °C. This trend is corroborated by later predictions using a different modeling approach [168] (Section 4.3.2.2) This finding is opposite the trend proposed by the high entropy effect, and is discussed further in Section 4.4.3.

The fraction of single-phase, SS alloys decreases with decreasing temperature, as expected from a less negative entropic energy, $-TS^{SS}$. Single-phase alloys are usually SS and are less frequently IM (Fig. 9b). Given that commonly studied HEAs have extended SS phase fields (Section 4.4.1.4) and that IM phases often have restricted composition ranges, single-phase IM alloys are expected to be relatively uncommon (Section 2.3.1). These CALPHAD calculation results are in good agreement with the experimental data (Fig. 9). If an alloy satisfies all 4 Hume-Rothery rules, then CALPHAD calculations always show such alloys to be SS. However, not all alloys that are calculated via CALPHAD to be SS satisfy all 4 rules. For example, SS alloys can have $\delta\chi$ as large as 30% and $\delta(VEC)$ as large as 55%. Atomic size is the most potent Hume-Rothery condition, and every SS alloy has $\delta r \leq 15\%$. CALPHAD calculations show only modest separation of SS from IM or (SS + IM) microstructures based on δr and $\delta(VEC)$, and no separation based on $\delta\chi$ or H^{SS} [56,125]. High-throughput CALPHAD calculations identify over 150 new CCAs that are single-phase SS at T_m, and some may be age-hardened at lower temperatures for a controlled distribution of strengthening particles (see Tables 9−15 in Ref. [56]). These alloys provide significant new opportunities for future development studies.

The most common predicted phases are BCC, M_5Si_3, FCC, B2 and Laves (C15) for the most credible calculations ($f_{AB} = 1$), and are BCC, HCP, M_5Si_3, B2 and FCC for the full dataset (any f_{AB} value). Thus, HCP phases are less commonly predicted for the fully credible calculations. Every Si-containing alloy forms silicide phases (all CALPHAD-calculated alloys in Refs. [56,125] are equimolar, so the Si concentrations are high). Along with f_{AB} values, additional validation is given by comparing predicted microstructures for the same alloy using different databases, where either good or nominal agreement are generally obtained (see Table 6 in Refs. [56,125]).

Elements are not used uniformly in reported CALPHAD calculations, since some elements are in more thermodynamic databases than others (see Table 1 in Ref. [56]). For example, Al and Cr are in every database used; Fe, Mo, Si, Ti and Zr are in all but one database; and Ni is in all but 2 databases. The elements Dy, Gd, Lu, Rh, Ru, Sc, Tm and Y each appear in only 1 or 2 databases. This bias is amplified in the $f_{AB} = 1$ dataset, since thermodynamic descriptions are usually only available for more commonly used elements. The

percentage of calculated alloys that use each element is shown for both CALPHAD datasets in Fig. 14. Elemental usage in experimental alloys is shown for comparison, where the bias is much stronger (Section 3.1, Section 4.4.1.2). The fractions of calculated BCC, FCC and HCP phases are different for the two published CALPHAD studies as a result of these biases. The frequency of calculated BCC, FCC and HCP phases, as a percentage of the total number of BCC, FCC and HCP phases in a calculated dataset, are BCC (65%), FCC (29%) and HCP (6%) for $f_{AB} = 1$ [56,125] and are BCC (62%), FCC (12%) and HCP (26%) for $f_{AB} =$ All [56,125] (Table 5). A SISO analysis gives good agreement with these values (Fig. 12).

The present analyses emphasize predictions of the type and number of phases. Uncertainties in predicted phase compositions, volume fractions and reaction temperatures (including T_m) may be larger and so are not reported in the literature. While approaches to evaluate the credibility of CALPHAD calculations are being developed, there are at present no approaches to estimate the errors that may be associated with CALPHAD calculations.

4.3.3. Atomistic methods

Though not yet sufficiently developed to routinely calculate complex, multi-phase microstructures, atomistic methods nevertheless give important insights into the phase stability of MPEAs. High-throughput atomistic calculations give H^{IM} values for thermodynamic models (Section 4.3.2.2). First principle calculations predict an order/disorder transition in MoNbTaW, stabilizing the B2 phase at intermediate temperatures due to strong Mo-Ta bonding [178]. This prediction however requires experimental verification, as only a disordered BCC phase was identified in this alloy [23]. First-principles calculations suggest that Ti interactions stabilize a Heusler-like L2$_1$ phase (cF16, AlCu$_2$Mn prototype) in CoCrCuFeNiAlTi. This phase has interesting magnetic properties and may enhance creep resistance in multi-phase alloys [179]. Morse pair-potentials from density-functional theory are used to model the structure of a single-phase AlCoCrCuFeNi MPEA [180]. The results show that the observed lattice structure is caused by the average of

the disordered composition and atomic position since there is neither short-range nor long-range order in the local atomic arrangement. Experimental data show this alloy to be multi-phase.

4.4. Discussion

4.4.1. Features biasing current microstructure observations

Six major considerations bias observed microstructures. Alloys are often characterized in the as-cast, non-equilibrium condition, and studying single-phase, SS microstructures is a motivation, leading to pre-selection of alloys that are likely to achieve this goal. These alloys are often characterized by low mixing enthalpies between constituents, and SS phases that are reported as separate may actually represent the same SS phase field in complex composition space so that the same SS phase field may be 'counted' many times. The characterization of ordered phases in MPEAs offers unique challenges, and IM phases are sometimes counted as SS. All six of these considerations increase the number of single-phase or SS microstructures and decrease the number of microstructures characterized as multi-phase or containing IM phases. The data in the literature, represented in Figs. 9 and 10, are therefore likely to over-represent the number of SS and single-phase microstructures. These points are described in more detail in the following sections.

4.4.1.1. As-cast condition.
Roughly 70% of MPEA microstructure studies characterize as-cast alloys. Such data do not represent the equilibrium state, and post-process annealing is required for reliable results. To study this effect, we analyze 46 alloys that are characterized in both as-cast and annealed conditions, giving 118 microstructural evaluations of the as-cast state and 121 of the annealed condition (see Table S1 in the Supplementary data, Appendix A). This analysis shows that annealing reduces the percentage of SS alloys and increases the number of (SS + IM) alloys (Fig. 15a). Further, the number of single-phase alloys is clearly reduced by annealing, while the percentage of microstructures with three or more phases increases (Fig. 15b). Finally, annealing reduces the extent of SS phases in phenomenological correlations (Fig. 11a). This analysis validates the concern that as-cast material does not represent the equilibrium state. As-cast analyses favor SS and single-phase microstructures, while annealing increases the number of phases and the probability of producing IM phases. Selected citations documenting these results include [159,166,169,181–190].

Post-process annealing is needed to establish the number and types of phases at equilibrium, but there is no standard thermal treatment to ensure that equilibrium is achieved. An annealing temperature above about half the absolute melting temperature is generally used, and the annealing time must support diffusion over distances needed to produce phases of sizes that can give reliable measurements. Electron-probe micro-analysis (EPMA) generally requires minimum phase dimensions of about 5 μm, while TEM and 3D atom probe need much smaller size scales. Diffusion coefficients in MPEAs are generally unknown (Section 5.2), so it is difficult to estimate appropriate annealing times. Annealing times of 100 h may be a practical starting point to approximate equilibrium, while experience from more conventional high temperature alloys suggest that times of up to 1000–2000 h may be required [191]. Annealing times for the MPEA studies discussed here are often 1–24 h.

Fig. 14. The frequency with which elements are used in experimental alloys and in the two CALPHAD datasets. Eight elements in the 3d transition metal alloy family are each in more than 20% of experimental alloys, and five of these elements are in over 2/3 of the studied alloys. The distributions are more uniform for CALPHAD calculated alloys, but biases are still seen. Elements are organized along the horizontal axis by atomic number. Elements that occur in fewer than 2% of alloys (Au, B, Be, C, Gd, Ge, Li, Nd, Pd, Tb and Zn) are omitted for clarity. The total number of experimental alloys is 408, in the CALPHAD dataset with $f_{AB} = 1$ is 5555, and in the CALPHAD dataset with $f_{AB} =$ All is 100,471.

4.4.1.2. Non-random alloy selection.
Principal elements in HEAs are not selected randomly. The goal of many HEA studies is to discover and characterize single-phase, SS alloys with simple crystal structures, and Hume-Rothery rules give an effective approach to favor such microstructures by choosing elements with similar sizes,
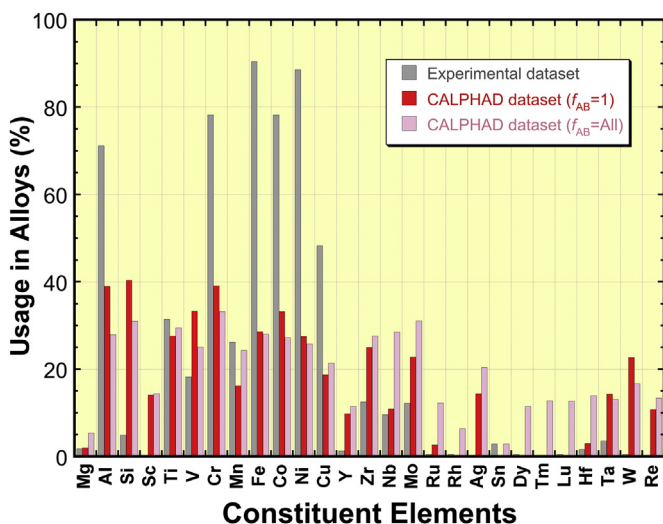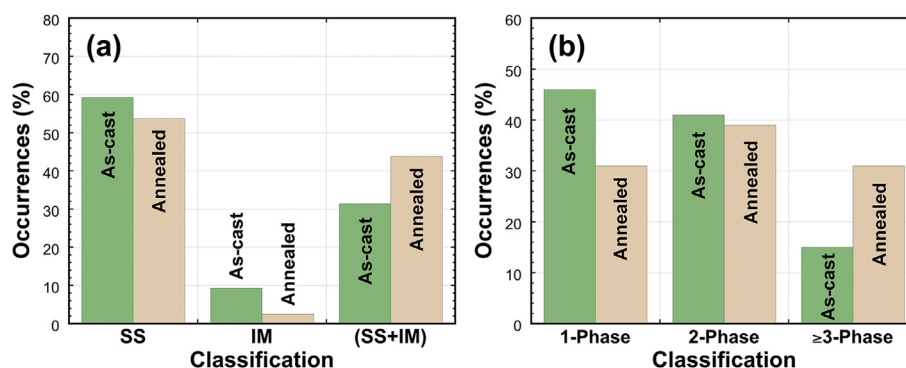
Fig. 15. Comparison of as-cast and annealed CCAs (a) by microstructures (SS, IM, (SS + IM)), and (b) by number of phases. The vertical axis is the percentage of the 239 microstructure reports from the same 46 alloys that give the indicated type or number of phases. Annealing reduces the percentage of SS and single-phase alloys and increases the percentage of (SS + IM) alloys and microstructures with 3 or more phases.

electronegativities and crystal structures. The selection of 3d transition metals in pioneering efforts [1,5] thus seems likely to favor single-phase solid solutions. Numerous subsequent efforts explore relatively small changes in concentrations or the addition of previously untried elements to a known single-phase, SS base alloy, further biasing data toward this result. The dramatic focus on this one alloy family (Section 3.2.1) therefore biases alloys to single-phase, SS microstructures with FCC crystal structures. This emphasizes one particular microstructure without equivalent consideration of other possible microstructures. This is not 'bad', it simply means that experimenters have been successful in achieving the desired outcome. Nevertheless, the scientific community must recognize the impact of this underlying intent and be cautious in interpreting the results from the field as a whole. The data generated to date cannot be analyzed as if it represents a random combination of elements or a random sampling of MPEA phases and microstructures. Stated simply, the current experimental dataset is not expected to give a representative sampling of phases or microstructures for the CCA field as a whole. The clear differences between experimental and calculated (CALPHAD) results underscore this expectation.

4.4.1.3. Low enthalpy alloys. Nearly all of the single-phase reports used to support the high entropy hypothesis come from the 3d transition metal family of alloys. This alloy family is unusual, since an exceptionally high fraction of the element pairs in this family have rather low mixing enthalpies, H^{SS}. For example, using data from Ref. [168], the 15 binary atom pairs in the CoCrCuFeMnNi alloy have an average mixing enthalpy of only -5 kJ mol^{-1}. Alloys in this family may thus be called 'low enthalpy' alloys. As a result, atom pairs in this family are far more likely to display ideal or regular solutions than typical (Section 4.3.1.3 and Table 4). It is difficult to determine if the prevalence of SS phases in this family result from low enthalpy, high entropy, or both.

4.4.1.4. Contiguity of SS phase fields in hyper-dimensional composition space. The HEA literature seems to report many different SS phases. But how can we tell when two SS phases are separate and distinct? Phases that appear to be separate in lower-order composition space may be connected in higher-order composition space. For example, Cu-Ni and Co-Fe are both extended binary solid solutions, and it appears that they are different from each other. However, CoCuFeNi is a single phase SS [192], and so it is likely that the Cu-Ni, Co-Fe and CoCuFeNi single-phase fields are all connected in Co-Cu-Fe-Ni phase space. As a result, the alloys CuNi, CoFe and CoCuFeNi may all represent different points in the same SS phase field. In the same way, CoFeNi, CoCrFeNi, CoCuFeNi,

CoCrCuFeNi, CoCrFeMnNi, CoCrFeNiTi, CoCuFeNiV, CrCuFeMoNi, CoCrCuFeMnNi and Al$_{0.5}$CoCrCuFeNi are all single-phase FCC, but they may be part of the same contiguous SS phase in hyper-dimensional composition space. Thus, the large number of single-phase SS phases reported for 3d transition metal MPEAs may actually represent a redundant oversampling of the same SS phase in hyper-dimensional phase space rather than a large number of different SS phases.

In fact, a quick analysis of the single-phase solid solutions with BCC, FCC or HCP crystal structures suggest only 13 different SS phase fields: three FCC, two BCC and an HCP phase in the 3d transition metal family; an FCC and an HCP SS phase field in the light metal CCAs; three BCC phase fields in the refractory metal CCAs; an HCP phase in 4f transition metal CCAs; and an HCP phase in the "other" category of CCA families (see Table S1 in the Supplementary data, Appendix A). This simple analysis infers at least 3 different FCC phases in the 3d transition metal CCAs from the CoCrCu$_{0.5}$FeNi alloy, which shows 3 distinct FCC phases [193,194], and counts at least 3 different BCC phases in the refractory metal CCAs from NbTiV$_2$Zr, which shows 3 distinct BCC phases [38].

Just as a ternary IM phase can exist that is disconnected from all bounding binary phases, it is possible that a SS phase field might occur in higher-order composition space that is not connected to any SS phase field in the bounding lower-order phase diagrams. We suggest that it is more likely that a SS phase that occurs in higher-order composition space is connected to one or more terminal SS phases in bounding lower-order phase diagrams. Nevertheless, this idea can be tested with CALPHAD calculations and is suggested for future work. For example, a series of isopleths such as those in Ref. [37] can be constructed to explore the contiguity of SS phases in multi-dimensional composition space.

4.4.1.5. Characterizing ordered, intermetallic phases in CCAs. Standard techniques are often adequate to characterize CCA SS phases, but compositional complexity introduces new challenges in identifying IM phases. Lattice distortions can decrease X-ray diffraction peak intensity [5,17,21], and a mixture of elements on different IM sub-lattices can decrease the scattering factor, further reducing super-lattice peak intensity. Finally, CCAs often contain both ordered and disordered phases with the same base structure and with nearly identical lattice constants. For example, the coexistence of BCC and ordered B2 phases or of FCC and ordered L1$_2$ phases is frequently reported [82,148,151]. These features work together to complicate identification of IM phases in MPEAs. TEM analyses often reveal IM phases in alloys that were initially reported to contain only SS phases [7,134,148,149,177,184,188,195—197]. For example, X-ray

analysis gives a BCC + FCC microstructure in AlCoCrCuFeNi [6,198], while TEM analysis reveals a modulated nanophase structure consisting of coherent BCC and B2 phases [184,197], as well as two L1$_2$ phases [148,149,188]. In some cases, a combination of X-ray and neutron diffraction is needed to characterize a phase, and the use of atomistic simulations further enriches the information content [59].

4.4.1.6. Classification of solid solutions. Some authors classify non-stoichiometric, IM compounds as SS phases (see for example [6,82]). This increases the number of reported SS phases and decreases the number of IM or (SS + IM) microstructures. As discussed in Section 4.1.3, this is considered inappropriate for HEAs since configurational entropy is proposed to favor solid solutions and the Boltzmann model used to estimate configurational entropy only applies to disordered solid solutions and cannot be applied directly to phases with two or more crystal sub-lattices.

4.4.2. Comparison of observed and calculated phases
Here we compare observed and calculated microstructures. These comparisons are tricky due to uncertainties in both observed (Section 4.4.1) and CALPHAD-predicted (Section 4.3.2.4) microstructures. Experimental challenges lead to different microstructures being reported for the same MPEA (Section 4.4.1.1), and calculations can give different results for the same alloy when different databases are used. These difficulties motivate a description of different levels of agreement. Direct agreement results when the types and numbers of phases match exactly. Nominal agreement occurs when the underlying structure of phases match, even if the distinction between ordered and disordered phases doesn't match or if the number of phases doesn't match. For example, (BCC + FCC), (B2+FCC) and (BCC + FCC1+FCC2) microstructures all show nominal agreement within the uncertainties described here [56,125]. The present comparisons focus on the types and numbers of phases and on broad trends rather than any particular detail.

Two CALPHAD datasets are available for equimolar alloys with 3—6 elements. The most credible dataset ($f_{AB} = 1$) gives 4983 distinct alloys, and 111,654 unique alloys are used when all f_{AB} values are included [56,125]. CALPHAD calculations are available at the alloy solidus (melting) temperature, T_m, and at 600 °C. The average number of elements for the experimental alloys studied here is 5.6, we compare with CALPHAD calculations for $N = 5$ elements.

Experiments show a strong preference for SS microstructures (48%) relative to CALPHAD calculations (5—17%) (Fig. 16a). Calculated (SS + IM) microstructures range from 73 to 82% of the total, but only 41% of observed microstructures are reported as (SS + IM). In both comparisons, measured microstructures fall well outside the range of values from calculations. The portion of observed IM microstructures (10%) is within the calculated range (7—22%). Far more single-phase (33%) and 2-phase (45%) microstructures are measured relative to CALPHAD microstructures (1—7% and 4—20%, respectively) (Fig. 16b). Far fewer 4-phase (3%) and 5-phase or 6-phase (1.5%) microstructures are observed compared to calculated fractions (27—32% and 38—48%, respectively). About 16% of the reported microstructures have 3 phases, while calculated percentages range from 15 to 28% depending on temperature and f_{AB}. Experiments show many more FCC phases (37%) relative to CAL-PHAD (9—14%) (Fig. 16c). The observed HCP fraction (1%) is close to the most credible calculations (6%), but calculations with lower credibility show a much higher percentage of HCP phases (26%). Hardly any silicide phases are observed, since Si is rarely used in experimental alloys. CALPHAD calculations identify as many as 453 different phases [56,125], only the most common are shown in Fig. 16c. As a result, the CALPHAD percentages of σ (D8$_b$, tP30, CrFe prototype) and L1$_2$ (cP4, Cu$_3$Au) phases are too low to report.

Different elements are used in experimental and CALPHAD-calculated datasets, and they are used with different frequencies (Fig. 14). By accounting for the elements used and their frequency of usage, the 'structure in − structure out' analysis gives a good explanation of the differences in fractions of BCC, FCC and HCP phases observed (Section 4.3.1.3 and Fig. 11).

From Gibbs phase rule, the maximum number of solid and liquid phases for an alloy with N elements is (N+1) and the minimum is 1 (Section 2.3.1). The number of solid phases is shown as a function of N for experimental data and CALPHAD calculations at T_m when $f_{AB} = 1$ [125] in Fig. 16d. CALPHAD and experimental results show the same general ranges of values up to $N = 5$, but the average experimental values are closer to the minimum and average CAL-PHAD results are closer to the maximum number allowed by Gibbs phase rule. The number of observed phases remains roughly constant for $N \geq 6$. About 98% of the experimental data in Fig. 16d are 3d transition metal alloys that appear to favor the single-phase FCC SS phase field (Section 4.4.1.2). The results in Fig. 16d are consistent with the discussion concluding that the most common microstructures are expected to have a number of phases that range from 1 to a number less than the maximum (Section 2.3.1).

Taken together, these comparisons all show related trends. Compared to calculated CALPHAD results, experimentally observed microstructures favor SS over (SS + IM), favor fewer phases over more phases, and favor FCC phases over BCC or HCP. Measured microstructures give a strong, non-random sampling of preferred elements (Section 3.1) and grouping of elements (Section 3.2), while the CALPHAD calculations represent a more uniform exploration of elements.

4.4.3. Analysis of the high entropy hypothesis
The hypothesis that configurational entropy may noticeably favor single-phase SS microstructures with simple (BCC, FCC or HCP) crystal structures is a major focus of the HEA field. Here we critically analyze information regarding this concept. Taken in total, the present data and analyses do not support an observable effect of configurational entropy on preferred formation of single-phase alloys, SS phases or simple crystal structures. Analyses supporting this conclusion are given in the following subsections. A recent review has come to the same conclusion by an independent evaluation of the published data [7].

4.4.3.1. Indirect experimental observations. The bulk of evidence commonly cited to support the high entropy effect comes from studies that are not designed to evaluate this hypothesis. These data do, indeed, show a marked preference for single-phase SS microstructures with a large fraction of FCC phases (Section 4.2.1), but the present assessment offers alternate interpretations of the data. Experimental data bias results toward fewer phases and simpler crystal structures (Sections 4.4.1.1, 4.4.1.5). Alloys selected for study are often chosen to maximize the probability of producing single-phase solid solutions rather than giving a random sampling of possible microstructures (Section 4.4.1.2). This has led to a remarkable focus on a small number of elements (Section 3.1 and Fig. 14) and one alloy family (Section 3.2.1). The contiguity of SS phase fields in hyper-dimensional composition space suggests that many studies may report different parts of the same phase field rather than different SS phase fields, and there may be no more than 13 different single-phase SS phase fields identified to date (Section 4.4.1.4). Finally, an inconsistent use of definitions leads to reporting some IM phases as SS (Section 4.4.1.6). All of these considerations have the same effect of increasing the number of single-phase SS microstructures, with an emphasis on FCC phases. A simple 'structure in − structure out' analysis shows that the observed preferences are predicted from the bias in crystal
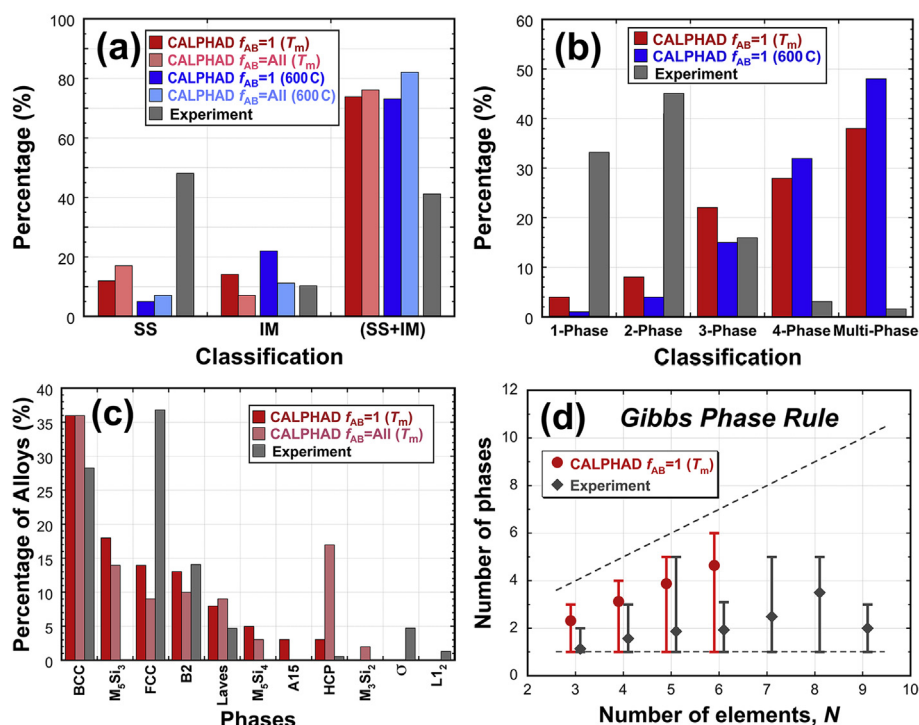
Fig. 16. Comparisons of experimentally measured and CALPHAD-predicted microstructures by: (a) microstructure type (SS, IM, SS + IM); (b) number of phases; (c) specific phases present; and (d) number of phases as a function of the number of alloy elements, N. Only the most common calculated phases are shown in (c), representing 62% of all alloy microstructures. Percentages from Refs. [56,125] are normalized by this value to allow comparison with observed percentages. Calculation temperatures (T_m or 600 °C) and credibility criteria ($f_{AB} = 1$ or $f_{AB} =$ All) are indicated. Dashed lines in (d) show the minimum and maximum values allowed by Gibbs phase rule.

structures of the input elements, without invoking configurational entropy (Section 4.3.1.3).

4.4.3.2. Direct experimental observations. Two studies allow a direct evaluation of the high entropy hypothesis. The first gives microstructures of equimolar alloys with 16 and 20 constituents [1]. These two alloys represent practical extremes in attempts to maximize configurational entropy, but both are multi-phase. Both microstructures include an FCC phase that contains Co, Cr, Fe, Mn and Ni, which is the basis for the well-known 'Cantor alloy.' The second test of the high entropy effect systematically substitutes, one element at a time, 4 of the 5 elements in the CoCrFeMnNi [169]. With only one exception, the substitute elements have equivalent atom radii and electronegativities and the same room temperature crystal structures as the atoms replaced. All alloys therefore have the same $S^{SS,ideal}$ and satisfy Hume-Rothery rules to equivalent extents (with one exception). All alloys are studied in the annealed condition. Only the baseline CoCrFeMnNi alloy is single phase, the remaining alloys contain multiple SS and/or IM phases. Thermodynamic modeling of the constituent binary systems shows that phase formation is controlled by minimization of the Gibbs energy, so that both enthalpy and entropy must be considered and that $S^{SS,ideal}$ alone is generally insufficient to control phase selection. Specifically, alloys are prone to IM formation when any of the element pairs in that alloy form compounds with large, negative H^{IM} values.

4.4.3.3. Thermodynamic phase calculations. Two different thermodynamic calculation approaches both predict that the probability of forming single-phase, SS microstructures decreases with an increasing number of constituents, N (Sections 4.3.2.2, 4.3.2.4). The rationale supporting this finding is that $S^{SS,ideal}$ increases slowly with N (as ln(N)), while the number of binary systems in an alloy

increases much faster (as $(N/2)(N-1)$) [125]. The probability of introducing a binary system with IM compounds that have formation enthalpies, H^{IM}, sufficiently negative to overcome $S^{SS,ideal}$ thus also increases rapidly with N. Stated differently, configurational entropy is not an independent variable, and there are important implications for the enthalpy of the alloy as composition is changed. In a pioneering HEA paper, Yeh predicted that entropy will not be able to overcome compounds with "very large heats of formation, such as strong ceramic compounds such as oxides, carbides nitrides and borides" [5]. Many metal-metal compounds have H^{IM} values that are much more negative than formation enthalpies of ceramics such as B_4C, SiC and WC, and are in the same range as formation enthalpies of ceramic compounds such as HfC, TaB_2, TaC, TaN, TiB_2, TiC and Ti_2N. The conclusion drawn from calculated results, that many metal-metal compounds have H^{IM} values sufficiently negative to overcome $S^{SS,ideal}$, therefore validates the early foresight provided by Yeh, and extends it to include many metal-metal compounds with sufficiently negative H^{IM} to overcome configurational entropy.

4.4.3.4. Thermodynamic concepts of complex, concentrated alloys. Several conventional thermodynamic simplifications are not likely to apply to SS and IM phases in CCAs. The configurational entropy of intermetallic compounds, S^{IM}, may make significant contributions to Gibbs energies when N exceeds the number of crystal sublattices (Section 2.2.2), and in many cases excess entropies significantly decrease the total entropy of an alloy relative to ideal estimates (Section 2.3.4). Mixing enthalpies for SS phases, H^{SS}, combine in rather complicated ways (Section 2.1.3) and there is no accepted approach for estimating formation enthalpies of N-component IM phases in CCAs (Section 2.2.3), making enthalpies in N-component alloys, $H^{SS,N}$ and $H^{IM,N}$, difficult to anticipate from binary data. These considerations support the conclusion that a

single thermodynamic term, such as $S^{SS,ideal}$, is not likely to consistently dominate the competition between IM and SS phases, and that all four primary terms, S^{SS}, S^{IM}, H^{SS} and H^{IM}, are needed to understand results broadly (Section 2.3.5). Rather than focusing on large, individual thermodynamic quantities such as $S^{SS,ideal}$ or H^{IM}, equilibrium phases are generally determined by relatively small differences between larger values in the competing phases, such as $\left(S^{SS,ideal} - S^{IM,ideal}\right)$ or $(H^{SS} - H^{IM})$.

4.4.4. Lattice distortion

The degree of lattice distortion is one of four proposed HEA 'core effects' (Section 1.3.3.2). It influences solid solution hardening models, it contributes to excess configurational entropy (Section 2.3.3), and it is implicated in the difficulty in distinguishing between ordered and disordered phases via standard X-ray diffraction techniques (Section 4.4.1.5). Crystal lattices in MPEA phases are almost certainly distorted, but there are no systematic studies to explore and quantify this feature directly. The commonly used δr parameter (Section 4.3.1.1, Section 4.3.1.2) quantifies the variability in atom sizes, but distortion in the structure can be less. For example, distortion is reduced in structures where the 1st shell surrounding a smaller atom is populated primarily by larger atoms, and where larger atoms are surrounded by smaller atoms. An approach to measure and model lattice distortions is needed. At present, there seems to be only one attempt to measure lattice distortions [102]. Lattice fringes are traced on inverse fast-Fourier transform (FFT) images taken from high-resolution transmission electron microscopy photographs. Future work is suggested to quantify the magnitude of lattice distortion and to evaluate its influence.

4.4.5. High-throughput calculations

Two different techniques for high-throughput calculations have been used (Section 4.3.2.2, Section 4.3.2.4). Taken together, high-throughput calculations are already making important contributions to the MPEA field. Using different computational methods, both approaches give the same result concerning the frequency of single-phase, SS microstructures as a function of the number of alloy constituents. These results combine to give the conclusion in this assessment that the high entropy hypothesis is not supported by available data. These high-throughput calculations have further contributed to the field by predicting nearly 200 new alloys that may be single-phase, SS alloys [56,168]. These lists form a basis for future studies.

4.5. Summary

4.5.1. Definition of terms

The following definitions are used (Section 4.1.5). Phases with no crystal structure are described as glassy or amorphous but not disordered. Phases with two or more crystal sub-lattices have chemical long-range order (LRO) and are called ordered or intermetallic (IM) or compound. These may exist at a fixed composition or may occur over a range of compositions. Solid solution (SS) phases have a single crystal lattice and are called disordered solid solutions. Chemical short-range order (SRO) may be present or absent in SS phases, but LRO is absent. Simple phases have BCC, FCC or HCP structures or their ordered derivatives, and complex phases have any other crystal structure. Although complex phases are often stereotyped in the HEA literature as being brittle with little usefulness, no properties or utility are implied by any of the labels used here. Microstructures that consist only of solid solution phases are abbreviated as SS, those with only intermetallic phases are labeled as IM, and microstructures containing both solid solution

and intermetallic phases are (SS + IM). The terms SS and IM can therefore refer to a phase, a microstructure or an alloy, depending on the context. CCAs can have any number of SS or IM phases, or a mixture of both.

4.5.2. Experimental results

This review evaluates data from 408 distinct experimental alloys that are described in 648 microstructural reports (Section 4.2.1). SS microstructures are the most common (48% of reported microstructures), but (SS + IM) microstructures are nearly as common (41%) and 10% have only IM phases. SS alloys are most often single-phase (53% of SS alloys), with fewer 2-phase and 3-phase SS alloys. There are 213 single-phase alloy reports (33% of reported microstructures), 294 2-phase alloy reports (45%), 105 3-phase alloy reports (16%), 21 4-phase alloys and 10 alloys with 5 or 6 phases. The most common phases by far are FCC (A1, Cu prototype, in 410 alloys) and BCC (A2, W prototype, in 306 alloys). The number of HCP SS phases (A3, Mg prototype) is small in this dataset. All but one single-phase FCC SS alloy, about 55% of single-phase BCC alloys and all (BCC + FCC) alloys belong to the 3d transition metal family of MPEAs. Nearly all (BCC + FCC) alloys contain >10 at.%Al. Commonly observed IM phases include B2 (cP2, ClCs prototype), σ (D8$_b$, tP30, CrFe prototype) and Laves (C14, hP12, MgZn$_2$ prototype or C15, cF24, Cu$_2$Mg prototype). B2 and BCC phases often appear together, as do FCC and L1$_2$ phases. All B2 and all but one of the L1$_2$ phases are in alloys that contain Al. The most common IM phases (B2, σ, Laves, L1$_2$) almost always contain Al, Cr or Si. Very few detailed studies of precipitate formation, kinetics or morphologies are available for MPEAs (Section 4.2.2). This is an essential foundation for precipitation hardening of structural alloys and is recommended for future work.

The HEA community has identified and explored an expansive single-phase, SS phase field that is contiguous in hyper-dimensional composition space (Section 4.2.1). Based on the 3d transition metal MPEA family, this phase field connects and expands solid solution, austenitic stainless steels and nickel alloys. This remarkable phase field contains at least seven different elements and it extends much farther than previously realized.

While single-phase SS alloys with FCC, BCC or HCP structures make up a significant fraction of reported phases and microstructures, there may be no more than 13 different SS phase fields in the present dataset (Section 4.4.1.4). This includes: three FCC, two BCC and an HCP phase in the 3d transition metal family; an FCC and an HCP SS phase field in light metal CCAs; three BCC phase fields in refractory metal CCAs; an HCP phase in 4f transition metal CCAs; and an HCP phase in the precious metal CCA family.

4.5.3. Calculated results

Empirical correlations, thermodynamic models and atomistic methods are used to predict the types of phases and to analyze trends in CCAs (Section 4.3.1). Empirical correlations use composition-weighted terms for differences in atom radii (δr), electronegativity ($\delta\chi$) and valence electron concentration ($\delta(VEC)$), valence electron concentration (VEC), enthalpy of mixing for SS phases (H^{SS}) and an Ω term that combines the SS entropy of mixing (S^{SS}), H^{SS} and melting temperature (T_m) (Section 4.3.2.2). Empirical correlations based on $\delta\chi$ or H^{SS} are unable to separate SS from IM or (SS + IM) microstructures, and correlations using δr and $\delta(VEC)$ only marginally separate these phases. The most successful correlations (H^{SS} vs δr or H^{SS} vs Ω) separate SS and amorphous (AM) phases, but IM phases are not well separated and overlap with these two fields. Using as-cast data and H^{SS} instead of IM formation enthalpies (H^{IM}) to compete with S^{SS} contributes to the overlap in these comparisons. Addressing these concerns improves separation of IM from SS and AM phases in an approach that assumes

$H^{IM}/H^{SS} = \kappa_1$ and $S^{IM}/S^{SS} = \kappa_2$, where S^{IM} is the configurational entropy of IM phases (Section 4.3.2.3) A simple 'structure in − structure out' (SISO) analysis accurately predicts the fraction of SS alloys from the weighted fraction of ideal or regular solution binary diagrams in an alloy dataset (Section 4.3.1.3, Section 4.5.6). Using the weighted fractions of constituent element crystal structures, the SISO analysis successfully predicts the fractions of BCC, FCC and HCP phases in three separate datasets, demonstrating a useful capability of a very simple concept. High-throughput atomistic calculations of H^{IM} are used with configurational entropy of ideal SS phases ($S^{SS,ideal}$) to successfully predict single-phase SS alloys and alloys with IM phases (Section 4.3.2.2).

The CALculated PHAse Diagram (CALPHAD) approach is making important contributions to CCAs (Section 4.3.2.4). The credibility of CALPHAD calculations is estimated by the fraction of assessed binary phase diagrams (f_{AB}), defined as the total number of binary phase diagrams common to the alloy being modeled and the thermodynamic database that models it, normalized by the total number of binary systems in the alloy modeled. Calculations with $f_{AB} = 1$ have the highest credibility, and $f_{AB} \geq 0.6$ can give a good predictions of the number and types of phases. High-throughput CALPHAD calculations of equimolar alloys with 3−6 elements show that the most common phases are BCC, M_5Si_3 silicides, FCC, B2 and Laves (C15) when $f_{AB} = 1$ (for 4983 unique alloys), and are BCC, HCP, M_5Si_3, B2 and FCC when any f_{AB} value is used (111,654 unique alloys). Alloys that satisfy all 4 Hume-Rothery rules are always calculated to be SS, but not all calculated SS alloys satisfy all 4 rules. Atom size is the most potent Hume-Rothery condition, since every calculated SS alloy has $\delta r \leq 15\%$, but calculated SS alloys can have $\delta\chi$ as large as 30% and $\delta(VEC)$ as large as 55%. Agreement between calculated and observed numbers and types of phases is good when $f_{AB} = 1$ and is nominal for the full dataset. Calculated phase volume fractions, compositions and transformation temperatures are less well-established.

High throughput calculations have identified nearly 200 unexplored CCA systems predicted to be single-phase SS at T_m for potential use as high temperature structural metals (Section 4.4.5). These new systems give many opportunities for future studies.

4.5.4. Comparison of experimental and calculated results

Significant distinctions exist between measured and calculated microstructures (Section 4.4.2). Measurements show significantly higher fractions of SS microstructures and lower fractions of (SS + IM) microstructures relative to calculations. Experimentally reported microstructures are far more likely to be single-phase or 2-phase and far less likely to have 4 or more phases compared to calculations. Finally, measured microstructures are more likely to contain FCC phases relative to CALPHAD calculations. These differences are concluded to result from the six issues that bias experimental results (Section 4.4.1, Section 4.5.5) and these trends are predicted by the 'structure in − structure out' (SISO) analysis (Section 4.3.1.3, Section 4.5.6). Single-phase alloys are usually SS and are less frequently IM. This is shown by experiments and calculations and is supported by a simple phase diagram analysis that does not require consideration of configurational entropy. Both calculations and experiments show that the number of phases is below the maximum value allowed by Gibbs phase rule. Calculations give results closer to the maximum value, while experimental results are closer to the minimum value. These results do not support claims regarding an influence of configurational entropy, and are correctly reflected by a simple phase diagram analysis.

4.5.5. Features biasing results

Six concerns bias experimental results toward fewer phases and SS rather than IM phases. About 70% of reported MPEA microstructures are as-cast and do not represent the equilibrium state (Section 4.4.1.1). Analysis of 46 alloys in both as-cast and annealed conditions shows that annealing decreases the number of SS and single-phase microstructures and increases the number of alloys with (SS + IM) microstructures and with 3 or more phases, validating this concern. An experimental bias comes from the motivation to study single-phase, SS microstructures with simple phases (Section 4.4.1.2). Alloy selection is guided by rules to improve the chances of achieving this goal or by studying small modifications to known single-phase, SS alloys. This has led to a remarkable emphasis on a single alloy family − 3d transition metal MPEAs (Section 3.2.1). The elements in this family generally have unusually low mixing enthalpies, H^{SS}, and are far more likely to form ideal or regular solid solutions. The resulting solid solutions may be considered to result as much from low mixing enthalpy as from high configurational entropy (Section 4.4.1.3). As a fourth concern, SS phases that appear separate in lower-order systems may be parts of the same phase field that is contiguous in multi-dimensional composition space, leading to an over-reporting of the number of distinct SS phase fields (Section 4.4.1.4). CCAs give new challenges in experimentally distinguishing IM phases from SS phases with similar lattice constants (Section 4.4.1.5). Finally, IM phases are sometimes reported as SS due to an inconsistent use of terms (Section 4.4.1.1). Each of these six concerns increase the number of single-phase, SS microstructures reported and the experimental bias also favors FCC phases, limiting the degree to which the existing data represents a random sampling of phases and microstructures in the full CCA field.

4.5.6. The 'structure in − structure out' (SISO) analysis

A 'structure in − structure out' (SISO) analysis is developed here that predicts the fraction of BCC, FCC and HCP phases in a dataset from a weighted fraction of the elements with the same crystal structures used to produce alloys in that dataset (Section 4.3.1.3). This approach extends the Hume-Rothery concept of the connection between the crystal structure of an extended SS and the crystal structures of the constituent elements. The SISO analysis shows that experimental alloys are more likely to form FCC solid solutions because they use FCC elements far more frequently (Table 3, Fig. 14). Similarly, refractory metal CCAs are dominated by BCC microstructures, since the refractory metal elements used to make these alloys are essentially all BCC elements. CALPHAD calculations use a more balanced fraction of BCC, FCC and HCP elements, and SISO predictions match these fractions. The SISO analysis also predicts the fraction of SS microstructures produced. Thus, as a major accomplishment, the 'structure in − structure out' analysis gives a basis for understanding both observed and calculated microstructural trends by comparing the crystal structures of SS phases formed in a dataset with the crystal structures of the elements used to produce those alloys.

4.5.7. Assessing the high entropy hypothesis

The present data and analyses do not support an observable effect of configurational entropy on preferred formation of single-phase alloys, SS phases or simple crystal structures (Section 4.4.3). This conclusion is supported by two experimental studies designed to test this hypothesis (Section 4.4.3.2) and by two different calculation approaches that show that the probability of forming single-phase or SS microstructures decreases as the number of constituents, N, increases (Section 4.4.3.3). This trend is opposite the result expected from the high entropy hypothesis, and is supported by noting that $S^{SS,ideal}$ increases slowly with N (as $\ln(N)$), while the number of binary systems in an alloy increases much faster (as $(N/2)(N-1)$). The probability of introducing IM

phases with H^{IM} sufficiently negative to overcome $S^{SS,ideal}$ thus also increases rapidly with N. The expectation that $S^{SS,ideal}$ can be overcome by compounds with very negative H^{IM} values was predicted in a pioneering HEA paper, and the present data support this early insight. The current data show that $S^{SS,ideal}$ may be overcome not only by ceramic compounds, but also by IM phases with sufficiently negative H^{IM}. Basic thermodynamic concepts show that minimizing the Gibbs energy difference between competing phases is needed to give a robust predictive capability for the type of phases formed in a given alloy. This minimization includes consideration of four thermodynamic terms: H^{SS}, S^{SS}, H^{IM} and S^{IM}. Each of these four terms has the potential to be significant, and equilibrium phases are ultimately determined by relatively small differences between these four larger values (Section 4.4.3.4).

A preference for single-phase microstructures to be SS rather than IM is shown by both experiment (Section 4.2.1) and calculations (Section 4.3.2.4). This is rationalized by observing that many IM single-phase fields occur as line compounds at a discrete composition while most SS single-phase fields occur over a range of compositions (Section 2.3.1).

4.5.8. The lattice distortion hypothesis

Lattice distortion is proposed to be more severe in MPEAs than in conventional materials, and this hypothesis has been used to rationalize several observations. An attempt to model this quantity via the distribution in atom sizes, δr (Eq. (4.1)) gives a maximum value, but actual lattice distortions can be less (Section 4.4.4). A single experimental observation via high-resolution transmission electron microscopy illustrates this feature but does not quantify it. Lattice distortion is likely to be important, but there are insufficient data to evaluate the hypothesis and future work is recommended to quantify its magnitude and to isolate its effect.

5. Properties

The field of multi-principal element alloys (MPEAs) offers new challenges in establishing relationships between composition, microstructure and properties. The vast range of compositions significantly increases the number of alloys to characterize. Even in the same alloy family, adjusting just one element can have a major effect on microstructure and properties since elements are usually more concentrated in MPEAs than in conventional alloys. The properties of MPEA phases may differ from the same phase in compositionally simpler alloys, changing previously-established relationships between microstructure and properties. The microstructure (including defects) is influenced by the production method and the post-process thermo-mechanical processing used. In much of the early work in the field, properties have been measured on materials where defects such as casting segregation, dendritic microstructures and residual stresses may influence or even dominate results. As a result of these issues, it is difficult to conduct a detailed assessment of properties. Nevertheless, here we give a report of general results and major trends. *We emphasize studies that best control the microstructure or defects and strive for chemical homogeneity and microstructural uniformity.*

Microstructures and properties depend sensitively on primary and secondary processing. Conventional processing approaches are used for MPEAs. It is assumed that the reader is familiar with primary and secondary processes and their influence on defects, microstructure and properties. This information is available elsewhere [11,16,17] and is not given here.

5.1. Functional properties

Most MPEAs for which functional properties are reported are based on the 3d transition metal alloy family. Functional properties of MPEAs are documented in recent reviews [10,11,16,17,82]. In this section, we summarize findings for thermal, electrical and magnetic properties and give a brief description of the breadth of studies for other functional properties. Readers are referred to the earlier reviews for more details.

5.1.1. Thermal properties

Thermal conductivity was studied in $Al_xCoCrFeNi$ ($0 \leq x \leq 2$) [131] and $Al_xCrFe_{1.5}MnNi_{0.5}Mo_y$ ($x = 0.3, 0.5; y = 0, 0.1$) systems [199]. Alloys of the first system were annealed at 1273 K and water quenched, while alloys of the second system were studied in the as-cast condition. Thermal conductivity and thermal diffusivity values for these alloys increase with increasing temperature from 293 to 573 K and are in the range of $10–27$ $Wm^{-1}K^{-1}$ and $2.8–3.5$ $mm^{-2}s^{-1}$, respectively. These values are lower than for pure metallic elements, but are similar to highly alloyed steels and nickel superalloys. The temperature influence is opposite that typically observed for pure metals, but is similar to that of alloys such as Inconel and stainless steels [10]. Single-phase FCC alloys (low Al content) have almost half the thermal conductivity of single-phase BCC alloys (high Al content). Within single-phase regions, thermal conductivity decreases with increasing Al content [131]. These behaviors are analyzed in terms of lattice distortions and an increased phonon mean free path due to lattice thermal expansion at higher temperatures [199].

Linear thermal expansion of $Al_xCoCrFeNi$ ($0 \leq x \leq 2$) is reported from 293 to 423 K [131]. The thermal expansion coefficient, a_T, decreases from 11.25×10^{-6} K^{-1} to 8.84×10^{-6} K^{-1} with increasing Al. Non-linear thermal expansion was observed in homogenized and annealed single-phase FCC CoCrFeMnNi [200]. a_T for this alloy increases with increasing temperature from 200 to 1273 K following the relationship: $a_T = 23.7 \times 10^{-6}[1-\exp(-T/299)]$ K^{-1}, similar to austenitic steels [201]. This relationship gives $a_T \approx 16.35 \times 10^{-6}$ K^{-1} at $T = 293–423$ K. Comparing this value with that reported for CoCrFeNi [131] concludes that adding Mn increases a_T of the MPEA.

5.1.2. Electrical properties

Electrical resistivity typically ranges from 100 to 200 $\mu\Omega–cm$ in $Al_xCoCrFeNi$ alloys ($0 \leq x \leq 2$) [131,202]. For each of these alloys, electrical resistivity increases linearly with temperature. Increasing the Al content transforms the microstructures from FCC to BCC + FCC to BCC, giving a non-monotonic dependence of electrical resistivity. Using experimental data [131], we show that the electrical resistivities of the BCC and FCC phases fit linear relations

$$\rho_{BCC} = 107 + 1.43(c_{A1}) \quad \rho_{FCC} = 107 + 5.50(c_{A1}) \quad (5.1)$$

where c_{Al} is the Al concentration in the respective phase in at.% (Fig. 17). The electrical resistivity of the FCC phase is higher than that of the BCC phase at the same composition, and the resistivity in the two-phase field follows a linear average of the volume fraction of the BCC and FCC phases. A non-monotonic dependence of electrical resistivity on Al content in Ref. [202] is also likely due to the transition from the BCC to FCC microstructures. Cold rolled alloys have higher resistivities than homogenized material [202].

Using $Al_xCoCrFeNi$ alloys as a baseline, other composition effects can be inferred but are difficult to determine precisely since the phases also change. Titanium additions give $Al_xCoCrFeNiTi$ alloys ($0 \leq x \leq 2$) that consist of BCC, B2 (cP2, ClCs prototype) and other intermetallic (IM) phases and show a non-monotonic dependence of resistivity on Al content [203]. The as-cast resistivity ranges from 60 to 114 $\mu\Omega–cm$ and increases to $132–396$ $\mu\Omega–cm$ after annealing due to increasing volume fraction of IM precipitates. Removing Cr
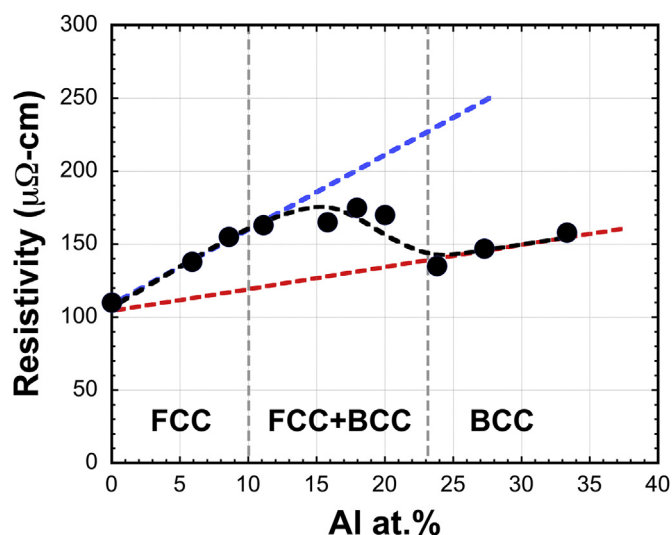
Fig. 17. Resistivity of Al$_x$CoCrFeNi alloys versus aluminum content at 400 K. Solid circles are experimental data [131]; red and blue dotted lines are linear fits to resistivities of BCC and FCC phases, respectively; and the black dashed line is the resistivity estimated by a rule of mixtures of BCC and FCC phases. The phase composition ranges are also shown and a linear decrease in the volume fraction of the FCC phase with increasing aluminum content is assumed in the BCC + FCC phase range. (For interpretation of the references to colour in this figure legend, the reader is referred to the web version of this article.)

from the baseline gives Al$_x$CoFeNi and CoFeNiSi$_x$ alloys ($0 \leq x \leq 1$) [204]. Increasing Al transforms CoFeNi from FCC to BCC + B2, while increasing Si forms silicide phases. Room temperature resistivities range from 17 to 83 μΩ–cm for this family of alloys. Removing Cr and adding both Al and Si in (AlSi)$_x$CoFeNi ($0 \leq x \leq 0.8$) gives resistivities ≤80 μΩ–cm except at the highest Al and Si contents, where the resistivity is 265 μΩ–cm [205]. X-ray diffraction identifies only a BCC phase in this latter alloy, but the microstructure clearly shows two phases. These alloys are studied in the as-cast condition, and elemental segregation is evident in most of the microstructures.

An MPEA of refractory elements that are all low temperature superconductors was studied [206]. In a zero magnetic field, the electrical resistivity of single-phase BCC Hf$_8$Nb$_{33}$Ta$_{34}$Ti$_{11}$Zr$_{14}$ decreases from 46 μΩ–cm to ~36 μΩ–cm with a decrease in temperature from 300 K to ~8 K, and then sharply drops to zero at $T_c \approx 7.3$ K. The lattice parameter and Debye temperature of the alloy obey a rule of mixtures of the pure elements, so that the elements are concluded to distribute randomly in the lattice. Electronic-dependent properties such as the normal-state electronic specific heat coefficient and the superconducting transition temperature do not obey this rule of mixtures. The resistivities of other refractory alloys, CrTiV and CrTiVYZr, range from 80 to 100 μΩ–cm [207]. These alloys were produced by magnetron sputtering.

Homogenized Al$_x$CoCrFeNi ($0 \leq x \leq 2$) alloys show a Hall effect. They have hole-type carriers with densities of 10^{22}-10^{23} cm^{-3}, similar to conventional alloys [208], but they have lower carrier mobility, which may be due to a higher density of lattice defects [202]. These alloys become ferromagnetic at 5 K, and so they also show an anomalous Hall effect. A Kondo-like behavior is seen at low temperatures in some alloys. The origins of these behaviors are not understood.

5.1.3. Magnetic properties

Nearly all complex, concentrated alloys (CCAs) studied for magnetic properties contain Co, Fe and Ni. CoFeNi is a single-phase SS alloy with an FCC crystal structure and is ferromagnetic with a saturation magnetization (M_s) of 151 emu/g [204]. For reference, M_s for pure Fe is 218 emu/g and for pure Ni is 55 emu/g [209]. The FCC structure transforms to FCC + BCC/B2 with Al additions in Al$_x$CoFeNi or to FCC + silicides in CoFeNiSi$_x$ [204]. All alloys are ferromagnetic, and M_s decreases to 102 emu/g as Al increases from $x = 0$ to 1, or to 80.5 emu/g as Si increases from $x = 0$ to 0.75. The magnetostriction effect is very small, which is essential to ensure that materials are not stressed in an external magnetic field. Adding Al and Si together in (AlSi)$_x$CoFeNi ($0 \leq x \leq 0.8$), the properties at $x = 0.2$ give M_s, coercivity, electrical resistivity, yield strength and strain without fracture that make the alloy an attractive soft magnetic material [205]. Adding Al and Cr to CoFeNi in homogenized Al$_x$CoCrFeNi ($0 \leq x \leq 2$) alloys gives ferromagnetic behavior at 5 K and 50 K but paramagnetic properties at 300 K due to changing alloy phases [202].

Combining AlCrCu and CoFeNi gives AlCoCrCuFeNi that is ferromagnetic in the as-cast state. It contains both paramagnetic (Cu-based FCC and Al-Ni based B2) and ferromagnetic (Co-Cr-Fe-based FCC and Cr-Fe-based BCC) phases [210]. Aging increases M_s and coercivity by decomposing Co-Cr-Fe-rich regions into ferromagnetic Co-Fe-rich and antiferromagnetic Cr-rich domains [211]. Adding Al$_x$CrTi to CoFeNi produces as-cast Al$_x$CoCrFeNiTi alloys ($0 \leq x \leq 2$) that are ferromagnetic at room temperature and consist of BCC (Cr + Fe-rich), B2 (Al + Ni-rich) and other intermetallic phases [203]. M_s is low, <16 emu/g, for both as-cast and annealed Al$_x$CoCrFeNiTi alloys. CoFeNi has also been combined with AlCrCuW [212], AlCrCuWZr [212] and Bi-Mn [213]. Other studied alloys include CuFeMnNiTiSn$_x$ ($0 \leq x \leq 1$) [214], AlBFeNiSi [215] and AlBFeNiSiNb [215]. The magnetic properties in these alloys are influenced by composition through the fraction of magnetic elements present [212]. Processing and thermal history also influence magnetic properties through the phases formed. As-processed material typically has different microstructures and magnetic properties compared to annealed materials.

5.1.4. Other functional properties

Limited studies characterize MPEAs for other functional properties. The MPEA concept is used to develop thin film nitride coatings as diffusion barriers [216–219]. Other functionalities include hydrogen storage [220–222], catalysts [223], thermoelectric properties [224], response to irradiation [225,226] and shape memory response [227]. Cu$_x$FeCoNiMn has been used as a substrate for graphene growth [228].

5.2. Diffusion

Sluggish diffusion is one of four proposed high entropy alloy (HEA) 'core effects' (Section 1.3.3). Diffusion is difficult to measure, so early considerations of this hypothesis rely on secondary observations. Appearance of nanocrystals in as-cast Al$_x$CoCrCuFeNi [149] and retention of nanocrystals in AlCrMoSiTi after annealing [229] were interpreted to signify slow diffusion. Furnace cooling of Al$_{0.5}$CoCrCuFeNi avoids formation of low-temperature phases [166], and AlMoNbSiTaTiVZr is a better diffusion barrier than TaN/TiN or Ru/TaN [219] – both of these results have been used to support the sluggish diffusion hypothesis. However, alternate analyses give equally satisfying explanations for all of these observations. HEAs in these studies have 1 to 5 refractory metals, each of which have $T_m > 2100$ K, and the thermal exposures in the studies are at rather low temperatures and short times (ranging from <1 min to 5 h), dramatically limiting mass transport. Using conventional alloys as a baseline for comparison, nanometer-sized precipitates persist in superalloys for tens or hundreds of hours at

temperatures that approach 85% of the absolute melting temperature (T_m). While the indirect observations cited above are consistent with slow kinetics, they do not show that diffusion is any slower in HEAs compared to conventional alloys.

Compositional complexity makes diffusion measurements difficult. These challenges are met in the only study that gives experimental diffusion data in MPEAs [32]. Our analysis of the data shows that diffusion coefficients in CoCrFeMn$_{0.5}$Ni are generally higher than in conventional materials when compared at the same temperature (Fig. 18a). For example, diffusion coefficients of Ni (D_{Ni}) in CoCrFeMn$_{0.5}$Ni, Fe-15Cr-20Ni stainless steel (this composition indicates weight percent, the atomic composition is Cr$_{16}$Fe$_{65}$Ni$_{19}$) and pure Fe at 1173 K (the lowest measurement temperature in Ref. [32]) are 14.3×10^{-18} m^2/s, 6.56×10^{-18} m^2/s and 3.12×10^{-18} m^2/s, respectively, and at 1323 K (the highest measurement temperature) are 5.74×10^{-16} m^2/s, 2.15×10^{-16} m^2/s and 1.2×10^{-16} m^2/s, respectively. Extrapolation to 873 K, where diffusion is often assumed to freeze, gives $D_{Ni} = 2.0 \times 10^{-22}$ m^2/s, 1.7×10^{-22} m^2/s, and 0.49×10^{-22} m^2/s, respectively, for these materials. This shows that D_{Ni} is higher in CoCrFeMn$_{0.5}$Ni than in austenitic steels and pure metals when compared at the same temperature, in the range of 873 K−1323 K.

Diffusion coefficients appear lower in CoCrFeMn$_{0.5}$Ni than in selected FCC elements and conventional alloys after normalizing activation energies by the melting temperature (or solidus temperature for alloys), T_m ([32] and Fig. 18b). This is based on the empirical observation that diffusion coefficients at T_m, D_{T_m}, are roughly equal for metals and alloys with the same crystal structure and the same bonding type, and on the assumption that the pre-exponential term, D_0, is constant at T_m [230]. D_{T_m} values in Table 1 of [230] range from 4.5×10^{-14} to 6.6×10^{-12} m^2 s^{-1} for a wide range of FCC elements and from 6.4×10^{-14} to 4.9×10^{-12} m^2 s^{-1} for a wide range of binary alloys. All of the D_{T_m} data for CoCrFeMn$_{0.5}$Ni fall in this range (see Table 2 in Ref. [32] and Fig. 18b). This shows that diffusion in CoCrFeMn$_{0.5}$Ni is not significantly different from a wide range of other FCC metals and alloys when the data are normalized at T_m.

The accurate measurement of diffusion coefficients is challenging, and viewed broadly, differences within one order of magnitude are not considered significant. We conclude that the measured diffusion coefficients in CoCrFeMn$_{0.5}$Ni are not essentially different from diffusion in elements and conventional alloys. We base this conclusion on comparison with a wide range of measured diffusion coefficients for FCC metals and alloys at T_m. This is further supported by the fact that the data measured in Ref. [32]

all fall essentially within a single order of magnitude, both before and after normalization by T_m. Finally, data supporting the sluggish diffusion hypothesis are available for only a single MPEA, and a wider dataset is needed to better explore the hypothesis that diffusion may be unusually slow in MPEAs as a class of materials. The present analysis and conclusion supports an earlier independent analysis that draws the same conclusion [7].

As a final note, additional work may be needed to test the assumption that D_0 is constant at T_m for CCAs. This assumption requires that the lattice constant, the vibrational frequency of atoms adjacent to a vacancy, and the entropy associated with the diffusion process are all constant for all materials with the same crystal structure and bond type [230]. The significant variation in atom sizes and masses and the high degree of chemical mixing in CCAs may challenge these assumptions.

5.3. Mechanical properties

Mechanical properties depend profoundly on composition and microstructure. Composition sets elastic properties and atomic interactions that dictate dislocation behaviors. Composition also defines the phases present and their volume fractions, which influence properties through the intrinsic properties of the phases. Even at a fixed composition and phase content, properties can vary dramatically by changing the size, shape and distribution of phases. Finally, defects are critical microstructural components that play a major role in mechanical properties. Atomic-level defects include vacancies, dislocations and grain boundaries, and microscopic or macroscopic defects include pores, chemical segregation, cracks and residual stresses. All of these must be considered for a clear understanding of mechanical properties.

Attention to the microstructure is needed prior to mechanical characterization. Mechanical properties of as-cast material can be degraded by defects that may include casting segregation, pores, a non-uniform grain size or structure, the presence of non-equilibrium phases, and residual stresses. In general, a better balance of strength and ductility is obtained in material after thermal treatment and/or thermo-mechanical processing. As a sign of growing maturity of the MPEA field, an increasing number of studies apply thermal treatment and/or deformation processing after casting to control the microstructure and to remove defects. These studies are emphasized here. Hardness and compression tests are done as an initial screening of mechanical properties, followed by more detailed characterization via tensile testing, fracture toughness, creep and fatigue properties. Results are described separately below for the two most mature families − 3d
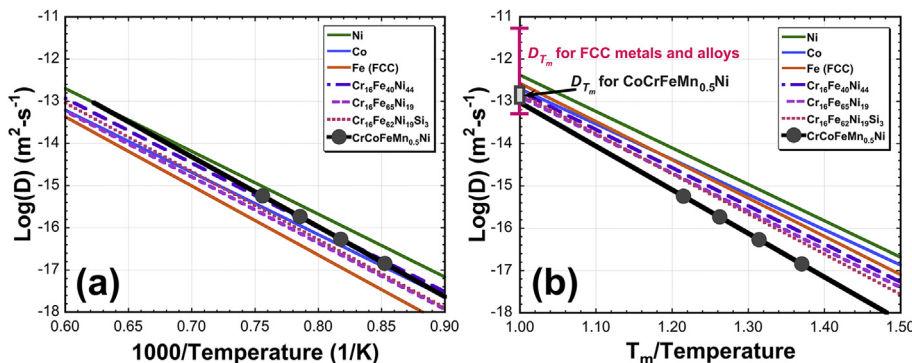
Fig. 18. Diffusion coefficients of Ni (D_{Ni}) in FCC elements, stainless steel alloys (compositions in the legend are shown in at.%) and CoCrFeMn$_{0.5}$Ni as a function of (a) inverse absolute temperature, and (b) inverse absolute temperature normalized by the melting or solidus temperature of the host alloy, T_m. In (b), all D_{T_m} values measured in CoCrFeMn$_{0.5}$Ni (for Co, Cr, Fe, Mn and Ni) are shown to fall within the range of D_{T_m} values for a broad range of FCC metals and alloys (taken from Table 1 of [230]). Measurements are taken from Ref. [32].

transition metal and refractory metal MPEAs − to better establish relationships between compositions, microstructures and properties of these distinct alloy families.

5.3.1. 3d transition metal alloys

5.3.1.1. Hardness and compression. Numerous studies report hardness of 3d transition metal MPEAs [231−241]. The hardness of $Al_x CoCrCuFeNi$ increases with Al content due to the transition from a single-phase FCC structure, to BCC + FCC and then to single-phase BCC [6]. Similar behavior is shown for $Al_x CoCrFeNi$ alloys in as-cast and homogenized conditions [132]. Single-phase FCC alloys have Vickers hardness in the range of 100−200 Hv, single-phase BCC alloys have hardness >600 Hv and BCC + FCC alloys have hardness values that increase from the lower to the higher levels with increasing BCC content. Transmission electron microscopy (TEM) shows that $Al_x CoCrCuFeNi$ alloys initially found by X-ray diffraction as single-phase BCC structures contain fine mixtures of BCC and B2 phases [184,197]. These phases have similar lattice parameters and are often coherent. The high density of interfaces between BCC and B2 phases may contribute to the high hardness of Al-containing alloys. Increasing hardness with increasing volume fraction of BCC + B2 phases is also reported for other alloys [135,198]. Increasing the volume fraction of other intermetallic phases, such as σ (D8$_b$, tP30, CrFe prototype) or Laves (C14, hP12, $MgZn_2$ prototype or C15, cF24, prototype Cu_2Mg), in FCC or BCC + FCC microstructures considerably increases hardness [190,242,243].

Compression testing is reported for many alloys [162,182,189,190,203,231−241,244−259]. Nearly all of the alloys include CoCrFeNi; the elements Al, Cu and Ti are commonly used; and Mo, Nd, Si, V, Y, Zn and Zr are added infrequently. Compression samples are generally produced by casting or powder metallurgy, e.g. by mechanical alloying followed by spark plasma sintering, hot isostatic pressing or powder sintering. Cast microstructures generally show inter-dendritic segregation, even after annealing, and mechanically alloyed materials usually have 1−2% porosity. BCC and FCC phases dominate most of the microstructures, but other phases are observed, including σ and Laves. The B2 phase is rarely reported in compression studies, even though most of the alloys have B2-forming elements. Given the results in Refs. [184,197], it is likely that many alloys studied in compression may also have the B2 phase present.

Compressive yield strengths can be very high in alloys with significant volume fractions of BCC and/or B2 phases, and range from 1300 to 2400 MPa with values as high as 3300 MPa. Compressive ductilities are often below 10%, which may be considered a practical minimum value for structural materials. As a general result, ductility decreases as strength increases, but this is not always the case. For example, the maximum compressive strength and ductility in $Al_x CrFeNiTi_{0.25}$ are found at $x = 0.5$, and both strength and ductility decrease as x increases or decreases [244]. The level of ductility is sometimes associated with the volume fraction of intermetallic (IM) phases − compression ductility drops rapidly after the volume fraction of IM phases reaches a critical value [162,190]. Lower strength and high ductility are also sometimes associated with increased volume fraction of the FCC phase [189]. Annealing to eliminate inter-dendritic segregation increases ductility but decreases strength [182]. Nano-twinning is often observed as a deformation mechanism.

5.3.1.2. Tensile properties. A growing body of CCA tensile data is becoming available (Table 6) [27,129,138,147,162,259−270]. All of the studies described here (except for 2 Al-containing alloys) give tensile properties after thermo-mechanical processing and annealing to produce a uniform, equiaxed, recrystallized microstructure, improving the quality of results. Direct comparison of

data is difficult, due to differences in the type and concentration of principal elements, the type and extent of thermo-mechanical processing, and the temperature and duration of post-process thermal treatment. The broad trends observed in this data are described below.

The most commonly studied alloy is CoCrFeMnNi [27,129,138,162,260,261,269,270]. Agreement between studies is good after accounting for differences in grain size and strain rates (Table 6). Microstructures are single-phase FCC solid solutions, with the exception of minority oxide [261], Cr-rich or Mn-rich second-phase particles [27]. Coarse annealing twins are often observed. The yield (σ_y) and ultimate (σ_{uts}) strengths both decrease continuously with increasing temperature over the full range of temperatures (Table 6, Fig. 19a,b). The drop in strength is steepest from 77 to 300 K, is relatively gentle from 300 to 800 K, then is more noticeable to the maximum test temperature. Tensile ductility, ε [7], generally increases with decreasing temperature below 900 K (Fig. 19c). This not unusual for solid solution (SS) austenitic alloys, as shown by data for the commercial alloy, INCONEL® 600 (nominal composition of the major alloy elements in at% is $Cr_{18}Fe_8Ni_{74}$) in Fig. 19c. Increasing strength and ductility below RT is also reported for solid solution aluminum alloys [271] and titanium alloys such as Ti-5Al-2.5Sn ELI (extra low interstitial, nominal composition in weight percent) [272].

Deformation in CoCrFeMnNi in the early stages ($\varepsilon \leq 2.4\%$) occurs by planar dislocation glide on 1/2<110>{111} systems that are typical for FCC metals [260]. Stacking faults are also frequently seen, suggesting that 1/2<110> dislocations dissociate into 1/6<112> partial dislocations. After plastic strains >20% at $T \geq 300$ K, dislocations lose their planar character and organize into cell structures that are typical for FCC metals. Extensive deformation via nano-twinning is seen at 77 K in tension when $\varepsilon \geq 20\%$ [27,260] and after plane-strain rolling at 77 K and 293 K [269]. Prolific nano-twinning is proposed to increase the alloy work-hardening and to postpone necking, contributing to increases in σ_{uts} and ε [129,260]. Nano-twinning is not observed at low strains below RT, and so cannot explain the increase in σ_y with decreasing T, which is instead proposed to result from an intrinsic solute effect in FCC metals [260].

Replotting yield data as $\ln(\sigma_y)$ v $1/T$ (Fig. 19d) emphasizes the thermally activated nature of yield in MPEAs. Athermal deformation in 3d transition metal CCAs extends from cryogenic temperatures to about 800 K, and thermally activated flow occurs at higher temperatures. While the increase in σ_y below RT seems rather dramatic when plotted on a linear scale, Fig. 19d shows that this is a natural consequence of athermal flow at low temperatures and mechanistically represents the same flow regime from cryogenic temperatures to 800 K. Additional details regarding analysis of thermally activated flow in CCAs is given in Ref. [268].

The strain rate dependence of CoCrFeMnNi is relatively weak from 10^{-3} s^{-1} to 10^{-1} s^{-1} [129]. Significant work-hardening is seen at all temperatures below about 1000 K, and is especially strong below RT. A detailed analysis of the strain-hardening rate and strain-hardening exponent show important effects of composition [261] and grain size [260,261]. The grain size effect is strongest at the smallest grain sizes, and σ_{uts} can be as high as 1200 MPa for extensively cold-rolled material [269] or 1950 MPa for CoCrFeMnNi processed by severe plastic deformation [138]. A Hall-Petch

---

[7] Tensile ductility can refer to the plastic strain at the ultimate load (uniform plastic strain) or the plastic strain to fracture, which includes non-uniform strain after necking. Elastic strain is usually subtracted to obtain these values. Published data often do not distinguish between these values, and the reader is cautioned that the term, ε, may represent any of these possibilities.

Table 6
Tensile properties of 3d transition metal CCAs (alloys containing Al are listed in order of increasing Al at%).

Alloy	Processing[a]	Microstructure[a]	$\dot{\varepsilon}$ (s^{-1})	T (°C)	σ_y (MPa)	σ_{uts} (MPa)	ε (%)	Ref
Al$_{0.3}$CoCrFeNi (7.0 at.% Al)	AC	FCC + L1$_2$	4×10^{-4}	23	224 ± 51	434 ± 94	48 ± 10	[264,265]
	AC, 700°C/72 h/WQ	FCC + L1$_2$	4×10^{-4}	23	310	525	44	[265]
	AC, 900°C/72 h/WQ	FCC + B2+L1$_2$	4×10^{-4}	23	240	570	45	[265]
	Bridgman casting	SX near [001]	4×10^{-4}	23	185	399	~80	[264]
Al$_{0.5}$CoCrCu$_{0.5}$FeNi$_2$ (8.3 at.% Al)	AC	FCC + L1$_2$	3.3×10^{-3}	23	357	459	9	[262]
				500	315 ± 12	334 ± 1	0.7 ± 0.3	[262]
	AC, 700°C/5 h/SC	FCC + L1$_2$+Cr-rich IM at GB	3.3×10^{-3}	23		365	0.1	[262]
				500		310 ± 2	0.02	[262]
	AC, 1150°C/5 h/WQ	FCC + L1$_2$	3.3×10^{-3}	23	215	489	39	[262]
				500	215 ± 11	248 ± 10	6.0 ± 3.0	[262]
Al$_{0.5}$CoCrCuFeNi (9.1 at.% Al)	AC	FCC + FCC	8×10^{-4}	23	360	707	19	[259]
	AC, 1000°C/6 h, CR 84%	FCC + L1$_2$	1×10^{-3}	23	1284	1344	7.6	[266]
	AC, 1000°C/6 h/WQ, CR 80%, 900°C/5 h	FCC + FCC, GS = 1 μm	1×10^{-3}	23	655	800 ± 30	29 ± 1	[147]
				300	460 ± 90	600 ± 50	6 ± 2	[147]
				400	500	590 ± 20	4 ± 2	[147]
				500	430 ± 20	450 ± 50	2 ± 2	[147]
				600	270 ± 20	310 ± 40	3 ± 1	[147]
				700	170 ± 40	190 ± 30	13 ± 4	[147]
Al$_{0.5}$CrCuFeNi$_2$ (9.1 at.% Al)	AC, CR 43%	FCC + FCC	1×10^{-3}	23	363 ± 60	500 ± 20	16 ± 7	[263]
	AC, CR 43%, 700°C/24 h	BCC + FCC + L1$_2$			630 ± 270	922 ± 240	4.2 ± 1.3	[263]
	AC, CR 43%, 900°C/24 h	BCC + FCC + L1$_2$			704 ± 180	1088 ± 20	5.6 ± 3.2	[263]
	AC, CR 43%, 1100°C/24 h	FCC + L1$_2$			360 ± 100	639 ± 5	3.4 ± 0.4	[263]
AlCoCrCuFeNi (16.7 at.% Al)	AC	BCC + FCC + B2+L1$_2$	1×10^{-3}	20	790	790	0.2	[267]
				600	648	551	0.4	[267]
				700	350	360	4.7	[267]
				800	161	180	12.1	[267]
				900	88	100	30	[267]
				1000	37	44	77	[267]
	AC, 960°C/50 h, a-b-c forged at 950 °C	BCC/B2+FCC + FCC+σ	1×10^{-3}	20	1040	1170	1.0	[267]
				300	810	880	0.4	[267]
				600	300	350	1.3	[267]
				700	63	91	63	[267]
			1×10^{-4}	800	8	17	325	[188]
			1×10^{-3}		29 ± 7	39 ± 12	382 ± 222	[188,267]
			1×10^{-2}		105	142	60	[188]
			1×10^{-4}	900	4	5	490	[188]
			1×10^{-3}		13 ± 1	16 ± 2	495 ± 90	[188,267]
			1×10^{-2}		42	53	350	[188]
			1×10^{-3}	1000	6 ± 3	14 ± 8	857 ± 7	[188,267]
			1×10^{-2}		12	14	1240	[188]
			1×10^{-1}		42	55	600	[188]
CoCrFeMnNi	AC, 1200°C/48 h, CR 87%, 800°C/1 h	FCC, GS = 4.4 μm	1×10^{-3}	−196	571	1099	72	[260]
				23	362	651	51	[260]
				200	292	524	36	[260]
				400	267	493	32	[260]
				600	241	423	42	[260]
				800	127	145	51	[260]
	AC, 1200°C/48 h, CR 87%, 1000°C/1 h	FCC, GS = 50 μm	1×10^{-3}	−196	390	973	84	[260]
				23	197	568	60	[260]
				200	146	461	44	[260]
				400	117	423	46	[260]
				600	98	366	40	[260]
				800	92	164	26	[260]
	AC, 1200°C/48 h, CR 87%, 1150°C/1 h	FCC, GS = 155 μm	1×10^{-3}	−196	356	909	83	[260]
				23	171	530	57	[260]
				200	121	423	46	[260]
				400	92	379	46	[260]
				600	76	328	41	[260]
				800	73	189	20	[260]
	AC, cold-forged + cross-rolled 60%, 800°C/1 h	FCC, GS = 6 μm	1×10^{-3}	−196	759	1280	71	[27]
				−77	518	925	60	[27]
				23	410	763	57	[27]
	AC, 1000°C/24 h, HR 92% @ 1000 °C, 900°C/1 h	FCC, GS = 32 μm	1×10^{-3}	−196	458	1010	61	[129]
				23	223	587	39	[129]
				200	188	506	36	[129]
				400	191	494	36	[129]
				600	150	395	36	[129]
				800	97	179	32	[129]

Table 6 (continued)

Alloy	Processing[a]	Microstructure[a]	$\dot{\epsilon}(s^{-1})$	T (°C)	σ_y (MPa)	σ_{uts} (MPa)	ε (%)	Ref
				1000	58	72	30	[129]
	AC, 1000°C/24 h/SC, CR 80%, 1100°C/1 h	FCC, GS = 60–80 μm	7.3 × 10^{-4}	23	135	497	53.5	[261]
CoCrFeNi	AC, 1000°C/24 h/SC, CR 80%, 1100°C/1 h	FCC, GS = 60–80 μm	7.3 × 10^{-4}	23	197	582	70.3	[261]
	AC, 1000°C/24 h, HR 92% @ 1000 °C, 900°C/1 h	FCC, GS = 11 μm	1 × 10^{-3}	−196	480	1109	66	[129]
				23	300	671	42	[129]
				200	214	559	34	[129]
				400	181	460	32	[129]
				600	155	396	34	[129]
				800	100	320	28	[129]
				1000	90	151	19	[129]
	AC, 1200°C/24 h, CR 92%, 900°C/1 h	FCC, GS = 24 μm	1 × 10^{-3}	−196	473	1170	50	[268]
				−70	328	917	44	[268]
				23	273	714	38	[268]
				200	215	582	34	[268]
				400	195	496	28	[268]
CoCrMnNi	AC, 1100°C/24 h, CR 90%, 1000°C/1 h	FCC, GS = 36 μm	1 × 10^{-3}	−196	499	1283	62	[268]
				−70	357	1006	54	[268]
				23	280	699	43	[268]
				200	215	582	36	[268]
				400	186	555	28	[268]
CoFeMnNi	AC, 1100°C/24 h, CR 90%, 1000°C/1 h	FCC, GS = 48 μm	1 × 10^{-3}	−196	300	835	48	[268]
				−70	210	656	44	[268]
				23	175	551	41	[268]
				200	135	488	36	[268]
				400	116	465	37	[268]

[a] The following acronyms are used: AC (as-cast); CR (cold-rolled); GB (grain boundary); GS (grain size); HR (hot-rolled); SC (slow cooled); SX (single crystal); WQ (water quench).
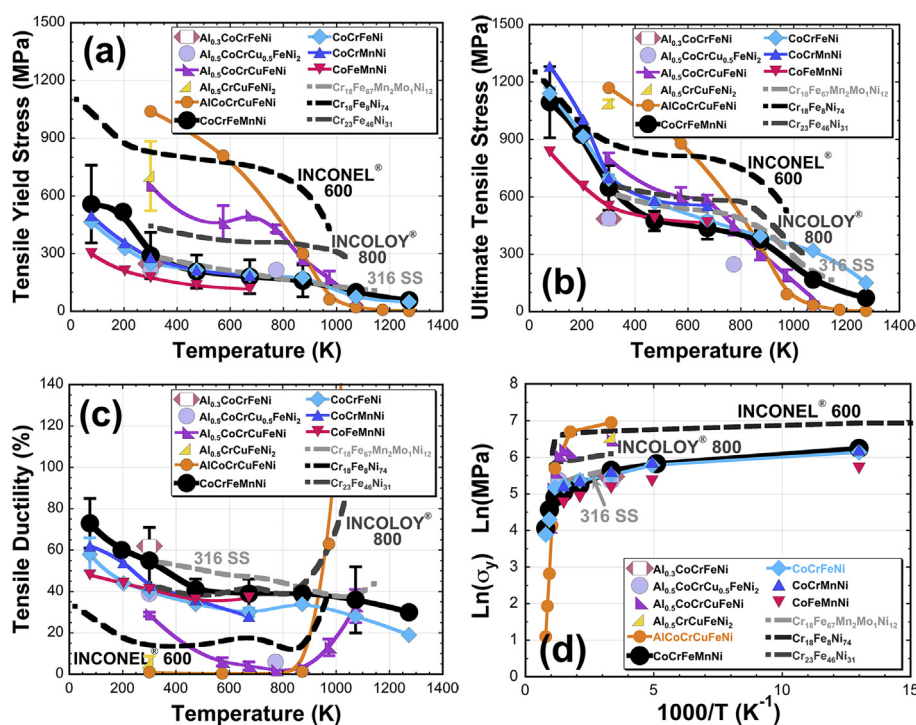

Fig. 19. Tensile data of 3d transition metal CCAs: (a) yield strength, σ_y, (b) ultimate strength, σ_{uts}, and (c) tensile ductility, ε, *vs.* temperature. (d) Data are shown as ln(σ_y) vs 1000/T to illustrate the thermally activated nature of yield. All MPEA data are for thermo-mechanically processed and/or annealed material (except Al$_{0.3}$CoCrFeNi and Al$_{0.5}$CoCrCu$_{0.5}$FeNi$_2$, which are annealed). Nominal strain rates, $\dot{\epsilon}$, range from 10^{-3} to 10^{-4} s^{-1}. Error bars show scatter in data from different studies. Data are taken from Refs. [27,129,138,147,162,260–263,269,270]. Data for three commercial solid solution, austenitic alloys are shown for comparison: 316 stainless steel, INCONEL$^{®}$ 600 and INCOLOY$^{®}$ 800, with the concentrations in at.% indicated in the legend.

analysis [260] shows the expected dependence of σ_y on (grain size)$^{-1/2}$. The Hall-Petch slope is relatively insensitive to temperature below 873 K, ranging from 538 MPa-μm$^{-1/2}$ at 77 K to 421 MPa-μm$^{-1/2}$ at 873 K. These values are lower than those obtained by hardness indents [273]. The Hall-Petch slope drops significantly at 1073 K to 127 MPa-μm$^{-1/2}$. Single crystal elastic constants have been measured for CoCrFeMnNi via neutron diffraction during in-situ tension testing of polycrystalline samples [270]. The shear anisotropy factor, $C_{44}/(C_{11}-C_{12}) = 2.84$, and Young's modulus anisotropy, $E_{(111)}/E_{(100)} = 1.98$, are comparable to values for FCC-Ni and BCC-Fe but are lower than for a typical austenitic stainless steel.

The Young's modulus and shear modulus of CoCrFeMnNi have been reported over a wide temperature range [200,274]. Elastic properties of CoCrFeMnNi appear lower than for the constituent elements over the same temperature range, but normalizing by the moduli at 0 K and the absolute melting temperatures collapses the data.

The properties of other Co-Cr-Fe-Mn-Ni alloys (including ternaries and quaternaries) are not substantially different than the equimolar quinary alloy [129,261,268,275,276]. This includes an alloy whose composition is tailored to reduce the stacking fault energy to <10 mJ-m^{-2}, and hence improve nano-twinning [261]. Ternary CoCrNi and quaternary CoCrFeNi and CoCrMnNi alloys give properties that are the same as or better than CoCrFeMnNi, but removing Cr reduces σ_y below 673 K and reduces σ_{uts} at $T \leq$ RT relative to CoCrFeMnNi (Fig. 19). Increasing Cr to 26 at.% gives the σ phase, increasing strength and decreasing ductility [261]. The tensile properties of three commercial austenitic, SS alloys are shown in Fig. 19 for comparison. These include 316 stainless steel (Cr$_{18}$Fe$_{67}$Mn$_2$Mo$_1$Ni$_{12}$), INCONEL® 600 (Cr$_{18}$Fe$_8$Ni$_{74}$) and INCOLOY® 800 (Cr$_{23}$Fe$_{46}$Ni$_{31}$). The tensile properties of 316 stainless steel are essentially the same as equimolar CoCrFeMnNi and Cr-containing quaternary alloys over the full range of tested temperatures. INCOLOY® 800 has higher σ_y, and INCONEL® 600 has higher σ_y and σ_{uts} relative to the CCAs above. Commercial alloys with higher Ni and lower Fe have higher strengths. The tensile ductility of the strongest commercial SS alloy (INCONEL® 600) is lower than other alloys, but is still in the range of 10−40% over the full range of use temperatures.

Tensile properties of 3d transition metal MPEAs with Al are commonly reported [188,259,262−267,277,278]. Alloys with the lowest Al concentrations (Al$_{0.3}$CoCrFeNi at 7.0 at.% Al and Al$_{0.5}$CoCrCu$_{0.5}$FeNi$_2$ at 8.1 at.% Al) have σ_y and room temperature (RT) ε values that are essentially the same as CoCrFeMnNi, but have lower σ_{uts} and ε at 773 K (Fig. 19). Increasing Al to 9.1 at.% in Al$_{0.5}$CoCrCuFeNi and Al$_{0.5}$CrCuFeNi$_2$ increases σ_y below 1073 K and σ_{uts} below 873 K, decreases ε below 1073 K, and gives properties essentially equivalent to CoCrFeMnNi otherwise. At the highest Al content (AlCoCrCuFeNi with 16.7 at.% Al), σ_y and σ_{uts} are higher relative to CoCrFeMnNi below 873 K and σ_y and σ_{uts} are lower than CoCrFeMnNi values at T $\geq$ 973 K. This alloy shows a classic brittle-to-ductile transition (BDT) above 873 K, and is superplastic at T $\geq$ 973 K, with tensile elongations as large as 1240% [188,267,277].

These property changes are tied to microstructural changes (Table 6). At low Al levels (7.0 and 8.3 at.%), the microstructure is primarily an FCC SS with L1$_2$ (cP4, AuCu$_3$ prototype) nano-precipitates [262,265]. Annealing at 1173 K adds B2 precipitates with a Kurdjumov-Sachs orientation relationship with the FCC matrix [265]. Intermediate Al levels (9.1 at.%) also give an FCC SS matrix with fine L1$_2$ precipitates, and a BCC phase is seen at some heat treatments [263,266]. TEM images [262,263,265] suggest that the L1$_2$ precipitates are larger in alloys with higher Al contents. The L1$_2$ vol fraction may increase with increasing Al, but data are not available to support this. Al$_{0.5}$CoCrCuFeNi and Al$_{0.5}$CrCuFeNi$_2$ have

the highest Cu concentration of alloys in this group (18.3 at.%), and a Cu-rich FCC solid solution phase with a lattice constant very close to the primary FCC phase is seen in these alloys [147,259,279]. Four phases are reported after annealing the most Al-rich alloy studied in tension, AlCoCrCuFeNi − two FCC phases, a BCC or B2 phase and the σ phase [188,267]. A fine grain size of 2.1 μm contributes to superplastic behavior of this alloy. Intermediate temperature embrittlement in one study results from phases that precipitate between 573 and 873 K [147], similar to behavior of some commercial alloys. Another study accounts for embrittlement by formation of Cr$_{23}$C$_6$ particles at grain boundaries [262].

Different microstructure trends are seen in a study of as-cast Al$_x$(CoCrFeMnNi)$_{100-x}$ ($0 \leq x \leq 20$) [143]. A single-phase FCC SS is found for $x \leq 4$ at.% Al; duplex BCC + FCC microstructures are reported when $8 \leq x \leq 16$ at.% Al; and a single-phase BCC microstructure is found at $x = 20$ at.% Al. Differences from other studies may be due to the presence of Mn, which is absent in the other Al-containing MPEAs studied in tension. Differences may also be due to the as-cast nature of this work. Nevertheless, the broad trend of increasing strength and decreasing ductility with increasing Al is shown in all alloys. The changes are small when the Al concentration is ≤ 7 at.%, and become stronger in the BCC + FCC region when $x \geq 8$ at.% Al. The as-cast alloys become brittle when $x > 11$ at.% Al. The σ_y, σ_{uts} and ε values of Al$_x$(CoCrFeMnNi)$_{100-x}$ ($x \leq 11$) alloys cover the same range as shown for the Al-containing alloys in Fig. 19.

The tensile properties of 3d transition metal MPEAs with Sn [192,280], Nb [281] and V [162] have been studied. Each of these elements produce intermetallic (IM) phases. Ductility increases with small Sn additions in CoCuFeMnNiSn$_x$, to $x = 0.03$ [280], and both strength and ductility increase in CoCuFeNiSn$_x$, to $x \leq 0.07$ [192]. In CoCrFeNb$_x$Ni, σ_y and σ_{uts} both increase and ε generally decreases with increasing x. Nevertheless, tensile ductility up to 20% is maintained when $x = 0.155$ (9.3 at.% Nb). The σ phase forms at the lowest Nb addition ($x = 0.103$), but the σ volume fraction is less than 10% when $x = 0.155$. In all of these alloys, both good strength and ductility are achieved as long as the IM phase is a minority microstructural constituent. Larger additions of the IM-forming element increase the size, volume fraction or contiguity of the IM phase, further increasing strength and decreasing ductility. All of the alloys studied here become brittle when the IM phase dominates.

Of special note is a novel eutectic alloy, AlCoCrFeNi$_{2.1}$, that is similar to AlCoCrCuFeNi, with Ni replacing Cu [144]. As-cast material has an FCC + B2 eutectic microstructure with a lamellae spacing of about 2 μm. The yield ('proof') stress of 75 MPa is much lower than typically reported for alloys in this family. A region of linear work-hardening at RT is followed by significant work-hardening. σ_{uts} is much higher than for AlCoCrCuFeNi at all temperatures except RT (where they are equal), and ε is significantly higher than AlCoCrCuFeNi at all temperatures below 973 K (Table 6). σ_{uts} and ε are equivalent to or higher than INCONEL® 600 (Fig. 19). Even more significant, these properties are obtained in the as-cast condition, potentially eliminating the need for wrought processing used to improve properties of INCONEL® 600 and other commercial austenitic solid solution alloys. The reasons behind the low proof stress and the linear work-hardening regime are not understood.

Tensile properties of a single-phase FCC single crystal Al$_{0.3}$CoCrFeNi are reported [264]. The sample has a crystallographic orientation near the [001] direction, and some low angle boundaries occur in the material. Mechanical properties at RT are $\sigma_y = 185$ MPa, $\sigma_{uts} = 399$ MPa and $\varepsilon \cong 80\%$. Although not reported, a critical resolved shear stress (τ_{crss}) can be estimated. Using

Schmid's law for a [001] tensile axis and the $[10\overline{1}](111)$ slip system, τ_{crss} is estimated to be about 76 MPa. This is just an estimate, as the tensile axis is not exactly along the [001] direction.

5.3.1.3. Other mechanical properties. Very few fracture toughness values are reported for 3d transition metal MPEAs. Crack lengths from indentation tests give qualitative toughness estimates in as-cast material [282], or give quantitative values (50.9 MPa-m$^{1/2}$) in rapidly solidified AlB$_{0.5}$CoCrCuFeMoNiSiTi [283]. The quench rate for this alloy is very high (10^4–10^6 K s^{-1}), giving a martensitic microstructure. Quantitative plane strain fracture toughness values are reported for as-cast Al$_{23}$Co$_{15}$Cr$_{23}$Cu$_8$Fe$_{15}$Ni$_{15}$ using single-edge notched bend (SENB) and chevron-notched rectangular bars [284]. Macroscopically, the microstructure is dendritic with a large primary grain size. At a finer scale, the microstructure consists of 200–500 nm Fe-Co rich BCC precipitates in an ordered BCC Al-Ni rich matrix. A small volume fraction of FCC Cu-rich precipitates is seen at grain boundaries. The K_{Ic} value from SENB tests is 5.8 ± 0.2 MPa-m$^{1/2}$ and is 5.4 ± 0.2 MPa-m$^{1/2}$ for chevron-notched samples.

The most detailed fracture toughness study is conducted on single-phase CoCrFeMnNi [27]. The material is cast, wrought and fully recrystallized with a uniform grain size of 6 μm. Compact tension samples are used with a non-linear fracture mechanics (*J*-integral) analysis. The crack initiation fracture toughness at RT is J_{Ic} = 250 kJ-m^{-2}, giving a stress intensity of K_{JIc} = 217 MPa-m$^{1/2}$. These values are relatively unchanged with decreasing temperature to 77 K. Toughness increases with increasing crack length, and after 2 mm crack extension the values rise to K = 300 MPa-m$^{1/2}$ (J = 500 kJ-m^{-2}), which is the limit of the test used. These are comparable to values for austenitic stainless steels and the best cryogenic steels. The high fracture toughness of CoCrFeMnNi is associated with a 100% ductile fracture by microvoid coalescence. The behavior is attributed to a transition from planar dislocation activity at RT to deformation by mechanical nano-twinning with decreasing temperature, resulting in continuous strain hardening. This gives an outstanding combination of strength, ductility and toughness that "exceeds that of virtually all pure metals and metallic alloys" [27].

Only one paper reports the fatigue behavior of MPEAs [266]. An Al$_{0.5}$CoCrCuFeNi MPEA is cast, annealed, and cold rolled to 85% reduction. The microstructure consists of FCC and L1$_2$ phases. The rolling deformation produces both morphological and crystallographic texturing of the microstructure. Four-point bending fatigue shows that the alloy has an endurance limit between 540 and 945 MPa, representing roughly 40–70% of the measured σ$_{uts}$. These values compare well with conventional steels and titanium alloys. The presence of aluminum oxide inclusions produce significant variability in the results.

Other properties reported for 3d transition metal CCAs include shear moduli and Poisson's ratios [268], stacking fault energies [261] and single crystal elastic modulus [264].

5.3.2. Refractory metal CCAs

Results in this family are not as mature as for 3d transition metal MPEAs. Most data are for hardness or compression, with very little tensile data. Material is often annealed but rarely deformation processed before measuring mechanical properties. Both equiaxed and dendritic microstructures are tested. Microstructures typically have one or more BCC phases, and a Laves phase is found in alloys with Cr and/or V. Differences in refractory metal elemental properties are greater than for 3d transition metal elements, and this is reflected in a broader span of mechanical properties. Current results are described below.

Hardness and compression data of refractory metal CCAs are given in Refs. [23,24,38,86,94–96,100–102,106,107,140,285–287]. Vickers hardness values range from 3.0 GPa for NbTiV$_2$Zr [38] to 5.8 GPa for AlMo$_{0.5}$NbTa$_{0.5}$TiZr [94]. Representative compression data are shown in Table 7 and Fig. 20a. The compressive yield stress, σ$_y$, drops with increasing temperature, and the rate of drop increases around 1000 K for most alloys. Several alloys retain a useful σ$_y$ near 400 MPa at 1373 K. Two refractory CCAs stand out. MoNbTaW and MoNbTaVW each contain W and retain useful strengths up to about 2000 K, but both alloys show a brittle to ductile transition between RT and 600 °C [24] and their densities, ρ, are high (Table 7). This motivated development of MPEAs with lower ρ refractory elements such as Cr, Ti, V and Zr, and by adding Al and/or Si. This produces refractory CCAs with ρ between 5.59 g cm^{-3} and 8.0 g cm^{-3} (Table 7). One of these alloys, AlMo$_{0.5}$NbTa$_{0.5}$TiZr with ρ of 7.40 g cm^{-3}, has the highest RT σ$_y$ and σ$_y$/ρ measured to date as well as 10% compressive RT ductility. The microstructure was initially reported as modulated nano-lamellae of two BCC phases [94], but detailed three-dimensional tomographic characterization via TEM dark field imaging later showed this to be BCC cuboids roughly 50 nm on a side surrounded by B2 nano-lamellae parallel to the cuboid faces [141,142].

The motivation for refractory CCAs is to extend the use temperature of structural metals, and so σ$_y$ of common superalloys are shown in Fig. 20 to gage early progress toward this goal. Haynes® 230® (Co$_4$Cr$_{27}$Fe$_3$Mo$_1$Ni$_{60}$W$_5$) is a SS alloy used for static sheet parts, INCONEL® 718 ((Al,Nb,Ti)$_5$Co$_1$Cr$_{21}$Fe$_{19}$Mo$_2$Ni$_{52}$) is a precipitation-strengthened alloy used widely in the gas turbine industry for rotating disks, and MAR-M 247® (Al$_{12}$Co$_{10}$Cr$_{10}$Hf$_{1}$-Ni$_{62}$Ta$_1$Ti$_1$W$_3$) is used for turbine blades. Direct comparison between refractory CCAs and superalloys based on strength alone is inappropriate, since refractory CCA data are for compression and superalloy data are in tension. Further, superalloys satisfy a wide range of additional requirements for high temperature structural applications, including tensile ductility, fracture toughness, oxidation resistance, creep strength, fatigue strength and processibility. None of these other properties have yet been demonstrated in the refractory CCAs, pointing toward directions of future research.

Density (ρ) is important for any component in a transportation system, and is especially important for rotating parts since much of the service stress comes from self-loading. Thus, the specific yield strength σ$_y$/ρ is shown in Fig. 20b. Typical σ$_y$/ρ requirements for thermal protection systems (TPS), turbine disks and turbine blades are also shown for reference. The maximum use temperature for the three conventional superalloys can be seen in Fig. 20b, where σ$_y$/ρ drops below the requirement for a particular application. Thus, Haynes® 230® can be used for thermal protective sheet (TPS) up to about 1150 K, MAR-M 247® can be used for turbine blades up to about 1150 K, and the maximum use temperature for INCONEL® 718 in disks is about 950 K.

Most refractory CCAs exceed Haynes® 230® (Fig. 20) and some show potential to extend the use temperature of blades and disks beyond current superalloys. A few refractory CCAs (Al$_{0.4}$Hf$_{0.6}$NbTaTiZr, AlMo$_{0.5}$NbTa$_{0.5}$TiZr, Al$_x$NbTaTiV (x = 0 to 1) and HfNbTiVZr) have sufficient RT compressive ductility (ε ≥ 10%) to suggest that tensile ductility may also be achieved, however, compressive fracture of these specimens indicates cleavage failure below about 900 K. Tensile characterization of these alloys is suggested for future work. Other alloys (Al$_{0.3}$NbTa$_{0.8}$Ti$_{1.4}$V$_{0.2}$Zr$_{1.3}$, Al$_{0.5}$NbTa$_{0.8}$Ti$_{1.5}$V$_{0.2}$Zr, Al$_{0.3}$NbTaTi$_{1.4}$Zr$_{1.3}$, AlNbTiV, CrMo$_{0.5}$NbTa$_{0.5}$TiZr, CrNbTiZr and HfMoNbTiZr) have attractive σ$_y$ with compressive ductilities high enough to give potential for further improvements via compositional modifications and microstructure control.

Table 7
Mechanical properties of refractory metal CCAs (all data are for compression unless noted otherwise).

Alloy	Processing[a]	Microstructure[a]	ρ g/cm^3	$\dot{\varepsilon}$(s^{-1})	T (°C)	σ_y (MPa)	σ_{uts} (MPa)	ε (%)	Ref
Al$_{0.4}$Hf$_{0.6}$NbTaTiZr	AC, HIP @ 1200C/207 MPa/2 h, 1200C/24 h	BCC	9.05	10^{-3}	23	1841		10	[94]
					800	796		>50	
					1000	298		>50	
AlMo$_{0.5}$NbTa$_{0.5}$TiZr	AC, HIP @ 1400C/207 MPa/2 h, 1400C/24 h	BCC + B2	7.40	10^{-3}	23	2000		10	[94]
					800	1597		11	
					1000	745		>50	
					1200	255		>50	
Al$_{0.25}$NbTaTiV	AC	BCC (dendritic)	8.80[b]	2 × 10^{-4}	23	1330		>50	[101]
Al$_{0.5}$NbTaTiV	AC	BCC (dendritic)	8.46[b]	2 × 10^{-4}	23	1012		>50	[101]
AlNbTaTiV	AC	BCC (dendritic)	7.89[b]	2 × 10^{-4}	23	991		>50	[101]
Al$_{0.3}$NbTa$_{0.8}$Ti$_{1.4}$V$_{0.2}$Zr$_{1.3}$	AC, HIP @ 1200C/207 MPa/2 h, 1200C/24 h	BCC	7.78	10^{-3}	25	1965		5	[95]
					800	678		>50	
					1000	166		>50	
Al$_{0.5}$NbTa$_{0.8}$Ti$_{1.5}$V$_{0.2}$Zr	AC, HIP @ 1200C/207 MPa/2 h, 1200C/24 h	BCC + BCC	7.42	10^{-3}	25	2035		4.5	[95]
					800	796		>50	
					1000	220		>50	
Al$_{0.3}$NbTaTi$_{1.4}$Zr$_{1.3}$	AC, HIP @ 1200C/207 MPa/2 h, 1200C/24 h	BCC + BCC	8.18	10^{-3}	25	1965		5	[95]
					800	362		>50	
					1000	236		>50	
AlNb$_{1.5}$Ta$_{0.5}$Ti$_{1.5}$Zr$_{0.5}$	AC, HIP @ 1400C/207 MPa/2 h, 1400C/24 h	BCC	6.88	10^{-3}	25	1280		3.5	[95]
					800	728		30	
					1000	403		>50	
AlNbTiV	AC, 1200C/24 h	BCC	5.59	10^{-3}	22	1020		5	[107]
					600	810		12	
					800	685		>50	
					1000	158		>50	
CrHfNbTiZr	AC	BCC + Laves + Laves	8.24[b]	5 × 10^{-4}	25	1375		2.8	[86]
CrMo$_{0.5}$NbTa$_{0.5}$TiZr	AC, HIP @ 1450C/207 MPa/2 h, 1200C/24 h	BCC + BCC + Laves	8.23	10^{-3}	23	1595		5	[96]
					800	983		5.5	
					1000	546		>50	
					1200	170		>50	
CrNbTiVZr	AC, HIP @ 1200C/207 MPa/2 h, 1200C/24 h	BCC + Laves	6.52	10^{-3}	25	1298		3	[38,286]
					600	1230		20	
					800	615		>50	
					1000	259		>50	
CrNbTiZr	AC, HIP @ 1200C/207 MPa/2 h, 1200C/24 h	BCC + Laves	6.70	10^{-3}	25	1260		6	[38,286]
					600	1035		>50	
					800	300		>50	
					1000	115		>50	
HfMoNbTiZr	AC, 1100C/10 h/SC	BCC (dendritic)	8.69[b]	10^{-3}	23	1575		9	[140]
					800	825		>50	
					1000	635		>50	
					1200	187		>50	
HfNbTaTiZr	AC, HIP @ 1200C/207 MPa/2 h, 1200C/24 h	BCC (dendritic and non-uniform)	9.94	10^{-3}	23	929		>50	[285]
					600	675		>50	
					800	535		>50	
					1000	295		>50	
					1200	92		>50	
	AC, HIP @ 1200C/207 MPa/2 h, 1200C/24 h, CR 90%, 1000C/2 h	BCC		10^{-3}	25	1145[c]	1262[c]	9.7[c]	[287]
HfNbTiVZr	AC	BCC + unknown	8.06[b]	5 × 10^{-4}	25	1170		30	[86]
HfNbTiZr	AC, 1300C/6 h/SC	BCC	8.40[b]	10^{-3}	25	879[c]	969[c]	14.9[c]	[100]

Table 7 (continued)

Alloy	Processing[a]	Microstructure[a]	ρ g/cm^3	$\dot{\varepsilon}$(s^{-1})	T (°C)	σ_y (MPa)	σ_{uts} (MPa)	ε (%)	Ref
MoNbTaVW	AC	BCC (dendritic)	12.36	10^{-3}	23	1246		1.7	[24]
					600	862		13	
					800	846		17	
					1000	842		19	
					1200	735		7.5	
					1400	656		18	
					1600	477		13	
MoNbTaW	AC	BCC (dendritic)	13.75	10^{-3}	23	1058		2.6	[24]
					600	561		>40	
					800	552		>40	
					1000	548		>40	
					1200	506		>40	
					1400	421		>40	
					1600	405		>40	
NbTaTiV	AC	BCC	9.17[b]	2 × 10^{-4}	23	1092		>50	[101]
NbTiVZr	AC, HIP @ 1200C/207 MPa/2 h, 1200C/24 h	BCC	6.5	10^{-3}	25	1105		>50	[38,286]
					600	834		>50	
					800	187		>50	
					1000	58		>50	
NbTiV$_2$Zr	AC, HIP @ 1200C/207 MPa/2 h, 1200C/24 h	BCC	6.38	10^{-3}	25	918		>50	[38,286]
					600	571		>50	
					800	240		>50	
					1000	72		>50	

[a] The following acronyms are used: AC (as-cast); CR (cold-rolled); HIP (hot isostatic pressed); SC (slow cooled).
[b] Calculated.
[c] Tensile data.

Only two publications currently report tensile properties in refractory MPEAs [100,287]. Both HfNbTiZr and HfNbTaTiZr are tested at RT. Both alloys are single-phase BCC, and both show significant tensile ductility (Table 7). HfNbTaTiZr is characterized after cold-rolling, and represents the first successful attempt to cold roll an MPEA with a BCC crystal structure.

5.4. Other properties

Alloy density is an important consideration for many applications. Densities of conventional alloys are typically clustered around the base element values: 2.7 g-cm^{-3} for Al alloys, 4.5 g-cm^{-3} for Ti alloys, 7.9 g-cm^{-3} for steels and 8 to 9 g-cm^{-3} for Ni-based superalloys. However, density covers a more continuous range for CCAs. Light metal CCAs range from 2.67 to 5.21 g-cm^{-3} [109–111] and refractory CCAs show a particularly wide range of densities, from 5.59 to 13.75 g-cm^{-3} (Table 7). Densities are not often reported for 3d transition metal MPEAs, but a weighted rule of mixtures [110] give densities that generally fall in the range of 5.1–8.9 g-cm^{-3}.

A number of studies appear on the corrosion and electrochemical properties of MPEAs [136,288–305]. Less work has been reported on wear resistance [3,146,243,306–311] and oxidation behavior [4,92,93,105,312,313]. As a general result, MPEAs have good properties in each of these areas. Additional details are discussed in other recent reviews [10,11,16,17,82].

5.5. Discussion

The alloys studied here cover extremely broad ranges of compositions and microstructures. It's clear that different alloy families must be considered separately. Thus, we discuss composition/microstructure/properties relationships in 3d transition metal CCAs
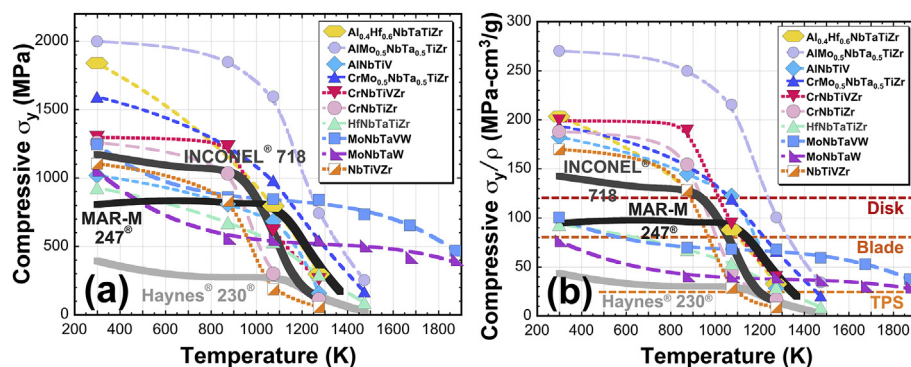

Fig. 20. Temperature dependence of (a) compressive yield strength, σ_y, and (b) σ_y normalized by alloy density, ρ, of refractory CCAs. Initial strain rates, $\dot{\varepsilon}$, range from 2 × 10^{-4} to 10^{-3} s^{-1}. Data are taken from Refs. [24,38,94,96,107,285,286]. Tensile σ_y for commercial superalloys (Haynes® 230®, INCONEL® 718 and MAR-M 247®) are shown for reference. Typical σ_y/ρ requirements for thermal protection sheet (TPS), turbine blades and disks are shown in (b).

separately from refractory metal CCAs. However, it's not as clear how to deal with different alloys in the same family. Strictly speaking, each combination of principal elements within a CCA family represents a significant composition change and could be considered a unique alloy base with distinct composition/structure/property relationships. Here we compare properties of alloys within the same family as representing similar relationships. For example, we describe the effect of Al on microstructure and properties in the 3d transition metal family, even though the other principal elements can change. For the time being, this approach seems to be adequate. It remains to be seen in the long run what are the limits of this approach.

5.5.1. Functional properties

There is much less work on CCA functional properties than on mechanical properties. This review includes 17 citations for magnetic, thermal and electrical properties of MPEAs, and 12 more for diffusion barriers, hydrogen storage, catalysis, thermoelectrics and shape memory alloys. By contrast, about 97 citations are used for mechanical properties, plus another 35 citations for environmental resistance of structural materials (corrosion, wear, oxidation and irradiation resistance). The exploration of functional materials using the MPEA philosophy represents a major opportunity for future work. This includes more studies in the functional materials already initiated, exploring a broader range of functional materials such as piezoelectric and optical sensor materials, and a more systematic approach to designing functional MPEAs. One such study has already appeared — the design of a low temperature superconducting CCA by the combination of elements that are themselves all superconductors [206]. See Section 6.3 and Section 7.2.1 for more discussion of these opportunities.

5.5.2. Mechanical properties

As a major accomplishment, broad relationships between composition, microstructure and mechanical properties are being established, especially in 3d transition metal MPEAs. Perhaps the most important — and most widely studied — is the effect of Al concentration [133,143,282]. This is shown systematically in as-cast $Al_x(CoCrFeMnNi)_{100-x}$, where tensile strength increases and ductility decreases with increasing Al. The microstructure is single-phase FCC for $x < 8$ (8 at.% Al), duplex BCC + FCC for $8 \leq x \leq 16$, and BCC or BCC + B2 for $x > 16$ [143]. The same general trends are seen by combining results from other studies [147,259,262−265,267], even though the principal elements are different, the type and amount of thermo-mechanical processing is different, the secondary phases formed may be different and grain sizes are different (Section 5.3.1.2). The influence of Al on the microstructure and properties of 3d transition metal CCAs is thus initially established.

Cr also has a distinctive role on microstructure and properties in 3d transition metal CCAs [268]. CCAs drawn from Co-Cr-Fe-Mn-Ni (including ternary, quaternary and non-equimolar quinary alloys) have properties similar to equimolar CoCrFeMnNi as long as Cr is included (Section 5.3.1.2). However, removing Cr reduces strength relative to CoCrFeMnNi. Increasing Cr above 26 at.% introduces the σ phase, which further increases strength and decreases ductility. Other principal elements in 3d transition metal CCAs appear to be less influential. Cu tends to phase-separate into a Cu-rich FCC phase. A mechanistic understanding of this phase's role on mechanical properties is not available, but tensile ductility is in the range of 40−60% for alloys without Cu and 10−20% for as-cast Cu-containing alloys [192,280]. Cu is also associated with nano-twinning that is an important mechanism for work-hardening, especially below RT [150]. Alloys without Co, Fe or Mn have properties that are not significantly different than alloys that contain these elements. This includes commercial austenitic, SS alloys such

as INCOLOY® 800 ($Cr_{23}Fe_{46}Ni_{31}$), INCONEL® 600 ($Ni_{74}Cr_{18}Fe_8$) and 316 stainless steel ($Cr_{18}Fe_{67}Mn_2Mo_1Ni_{12}$). Ti is generally considered to be a compound former, but clear trends are not yet established.

Nb and Sn additions show clear microstructure and properties trends [192,280,281]. Increasing Nb or Sn increases the volume fraction of IM phases, increasing strength and decreasing ductility. A balance of strength and ductility are retained in microstructures with a modest IM content, but ductility is lost when the IM phase dominates the microstructure. This same trend is well-known in commercial alloys and other advanced structural metals. The trends established for Al, Sn and Nb additions in 3d transition metal MPEAs thus suggest that these alloys are likely to respond to microstructural control as do conventional alloys. This supports the exploration and development of multi-phase microstructures, including IM phases, to achieve a balance of strength and fracture tolerance [26]. Control of the IM volume fraction can be achieved through alloy composition, and the size, spacing and distribution can be controlled by deformation processing and by heat treatments such as solutionizing, quench and aging.

As a family, 3d transition metal CCAs with an FCC structure are not particularly strong, with σ_y generally below 300 MPa and σ_{uts} below about 700 MPa. They have mechanical properties very similar to 316 stainless steel. Significant strengthening can be achieved by strain hardening [132,150,269] and grain refinement [27,147,260], but these approaches are used in conventional alloys and are not expected to give a competitive advantage to MPEAs. As mentioned above, Al additions give a third strategy for increasing the strength of 3d transition metal MPEAs. None of these approaches are expected to be effective above about half the absolute melting temperature, where thermally activated flow begins to dominate. Using $T_m = 1607$ K for CoCrFeMnNi [32] as a representative melting point, the tensile data for all 3d transition metal MPEAs collected to date begin to drop quickly at about 800 K (Fig. 19), and the onset of thermally activated flow is especially apparent at this temperature in Fig. 19d. None of the 3d transition metal alloys have properties that compete with nickel-based superalloys (compare Fig. 19a with Fig. 20) or with precipitation hardened stainless steels [30,314].

It may seem surprising that some commercial austenitic alloys have properties essentially identical to 3d transition metal CCAs. A casual analysis might conclude that CCAs offer no unusual strengthening. However, even though these commercial alloys do not satisfy HEA definitions (Section 1.2), they are nevertheless complex, concentrated SS alloys with 3 or more principal elements. Considering elements with concentrations >5 at.% as principal elements, these alloys are all concentrated, non-equimolar Cr-Fe-Ni alloys. The motivation for including a minimum of 5 elements in the HEA definition is to increase configurational entropy. It is not clear how many elements are needed to increase strengthening potency beyond dilute solution hardening (see Section 5.5.3). Tensile data in Section 5.3.1.2 show that ternary and quaternary alloys can have the same strengths as equimolar 5-component alloys, supporting the finding that, "The stronger alloys are not necessarily the ones with the most elements. The nature of the constituent elements is also important, with the Cr-containing alloys in general being the strongest." [268].

Precipitation hardening of 3d transition metal MPEAs is a relatively undeveloped area. Initial studies show some promise for this approach [265,315−321]. Hardness shows a typical under-aged, peak-aged and over-aged response to aging time and temperature. Current studies apply aging treatments to as-cast material. Solution treated and quenched microstructures are suggested for future aging studies to better control the starting point of the precipitation reaction.

Refractory metal CCAs have mechanical properties that show

potential for high temperature applications in gas turbines. Several alloys tested to date exceed currently used alloys in strength, specific strength, and maximum use temperature. As important, these candidate refractory CCAs have some compressive ductility at RT to suggest the possibility of eventually achieving useful tensile ductility. Nevertheless, significant additional work is needed. Very few tensile data have been measured, and this is a clear direction for future work. Many studies apply thermal treatment after casting to reduce chemical segregation, but very few use deformation processing to control microstructure. An understanding of the distinct roles that particular constituent elements fill in 3d transition metal MPEAs is building, but such knowledge is lacking for refractory metal CCAs. Intentional alloy design for precipitation hardening is also recommended. Finally, oxidation resistance is a serious potential barrier to the use of any refractory metal alloy for extended time at elevated temperature. One study shows parabolic weight gain after 100 h at 1273 K [93] and a second study shows non-protective, linear oxidation in a different alloy at 1573 K [92]. More studies characterizing the oxidation behavior are needed, along with efforts to explore alloying approaches to improve the environmental stability of this class of alloys. These are all important directions for future research (Section 7.2.2.2).

5.5.3. Solid solution hardening model

The MPEA field still lacks a validated, general model to predict solid solution hardening. This is a major scientific gap with important practical implications. An early effort modifies classical hardening concepts to calculate the strengthening increment in HfNbTaTiZr [139]. This approach develops concentration-dependent terms for atom size misfit and elastic misfit. The alloy is modeled as a pseudo-binary for atomic size misfit since Hf and Zr have nearly identical atom radii and Nb, Ta and Ti atom radii are also similar. It is also modeled as a pseudo-binary for modulus misfit, since the shear moduli of Hf, Nb, Ti and Zr are all similar and the shear modulus of Ta is much higher. Nevertheless, the approach is sufficiently general and should be applicable to alloys with greater dispersity in atom sizes and moduli. The predicted strengthening increment is 18% higher than the measured value, which is reasonable agreement for this initial model. Thermally activated flow was not considered, and this would improve agreement.

A more recent paper outlines approaches for the temperature dependence of solute hardening in concentrated solutions and develops a work-hardening model [268], and a subsequent paper gives the first detailed approach to modeling solid solution strengthening in MPEAs [322]. The model in the second paper includes a concentration-dependent term, a term that accounts for the elastic misfit of the atoms, and a term that quantifies the contribution from lattice distortions. Agreement with experiment is modest. The authors give a good account of the many difficulties in comparing experiments with the model — substructure hardening, short-range atomic order, grain size effects and the presence of second phases are some of the concerns. It is also possible that a chemical term may need to be built into the model to account for changes to stacking fault energies [268]. Continued development and validation of solid solution hardening models is a major future effort that is needed to guide alloy development (Section 7.1.3).

5.6. Summary

A detailed analysis of MPEA properties is complicated by differences in the number, type and concentration of principal elements in the alloys studied, the extent of post-process deformation processing, and the temperature and duration of post-process thermal treatment. These each can have important effects on microstructure and properties. We therefore focus on broad trends and major results rather than a detailed analysis of specific features. To improve consistency, we emphasize studies that strive to produce chemically and microstructurally uniform materials and to reduce defects that may influence measured properties. For mechanical properties, the 3d transition metal and refractory metal alloy families are discussed separately.

Thermal conductivity, thermal diffusivity and thermal expansion of 3d transition metal CCAs are generally similar to highly alloyed steels and superalloys (Section 5.1). Increasing Al in these alloys transforms the microstructure from FCC, to BCC + FCC, to BCC. Thermal conductivity increases with increasing Al. Magnetic properties are reported for 3d transition metal MPEAs that contain the ferromagnetic elements Co, Fe and Ni. A non-equimolar CCA superconductor is made from refractory elements that are themselves all superconductors. Very few studies are available on other functional properties that include diffusion barriers, hydrogen storage, catalysis, thermoelectric response, shape memory and irradiation resistance (Section 5.5.1). This topic is recommended for future work (Section 7.2.1).

Diffusion coefficients of Co, Cr, Fe, Mn and Ni are measured in CoCrFeMn$_{0.5}$Ni and compared with diffusion coefficients for the same elements in FCC hosts (Co, Fe and Ni) and in four different austenitic stainless steels (Section 5.2). We compare diffusion in CoCrFeMn$_{0.5}$Ni with selected elements and alloys at the same diffusion temperature, and with a wide range of FCC elements and alloys at the melting temperature of the host, T_m. Diffusion coefficients in CoCrFeMn$_{0.5}$Ni fall in the same range (within an order of magnitude) of values in other FCC metals and alloys for both comparisons. We conclude that the current data do not support the sluggish diffusion hypothesis. Data are available for only one alloy, and additional diffusion studies are suggested. It is also recommended that the assumption that D_0 is constant at T_m for all metals with the same crystal structure and bonding type be assessed for CCAs.

A growing maturity is evident in the characterization of mechanical properties for 3d transition metal MPEAs (Section 5.3.1.2). This is shown by a growing amount of tensile data on material that has been homogenized and/or deformation processed to produce homogeneous compositions and uniform microstructures. 3d transition metal MPEAs with single-phase, FCC microstructures and without Al (e.g. CoCrFeMnNi as the most commonly studied alloy in this category) are characterized by relatively low tensile yield and ultimate strengths at room temperature (RT). Deformation at RT and above is by planar glide of ½<110>{111} dislocations that organize into cell structures at high strains, giving significant work-hardening. Extensive nano-twinning operates below RT, significantly increasing tensile strength while also increasing tensile ductility. Yield and ultimate tensile strengths are relatively constant from RT to about 800 K, but thermally activated flow at higher temperatures produces a drop in strength. The fracture toughness of CoCrFeMnNi is as high as any metal alloy produced to date.

The tensile properties of alloys in the Co-Cr-Fe-Mn-Ni system depend less on the number of principal elements and more on the particular elements used (Section 5.3.1.2). Quaternary and even ternary equimolar alloys have tensile properties that are essentially identical to CoCrFeMnNi, as long as Cr is included. The tensile properties of these CCAs are very similar to well-known commercial austenitic alloys such as 316 stainless steel and INCOLOY® 800. HEAs have a minimum of 5 elements by definition, but it is not clear how many (or how few) principal elements are needed to give unusual hardening that may exist in concentrated solutions. Although developed decades before the HEA concept, commercial austenitic stainless steel alloys are nevertheless complex, concentrated, non-equimolar Cr-Fe-Ni alloys. The commercial austenitic

alloy, INCONEL® 600, is also a single-phase, FCC, non-equimolar ternary Cr-Fe-Ni alloy and has a balance of tensile properties (including a minimum 10% ductility over the full range of use temperatures) superior to any recently-studied 3d transition metal MPEA. Based on an assessment of alloy compositions, we include the full range of austenitic stainless steels, precipitation hardened stainless steels, austenitic nickel alloys and precipitation hardened nickel alloys as 3d transition metal CCAs. All of these alloy families have at least three principal elements, and some have as many as five.

As a major accomplishment of the field, the broad influence of Al on the microstructure and properties of 3d transition metal CCAs is established (Section 5.3.1.2). These trends are established in studies of MPEAs with different principal elements and apply different thermal treatments. In general, the tensile strength increases and the ductility decreases with increasing Al. RT tensile ductility $\geq 10\%$ is retained for Al concentrations ≤ 9.1 at.%, representing MPEAs such as $Al_{0.5}CrCuFeNi_2$ and $Al_{0.5}CoCrCuFeNi$. The RT tensile ductility drops to zero at 16.7 at.% Al. These properties trends are associated with a broad transition from predominantly FCC microstructures in alloys with no Al, to FCC with $L1_2$ nano-precipitates at 7 and 8.3 at.% Al, to FCC + $L1_2$ and perhaps BCC phases at 9.1 at.% Al, to multi-phase alloys that include one or more FCC phases, a BCC or B2 phase, and the σ phase at 16.7 at.% Al.

The influence of other principal elements on 3d transition metal MPEA properties are also becoming established (Section 5.3.1.2). Cr is required to give good strength, but it decreases ductility when the concentration reaches 26 at.% due to σ phase formation. The tensile properties of alloys without Co or Fe are not significantly different from alloys that contain these elements. Cu often phase-separates into a Cu-rich FCC phase, and tensile ductility drops from 40 to 60% in alloys without Cu to 10−20% in alloys with Cu. Cu is also associated with nano-twinning, which is responsible for significant work-hardening below RT. Clear trends for the influence of Ti on mechanical properties are not yet apparent.

A consistent role of intermetallic (IM) phases on tensile properties of 3d transition metal MPEAs is seen (Section 5.3.1.2). Small IM volume fractions increase strength while retaining useful ductility, but ductility drops when the IM becomes a dominant phase. The beneficial role of modest IM additions supports the approach of developing precipitation-strengthened microstructures in multi-phase CCAs. A small number of aging studies have been conducted to control the size and distribution of strengthening phases in 3d transition metal CCAs, showing a typical under-aged, peak-aged, over-aged response to aging time and temperature. This area is suggested as a major direction for future research, and is discussed further in Section 7.2.2.

Refractory metal CCAs are still in relatively early stages of exploration (Section 5.3.2). Mechanical properties are generally measured in compressive loading, with only a small number of tensile studies. A wide range of densities has been produced, from 5.59 to 13.75 g cm^{-3}. Most alloys have one or two BCC phases, some alloys have one or more Laves phases, and one alloy reports a B2 phase. Several alloys have compressive yield strengths and yield strengths normalized by density that show potential to increase the operating stresses and/or temperatures compared to conventional nickel-based superalloys. The strongest alloys also have $\geq 10\%$ RT compressive ductility, and one has been cold-rolled to sheet, offering the possibility of useful tensile ductility. Future work is suggested on this family, emphasizing tensile data, continued exploration of the range of principal element combinations, modifying alloy compositions to intentionally design precipitation strengthened microstructures and studying oxidation resistance (Section 7.2.2.2).

A model to predict solid solution hardening has not yet been

validated for CCAs (Section 5.5.3). An initial model gives reasonable agreement for a single alloy studied using concentration dependent terms for atom size misfit and shear modulus misfit. A recent attempt at modeling this essential property includes a concentration-dependent term, a lattice distortion term, and a term that accounts for the elastic misfit of the atoms. The agreement is modest, but there are many challenges in comparing predictions with experimental data, which can include variations in substructure hardening, grain size hardening, short-range atomic ordering and the presence of second phases. This is a major scientific gap − a practical model is needed to help guide alloy development. Future work is needed to overcome this barrier, including consideration of a chemical term to account for changes in stacking fault energies (Section 7.1.3).

6. MPEA applications and materials design

The suitability of multi-principal element alloys (MPEAs) for potential applications is usually evaluated by characterizing a single dominant 'first-tier' property. For example, tensile properties represent structural applications, magnetic saturation is measured for hard magnets, and low temperature electrical conductivity is given for superconductors. But multiple properties are required for any use. In addition to good tensile properties, structural metals need many other properties that include damage tolerance, environmental resistance and the ability to join and form into shapes [31]. By definition, superconductors have no resistance to electrical current, but are also selected by maximum current capacity, material cost and ability to process into useful forms. Measuring these next-tier properties shows a growing maturity in application-driven alloy development. MPEA efforts are already moving in this direction, especially for structural materials.

Comparing measured properties with requirements evaluates the suitability of complex, concentrated alloys (CCAs) for an intended application and focuses future efforts by identifying gaps. However, it limits discussion to CCAs already defined. We refer the reader to earlier discussions of applications for existing CCAs [11,16,17]. In this section we take a different approach to assessing CCA applications.

Here we envision a much wider range of MPEA applications. We support this vision by describing a broader, more general use of the CCA philosophy. We further support this view by recognizing that CCAs are already in use, although not by that name, representing structural alloys over half a century old and functional materials currently under development. The purpose of recognizing this connection is to synergize the still new idea to investigate the vast, unexplored central regions of multi-principal element composition and phase space with a broad range of practical knowledge and experience. To date, the full potential of this idea has hardly been realized. The seminal papers in 2004 [1−6] emphasize 3d transition metal alloys (including borides and nitrides), and it was 6 years before a new alloy family (refractory metal CCAs) was introduced. Four more families followed four years later − three of these are motivated by applications and one by scientific curiosity. In a field that promises thousands or millions of new alloy families, developing 7 new alloy families in 12 years seems a rather slow beginning. By expanding the scope of CCA applications through a more general description of the MPEA approach, we hope to stimulate new ideas that will accelerate growth of the field.

This section starts with a general description of how applications or scientific curiosity can define a new alloy family (Section 6.1). Alloy families for structural applications are presented in Section 6.2, including those CCAs already developed and those that are suggested by classes of structural metals for which no CCA analog currently exists. The same template is followed for

functional materials in Section 6.3. A discussion that builds on the general findings of these considerations (Section 6.4) is followed by a brief summary (Section 6.5).

6.1. Applications as a guide to defining CCA families

We briefly review how an application or scientific curiosity leads to the definition of a new alloy family. The application gives the properties of interest, which in turn inspires a palette of elements that may produce these properties. In many cases, elements can be selected directly. For example, low density metallic elements are used in light metals MPEAs, elements with high melting temperatures (T_m) are selected for refractory metal CCAs, and metals with the hexagonal close-packed (HCP) crystal structure are used to produce single-phase HCP solid solution high entropy alloys (HEAs). However, selecting elements can be more complicated, since interactions between two or more elements can give a desired property that is missing in individual elements (Section 3.3) – this is the essence of the 'cocktail effect'. Selecting the palette of candidate elements can be guided by tools that give information on interactions between atoms. These tools include phase diagrams, computational techniques (including data-driven models and maching learning), scientific theory, or experimental data. These tools may greatly expand the palette of elements for a given application, redefining the concept of an alloy family (Section 3.3).

The simple description given here generalizes an earlier approach for selecting palettes of elements for structural applications [25]. In the following sections, we show that these ideas can define palettes of elements for any application for which materials are designed or used. This includes functional and structural materials, and it also includes metal alloys as well as compounds such as oxides, carbides, borides and nitrides. This idea opens up a broad range of applications for which CCAs are not presently being considered.

6.2. MPEAs for structural applications

6.2.1. Existing structural CCA families

Four of the seven MPEA families are inspired by structural applications. These are the 3d transition metal family, the refractory metal CCA family, the light metal family, and CCA brasses and bronzes (Section 3.2). These are discussed below.

6.2.1.1. 3d transition metal CCAs.
3d transition metal MPEAs compare directly with austenitic stainless steels, duplex (FCC + BCC) stainless steels, precipitation hardened stainless steels, austenitic nickel alloys and nickel-based superalloys [30,314]. Austenitic stainless steels can be considered as Cr-Fe-Ni and Cr-Fe-Mn non-equimolar ternary CCAs and Cr-Fe-Mn-Ni non-equimolar quaternary CCAs. Principal element concentration ranges are Cr (16–28 at.%), Fe (52–78 at.%), Ni (8–21 at.%) and Mn (2–19 at.%) [30]. All austenitic stainless steels contain Cr as a principal element. This confers corrosion resistance that gives the steels their name, but work in the MPEA community shows that Cr is also essential for good strength (Section 5.3.1.2, Section 5.5.2). Duplex stainless steels generally have lower Ni (3–8 at.%) with Mo (1–3 at.%), and precipitation hardened stainless steels are similar to duplex stainless steels with 3 at.% Al. Austenitic stainless steels have 0.08–0.25 wt% C (0.4–1.1 at.% C).

Commercial austenitic nickel alloys include non-equimolar Cr-Fe-Ni ternaries, non-equimolar Co-Cr-Mo-Ni and Cr-Fe-Mo-Ni quaternary alloys and a non-equimolar Co-Cr-Fe-Mo-Ni quinary alloy. INCOLOY® 800 ($Cr_{23}Fe_{46}Ni_{31}$) is nearly an equimolar ternary alloy. The carbon content in Cu-Ni alloys ranges from 0.10 to 0.30 wt % C (0.50–1.50 at.% C) and in other nickel alloys is usually ≤0.10 wt%

C (≤0.50 at.% C). The distinction between austenitic stainless steels and nickel alloys is not sharp, and the unified numbering system of alloys (UNS) classifies some Ni-rich alloys as stainless steels [30]. Though the composition ranges are not given here, nickel superalloys are similarly included as CCAs. Superalloys generally have three to five principal elements of Al, Co, Cr, Fe, Ni, Mo, Ti and/or W.

The compositional overlap between 3d transition metal CCAs and commercial stainless steels and nickel alloys is obvious. Even though many of these commercial alloys don't satisfy HEA definitions and were developed empirically decades before the HEA concept, they are nevertheless concentrated alloys with 3 or more principal elements and embody the spirit of CCAs. This supports the conclusion that these conventional alloys are 3d transition metal MPEAs (Section 5.5.2, Section 5.6). This equality gives a fresh perspective on the application of 3d transition metal CCAs. Opportunities may be found by identifying critical gaps in the performance of existing commercial alloys, since the CCA field offers new approaches to modify properties in this class of alloys. The extent of the FCC single-phase solid solution (SS) phase field is broader than represented by austenitic nickel and stainless steels, offering new alloys not previously studied. The MPEA community can also learn from the extensive data on commercial alloys, especially regarding the effect of non-equimolar compositions, the influence of minor alloy additions such as C, N, Si, Mo, Nb and Ta on microstructure and properties, and the role of deformation processing.

There are also cautions in this partnership between commercial alloys and 3d transition metal CCAs. Commercial alloys represent an exhaustive amount of research and experience to satisfy an exquisite balance of requirements that go far beyond first- and second-tier properties. Efforts to displace these alloys must be approached cautiously. The cost and time to develop and certify a new alloy for commercial use are tremendous. These obstacles are often underestimated, even within the commercial realm. Better mechanical properties or improved corrosion resistance alone may give insufficient motivation to tackle these challenges. It is also a risk that extensive pursuit of the MPEA approach may end up with essentially similar alloys as are commercially in use. These comments are not intended to discourage work in this direction, but rather to frankly discuss the substantial practical barriers associated with the development and insertion of a new technology. It is important to understand the prospects of continued work, and scientific curiosity remains a powerful motivation.

None of the 3d transition metal MPEAs included in this review have strengths that compete with precipitation hardened stainless steels or nickel superalloys (Section 5.5.2). σ_y of 1st row transition metal MPEAs generally drops below 100 MPa at about 1100 K, but superalloys require strengths at this temperature of about 200 MPa for static sheet and over 600 MPa for blades. Although the maximum use temperature for superalloy disks is lower, about 950 K, the required strength is much higher, about 1000 MPa (Fig. 20a).

6.2.1.2. Refractory metal CCAs.
Refractory metal CCAs were devised to compete with nickel superalloys. Although only a small number of refractory metal CCAs have been evaluated, several show potential toward this goal (Section 5.3.2, Section 5.5.2). Possible applications include lightly loaded static parts such as thermal protection sheet as well as more highly loaded components such as turbine blades and disks. Refractory metal CCAs show the potential to increase the operating stress or the operating temperature, or both. The results to date are only cursory. Almost no tensile data are available and many other properties need to be measured for candidate alloys, especially environmental resistance. Suggested future efforts are described in Section 7.2.2.2.

The same caveats mentioned for the technology transition of 3d transition metals apply to refractory metal CCAs. However, performance improvements in transportation applications can offer more significant benefits, helping overcome the barriers. For both aerospace and land-based turbine engines, even small increases in operating temperature or strength can have substantial benefits in operating efficiency and power conversion that help offset the risks. Further, concentrated refractory alloys have not been pursued nearly as intensively as have austenitic stainless steels and nickel alloys, and so there is less risk of duplicating earlier work.

6.2.1.3. Other structural CCAs. Light metal MPEAs were conceived to compete with Al- and Mg-based structural metal alloys. Very few alloys have been made, and none yet show a combination of strength and ductility. CCA brasses and bronzes were devised to improve the strength of conventional brasses and bronzes. A list of applications that currently use brasses or bronzes, and that would benefit from higher strength, include lubricated bearings, marine-grade alloys, currency (by replacing Cu and Ni with cheaper elements such as Al, Sn or Zn), munitions casings, zippers, keys, door fixtures and locking mechanisms, plumbing hardware and fittings, chrome-able bezels, and non-magnetic watch mechanism components [112]. The light metal MPEA family and CCA brasses and bronzes are new concepts that have just been started. Neither are sufficiently developed to discuss potential toward applications. Continued work in these new areas is recommended (Section 7.2.2.3).

6.2.2. CCAs as future structural materials

We ask a simple question, "what conventional structural materials exist for which no parallel CCA activity exists?" Answering this question can inspire new CCAs. We list a few examples here, the reader is encouraged to consider other possibilities.

6.2.2.1. Potential future structural CCA families (metallic). No CCA family is currently targeted for the balance of properties displayed by titanium alloys. Broadly speaking, titanium alloys have densities, elastic moduli and use temperatures that are between Al-based alloys and steels or nickel alloys, but they have strengths that are comparable to nickel alloys [25]. These alloys fill an important role, especially in the aerospace and sports industries. This alloy family is referred to as medium-temperature HEAs, and a suggested palette of elements has been proposed [25]. Further, developing CCAs to fill the gap in density and operating temperature between titanium alloys and nickel alloys represents an important challenge that has not yet been addressed.

As a class of materials, MPEAs may have intrinsic behaviors that make them attractive as irradiation-resistant materials [226]. Alloys based on the ternary Hf-Nb-Zr system have been evaluated [225,226,323], but a broad family of alloys has not yet been defined.

Cu-Be alloys are used for their high strength (up to 1400 MPa) along with non-magnetic and non-sparking properties. They are used in specialized applications that include non-sparking tools such as hammers in hazardous industrial settings, precision measurement devices, aerospace applications and musical instruments. Be can be toxic and its use is restricted. The motivation to develop CCAs would be to produce a strong, non-magnetic and non-sparking material that is Be-free.

6.2.2.2. Potential future structural CCA families (non-metallic). A recent paper extends the high entropy concept to entropy-stabilized oxides [324]. This work shows that entropy plays a decisive role in stabilizing a high temperature, single-phase oxide in an equimolar mixture of CoO, CuO, MgO, NiO and ZnO. The cations randomly substitute on one sub-lattice while oxygen anions occupy the second sub-lattice as normal. Intermixing on a cation sub-lattice in oxide structures is not new — random cation occupancy is well-known in spinels ($H1_1$, cF56, $MgAl_2O_4$ prototype), and order-disorder transformations show this effect in feldspars. However, this recent work shows that it is now possible to stabilize a compositionally complex oxide with a single cation sub-lattice and unusual cation coordination values by controlling configurational entropy. This inspires the exploration of many more complex compounds than previously considered. Thus, the concept of dramatically expanding the number of materials in the central regions of multi-component phase space is demonstrated to include oxide compounds. Ceramic matrix composites using oxide matrices and oxide fibers are now being inserted as structural materials into aerospace applications [325,326]. We therefore include complex oxides in this assessment as a new branch of MPEA structural materials.

It is a simple step to include other ionic and covalent compounds such as borides, carbides, nitrides and silicides as structural MPEAs. MPEA efforts have included borides and nitrides from the very start [2,217,327], but those studies are often conducted on thin films and the product is often amorphous. The recent work on high entropy oxides demonstrates the concepts of complex substitution within a crystalline compound in bulk, monolithic form. Potential applications include wear-resistant coatings and diffusion barriers previously considered [11], as well as bulk products such as cutting tools and high temperature structural components.

6.3. MPEAs for functional applications

Far fewer studies have been conducted on functional properties than for structural use (Section 5.5.1). Two CCA families are currently targeted for functional applications, MPEA nitrides and borides, and precious metal CCAs. In some cases functional properties are measured on alloys designed for another purpose (for example, magnetic properties measured in 3d transition metal CCAs). Here we discuss current and future functional CCAs.

6.3.1. Existing functional CCA families

MPEA borides and nitrides are potential wear resistant coatings and diffusion barriers [2,117,123,217,327–332]. Material is usually produced by reactive magnetron sputtering or plasma nitriding of 3d transition metal or refractory metal CCAs. The influence of process parameters (gas flow rate, bias, substrate temperature) on composition, microstructure and properties are usually studied. Hardness is the most commonly measured property, but tribology [333–338] and adhesive wear resistance [123] are also reported. Properties under conditions relevant for wear-resistant coatings or diffusion barriers do not yet seem to be emphasized, making an objective assessment of the potential for MPEAs in these applications uncertain. This is a relatively small effort within the MPEA field.

A superconducting MPEA with a critical temperature, T_c, of 7.3 K has been made from refractory elements that are all superconductors [206]. A broader effort to increase T_c has not been undertaken. Thermal, electrical and magnetic properties are measured in 3d transition metal MPEAs (Section 5.1). These measurements seem to be motivated more by completeness and scientific curiosity than by the intent to develop alloys with properties that will compete with current functional materials. Precious metal CCAs are motivated by catalyst applications such as catalytic converters and water splitting, catalysts for fuel cell anodes, dental alloys, memory storage devices enabled by magnetic switching properties, and jewelry [113]. Pt is often used in these applications, and precious metal CCAs are motivated by the opportunity to achieve similar properties in alloys with reduced Pt content, and hence

significantly lower cost. Studies on these alloys have just been initiated and the potential for these applications has not yet been established.

6.3.2. Future functional CCA families

Functional materials are typically single-phase, ordered compounds of metals, semi-metals and/or non-metals. Disordered substitution on the cation sub-lattice of an ordered oxide phase is proposed as a new alloying approach in structural materials (Section 6.2.2.2). Here we extend this idea to include long-range ordered phases with intentional, complex element substitution on one or more sub-lattice in functional materials. This includes broad classes of phases such as oxides, borides, carbides, nitrides, halides, chalcogenides, skudderudites (DO_2, cI32, As_3Co), Heusler ($L2_1$, $AlCu_2Mn$, cF16), half-Heusler ($C1_b$, cF12, AgAsMg) and III-V compounds. The nature of atomic bonding in these phases can be metallic, ionic and/or covalent, though the degree of covalent bonding will usually be modest [324]. We also include as potential functional alloys more conventional CCAs with elemental substitution in disordered phases.

The list of functional applications for which there are no current CCA activities is long. A few are listed here to illustrate the breadth of opportunities for future efforts. This is only a partial list, and it is not intended to limit the scope of future functional applications of CCAs. Many of these are taken from a current review of high-throughput experiments [339].

Complementary metal oxide semiconductor (CMOS) transistors need high capacitance gate dielectric materials to reduce leakage current in very thin layers. Ternary oxides are already used for this application [339], and more complex materials offer new opportunities. Ferroelectric materials (which are also good piezoelectrics) are used in a wide range of sensor and actuator applications. Ferroelectrics are also used for tunable microwave devices for phased array antennae and other communication devices. Identifying a lead-free replacement for the commonly used ferroelectric compound $Pb(Zr,Ti)O_3$ (PZT) is an important motivation. Studies are already underway to explore site doping in pseudo-binary and pseudo-ternary ferroelectric systems such as $Ba_{1-x}Sr_xTiO_3$ and $(Bi,Sm)FeO_3$. More complex substitutions are also possible (Section 6.4.2). The parallel with the MPEA concept of equiatomic alloy substitution [19], commonly referred to as iso-structure substitution in the functional materials discipline, is clear.

Thermoelectric (TE) materials convert heat directly into electrical energy. The figure of merit is $ZT = \alpha^2 \sigma T/\kappa$ where α is the Seebeck coefficient, σ is electrical conductivity, κ is thermal conductivity and T is absolute temperature. A wide range of compounds have attractive TE properties, including bismuth chalcogenides, oxides, skudderudites and half-Heusler phases [339,340]. Here we describe the half-Heusler phase to illustrate opportunities with the MPEA approach. The half-Heusler phase has a cubic structure with four interpenetrating FCC sub-lattices. Two different transition metals typically occupy the (0,0,0) and (¼, ¼, ¼) sites, the (½, ½, ½) sites are occupied by basic metals or semi-metals such as Bi, Ga, Sb or Sn, and the (¾, ¾, ¾) sites are vacant. TE properties can be adjusted by atomic substitutions on each occupied sub-lattice [341], opening a vast range of possibilities for TE CCAs. For example, half-Heusler compositions can be listed as XYZ, where X = Au, Co, Fe, Ir, Ni, Pd, Pt, Rh or Ru; Y = Hf, Mn, Ti or Zr; and Z = Bi, Ga, Sb or Sn [342]. Complex half-Heusler phases are already being pursued, such as the five and six component alloys $Hf_{1-x}NiSb_ySn_{1-y}Zr_x$, $CoHf_{0.5}Sb_{0.8}Sn_{0.2}Zr_{0.5}$ and $Co_{1-x}Hf_{0.25}Ni_xSbTi_{0.5}Zr_{0.25}$ [343]. Other intermetallic (IM) phases offer similar opportunities for complex, concentrated substitutions in the thermoelectric field [339]. Again, this illustrates that the CCA concept of equiatomic alloy substitution is already being applied in

functional materials, but under a different name (iso-structure substitution).

It has been found that mixing complex hydride compounds can reduce the hydride formation enthalpy, significantly improving the performance of hydrogen storage materials [339]. A range of cation (alkali metals and alkaline earth elements) and anion (basic metals, semi-metals and non-metals) substitutions open up a broad, multi-dimensional composition space for exploration. Shape memory alloys (SMAs) provide a reversible change in shape as a result of a martensitic transformation. SMAs are used in aerospace and automotive components, robotics, civil structures, piping, telecommunications, orthopedic surgery and dental appliances. As many as 18 elements are known to produce SMAs, giving opportunities for concentrated alloying. Other functional materials can include thermal barrier materials, luminescent and phosphorescent materials and magnetic materials. This is only a partial list of functional materials that may benefit from an intentional application of the CCA approach.

6.4. Discussion

6.4.1. Multi-principal element alloying as a general approach to materials design

Throughout Section 6 we develop the idea that multi-principal element alloying is a general approach that can be applied to essentially any class of material for any application. This concept is implicit in early MPEA papers, but it seems to have been hidden by a focus on structural materials and on the small number of alloy families considered. We illustrate this concept here by describing diverse alloy development efforts that may be considered to use the MPEA approach. Stainless steels and nickel alloys typically have 3 to 5 principal elements and are an early manifestation of the CCA approach − even before the field was initiated (Section 6.2.1.1). Functional materials use the concept of iso-structure substitution on crystal sub-lattices, leading to complex, concentrated alloys with 3−6 elements (Section 6.3.2).

Although these classes of materials were developed independent of the MPEA philosophy, there are two important benefits from acknowledging this connection. A large amount of new data is made available to the CCA community, offering greatly expanded opportunities to explore and validate concepts between composition, structure and properties. And the functional materials community can learn from MPEA results by expanding alloying possibilities beyond the intuitive approaches currently offered by iso-structure substitution (Section 6.4.2). This connection supports a more intentional and systematic use of the multi-principal element alloying approach.

6.4.2. Expanding beyond iso-structure substitution for functional materials

As discussed in Section 6.1, selecting a palette of elements for functional materials can be guided by intuition. For example, elements with low thermal conductivity are candidates for thermal barrier materials and magnetic elements are obvious candidates for magnetic alloys. Using elements that form identical functional compounds is another widely used approach for selecting elements. For example, new thermoelectric materials are currently devised by combining elements from different half-Heusler compounds with useful thermoelectric properties, giving new half-Heusler compositions via atom substitution on selected sub-lattices with the potential for even better thermoelectric properties. However, this limits options to elements that form the same structure, giving the so-called iso-structure substitution approach. The MPEA community has demonstrated that a targeted structure or phase can be produced by mixing *different* structures or phases.

For example, CoCrFeMnNi is a single-phase, FCC SS at RT, even though the constituent elements have BCC, HCP, FCC and A12 (cI58) structures at RT. Further, the rocksalt structure (B1, cF8, NaCl) is produced when mixing oxides with rocksalt, wurtzite (B4, hP4, ZnS) and tenorite (B26, mS8, CuO) structures [324]. These different structures have different cation coordinations, and some pairs of the constituent compounds do not exhibit extensive solubility. Thus, the MPEA approach may offer new combinations of elements not currently being considered in the functional materials field. Such mixtures will be non-intuitive, and guidance from appropriate calculations and modeling tools are expected to be essential. This opens many new opportunities.

6.4.3. Single-phase, intermetallic CCAs

Single-phase, SS microstructures are a major part of the MPEA field. Multi-phase microstructures with two or more SS and/or IM phases are also included as MPEAs (Section 1.2.4 and [25,26]). In this section, we further include the essentially unexplored microstructural category of single-phase CCA ordered compounds. This includes all long-range ordered inorganic phases, representing metal-metal compounds (called IM in this manuscript) and compounds with ionic and/or covalent bonding (borides, oxides, nitrides, carbides, chalcogenides, and so on). This inclusion completes the microstructural palette of MPEAs: single-phase and multi-phase mixtures of ordered and/or disordered phases in any combination. By placing no restrictions on CCA microstructures, we take full advantage of the motivation to explore the vast, central regions of hyper-dimensional composition and phase space.

Studying single-phase CCA compounds for structural or functional applications give one motivation, but there are others. Thermodynamic properties of compositionally complex compounds may vary significantly from binary or ternary alloys (Section 2.2), but these effects have hardly been explored. Also, characterizing these phases challenges existing experimental and computational techniques. The mechanical properties of MPEAs are expected to depend sensitively on the presence and volume fraction of IM phases [26], and isolating the properties of these compositionally complex IM phases may give useful information in guiding both theory and alloy development. Addressing each of these basic scientific issues gives additional motivations for studying single-phase MPEA compounds.

6.5. Summary

Throughout this section, we develop the idea that CCAs can be developed for any application where materials are used. This idea is supported by discussion of the general approach for designing CCAs for a targeted application. It is further supported by specific examples of well-known commercial alloys and current alloy development efforts that use the CCA approach and produce alloys consistent with the CCA intent. This broadens discussion beyond applications suggested by current MPEAs to also include many other applications for which CCAs are not yet being studied. A few structural materials are suggested, and many functional applications are recommended for future studies.

Analysis of commercial stainless steels (austenitic, duplex, precipitation hardened) and nickel alloys (austenitic, superalloys) shows that these are 3d transition metal CCAs (Section 6.2.1.1). This equivalence helps focus efforts to develop 3d transition metal CCAs for structural applications by looking for technology gaps in the current use of these alloys. It also provides new information to the MPEA community by including the vast amount of practical experience and engineering data from these commercial alloys as part of the 3d transition metal dataset.

Commercial nickel-based superalloy properties are used to evaluate the potential for CCA applications as high temperature structural metals. 3d transition metal properties do not compete with this class of materials (Section 6.2.1.1). Refractory metal CCAs are still rather immature, but nevertheless show potential to increase the operating strength, the operating temperature, or both, relative to superalloys (Section 6.2.1.2). Applications may include static sheet and rotating hardware such as disks and blades. The data are still cursory, and more work is needed to better support this potential (Section 7.2.2.2).

Work in the remaining two CCA families inspired by structural applications — light metal CCAs (to replace Al- and Mg-based alloys) and CCA brasses and bronzes — has just begun (Section 6.2.1.3). There is insufficient data to evaluate their potential in the respective application domains.

To inspire new CCA families, a challenge is offered to consider existing classes of structural metals for which a parallel CCA activity does not yet exist (Section 6.2.2.1). MPEAs that can compete with titanium alloys; that can fill the density and use temperature gap between titanium and nickel alloys; that offer new radiation-resistant alloys and Cu-Be alloys are suggested for consideration, but other possibilities may also exist.

A recent paper on entropy-stabilized oxides introduces ionic compounds to the MPEA field (Section 6.2.2.2). This expands earlier work on thin films and coatings of 3d transition metal nitrides and borides to now include bulk, monolithic MPEA compounds with ionic or covalent bonding. Bulk, monolithic oxides, borides, nitrides and carbides are described here as a new class of CCA structural materials.

MPEA work seems to be primarily motivated by structural applications, and much less work is targeted at measuring properties for functional applications. Electrical, thermal and magnetic properties have been measured in 3d transition metal MPEAs, and superconducting properties of a refractory metal CCA are reported (Section 6.3.1). None of these properties are exceptional, and efforts to develop particular alloys with a balance of properties needed for these functional applications are not apparent. Wear properties have been measured for 3d transition metal nitride coatings, and a few MPEAs have been evaluated as diffusion barriers. Work on CCAs as catalysts and jewelry is just beginning and no data are yet published.

Functional applications give broad and relatively unexplored opportunities for new CCAs (Section 6.3.2). A few are briefly mentioned here (semi-conducting applications for computer chip technology; ferroelectrics for sensors, actuators and communication devices; thermoelectric materials; shape memory alloys; hydrogen storage; thermal barrier materials; and magnetic materials), the reader is encouraged to consider others.

An alloying strategy used in functional materials (iso-structure substitution) mixes elements from different compounds with the same structure, producing a new composition with the same structure via substitution on selected sub-lattices. Many alloys produced by this approach represent complex, concentrated materials, even though that is not the intent of the studies. A more systematic use of the CCA approach is suggested here that does not limit candidate elements to iso-structural compounds (Section 6.4.2). This broader approach is validated by data collected in the MPEA field.

Consideration of functional materials expands the CCA field to include microstructures consisting of a single-phase ordered compound (Section 6.4.3). This completes the microstructural palette to include single-phase disordered solid solutions, single-phase ordered (including IM) compounds, and microstructures with a mixture of any number of disordered and ordered phases.

7. Future work

There is much to do in the field of multi-principal element alloys (MPEAs). Suggestions for future work are summarized here with cross-references to additional discussion elsewhere in this review. Suggestions are organized under two themes: basic scientific studies (Section 7.1) and application-driven efforts (Section 7.2).

7.1. Basic scientific studies

7.1.1. Vastness of composition and microstructure space

A bolder, more expansive exploration of the vastness of alloys is essential. This remains the most compelling idea in the complex, concentrated alloys (CCAs) field. The potential for new discoveries associated with this concept has hardly been scratched. Thirty-seven elements have been used to date in CCAs (Section 3.1), giving 435,897 possible 5-element combinations and a total of 2,834,496 alloy systems with 3−6 elements. Considering the 72 elements that are not toxic, radioactive or noble gases, the number of 5-element systems expands to 13,991,544 and the number of systems with 3−6 elements explodes to 171,318,882. Roughly 400 MPEAs have been reported to date, and many of those are non-equimolar variations of the same elements, giving only 112 different element combinations considered so far.

In this review, compositional complexity is shown to include not only metallic alloys, but also bulk materials where ionic and/or covalent bonding are important. Nitride, boride and carbide MPEAs have been studied from the start (Section 3.2.3), but primarily as thin films. Inspired by work on high entropy oxides [324], the present review shows that CCAs include any long-range ordered inorganic compound in bulk form (Section 6.2.2.2). This includes intermetallic compounds (IMs), as well as compounds where ionic and/or covalent bonding exists. This opens an enormous range of new materials to explore via the CCA approach.

The expansiveness of the CCA field also includes microstructure. High entropy alloys (HEAs) emphasize microstructurally simple alloys (Section 1.2.4), defined as single-phase, solid solution alloys with 'simple' crystal structures (BCC, FCC, HCP or their ordered derivatives) (Section 4.1.1). Motivated by the broad field of functional materials (Section 6.3.2) and basic scientific studies (Section 6.4.3), microstructurally simple alloys are expanded to include single-phase microstructures of complex disordered solid solution (SS) or ordered compound phases (Section 4.1.4). CCAs also include multi-phase microstructures with two or more phases that are SS, ordered compounds (including IM phases), or a mixture of these two (Section 4.1.5). Phase volume fraction can be controlled by alloy composition (Section 5.3.1.2), and phase size, spacing and distribution can be controlled by deformation processing or thermal treatment (Section 5.5.2). When understood and controlled, microstructural complexity produces alloys with an exquisite balance of properties, especially in structural materials. The CCA field thus includes an expansive range of microstructures with any number and any type of phases.

Future studies that boldly embrace and explore this expansiveness are required. Such boldness is shown in a pioneering CCA paper that studied equimolar 16- and 20-element alloys [1]. A key discovery from that paper is the single-phase, SS CoCrFeMnNi alloy with exceptional properties (Section 5.3.1.3). This discovery inspires a general approach to explore complexity in Section 7.1.2.3, and specific directions for applying this approach are discussed in Section 7.2. To accelerate the exploration of complex compositions and microstructures, the CCA community is encouraged to develop and apply high-throughput computations and experiments (Section 7.1.2) and to include data on complex, concentrated materials from other fields. The entire field of stainless steels, austenitic nickel alloys (Section 6.2.1.1) and functional materials produced by iso-structure substitution (Section 6.3.2) are such examples. Including data from these fields can help build new relationships between composition, microstructure and properties of CCAs (Section 6.4.1), accelerating progress in the field.

7.1.2. High-throughput techniques

The vastness of compositions and microstructures is both the most compelling reason to study CCAs, and the largest challenge offered by the field. It is impossible to evaluate such huge numbers of alloy systems in the time available using traditional methods. High-throughput, combinatorial techniques are needed to enable the full potential of the CCA field to be realized. Such approaches are already widely used in functional materials [339,344−346]. In fact, many conventional functional materials are MPEAs, especially many of those produced by elemental substitution on one or more sub-lattice of ordered crystals (Section 6.3.2, Section 6.4.1). Current high-throughput tools are therefore useful for continued development of functional MPEAs.

Some useful high-throughput experimental techniques already exist for structural materials, especially for microstructural characterization [31]. Composition, simple crystal structures and crystallographic texture can be obtained in an automated, high-throughput fashion on conventional scanning electron microscopes with appropriate sensors and software. Nano-indentation gives localized hardness and modulus values, which can be correlated with strength. However, the indents are very small, and may not represent strengths that rely on microstructural features beyond a few hundred nanometers. Bulk hardness measurements are better for assessing strength in microstructures at these length scales, but producing materials libraries is a challenge.

Structural materials offer major, unmet challenges for high-throughput techniques [25,26,31]. The main issue is that structural properties depend sensitively on microstructure, limiting the utility of conventional high-throughput tools. The vastness of compositions offers other challenges. These challenges suggest three future research directions described below: development of new high-throughput experiments for structural materials; high-throughput calculations to rapidly assess and design structural materials; and new approaches to produce structural materials libraries. Progress in all three directions is needed, and these advances must be integrated with each other to offer full benefit. Each of these topics represents vibrant scientific endeavors in their own right, and the MPEA field is the ideal platform for developing, validating and applying these new techniques.

7.1.2.1. New high-throughput experiments for structural materials.
New high-throughput experiments are needed to evaluate microstructure-sensitive properties for structural materials. Essential properties include tensile strength (yield and/or ultimate), tensile ductility, fracture toughness, creep and fatigue. The actual property doesn't need to be quantified as long as a correlation is established between the measurement and the required property. Thus, a test that establishes the 'capacity for plasticity' is useful if it is correlated with tensile ductility, and the 'capacity for strength' can be correlated with tensile yield or ultimate strength. Such correlations are commonly used to relate hardness to strength. These correlations distinguish a successful test from an unsuccessful one. In addition to the two tests just mentioned, tests that measure responses that correlate with primary creep strain, secondary creep rate, fatigue crack growth rate or mode I fracture toughness are all useful future contributions.

Structural materials also depend on structure-insensitive properties. Environmental resistance is needed for nearly all structural applications, and can include aqueous corrosion, erosion

resistance, high temperature oxidation or the ability to withstand radiation damage. High-throughput, accelerated tests for such properties would be very valuable. Calorimetry gives important information on phase transformation temperatures. Characterizing melting (including both solidus and liquidus) is particularly important, since it is essential in the primary production of most metals and is also important for joining and repair. Parallelized techniques are being developed [347], but higher throughput and higher temperatures are still needed.

The properties listed above are not exclusive, and other properties may also be useful in structural metals. By definition, these methods must be very fast and inexpensive, at least 100 to 1000 times better than conventional techniques. Microstructure complicates this challenge by setting a length scale that limits the ability to miniaturize tests [25,26,31]. It also becomes a new variable in the search for an effective structural material (Section 7.1.2.3), increasing the number of high-throughput tests required. A recent paper suggests a sequential approach to improve the efficiency of high-throughput experiments for structural materials [31]. After an initial stage of computational screening, candidate alloys are first evaluated experimentally for properties that depend primarily on composition but do not strongly depend on microstructure. This allows a large number of candidates to be screened quickly, since time and effort are not needed to ensure the materials library has a microstructure that is optimized for the properties being measured. This also reduces the number of candidates, decreasing the number of alloys that need to be evaluated in the second experimental stage, using materials libraries of fixed composition and controlled microstructure gradients. This new strategy for high-throughput experiments is discussed in more detail elsewhere [31].

7.1.2.2. High-throughput computational design of structural materials.
High-throughput computational materials design offers new tools to explore the enormous space of possible materials in search of desired properties. It combines quantum mechanical and thermodynamic computations with database construction and intelligent data analysis techniques [348]. Materials databases are being constructed to support this need [36,170]. This field represents a vibrant scientific activity that is already making important contributions to the discovery of new materials [349,350]. However, as with high-throughput experiments, the vast majority of work is on functional materials such as thermoelectrics, batteries, and photovoltaics. Additional emphasis on structural materials is suggested. Further, the work to date emphasizes binary and ternary inorganic compounds, and the CCA field establishes a need for materials that are compositionally much more complex.

The CALculated PHAse Diagram (CALPHAD) method has been used to explore complex, concentrated structural materials [56,125]. CALPHAD is a semi-empirical approach that uses thermodynamic databases to calculate phase diagrams (Section 4.3.2.4). A database is typically built for an alloy system with a single dominant element such as Al, Fe, Ti or Ni. When used for alloys within the targeted system, calculations are reliable and are used extensively in the metals industry. However, extrapolation to complex, concentrated alloys requires some care. Current experience suggests that the number and type of phases predicted are often reliable, but transformation temperatures, volume fractions and phase compositions are less accurate. Work is underway to establish credibility criteria (Section 4.3.2.4). Efforts to estimate uncertainties in reaction temperatures, phase compositions and volume fractions are needed.

There are no high-throughput computational tools that can predict microstructures and their contributions to mechanical properties. In the long term, such capabilities will make an essential

contribution. The search for complex relationships in existing data may be useful, but databases and search routines need to be built and made available to the materials community. The Materials Genome Initiative provides a framework for pursuing such goals [349].

7.1.2.3. New materials libraries for structural materials.
Current materials libraries are heavily biased toward thin films with thicknesses less than 1 μm. This supports the combinatorial search for functional properties, but structural materials may require more bulk-like materials libraries, especially if the structural properties depend on microstructural features that can't be produced in thin films [31]. Additive manufacturing is a developing field that offers new capabilities to produce materials libraries with continuous composition gradients in a thicker product. Efforts to develop this capability are suggested.

Given the vastness of alloy systems, continuous composition gradients may not be the only architecture for CCA materials libraries. Current libraries usually vary up to 5 elements, which is useful to explore a single CCA system. However, a typical CCA family has 9 elements (Section 3.2), some have a dozen or more elements [25], and recent high-throughput CALPHAD calculations of over 130,000 equimolar alloys use 27 elements [56]. Clearly, new approaches are needed for materials libraries that can deal with the large number of elements. High-throughput calculations dramatically reduce the number of alloys that need to be made, but the candidate alloys found by computations may have non-contiguous compositions (for example, see Tables 9–15 in Ref. [56]). This suggests an 'alloy-on-demand' approach, where distinct concentrations and combinations of elements are produced at each point in a materials library. Adjacent points in the library may have a discontinuous change in concentrations, including completely different elements. Additive manufacturing may be able to produce such 'alloy-on-demand' libraries.

Microstructure exerts a potent influence on the properties of structural materials and must be included in a combinatorial search. Finding alloys with desired phases is an essential first step. Here we suggest an approach inspired by one of the first MPEA papers [1]. In that work, the FCC solid solution CoCrFeMnNi phase dominates the microstructure of a 16-element equimolar alloy. The formation of a 5-component SS phase is remarkable, and the HEA field has focused on alloys in this family (Section 3.2.1). However, 4368 five-element combinations exist in the 16-element alloy, and 4367 of them did not form a SS phase. Further, the 5-element SS that does form is more stable than any competing 4-element or 6-element SS in that alloy. Stated simply, a complex alloy shows at once which phase or phases are the most stable in a very long list of competing phases. The useful information from such a sample includes the phases that form (and their compositions), as well as those that do not. The design of single-composition bulk samples that are compositionally very complex is a new way to think about a materials library. This approach can use as few or as many elements as desired. Care is taken to produce a chemically equilibrated and microstructurally uniform material with no intentional composition gradients. Element selection can be guided by the search for SS or IM phases. It can emphasize particular crystal structures, particular regions of the periodic table, or elements with similar characteristics. An obvious suggested first step is to combine all the elements in other structural metal alloy families (for example, the 10 elements in the refractory metal CCA family) to see if any SS phases form. Such phases can be an alloy by itself, or the matrix of precipitation-strengthened microstructures.

The combinatorial search for structural materials also requires libraries with microstructure gradients. Two such examples already exist — the well-known Jominy bar varies quench rate and a

double-cone sample, when forged, produces a deformation strain gradient [25]. Other concepts can be devised, including the use of rods or sheet in furnaces with controlled thermal gradients to vary solution or aging temperatures [31]. This approach can be combined with a composition gradient to explore the effect of composition and heat treatment on microstructure in a given alloy family. For example, a sheet can be produced with a composition gradient along one direction, and the thermal gradient can be applied along the second major direction of the sheet. One sample can thus explore the effects of both composition and heat treatment on microstructure.

7.1.3. Solid solution hardening models

There is no adequate model to predict solid solution strengthening in CCAs (Section 5.5.3, Section 5.6). This is a major scientific challenge. At least three contributions (lattice distortion, elastic misfit and a chemical term) need to be addressed in a structure where no single element dominates, so that there is no simplifying 'solvent' or 'solute'. This is also a significant practical barrier to the informed development of CCA structural alloys. Focused efforts to build validated, physics-based models for solid solution strengthening in concentrated, multi-element alloys are highly recommended.

7.1.4. Deformation mechanisms in CCAs

Almost no work has been performed on the deformation mechanisms in CCAs. Initial studies in CoCrFeMnNi show that the slip systems are the same as for conventional FCC metals (Section 5.3.1.2), but similar work has not been performed in BCC metals. Nano-twinning is an important deformation mechanism, but its generality has not been established. A novel FCC + B2 eutectic microstructure has unusually low yield strength, and the mechanisms responsible for this are not yet known (Section 5.3.1.2). The atomic structure of CCAs raises questions at a more fundamental level. Are lattice strains sufficient to influence dislocation core structure or dislocation motion? Can local chemical variations produce local variations in core structure or stacking fault energies, and hence differences in separation between leading and trailing partial dislocations? These questions suggest future experimental and computational research.

7.1.5. Diffusion data and models

A better understanding of diffusion is essential in MPEAs. Diffusion data and models are needed to better understand practical features such as grain growth, nucleation and growth of strengthening phases, thermally-activated deformation and oxidation resistance in CCAs. An empirical model suggests that diffusion coefficients are the same in all metals with the same crystal structure when compared at their melting temperatures, but the assumptions that underlie this model may not be valid in CCAs (Section 5.2). Finally, sluggish diffusion is one of the four major MPEA hypotheses. In spite its importance, diffusion has been measured in only one MPEA study, and for only one alloy [32]. More diffusion studies are needed to establish basic features and to provide practical data for the development of CCAs.

7.1.6. Thermodynamics of complex, concentrated phases

In spite of the fact that a thermodynamic term (entropy) is a defining quantity of HEAs, there is very little thermodynamic knowledge of complex, concentrated phases. Idealized models are often used to guide research or to support analyses, but these may be poor guides to understand the thermodynamics of CCA phases (Section 2). For example, SS phases are usually modeled as ideal or regular solutions, and IM phases are thought of as structures where a single element dominates a particular sub-lattice. None of these assumptions commonly hold in CCAs. The degree of chemical short-range order (SRO) influences the entropy (S^{SS}) and enthalpy (H^{SS}) of complex, concentrated SS phases and needs to be included in SS models. In IM phases with more elements than sub-lattices, the configurational entropy (S^{IM}) can be a significant fraction of the SS phase with the same composition, and H^{IM} can be very different from binary compounds upon which the IM is based. The thermodynamic properties of complex phases need to be measured and modeled.

A more thorough analysis of individual contributions to total entropy is recommended. The relative magnitudes of excess entropy contributions from size misfit, vibrations, electronic and magnetic terms need to be quantified and their influence on the competition between different phases needs to be evaluated (Section 2.3.4)

7.1.7. Characterizing complex, concentrated phases

Measuring CCA thermodynamic properties is no more challenging than for compositionally simpler phases and alloys. However, characterizing the structure of CCA phases can be daunting. Distinguishing between disordered and ordered phases in MPEAs requires more care than is typically needed for compositionally simpler phases (Section 4.4.1.4). X-ray diffraction (XRD) is often inadequate to distinguish between ordered and disordered phases with the same base crystal structure, and transmission electron microscopy (TEM) often finds phases missed by XRD alone. Future studies are highly encouraged to characterize microstructures with a combination of XRD and TEM for a more complete and reliable analysis.

Section 7.1.6 requires additional structural details. Measuring SRO can distinguish ideal and regular solutions from sub-regular solutions (Section 2.1.1). The degree of SRO requires knowledge of the type and number of 1st neighbor atoms surrounding a given reference atom. This is difficult to measure, and the complexity increases dramatically with increasing number of elements. Techniques such as X-ray absorption spectroscopy offer measurement approaches. Measuring which atoms occupy which sub-lattices, and to what degree, is important for IM phases in CCAs. In addition to supporting thermodynamic models, knowing site occupancy in IM phases or SRO in SS phases is essential to understanding other properties such as stacking fault energies, interface energies and critical resolved shear stresses. This is also of key importance in developing and modeling functional materials.

7.1.8. Lattice distortion

Lattice distortion is one of the four HEA hypotheses, and it may influence thermodynamic stability, deformation mechanisms and a wide range of properties (Section 1.3.3.2). The MPEA community is encouraged to develop approaches to quantify lattice distortion experimentally and to predict its magnitude in models (Section 4.4.4). Efforts to systematically isolate these effects from other features of CCAs and to establish relationships between lattice distortion and properties are an area for future work.

These characterizations are all extremely challenging. A partnership between more than one experimental technique is often beneficial, as well as integration with computational tools [59]. Such approaches are recommended in the future as an emphasis.

7.2. Applied studies

Much of the early work has explored their broad features and

potential as a class of materials, but MPEAs have passed their first decade as a new idea and a time has come to include more focused efforts to develop particular alloys for specific uses. Any application for which a material can be developed is a candidate for future CCA use. Application-driven future studies are described below for functional (Section 7.2.1) and structural (Section 7.2.2) materials.

7.2.1. Functional materials

CCA functional materials are nearly unexplored (Section 6.3). Two current alloy families are motivated by functional applications, but one has only recently been defined with no published results and the other is a minor area (Section 6.3.1). Conventional functional materials efforts have developed complex, concentrated alloys (Section 6.3.2), but the alloying strategy used (iso-structure substitution) is limited and a more systematic application of CCA concepts may significantly expand opportunities (Section 6.4.2). Three broad areas are recommended for future development of functional CCAs. Continued work on the two MPEA families of functional materials (precious metals, borides and nitrides) is encouraged. Pursuit of new functional applications from within the CCA framework is strongly recommended — a wide range of functional applications have not been addressed by the MPEA community. Finally, new approaches to broaden alloying in functional materials beyond iso-structural site substitution are encouraged. These new approaches are inspired by the finding in the MPEA field that a single target crystal structure can be produced even when mixing elements or phases with different crystal structures (Section 6.4.2). This is a nuanced approach, and requires insights from theory, computations, and experience within the traditional functional materials discipline.

7.2.2. Structural materials

7.2.2.1. 3d transition metal MPEAs.
The most mature MPEA structural alloys are in the 3d transition metal family. Work has focused on exploring compositions, characterizing the phases present and measuring 1st tier mechanical properties. First tier tensile properties are available on chemically and microstructurally homogeneous material in the most widely studied alloys, and some 2nd tier properties (fracture toughness, fatigue) are reported (Section 5.3.1). Current 3d transition metal MPEAs show no major advantage over existing commercial stainless steel alloys, and do not compete with either solid solution or precipitation strengthened nickel superalloys (Section 5.5.2). More detailed characterization of this family of alloys is therefore not expected to show great promise from an application point of view, and is not considered a high priority for future studies.

Future studies may be pursued in the microstructural control of 3d transition metal CCAs. Systematic trends of increasing strength and decreasing ductility are established in duplex, BCC + FCC microstructures (Section 5.3.1.2, Section 5.5.2). Specific elements, especially Al, are shown to directly influence the fraction of BCC and FCC phases. Other phases may have similar effects and may also be explored. Studies to determine FCC and BCC volume fractions with a competitive balance of strength and ductility may be pursued. Careful microstructural characterization may show the presence of the ordered B2 phase in addition to BCC (Section 4.4.1.5). No work has yet been performed to control the size, shape and distribution of FCC and BCC phases. Deformation processing and thermal treatment may provide this control. Extensive experience on commercial duplex stainless steels can guide these studies [30]. Duplex stainless steels have roughly equal volume fractions of austenite (FCC) and ferrite (BCC) phases, giving yield strengths

roughly twice that of 300-series austenitic stainless steels with good ductility. These commercial alloys will not only guide development of duplex BCC + FCC CCAs, they also give the properties against which progress will be measured.

Precipitation strengthening is a second approach to design 3d transition metal CCA microstructures (Section 5.5.2). There are relatively few studies in the MPEA literature to control the type, volume fraction, size and distribution of precipitates to give both high strength and useful ductility (Section 4.2.2). The role of particular elements in forming phases such as L1$_2$ (cP4, Cu$_3$Au) is sufficiently established to guide the design of precipitation-strengthened microstructures. Al, Ti or Nb are used in commercial precipitation-strengthened stainless steels [30], and this experience can also guide MPEA studies. CALPHAD calculations also offer a major opportunity for the intelligent design of precipitation-strengthened 3d transition metal MPEAs. Early results show that nanometer-sized precipitates are possible, and are often coherent with the matrix (Section 4.2.2). Early aging studies show some promise, but future work should start with homogenized material and then solutionize, quench and age the alloy (Section 5.5.2).

Discussion of future research on 3d transition metal CCAs ends with a caution. Commercial stainless steels include four alloy families: austenitic solid solution alloys; martensitic alloys; duplex (austenite plus ferrite) alloys; and precipitation-hardened alloys. Commercial nickel alloys include solid solution and precipitation-aged alloy families. These are all concentrated alloys based on Cr-Fe-Ni. They represent well-established CCAs with exhaustive previous research and practical experience (Section 5.5.2). They set very high standards against which future MPEA research must be evaluated. The mechanical properties of solid solution commercial alloys are compared with 3d transition metal MPEAs in Section 5.3.1.2. The properties of precipitation-strengthened stainless steels are much higher — yield strengths range from 1000 to 1400 MPa, ultimate strengths range from 1200 to 1500 MPa and tensile ductility ranges from 2 to 10% [30]. The prospects for new discoveries certainly exist, but may be less promising than in other CCA families that do not have competing commercial alloys already established. As a starting point, 3d transition metals are the basis for many new alloys predicted to have potential as high-temperature structural metals [56]. These alloys include elements not typically used in commercial stainless steels or austenitic nickel alloys, and so may give new and useful results. A thorough knowledge of the physical metallurgy, compositions, microstructures, processing and properties of commercial stainless steels and nickel alloys is suggested as required reading for researchers in the 3d transition metal MPEA field [30,314].

7.2.2.2. Refractory metal CCAs.
Refractory metal CCAs are motivated by high temperature structural applications. There are no concentrated, commercial refractory metal structural alloys for comparison, and so refractory metal CCAs compete with nickel superalloys. Only 7% of the CCAs in this review are in the refractory metal family (Section 3.2.2). They are therefore less mature than 3d transition metal alloys, and there are many directions for future efforts. Several of these are described below.

Only 29 refractory metal CCAs are found in this assessment, and so exploring new element combinations and concentrations is essential. The full extent of the BCC solid solution phase field has not been explored, giving new opportunities for research. For example, the alloys AlNbTaTiV, HfMoNbTiZr, HfNbTaTiZr, MoNbTaVW and NbTiVZr are all single-phase BCC SS alloys (Table 7). All of the elements in the refractory metal CCA palette are included in

these alloys, except for Cr. However, the alloy AlHfMoNbTaTiVWZr has not yet been studied. Such a complex SS phase would be remarkable.

Future compositional studies are also needed to control microstructures. There is hardly any work to control the type, volume fraction, size, morphology or distribution of second phases in refractory metal CCAs (Section 5.6). Establishing the bounds of the BCC SS phase field for non-equimolar concentrations is essential to guide the design of multi-phase microstructures by informing the search for 2-phase, BCC + BCC microstructures and precipitation-hardened refractory metal CCAs. For example, AlNbTaTiV with 20 at.% Al is single-phase BCC, while AlMo$_{0.5}$NbTa$_{0.5}$TiZr, also with 20 at.% Al, is a 2-phase microstructure with an elegant distribution of coherent, nanometer-sized BCC cuboids surrounded by nanometer-sized B2 (cP2, ClCs) platelets [141,142]. This alloy has attractive mechanical properties, even though the BCC phase appears to be discontinuous. It is unknown how small compositional variations might alter this microstructure and mechanical properties. Such studies are worth considering.

Exploration of compositional variations is also recommended to more directly control refractory metal CCA properties. The refractory element palette covers a very wide range of elemental densities, moduli and oxidation characteristics, giving a broad scope to tailor these properties in alloys (Section 3.2.2). This has been used to develop low density refractory metal CCAs, but additional opportunities exist, especially for oxidation resistance.

Tensile characterization is highly recommended for future research (Section 5.5.2, Section 6.2.1.2). Several alloys show good compressive strength with sufficient compressive ductility (≥10%) to warrant tensile tests. Other properties are also recommended in selected alloys, such as fracture toughness, creep and fatigue. Oxidation resistance is a major concern in any refractory metal alloy (Section 5.5.2), and should be evaluated early in the search for new alloys [31]. In the spirit of rapid assessments (Section 7.1.2.1), simple tests to screen for catastrophic oxidation may quickly eliminate alloys from further consideration, saving time otherwise spent on characterizating the alloy. Oxidation has the additional advantage of being relatively insensitive to microstructure, so that a failure to pass in one microstructural condition is likely to represent failure in other microstructural conditions.

Thermo-mechanical processing of refractory metal CCAs has hardly been explored (Section 5.5.2). Cold-rolling has been demonstrated in one study [287] but otherwise has not been used. Future research on deformation processing and its effect on microstructure and properties of refractory metal CCAs is suggested.

7.2.2.3. Other structural CCAs. Very little work has yet been published in the light metal CCAs and CCA brasses and bronzes (Section 3.2.3). Future work in both families is strongly encouraged. Focused work to define and explore MPEAs to compete with titanium alloys and work to explore MPEAs for radiation-resistant applications is also suggested (Section 6.2.2.1). The possibility of non-metallic MPEAs (Section 6.2.2.2), inspired by a recent paper [324], is a new direction for research with importance for both structural and functional applications.

We close this section with a quote from Section 6.2.2: "What conventional structural materials exist for which no parallel CCA activity exists?" The answer to this question may also be a direction for future research.

8. Major accomplishments and concluding remarks

Main findings from the present assessment are given in summaries at the end of each major section in this review. Readers are referred to these sections for topical summaries and specific results. Concluding remarks are given here discussing insights gained from the major achievements in the field over the first 12 years of effort.

8.1. Major new ideas from high entropy alloys and related concepts

Two major ideas define the field of high entropy alloys (HEAs) and the related concepts of multi-principal element alloys (MPEAs) and complex, concentrated alloys (CCAs) [8] (Section 1.3). One idea is to explore the inconceivably vast number of materials offered by MPEAs, and the second is that high configurational entropy may favor formation of single-phase, solid solution microstructures. The high entropy concept, perhaps more than the concept of vastness, has sparked the intellectual curiosity of the scientific community and is responsible for opening this major new topical area. Concluding remarks on these two major ideas are offered below.

8.1.1. Vastness of composition and microstructure space

The first idea — exploring the vast, unexplored central regions of multi-principal element phase diagrams and microstructures — remains the most compelling reason for research in this field. This vastness has grown to include three dimensions: compositional complexity, microstructural complexity, and the full range of any application for which a material can be made or used (Section 7.1.1, Section 7.2). Although often thought of within a framework of metallic alloys, the field now includes alloys and phases with metallic, covalent, and/or ionic bonding (Section 6.2.2.2, Section 6.3.2). This cosmic vastness supports the expectation for new discoveries of scientific and practical benefit. Many scientific questions in this field challenge conventional knowledge and require re-evaluation of basic concepts in thermodynamics, dislocation theory, strengthening models, phase stability and combinatorial methods. New structural and functional materials with attractive properties and potential for further development have been conceived and developed through the multi-principal element approach. Commercial materials with three or more principal elements, developed empirically before the HEA field began (stainless steels, nickel alloys, some functional materials) are shown here to be MPEAs, validating basic concepts of the field and paving the way to future efforts.

8.1.2. The high entropy effect

The second major idea is that configurational entropy can be used to control microstructure, and especially to favor disordered, solid solution (SS) phases with simple crystal structures (BCC, FCC or HCP) (Section 1.3.3). This is the signature concept of the HEA field. This assessment concludes that configurational entropy alone does not have a dominant role in favoring single-phase microstructures or SS alloys with simple crystal structures (Section 4.4.3). But what does this mean? Of course configurational entropy is important in selecting equilibrium phases. The present work does not show that entropy is unimportant, but rather that it is not the only important term. The competition between SS and ordered intermetallic (IM) phases is decided by four thermodynamic terms (entropy and enthalpy of SS and IM phases). Each of these four terms can be significant in CCAs, so that no single term consistently dominates (Section 2.3.5) and phase selection is ultimately determined by relatively small differences between these four larger

---

[8] To acknowledge common usage in the literature, we use the term, HEA, when configurational entropy or single-phase, SS microstructures are important. We use the terms MPEA or CCA interchangeably to evoke the vastness of compositions and microstructures without any implications regarding the magnitude or importance of configurational entropy or the types of phases present (Section 1.2.4).

values. Further, entropy and enthalpy are not independent – both depend strongly on alloy composition, complicating attempts to isolate the effect of individual thermodynamic terms.

An enduring contribution of the HEA field is to bring entropy into the discussion after decades of apparent neglect. A quick review of classical thermodynamic literature suggests that enthalpy has had a favored position, especially regarding collection of thermodynamic data [54,62,64,351] and approaches to predict stable phases [170,348,352]. Relatively little has been said about the role of entropy until recently. The HEA field thus highlights a previously underappreciated thermodynamic contribution. Although the role of configurational entropy has been known since the time of Gibbs, there have never been focused, systematic attempts to use it to influence microstructure. The HEA field has inspired a new way to think about configurational entropy and its influence on equilibrium phases. Since entropy is magnified by temperature, it also gives a new way to influence phase transformation temperatures. In fact, recent work shows that phase transformation temperatures can be controlled in high entropy oxides by controlling configurational entropy [324]. This is exactly one of the roles proposed earlier for configurational entropy [25]. Through research inspired by the high entropy concept, a clearer understanding has emerged on the role of configurational entropy, its partnership with enthalpy, and its measurable influence on phase stability.

8.2. Major accomplishments

Here we give summary comments of the most significant achievements from the first 12 years of work on HEAs and related concepts. Many of these accomplishments appear in the literature, a few are shown in this review for the first time. All are discussed in more detail in preceding summary sections and elsewhere in the review.

8.2.1. Define and explore seven new alloy families

The field has grown from a strong initial focus on one alloy family (3d transition metal MPEAs) to include a total of 7 alloy families (Section 3). Each alloy family includes six to ten elements, and together these have produced over 408 new alloys based on 112 never-before-tried combinations of principal elements. Every one of these is an uncommon accomplishment in materials science. Each month, over the past 12 years, the field has created on average nearly 1 new combination of elements and 3 new alloys (different element concentrations within each combination of elements). The rate is accelerating – four new systems were first reported in the past two years. A specific motivation underlies each new alloy family. Four are designed for particular applications (high temperature structural metals, low density structural metals, brasses and bronzes with improved strength, catalytic materials with reduced cost) and one is inspired by scientific curiosity (single-phase HCP alloy). Some of the new alloys show potential to achieve properties that may exceed existing materials and fill important needs. This accomplishment shows progress toward one of the major MPEA concepts – to offer a vast number of new alloy systems (combinations of elements) and even more alloys (variations of element concentrations within an alloy system).

8.2.2. Identify and explore an expansive FCC single-phase field

The HEA community has identified and explored an expansive FCC single-phase field in the 3d transition metal alloy family (Section 4.2.1). This phase field extends much farther in hyperdimensional composition space than hinted at by previous experience with austenitic stainless steels and nickel alloys. Using CoCrFeNi as a base, the influence of Cu, Mn, Mo, Pd and V has been explored in equimolar and non-equimolar concentrations,

separately and in combinations. The influence of compound-forming elements Al, Si, Sn and Ti has also been studied. The extent of the FCC single-phase field is established for most of these elements. A single-phase FCC microstructure is retained in equimolar alloys with as many as 6 elements (CoCrCuFeMnNi), and in alloys with as many as 7 elements in non-equimolar concentrations. Functional and mechanical properties have been measured on some of these alloys. This is a major accomplishment of the HEA effort. In addition to this 3d transition metal FCC phase field, at least 12 other single-phase fields have been identified, including two additional FCC phases in 3d transition metal CCAs and an FCC phase in light metal CCAs; five BCC phases (two in 3d transition metal CCAs and three in refractory metal MPEAs); and four HCP phase fields (Section 4.4.1.4).

8.2.3. High-throughput calculations predict nearly 200 unexplored alloys

High-throughput calculations are being used to accelerate the discovery of new CCAs (Section 4.4.5). Two different computational methods are used, identifying nearly 200 potential high temperature structural alloys. Criteria used to select these alloys include: single-phase solid solution alloys; multi-phase alloys that can be precipitation strengthened via solution-treatment, quench and aging thermal treatments; and projected use temperatures. High throughput calculations are also enriching knowledge of the types and numbers of phases formed. Both computational methods predict that the fraction of alloys that are single-phase solid solutions decrease as the number of elements increases, helping to resolve the high entropy hypothesis.

8.2.4. A comprehensive assessment of the types and number of phases is available

A comprehensive evaluation of CCA microstructures is given in this review (Section 4). We analyze the types of microstructures (SS phases only, IM phases only, both SS + IM), the number of phases present and the crystal structures produced. Microstructures observed in 408 alloys and 648 different microstructure reports are used to generate findings and are documented in Table S1 of the accompanying Supplementary data, Appendix A. Observed microstructures are compared with two datasets predicted by the CALculated PHAse Diagram (CALPHAD) method, giving a more robust analysis. Microstructural trends resulting from increasing the number of alloy elements and from different processing conditions (as-cast or annealed) are both analyzed. Additional insights come from considering six issues that bias observations. A 'structure in – structure out' (SISO) analysis developed here corrects for the most significant bias. Building on Hume-Rothery concepts, the SISO analysis estimates the fraction of SS phases in a dataset that will have a given crystal structure (BCC, FCC, HCP) from the weighted fractions of elements with the same crystal structure used to produce the alloys in that dataset. This analysis correctly predicts the fraction of SS phases that are BCC, FCC or HCP in the three major datasets, and also predicts the fraction of SS microstructures.

8.2.5. Major hypotheses have been evaluated and resolved

Data collected in the first 12 years enable resolution of two major HEA hypotheses (called 'core effects', Section 1.3). By far the most widely considered is the high entropy effect (Section 1.3.3.1). Although the data and analyses do not support this hypothesis, it has nevertheless had a major positive impact by motivating a better understanding of the role of configurational entropy in its partnership with other thermodynamic terms (Section 8.1.2). It has also inspired a re-evaluation of classical thermodynamic concepts as they apply to complex, concentrated alloys (Section 2). Finally, this

conclusion validates an early insight by one of the HEA pioneers — that ionic and covalent compounds with sufficiently negative formation enthalpies (oxides, carbides nitrides, borides) will overcome configurational entropy (Section 4.4.3.3). The present resolution shows that many intermetallic compounds also have sufficiently negative formation enthalpies to out-compete configurational entropy.

The hypothesis that atomic diffusion is unusually sluggish in HEAs is also not supported by the available data (Section 5.2). However, this analysis raises questions regarding a long-standing empirical relationship that states that diffusion coefficients are equal in metals with the same crystal structure at their melting temperatures. Additional work is needed to address a third 'core effect' on lattice distortion (Section 7.1.8). The final 'core effect', known as the 'cocktail' effect, is not an hypothesis and requires no proof (Section 1.3.3.4). It is a colorful and evocative statement of the often surprising and unpredictable nature of unknown materials. This continues to capture the essence and the allure of the present field.

8.2.6. Composition/microstructure/properties relationships are established

Clear relationships are emerging between composition, microstructure and properties in the 3d transition metal alloy family (Section 5.3.1, Section 5.5.2). The effect of Al is most widely studied — increasing Al increases strength and decreases ductility by transforming FCC microstructures to duplex BCC + FCC, and then to BCC alloys. Cr is essential for good strength — quaternary and even ternary alloys have strengths as good as 5-element alloys as long as Cr is included. Cu partitions to a second FCC phase, decreasing ductility. The roles of Co and Fe are less impactful. Small volume fractions of IM phases increase strength while retaining ductility, but ductility drops when the IM becomes a dominant phase (Section 5.6). Dislocation mechanisms in CoCrFeMnNi are similar to other austenitic alloys. Nano-twinning is an important deformation mechanism. Tensile properties are similar to commercial austenitic stainless steels and nickel alloys. The fracture toughness of one alloy (CoCrFeMnNi) is as high as any material produced to date.

Refractory metal CCAs are less mature, and relationships between composition, microstructure and properties are now being studied (Section 5.3.2). The BCC phase dominates this alloy family. Several alloys have properties with potential to increase the strength, or the operating temperature, or both, in each of three major application areas for turbine engines.

8.2.7. Unanswered questions and future directions

An entire section of this review is dedicated to unanswered questions and future directions (Section 7). Eight major directions are discussed for basic scientific studies (Section 7.1). Some of these, such as high-throughput computational and experimental methods for structural materials, are rich fields of study in their own right and are essential tools to cope with the enormous compositional and microstructural possibilities. Future work is further outlined for a broad spectrum of applications. Structural metal alloys have formed a focus over the first 12 years, and specific approaches are suggested to continue in this direction. Based on a recent study of entropy-stabilized oxides, we add the possibility of non-metallic structural materials. Finally, the present review develops a rationale for extensive efforts on complex, concentrated functional materials. Many major accomplishments have been achieved in the first 12 years. However, like any vibrant field, there appear to be more questions now than when the field was started.

8.3. Closing

The concept of vast compositions and microstructures associated with multi-principal element alloys has lost none of its potency in the first 12 years. Significant progress has been made, and it continues to motivate new research questions and to inspire major new scientific themes. The combinatorial vastness of this idea also gives the biggest technical challenge offered by the field. Out of literally hundreds of millions of possible element combinations, barely a hundred have been studied so far. This vastness challenges the scientific community to look beyond the glass ceiling that has bounded the field of materials science. No longer safe along corners and edges of ternary phase diagrams, the materials community is now thrust into an uncharted, hyper-dimensional territory that is difficult to conceive, difficult to visualize, and difficult to explore systematically. The vastness is frightening, and it beckons.

Acknowledgements

Appendix A. Supplementary data

Supplementary data related to this article can be found at http://dx.doi.org/10.1016/j.actamat.2016.08.081.

References

[1] B. Cantor, I.T.H. Chang, P. Knight, A.J.B. Vincent, Microstructural development in equiatomic multicomponent alloys, Mater. Sci. Eng. A 375—377 (2004) 213—218.

[2] T.K. Chen, T.T. Shun, J.-W. Yeh, M.S. Wong, Nanostructured nitride films of multi-element high-entropy alloys by reactive DC sputtering, Surf. Coat. Technol. 188—189 (2004) 193—200.

[3] C.-Y. Hsu, J.-W. Yeh, S.-K. Chen, T.-T. Shun, Wear resistance and high-temperature compression strength of FCC CuCoNiCrAl$_{0.5}$Fe alloy with boron addition, Metall. Mater. Trans. A 35A (2004) 1465—1469.

[4] P.-K. Huang, J.-W. Yeh, T.-T. Shun, S.-K. Chen, Multi-principal-element alloys with improved oxidation and wear resistance for thermal spray coating, Adv.

Eng. Mater. 6 (2004) 74—78.

[5] J.-W. Yeh, S.-K. Chen, J.-W. Gan, S.-J. Lin, T.-S. Chin, T.-T. Shun, C.-H. Tsau, S.-Y. Chang, Formation of simple crystal structures in Cu-Co-Ni-Cr-Al-Fe-Ti-V alloys with multiprincipal metallic elements, Metall. Mater. Trans. A 35A (2004) 2533—2536.

[6] J.-W. Yeh, S.-K. Chen, S.-J. Lin, J.-Y. Gan, T.-S. Chin, T.-T. Shun, C.-H. Tsau, S.-Y. Chang, Nanostructured high-entropy alloys with multiple principal elements: Novel alloy design concepts and outcomes, Adv. Eng. Mater. 6 (2004) 299—303.

[7] E.J. Pickering, N.G. Jones, High-entropy alloys: a critical assessment of their founding principles and future prospects, Int. Mater. Rev. 61 (2016) 183—202.

[8] I. Florea, R.M. Florea, O. Baltatescu, V. Soare, R. Chelariu, I. Carcea, High entropy alloys, J. Optoelectron. Adv. Mater. 15 (2013) 761—767.

[9] R. Kozak, A. Sologubenko, W. Steurer, Single-phase high-entropy alloys - an overview, Z. Krist. 230 (2015) 55—68.

[10] M.-H. Tsai, Physical Properties of High Entropy Alloys, Entropy 15 (2013) 5338—5345.

[11] Y. Zhang, T.T. Zuo, Z. Tang, M.C. Gao, K.A. Dahmen, P.K. Liaw, Z.P. Lu, Microstructures and properties of high-entropy alloys, Prog. Mat. Sci. 61 (2014) 1—93.

[12] H.K.D.H. Bhadeshia, High Entropy Alloys, Mat. Sci. Technol. 31 (2015) 1139—1141.

[13] M.C. Gao, Progress in High-Entropy Alloys, JOM 65 (2013) 1749—1750.

[14] M.C. Gao, Progress in High-Entropy Alloys, JOM 66 (2014) 1964—1965.

[15] M.C. Gao, Progress in High-Entropy Alloys, JOM 67 (2015) 2251—2253.

[16] M.C. Gao, J.-W. Yeh, P.K. Liaw, Y. Zhang, High-entropy Alloys: Fundamentals and Applications, Springer Publishing Co., New York, NY, 2016.

[17] B.S. Murty, J.-W. Yeh, S. Ranganathan, High-entropy Alloys, 2014.

[18] C.S. Smith, Four Outstanding Researchers in Metallurgical History, American Society for Testing and Materials, 1963.

[19] B. Cantor, K.B. Kim, P.J. Warren, Novel multicomponent amorphous alloys, Mater. Sci. Forum 386—388 (2002) 27—32.

[20] S. Ranganathan, Alloyed pleasures: Multimetallic cocktails, Curr. Sci. 85 (2003) 1404—1406.

[21] J.-W. Yeh, Recent Progress in High Entropy Alloys, Ann. Chim. Sci. Mat. 31 (2006) 633—648.

[22] I.A. Tomlin, S.D. Kaloshkin, 'High entropy alloys'—'semi-impossible' regular solid solutions? Mat. Sci. Technol. 31 (2015) 1231—1234.

[23] O.N. Senkov, G.B. Wilks, D.B. Miracle, C.P. Chuang, P.K. Liaw, Refractory high-entropy alloys, Intermetallics 18 (2010) 1758—1765.

[24] O.N. Senkov, G.B. Wilks, J.M. Scott, D.B. Miracle, Mechanical properties of Nb$_{25}$Mo$_{25}$Ta$_{25}$W$_{25}$ and V$_{20}$Nb$_{20}$Mo$_{20}$Ta$_{20}$W$_{20}$ refractory high entropy alloys, Intermetallics 19 (2011) 698—706.

[25] D.B. Miracle, J.D. Miller, O.N. Senkov, C. Woodward, M.D. Uchic, J. Tiley, Exploration and development of high entropy alloys for structural applications, Entropy 16 (2014) 494—525.

[26] D.B. Miracle, Critical Assessment 14: High entropy alloys and their development as structural materials, Mat. Sci. Technol. 31 (2015) 1142—1147.

[27] B. Gludovatz, A. Hohenwarter, D. Catoor, E.H. Chang, E.P. George, R.O. Ritchie, A fracture-resistant high-entropy alloy for cryogenic applications, Science 345 (2014) 1153—1158.

[28] C. Tiwary, V.V. Gunjal, D. Banerjee, K. Chattopadhyay, Intermetallic eutectic alloys in the Ni-Al-Zr system with attractive high temperature properties, in: MATEC Web of Conferences 14, 01005, EDP Sciences, 2014, 2014.

[29] S. Guo, C. Ng, J. Lu, C.T. Liu, Effect of valence electron concentration on stability of fcc or bcc phase in high entropy alloys, J. Appl. Phys. 109 (2011) 103505.

[30] J.R. Davis (Ed.), Metals Handbook, Desk Edition, second ed., ASM, International, Metals Park, OH USA, 1998.

[31] D.B. Miracle, B. Majumdar, K. Wertz, S. Gorsse, New strategies and tests to accelerate discovery and development of multi-principal element structural alloys, Scr. Mater (2016), http://dx.doi.org/10.1016/j.scriptamat.2016.08.001.

[32] K.-Y. Tsai, M.-H. Tsai, J.-W. Yeh, Sluggish diffusion in Co-Cr-Fe-Mn-Ni high-entropy alloys, Acta Mater 61 (2013) 4887—4897.

[33] S. Ranganathan, Personal Communication, 2015.

[34] T. Saito, T. Furuta, J.-H. Hwang, S. Kuramoto, K. Nishino, N. Suzuki, R. Chen, A. Yamada, K. Ito, Y. Seno, T. Nonaka, H. Ikehata, N. Nagasako, C. Iwamoto, Y. Ikuhara, T. Sakamura, Multifunctional Alloys Obtained via a Dislocation-Free Plastic Deformation Mechanism, Science 300 (2003) 464—467.

[35] Open Quantum Materials Database. http://oqmd.org/analysis/phase_diagram/.

[36] J.E. Saal, S. Kirklin, M. Aykol, B. Meredig, C. Wolverton, Materials design and discovery with high-throughput density functional theory: The Open Quantum Materials Database (OQMD), JOM 65 (2013) 1501—1509.

[37] C. Zhang, F. Zhang, S. Chen, W. Cao, Computational Thermodynamics Aided High-Entropy Alloy Design, JOM 64 (2012) 839—845.

[38] O.N. Senkov, S.V. Senkova, C. Woodward, D.B. Miracle, Low-density, refractory multi-principal element alloys of the Cr—Nb—Ti—V—Zr system: Microstructure and phase analysis, Acta Mater 61 (2013) 1545—1557.

[39] 4-dimensional polytopes. Wikipedia, 2016. https://en.wikipedia.org/wiki/4-polytope.

[40] M. Hillert, Phase Equilibria, Phase Diagrams and Phase Transformations: Their Thermodynamic Basis, second ed., Cambridge University Press, Cambridge, UK, 2008.

[41] H.L. Lukas, S.G. Fries, B. Sundman, Computational Thermodynamics: the Calphad Method, Cambridge University Press, Cambridge UK, 2007.

[42] D.R. Gaskell, Introduction to the Thermodynamics of Materials, third ed., Taylor & Francis, Washington, DC USA, 1995.

[43] C.H.P. Lupis, Chemical Thermodynamics of Materials, Elsevier Science Publishing Co., Inc., New York, NY, 1983.

[44] D.A. Porter, K.E. Easterling, Phase Transformations in Metals and Alloys, Van Nostrand Reinhold Co Ltd., Wokingham, Berkshire, England, 1984.

[45] A. Takeuchi, A. Inoue, Mixing enthalpy of liquid phase calculated by Miedema's scheme and approximated with sub-regular solution model for assessing forming ability of amorphous and glassy alloys, Intermetallics 18 (2010) 1779—1789.

[46] S. Guo, C.T. Liu, Phase stability in high entropy alloys: Formation of solid-solution phase or amorphous phase, Prog. Nat. Sci. 21 (2011) 433—446.

[47] S. Guo, C.T. Liu, Phase selection rules for complex multi-component alloys with equiatomic or close-to-equiatomic compositions, Chin. J. Nat. 35 (2013) 85—96.

[48] X. Yang, Y. Zhang, Prediction of high-entropy stabilized solid-solution in multi-component alloys, Mater. Chem. Phys. 132 (2012) 233—238.

[49] Y. Zhang, Y.J. Zhou, J.P. Lin, G.L. Chen, P.K. Liaw, Solid-solution phase formation rules for multi-component alloys, Adv. Eng. Mater. 10 (2008) 534—538.

[50] F. Zhang, C. Zhang, S.L. Chen, J. Zhu, W.S. Cao, U.R. Kattner, An understanding of high entropy alloys from phase diagram calculations, Calphad 45 (2014) 1—10.

[51] M.S. Lucas, G.B. Wilks, L. Mauger, J.A. Munoz, O.N. Senkov, E. Michel, J. Horwath, S.L. Semiatin, M.B. Stone, D.L. Abernathy, E. Karapetrova, Absence of long-range chemical ordering in equimolar FeCoCrNi, Appl. Phys. Lett. 100 (2012).

[52] R. Hultgren, R.L. Orr, P.D. Anderson, K.K. Kelley, Selected Values of Thermodynamic Properties of Metals and Alloys, John Wiley & Sons, Inc., New York, NY, 1963.

[53] O. Kubaschewski, J.A. Catterall, Thermochemical Data of Alloys, Pergamon Press, London, England, 1956.

[54] F.R. de Boer, B. Boom, W.C.M. Mattens, A.R. Miedema, A.K. Niessen, Cohesion in Metals: Transition Metal Alloys, Elsevier Science Publishers, Amsterdam, The Netherlands, 1989.

[55] P. Franke, D. Neuschutz (Eds.), Thermodynamic Properties of Inorganic Materials compiled by SGTE, Springer-Verlag, Berlin, Germany, 2002.

[56] O.N. Senkov, J.D. Miller, D.B. Miracle, C. Woodward, Accelerated exploration of multi-principal element alloys for structural applications, Calphad 50 (2015) 32—48.

[57] R. Darolia, J.J. Lewandowski, C.T. Liu, P.L. Martin, D.B. Miracle, M.V. Nathal (Eds.), Structural Intermetallics, TMS, Warrendale, PA USA, Champion, PA USA, 1993.

[58] J.H. Westbrook, R.L. Fleischer, in: Intermetallic Compounds: Principles and Practice, John Wiley & Sons, Ltd., West Sussex, England, 1995.

[59] L.J. Santodonato, Y. Zhang, M. Feygenson, C.M. Parish, M.C. Gao, R.J.K. Weber, J.C. Neuefeind, Z. Tang, P.K. Liaw, Deviation from high-entropy configurations in the atomic distributions of a multi-principal-element alloy, Nat. Commun. 6 (2015) 5964.

[60] D.B. Miracle, G.B. Wilks, A.G. Dahlman, J.E. Dahlman, The strength of chemical bonds in solids and liquids, Acta Mater 59 (2011) 7840—7854.

[61] C. Colinet, The thermodynamic properties of rare earth metallic systems, J. Alloys Compd. 225 (1995) 409—422.

[62] S. Fries, T. Jantzen, Compilation of 'CALPHAD' formation enthalpy data: Binary intermetallic compounds in the COST 507 Gibbsian database, Thermochim. Acta 314 (1998) 23—33.

[63] Q. Guo, O.J. Kleppa, Standard enthalpies of formation of some alloys formed between group IV elements and group VIII elements, determined by high-temperature direct synthesis calorimetry II. Alloys of (Ti,Zr,Hf) with (Co,Ni), J. Alloys Compd. 269 (1998) 181—186.

[64] Q. Guo, O.J. Kleppa, The standard enthalpies of formation of the compounds of early transition metals with late transition metals and with noble metals as determined by Kleppa and co-workers at the University of Chicago - A review, J. Alloys Compd. 321 (2001) 169—182.

[65] O. Kubaschewski, C.B. Alcock, P.J. Spencer, Materials Thermochemistry, sixth ed., Pergamon Press, Oxford, UK, 1993.

[66] L.A. Dominguez, R. Goodall, I. Todd, Prediction and validation of quaternary high entropy alloys using statistical approaches, Mat. Sci. Technol. 31 (2015) 1201—1206.

[67] A. Takeuchi, K. Amiya, T. Wada, K. Yubuta, W. Zhang, High-entropy alloys with a hexagonal close-packed structure designed by equi-atomic alloy strategy and binary phase diagrams, JOM 66 (2014) 1984—1992.

[68] C.-J. Tong, M.-R. Chen, S.-K. Chen, J.-W. Yeh, T.-T. Shun, S.-J. Lin, S.-Y. Chang, Mechanical performance of the Al$_x$CoCrCuFeNi high-entropy alloy system with multiprincipal elements, Metall. Mater. Trans. A 36A (2005) 1263—1271.

[69] J.M. Zhu, H.M. Fu, H.F. Zhang, A.M. Wang, H. Li, Z.Q. Hu, Microstructures and compressive properties of multicomponent AlCoCrFeNiMo$_x$ alloys, Mater. Sci. Eng. A 527 (2010) 6975—6979.

[70] J.M. Zhu, H.M. Fu, H.F. Zhang, A.M. Wang, H. Li, Z.Q. Hu, Synthesis and properties of multiprincipal component AlCoCrFeNiSi$_x$ alloys, Mater. Sci. Eng. A 527 (2010) 7210—7214.

[71] J.M. Zhu, H.M. Fu, H.F. Zhang, A.M. Wang, H. Li, Z.Q. Hu, Microstructure and

compressive properties of multiprincipal component AlCoCrFeNiC$_x$ alloys, J. Alloys Compd. 509 (2011) 3476—3480.

[72] G.A. Mansoori, N.F. Carnahan, K.E. Starling, J.T.W. Leland, Equilibrium Thermodynamic Properties of the Mixture of Hard Spheres, J. Chem. Phys. 54 (1971) 1523—1525.

[73] A. Takeuchi, A. Inoue, Calculations of mixing enthalpy and mismatch entropy for ternary amorphous alloys, Mater. Trans. JIM 41 (2000) 1372—1378.

[74] P. Villars, L.D. Calvert, Pearson's Handbook of Crystallographic Data for Intermetallic Phases, ASM, International, Materials Park, OH, 1991.

[75] D.B. Miracle, K. Laws, O.N. Senkov, G.B. Wilks, Partial coordination numbers in binary metallic glasses, Metall. Mater. Trans. A 43A (2012) 2649—2661.

[76] L. Anthony, L.J. Nagel, J.K. Okamoto, B. Fultz, Magnitude and origin of the difference in vibrational entropy between ordered and disordered Fe$_3$Al, Phys. Rev. Lett. 73 (1994) 3034—3037.

[77] T.L. Swan-Wood, O. Delaire, B. Fultz, Vibrational entropy of spinodal decomposition in FeCr, Phys. Rev. B 72 (2005), 024305 024301—024307.

[78] A. van de Walle, G. Ceder, The effect of lattice vibrations on substitutional alloy thermodynamics, Rev. Mod. Phys. 74 (2002) 11—45.

[79] O.N. Senkov, D.B. Miracle, A new thermodynamic parameter to predict formation of solid solution or intermetallic phases in high entropy alloys, J. Alloys Cmpds. 658 (2016) 603—607.

[80] C.H. MacGillavry, G. Reick (Eds.), Interatomic Distances in Metallic Crystals, second ed., Kluwer Academic Publishers, Dordrecht, Holland, 1985.

[81] M. Winter, WebElements: the periodic table on the WWW, vol. 2015, The University of Sheffield and WebElements Ltd, UK, 2015.

[82] M.-H. Tsai, J.-W. Yeh, High-entropy alloys: a critical review, Mater. Res. Lett. 2 (2014) 107—123.

[83] J.-W. Yeh, Y.-L. Chen, S.-J. Lin, S.-K. Chen, High-entropy alloys - a new era of exploitation, Mater. Sci. Forum 560 (2007) 1—10.

[84] Y. Zhang, X. Yang, P.K. Liaw, Alloy design and properties optimization of high-entropy alloys, JOM 64 (2012) 830—838.

[85] J.P. Couzinie, G. Dirras, L. Perriere, T. Chauveau, E. Leroy, Y. Champion, I. Guillot, Microstructure of a near-equimolar refractory high-entropy alloy, Mater. Lett. 126 (2014) 285—287.

[86] E. Fazakas, V. Zadorozhnyy, L.K. Varga, A. Inoue, D.V. Louzguine-Luzgin, F. Tian, L. Vitos, Experimental and theoretical study of Ti$_{20}$Zr$_{20}$Hf$_{20}$Nb$_{20}$X$_{20}$ (X = V or Cr) refractory high-entropy alloys, Int. J. Refract. Met. Hard Mater. 47 (2014) 131—138.

[87] M.C. Gao, D.E. Alman, Searching for next single-phase high-entropy alloy compositions, Entropy 15 (2013) 4504—4519.

[88] M.F. del Grosso, G. Bozzolo, H.O. Mosca, Determination of the transition to the high entropy regime for alloys of refractory elements, J. Alloys Compd. 534 (2012) 25—31.

[89] M.F. del Grosso, G. Bozzolo, H.O. Mosca, Modeling of high entropy alloys of refractory elements, Phys. B-Condens. Matter 407 (2012) 3285—3287.

[90] J. Lei, S. Guo, E. Khosravi, S. Yang, The Stability and Stiffness of TaNbHfZrTi Alloy from First Principles Simulation. MS & T 2012, October 7-11, 2012, Association for Iron and Steel Technology, AISTECH, Pittsburgh, PA, United States, 2012, pp. 196—201.

[91] L. Lilensten, J.P. Couzinie, L. Perriere, J. Bourgon, N. Emery, I. Guillot, New structure in refractory high-entropy alloys, Mater. Lett. 132 (2014) 123—125.

[92] C.M. Liu, H.M. Wang, S.Q. Zhang, H.B. Tang, A.L. Zhang, Microstructure and oxidation behavior of new refractory high entropy alloys, J. Alloys Compd. 583 (2014) 162—169.

[93] O.N. Senkov, S.V. Senkova, D.M. Dimiduk, C. Woodward, D.B. Miracle, Oxidation behavior of a refractory NbCrMo$_{0.5}$Ta$_{0.5}$TiZr alloy, J. Mater. Sci. 47 (2012) 6522—6534.

[94] O.N. Senkov, S.V. Senkova, C. Woodward, Effect of aluminum on the microstructure and properties of two refractory high entropy alloys, Acta Mater 68 (2014) 214—228.

[95] O.N. Senkov, C. Woodward, D.B. Miracle, Microstructure and properties of aluminum-containing refractory high-entropy alloys, JOM 66 (2014) 2030—2042.

[96] O.N. Senkov, C.F. Woodward, Microstructure and properties of a refractory NbCrMo$_{0.5}$Ta$_{0.5}$TiZr alloy, Mater. Sci. Eng. A 529 (2011) 311—320.

[97] O.N. Senkov, F. Zhang, J.D. Miller, Phase composition of a CrMo$_{0.5}$NbTa$_{0.5}$TiZr high entropy alloy: comparison of experimental and simulated data, Entropy 15 (2013) 3769—3809.

[98] F.Y. Tian, L.K. Varga, N.X. Chen, J. Shen, L. Vitos, Ab initio design of elastically isotropic TiZrNbMoV$_x$ high-entropy alloys, J. Alloys Compd. 599 (2014) 19—25.

[99] M. Widom, W.P. Huhn, S. Maiti, W. Steurer, Hybrid monte carlo/molecular dynamics simulation of a refractory metal high entropy alloy, Metall. Mater. Trans. A 45A (2014) 196—200.

[100] Y.D. Wu, Y.H. Cai, T. Wang, J.J. Si, J. Zhu, Y.D. Wang, X.D. Hui, A refractory Hf$_{25}$Nb$_{25}$Ti$_{25}$Zr$_{25}$ high-entropy alloy with excellent structural stability and tensile properties, Mater. Lett. 130 (2014) 277—280.

[101] X. Yang, Y. Zhang, P.K. Liaw, Microstructure and compressive properties of NbTiVTaAl$_x$ high entropy alloys, Procedia Eng. 36 (2012) 292—298.

[102] Y. Zou, S. Maiti, W. Steurer, R. Spolenak, Size-dependent plasticity in an Nb$_{25}$Mo$_{25}$Ta$_{25}$W$_{25}$ refractory high-entropy alloy, Acta Mater 65 (2014) 85—97.

[103] S.N. Grigoriev, O.V. Sobol, V.M. Beresnev, I.V. Serdyuk, A.D. Pogrebnjak, D.A. Kolesnikov, U.S. Nemchenko, Tribological characteristics of (TiZrHfVNbTa)N coatings applied using the vacuum arc deposition method,

[104] S. Maiti, W. Steurer, Structure and properties of refractory high-entropy alloys, in: 143rd Annual Meeting and Exhibition, TMS 2014, February 16, 2014-February 20, 2014. San Diego, CA, United states, Minerals, Metals and Materials Society, 2014, pp. 1093—1097.

[105] B. Gorr, M. Azim, H.J. Christ, T. Mueller, D. Schliephake, M. Heilmaier, Phase equilibria, microstructure, and high temperature oxidation resistance of novel refractory high-entropy alloys, J. Alloys Compd. 624 (2015) 270—278.

[106] C.-M. Lin, C.-C. Juan, C.-H. Chang, C.-W. Tsai, J.-W. Yeh, Effect of Al addition on mechanical properties and microstructure of refractory Al$_x$HfNbTaTiZr alloys, J. Alloys Compd. 624 (2015) 100—107.

[107] N.D. Stepanov, D.G. Shaysultanov, G.A. Salishchev, M.A. Tikhonovsky, Structure and mechanical properties of a light-weight AlNbTiV high entropy alloy, Mater. Lett. 142 (2015) 153—155.

[108] F.Y. Tian, L.K. Varga, N. Chen, J. Shen, L. Vitos, Empirical design of single phase high-entropy alloys with high hardness, Intermetallics 58 (2015) 1—6.

[109] V.H. Hammond, M.A. Atwater, K.A. Darling, H.Q. Nguyen, L.J. Kecskes, Equal-channel angular extrusion of a low-density high-entropy alloy produced by high-energy cryogenic mechanical alloying, JOM 66 (2014) 2021—2029.

[110] X. Yang, S.Y. Chen, J.D. Cotton, Y. Zhang, Phase stability of low-density, multiprincipal component alloys containing aluminum, magnesium, and lithium, JOM 66 (2014) 2009—2020.

[111] K.M. Youssef, A.J. Zaddach, C. Niu, D.L. Irving, C.C. Koch, A novel low density, high hardness, high-entropy alloy with close-packed single-phase nanocrystalline structures, Mater. Res. Lett. 3 (2014) 95—99.

[112] K.J. Laws, C. Crosby, A. Sridhar, P.L.J. Conway, L.S. Koloadin, M. Zhao, S. Aron-Dine, L.C. Bassman, High entropy brasses and bronzes - microstructure, phase evolution and properties, J. Alloys Cmpds. 650 (2015) 949—961.

[113] K. Laws, Equiatomic solid solutions of noble metals, 2015. Personal Communication.

[114] J.O.A. Paschoal, H. Kleykamp, F. Thummler, Phase equilibria in the quaternary molybdenum-ruthenium-rhodium-palladium system, Z. Met. 74 (1983) 652.

[115] K.-H. Cheng, C.-H. Lai, S.-J. Lin, J.-W. Yeh, Recent progress in multi-element alloy and nitride coatings sputtered from high-entropy alloy targets, Ann. Chim. Sci. Mat. 31 (2006) 723—736.

[116] K.-H. Cheng, C.-H. Lai, S.-J. Lin, J.-W. Yeh, Structural and mechanical properties of multi-element (AlCrMoTaTiZr)N$_x$ coatings by reactive magnetron sputtering, Thin Solid Films 519 (2011) 3185—3190.

[117] M.-H. Hsieh, M.-H. Tsai, W.-J. Shen, J.-W. Yeh, Structure and properties of two Al-Cr-Nb-Si-Ti high-entropy nitride coatings, Surf. Coat. Technol. 221 (2013) 118—123.

[118] H.-T. Hsueh, W.-J. Shen, M.-H. Tsai, J.-W. Yeh, Effect of nitrogen content and substrate bias on mechanical and corrosion properties of high-entropy films (AlCrSiTiZr)$_{100-x}$N$_x$, Surf. Coat. Technol. 206 (2012) 4106—4112.

[119] S.-Y. Lin, S.-Y. Chang, C.-J. Chang, Y.-C. Huang, Nanomechanical properties and deformation behaviors of multi-component (AlCrTaTiZr)N$_x$Si$_y$ high-entropy coatings, Entropy 16 (2014) 405—417.

[120] B. Ren, Z.X. Liu, L. Shi, B. Cai, M.X. Wang, Structure and properties of (AlCrMnMoNiZrB$_{0.1}$)N$_x$ coatings prepared by reactive DC sputtering, Appl. Surf. Sci. 257 (2011) 7172—7178.

[121] W.-J. Shen, M.-H. Tsai, Y.-S. Chang, J.-W. Yeh, Effects of substrate bias on the structure and mechanical properties of (Al$_{1.5}$CrNb$_{0.5}$Si$_{0.5}$Ti)N$_x$ coatings, Thin Solid Films 520 (2012) 6183—6188.

[122] W.-Y. Tang, M.-H. Chuang, H.-Y. Chen, Y.-W. Yeh, Microstructure and mechanical performance of new Al$_{0.5}$CrFe$_{1.5}$MnNi0.5 high-entropy alloys improved by plasma nitriding, Surf. Coat. Technol. 204 (2010) 3118—3124.

[123] W.-Y. Tang, M.-H. Chuang, S.J. Lin, J.-W. Yeh, Microstructures and mechanical performance of plasma-nitrided Al0.3CrFe1.5MnNi0.5 high-entropy alloys, Metall. Mater. Trans. A 43A (2012) 2390—2400.

[124] V. Braic, A. Vladescu, M. Balaceanu, C.R. Luculescu, M. Braic, Nanostructured multi-element (TiZrNbHfTa)N and (TiZrNbHfTa)C hard coatings, Surf. Coat. Technol. 211 (2012) 117—121.

[125] O.N. Senkov, J.D. Miller, D.B. Miracle, C. Woodward, Accelerated exploration of multi-principal element alloys with solid solution phases, Nat. Commun. 6 (2015) 6529.

[126] Y.-L. Chen, Y.-H. Hu, C.-W. Tsai, C.-A. Hsieh, S.-W. Kao, J.-W. Yeh, T.-S. Chin, S.-K. Chen, Alloying behavior of binary to octonary alloys based on Cu—Ni—Al—Co—Cr—Fe—Ti—Mo during mechanical alloying, J. Alloys Compd. 477 (2009) 696—705.

[127] A. Takeuchi, K. Amiya, T. Wada, K. Yubuta, W. Zhang, A. Makino, Entropies in alloy design for high-entropy and bulk glassy alloys, Entropy 15 (2013) 3810—3821.

[128] B. Cantor, Multicomponent and high entropy alloys, Entropy 16 (2014) 4749—4768.

[129] A. Gali, E.P. George, Tensile properties of high- and medium-entropy alloys, Intermetallics 39 (2013) 74—78.

[130] M.S. Lucas, D. Belyea, C. Bauer, N. Bryant, E. Michel, Z. Turgut, S.O. Leontsev, J. Horwath, S.L. Semiatin, M.E. McHenry, C.W. Miller, Thermomagnetic Analysis of FeCoCrxNi Alloys: Magnetic Entropy of High-entropy Alloys, vol. 113, American Institute of Physics, 2 Huntington Quadrangle, Suite N101, Melville, NY 11747-4502, United States, 2013.

[131] H.-P. Chou, Y.-S. Chang, S.-K. Chen, J.-W. Yeh, Microstructure, thermophysical and electrical properties in Al$_x$CoCrFeNi ($0 \leq x \leq 2$) high-entropy alloys, Mater. Sci. Eng. B 163 (2009) 184—189.

[132] Y.-F. Kao, T.-J. Chen, S.-K. Chen, J.-W. Yeh, Microstructure and mechanical

property of as-cast, -homogenized, and -deformed AlxCoCrFeNi (0≤x≤2) high-entropy alloys, J. Alloys Compd. 488 (2009) 57–64.

[133] C. Li, J.C. Li, M. Zhao, Q. Jiang, Effect of aluminum contents on microstructure and properties of Al$_x$CoCrFeNi alloys, J. Alloys Compd. 504 (2010) S515–S518.

[134] C.-M. Lin, H.-L. Tsai, Effect of annealing treatment on microstructure and properties of high-entropy FeCoNiCrCu$_{0.5}$ alloy, Mater. Chem. Phys. 128 (2011) 50–56.

[135] C. Li, J.C. Li, M. Zhao, Q. Jiang, Effect of alloying elements on microstructure and properties of multiprincipal elements high-entropy alloys, J. Alloys Compd. 475 (2009) 752–757.

[136] H.B. Cui, L.F. Zheng, J.Y. Wang, Microstructure evolution and corrosion behavior of directionally solidified FeCoNiCrCu high entropy alloy, Appl. Mech. Mater 66–68 (2011) 146–149.

[137] X. Wang, H. Xie, L. Jia, Z.L. Lu, Effect of Ti, Al and Cu addition on structural evolution and phase constitution of FeCoNi system equimolar alloys, Mater. Sci. Forum 724 (2012) 335–338.

[138] B. Schuh, F. Mendez-Martin, B. Volker, E.P. George, H. Clemens, R. Pippan, A. Hohenwarter, Mechanical properties, microstructure and thermal stability of a nanocrystalline CoCrFeMnNi high-entropy alloy after severe plastic deformation, Acta Mater 96 (2015) 258–268.

[139] O.N. Senkov, J.M. Scott, S.V. Senkova, D.B. Miracle, C.F. Woodward, Microstructure and room temperature properties of a high-entropy TaNbHfZrTi alloy, J. Alloys Compd. 509 (2011) 6043–6048.

[140] N.N. Guo, L. Wang, L.S. Luo, X.Z. Li, Y.Q. Su, J.J. Guo, H.Z. Fu, Microstructure and mechanical properties of refractory MoNbHfZrTi high-entropy alloy, Mater. Des. 81 (2015) 87–94.

[141] J.K. Jensen, B.A. Welk, R.E.A. Williams, J.M. Sosa, D.E. Huber, O.N. Senkov, G.B. Viswanathan, H.L. Fraser, Characterization of the microstructure of the compositionally complex alloy Al$_1$Mo$_{0.5}$Nb$_1$Ta$_{0.5}$Ti$_1$Zr$_1$, Scr. Mater. 121 (2016) 1–4.

[142] O.N. Senkov, D. Isheim, D.N. Seidman, A.L. Pilchak, Development of a refractory high entropy superalloy, Entropy 18 (2016) 102.

[143] J.Y. He, W.H. Liu, H. Wang, Y. Wu, X.J. Liu, T.G. Nieh, Z.P. Lu, Effects of Al addition on structural evolution and tensile properties of the FeCoNiCrMn high-entropy alloy system, Acta Mater 62 (2014) 105–113.

[144] Y. Lu, Y. Dong, S. Guo, L. Jiang, H. Kang, T. Wang, B. Wen, Z. Wang, J. Jie, Z. Cao, H. Ruan, T. Li, A promising new class of high-temperature alloys: eutectic high-entropy alloys, Sci. Rep. 4 (2014).

[145] S.-T. Chen, W.-Y. Tang, Y.-F. Kuo, S.-Y. Chen, C.-H. Tsau, T.-T. Shun, J.-W. Yeh, Microstructure and properties of age-hardenable Al$_x$CrFe$_{1.5}$MnNi$_{0.5}$ alloys, Mater. Sci. Eng. A 527 (2010) 5818–5825.

[146] M.-H. Chuang, M.-H. Tsai, W.-R. Wang, S.-J. Lin, J.-W. Yeh, Microstructure and wear behavior of Al$_x$Co$_{1.5}$CrNi$_{1.5}$Tiy high-entropy alloys, Acta Mater 59 (2011) 6308–6317.

[147] C.-W. Tsai, M.-H. Tsai, J.-W. Yeh, C.-C. Yang, Effect of temperature on mechanical properties of Al$_{0.5}$CoCrCuFeNi wrought alloy, J. Alloys Compd. 490 (2010) 160–165.

[148] S. Singh, N. Wanderka, B.S. Murty, U. Glatzel, J. Banhart, Decomposition in multi-component AlCoCrCuFeNi high-entropy alloy, Acta Mater 59 (2011) 182–190.

[149] C.-J. Tong, Y.-L. Chen, S.-K. Chen, J.-W. Yeh, T.-T. Shun, C.-H. Tsau, S.-J. Lin, S.-Y. Chang, Microstructure characterization of Al$_x$CoCrCuFeNi high-entropy alloy system with multiprincipal elements, Metall. Mater. Trans. A 36A (2005) 881–893.

[150] C.-W. Tsai, Y.-L. Chen, M.-H. Tsai, J.-W. Yeh, T.-T. Shun, S.-K. Chen, Deformation and annealing behaviors of high-entropy alloy Al$_{0.5}$CoCrCuFeNi, J. Alloys Compd. 486 (2009) 427–435.

[151] M.-H. Tsai, Y. Yuan, G. Cheng, W. Xu, K.-Y. Tsai, C.-W. Tsai, W.W. Jian, C.-C. Juan, W.-J. Shen, M.-H. Chuang, J.-W. Yeh, Y.T. Zhu, Morphology, structure and composition of precipitates in Al$_{0.3}$CoCrCu$_{0.5}$FeNi high-entropy alloy, Intermetallics 32 (2013) 329–336.

[152] Y.P. Wang, B.S. Li, M.X. Ren, C. Yang, H.Z. Fu, Microstructure and compressive properties of AlCrFeCoNi high entropy alloy, Mater. Sci. Eng. A 491 (2008) 154–158.

[153] M.-H. Chuang, M.-H. Tsai, C.-W. Tsai, N.-H. Yang, S.-Y. Chang, J.-W. Yeh, S.-K. Chen, S.-J. Lin, Intrinsic surface hardening and precipitation kinetics of Al$_{0.3}$CrFe$_{1.5}$MnNi$_{0.5}$ multi-component alloy, J. Alloys Compd. 551 (2013) 12–18.

[154] W. Hume-Rothery, Atomic Theory for Students of Metallurgy, The Institute of Metals, London, UK, 1969.

[155] W. Hume-Rothery, H.M. Powell, On the theory of super-lattice structures in alloys, Z. Krist. 91 (1935) 23–47.

[156] W. Hume-Rothery, R.W. Smallman, C.W. Haworth, The Structure of Metals and Alloys, The Institute of Metals, London, 1969.

[157] S. Guo, Phase selection rules for cast high entropy alloys: an overview, Mater. Sci. Technol. 31 (2015) 1223–1230.

[158] A. Takeuchi, A. Inoue, Classification of bulk metallic glasses by atomic size difference, heat of mixing and period of constituent elements and its application to characterization of the main alloying element, Mater. Trans. JIM 46 (2005) 2817–2829.

[159] M.-H. Tsai, K.-Y. Tsai, C.-W. Tsai, C. Lee, C.-C. Juan, J.-W. Yeh, Criterion for sigma phase formation in Cr- and V-containing high-entropy alloys, Mater. Res. Lett. 1 (2013) 207–212.

[160] S. Guo, Q. Hu, C. Ng, C.T. Liu, More than entropy in high-entropy alloys: forming solid solutions or amorphous phase, Intermetallics 41 (2013) 96–103.

[161] M.G. Poletti, L. Battezzati, Electronic and thermodynamic criteria for the occurrence of high entropy alloys in metallic systems, Acta Mater 75 (2014) 297–306.

[162] G.A. Salishchev, M.A. Tikhonovsky, D.G. Shaysultanov, N.D. Stepanov, A.V. Kuznetsov, I.V. Kolodiy, A.S. Tortika, O.N. Senkov, Effect of Mn and V on structure and mechanical properties of high-entropy alloys based on CoCrFeNi system, J. Alloys Compd. 591 (2014) 11–21.

[163] Z.-S. Nong, J.-C. Zhu, Y. Cao, X.-W. Yang, Z.H. Lai, Y. Liu, Stability and structure prediction of cubic phase in as cast high entropy alloys, Mater. Sci. Technol. 30 (2014) 363–369.

[164] M.-X. Ren, B.-X. Li, H.-Z. Fu, Formation condition of solid solution type high-entropy alloy, Trans. Nonferrous Metals Soc. China (English Edition) 23 (2013) 991–995.

[165] A. Inoue, Stabilization of metallic supercooled liquid and bulk amorphous alloys, Acta Mater 48 (2000) 279–306.

[166] C. Ng, S. Guo, J.H. Luan, S.Q. Shi, C.T. Liu, Entropy-driven phase stability and slow diffusion kinetics in an Al$_{0.5}$CoCrCuFeNi high entropy alloy, Intermetallics 31 (2012) 165–172.

[167] Z. Wang, S. Guo, C.T. Liu, Phase selection in high-entropy alloys: from nonequilibrium to equilibrium, JOM 66 (2014) 1966–1972.

[168] M.C. Troparevsky, J.R. Morris, P.R.C. Kent, A.R. Lupini, G.M. Stocks, Criteria for predicting the formation of single-phase high-entropy alloys, Phys. Rev. X 5 (2015), 011041 (011046 pp.).

[169] F. Otto, Y. Yang, H. Bei, E.P. George, Relative effects of enthalpy and entropy on the phase stability of equiatomic high-entropy alloys, Acta Mater 61 (2013) 2628–2638.

[170] S. Curtarolo, W. Setyawan, S. Wanga, J. Xue, K. Yang, R.H. Taylor, L.J. Nelsond, G.L.W. Hart, S. Sanvito, M. Buongiorno-Nardelli, N. Mingo, O. Levy, AFLOWLIB.ORG: a distributed materials properties repository from high-throughput ab initio calculations, Comput. Mater. Sci. 58 (2012) 227–235.

[171] S. Curtarolo, W. Setyawan, G.L.W. Hart, M. Jahnatek, R.V. Chepulskii, R.H. Taylor, S. Wang, J. Xue, K. Yang, O. Levy, M. Mehl, H.T. Stokes, D.O. Demchenko, D. Morgan, AFLOW: an automatic framework for high-throughput materials discovery, Comput. Mater. Sci. 58 (2012) 218–226.

[172] A. Durga, K.C. Kumar, B.S. Murty, Phase formation in equiatomic high entropy alloys: CALPHAD approach and experimental studies, Trans. Indian Inst. Met. 65 (2012) 375–380.

[173] R. Raghavan, K.C.H. Kumar, B.S. Murty, Analysis of phase formation in multi-component alloys, J. Alloys Compd. 544 (2012) 152–158.

[174] A.C. Chang, S.L., F. Zhang, X.Y. Yan, F.Y. Xie, Phase diagram calculation: past, present and future, Prog. Mat. Sci. 49 (2004) 313–345.

[175] K.C. Chou, Y.A. Chang, A study of ternary geometrical models, Ber. Bunsenges. Phys. Chem. 93 (1989) 735–741.

[176] N. Saunders, A.P. Miodownik, CALPHAD | Calculation of Phase Diagrams | a Comprehensive Guide, Pergamon Press, Elsevier Science, Ltd., Oxford OX5 1GB UK, 1998.

[177] A. Manzoni, H. Daoud, S. Mondal, S. van Smaalen, R. Volkl, U. Glatzel, N. Wanderka, Investigation of phases in Al$_{23}$Co$_{15}$Cr$_{23}$Cu$_8$Fe$_{15}$Ni$_{16}$ and Al$_8$Co$_{17}$Cr$_{17}$Cu$_8$Fe$_{17}$Ni$_{33}$ high entropy alloys and comparison with equilibrium phases predicted by Thermo-Calc, J. Alloys Compd. 552 (2013) 430–436.

[178] W.P. Huhn, M. Widom, Prediction of A2 to B2 phase transition in the high-entropy alloy Mo-Nb-Ta-W, JOM 65 (2013) 1772–1779.

[179] D. Choudhuri, T. Alam, T. Borkar, B. Gwalani, A.S. Mantri, S.G. Srinivasan, M.A. Gibson, R. Banerjee, Formation of a huesler-like L2$_1$ phase in a CoCrCuFeNiAlTi high-entropy alloy, Scr. Mater. 100 (2015) 36–39.

[180] S.Q. Wang, Atomic modeling and simulation of AlCoCrCuFeNi multi-principal-element alloy, in: Y. Han, X. Liu, G.H. Lv (Eds.), Materials Performance, Modeling and Simulation, vol. 749, 2013, pp. 479–483.

[181] C.H. Tsau, Phase transformation and mechanical behavior of TiFeCoNi alloy during annealing, Mater. Sci. Eng. A 501 (2009) 81–86.

[182] Y.X. Zhuang, H.D. Xue, Z.Y. Chen, Z.Y. Hu, J.C. He, Effect of annealing treatment on microstructures and mechanical properties of FeCoNiCuAl high entropy alloys, Mater. Sci. Eng. A 572 (2013) 30–35.

[183] S. Ma, Z. Chen, Y. Zhang, Evolution of microstructures and properties of the Al$_x$CrCuFeNi$_2$ high-entropy alloys, Mater. Sci. Forum 745–746 (2013) 706–714.

[184] M.V. Ivchenko, V.G. Pushin, N. Wanderka, High-entropy equiatomic AlCrFeCoNiCu alloy: hypotheses and experimental data, Tech. Phys. 59 (2014) 211–223.

[185] A.K. Singh, A. Subramanian, On the formation of disordered solid solutions in multicomponent alloys, J. Alloys Compd. 587 (2014) 113–119.

[186] F. Otto, N.L. Hanold, E.P. George, Microstructural evolution after thermomechanical processing in an equiatomic, single-phase CoCrFeMnNi high-entropy alloy with special focus on twin boundaries, Intermetallics 54 (2014) 39–48.

[187] P.P. Bhattacharjee, G.D. Sathiaraj, M. Zaid, J.R. Gatti, C. Lee, C.W. Tsai, J.W. Yeh, Microstructure and texture evolution during annealing of equiatomic CoCrFeMnNi high-entropy alloy, J. Alloys Compd. 587 (2014) 544–552.

[188] D.G. Shaysultanov, N.D. Stepanov, A.V. Kuznetsov, G.A. Salishchev, O.N. Senkov, Phase composition and superplastic behavior of a wrought AlCoCrCuFeNi high-entropy alloy, JOM 65 (2013) 1815–1828.

[189] L.H. Wen, H.C. Kou, J.S. Li, H. Chang, X.Y. Xue, L. Zhou, Effect of aging temperature on microstructure and properties of AlCoCrCuFeNi high-entropy alloy, Intermetallics 17 (2009) 266–269.

[190] N.D. Stepanov, D.G. Shaysultanov, G.A. Salishchev, M.A. Tikhonovsky, E.E. Oleynik, A.S. Tortika, O.N. Senkov, Effect of V content on microstructure and mechanical properties of the CoCrFeMnNiV$_x$ high entropy alloys, J. Alloys Compd. 628 (2015) 170–185.

[191] D.B. Miracle, K.A. Lark, V. Srinivasan, H.A. Lipsitt, Nickel-aluminum-molybdenum phase equilibria, Metall. Trans. A 15A (1984) 481–486.

[192] L. Liu, J.B. Zhu, C. Zhang, J.C. Li, Q. Jiang, Microstructure and the properties of FeCoCuNiSn$_x$ high entropy alloys, Mater. Sci. Eng. A 548 (2012) 64–68.

[193] C.-M. Lin, H.-L. Tsai, H.-Y. Bor, Effect of aging treatment on microstructure and properties of high-entropy Cu$_{0.5}$CoCrFeNi alloy, Intermetallics 18 (2010) 1244–1250.

[194] C.-M. Lin, H.-L. Tsai, Equilibrium phase of high-entropy FeCoNiCrCu$_{0.5}$ alloy at elevated temperature, J. Alloys Compd. 489 (2010) 30–35.

[195] X.D. Xu, P. Liu, S. Guo, A. Hirata, T. Fujita, T.G. Nieh, C.T. Liu, M.W. Chen, Nanoscale phase separation in a fcc-based CoCrCuFeNiAl$_{0.5}$ high-entropy alloy, Acta Mater. 84 (2015) 145–152.

[196] C.-H. Zhang, M.-H. Lin, B. Wu, G.-X. Ye, L.-K. Zhang, T. Chen, W.-J. Zhang, Z.-H. Zheng, Q. Li, Y.-Q. Shao, B.-Y. Zhou, C. Wang, Explore the possibility of forming fcc high entropy alloys in equal-atomic systems CoFeMnNiM and CoFeMnNiSmM, J. Shanghai Jiaot. Univ. (Sci.) 16 (2011) 173–179.

[197] B.A. Welk, R.E.A. Williams, G.B. Viswanathan, M.A. Gibson, P.K. Liaw, H.L. Fraser, Nature of the interfaces between the constituent phases in the high entropy alloy CoCrCuFeNiAl, Ultramicroscopy 134 (2013) 193–199.

[198] C.-C. Tung, J.-W. Yeh, T.-T. Shun, S.-K. Chen, Y.-S. Huang, H.-C. Chen, On the elemental effect of AlCoCrCuFeNi high-entropy alloy system, Mater. Lett. 61 (2007) 1–5.

[199] C.-L. Lu, S.-Y. Lu, J.-W. Yeh, W.-K. Hsu, Thermal expansion and enhanced heat transfer in high-entropy alloys, J. Appl. Crystallogr. 46 (2013) 736–739.

[200] G. Laplanche, P. Gadaud, O. Horst, F. Otto, G. Eggeler, E.P. George, Temperature dependencies of the elastic moduli and thermal expansion coefficient of an equiatomic, single-phase CoCrFeMnNi high-entropy alloy, J. Alloys Cmpds. 623 (2015) 348–353.

[201] S.M.C. van Bohemen, The nonlinear lattice expansion of iron alloys in the range 100–1600 K, Scr. Mater. 69 (2013) 315–318.

[202] Y.-F. Kao, S.-K. Chen, T.-J. Chen, P.-C. Chu, J.-W. Yeh, S.-J. Lin, Electrical, magnetic, and Hall properties of Al$_x$CoCrFeNi high-entropy alloys, J. Alloys Compd. 509 (2011) 1607–1614.

[203] K. Zhang, Z. Fu, Effects of annealing treatment on properties of CoCrFeNiTiAl$_x$ multi-component alloys, Intermetallics 28 (2012) 34–39.

[204] T.T. Zuo, R.B. Li, X.J. Ren, Y. Zhang, Effects of Al and Si addition on the structure and properties of CoFeNi equal atomic ratio alloy, J. Magn. Magn. Mater 371 (2014) 60–68.

[205] Y. Zhang, T.T. Zuo, Y.Q. Cheng, P.K. Liaw, High-entropy alloys with high saturation magnetization, electrical resistivity, and malleability, Sci. Rep. 3 (2013).

[206] P. Kozelj, S. Vrtnik, A. Jelen, S. Jazbec, Z. Jaglicic, S. Maiti, M. Feuerbacher, W. Steurer, J. Dolinsek, Discovery of a superconducting high-entropy alloy, Phys. Rev. Lett. 113 (2014), 107001 (107005 pp.).

[207] D.C. Tsai, F.S. Shieu, S.Y. Chang, H.C. Yao, M.J. Deng, Structures and characterizations of TiVCr and TiVCrZrY films deposited by magnetron sputtering under different bias powers, J. Electrochem. Soc. 157 (2010) K52–K58.

[208] S.K. Chen, Y.F. Kao, Near-constant resistivity in 4.2-360 K in a B2 Al$_{2.08}$CoCrFeNi, AIP Adv. 2 (2012).

[209] J. Crangle, G.M. Goodman, The magnetization of pure iron and nickel, Proc. Roy. Soc. Lond. A 321 (1971) 477–491.

[210] Y.-P. Wang, B.-S. Li, H.-Z. Fu, Solid solution or intermetallics in a high-entropy alloy, Adv. Eng. Mater. 11 (2009) 641–644.

[211] S. Singh, N. Wanderka, K. Kiefer, K. Siemensmeyer, J. Banhart, Effect of decomposition of the Cr-Fe-Co rich phase of AlCoCrCuFeNi high entropy alloy on magnetic properties, Ultramicroscopy 111 (2011) 619–622.

[212] N.H. Tariq, M. Naeem, B.A. Hasan, J.I. Akhter, M. Siddique, Effect of W and Zr on structural, thermal and magnetic properties of AlCoCrCuFeNi high entropy alloy, J. Alloys Compd. 556 (2013) 79–85.

[213] C.-Z. Yao, P. Zhang, M. Liu, G.-R. Li, J.-Q. Ye, P. Liu, Y.-X. Tong, Electrochemical preparation and magnetic study of Bi-Fe-Co-Ni-Mn high entropy alloy, Electrochim. Acta 53 (2008) 8359–8365.

[214] L. Liu, J.B. Zhu, J.C. Li, Q. Jiang, Microstructure and magnetic properties of FeNiCuMnTiSn$_x$ high entropy alloys, Adv. Eng. Mat. 14 (2012) 919–922.

[215] J. Wang, Z. Zheng, J. Xu, Y. Wang, Microstructure and magnetic properties of mechanically alloyed FeSiBAlNi (Nb) high entropy alloys, J. Magn. Magn. Mater 355 (2014) 58–64.

[216] L. Zhang, F. Wang, S. Chen, Y. Wang, Fabrication and thermal stability of AlCrTaTiNi/(AlCrTaTiNi)N bilayer diffusion barrier, Acta Metall. Sin. 49 (2013) 1611–1616.

[217] M.-H. Tsai, C.-W. Wang, C.-H. Lai, J.-W. Yeh, J.-W. Gan, Thermally stable amorphous (AlMoNbSiTaTiVZr)$_{50}$N$_{50}$ nitride film as diffusion barrier in copper metallization, Appl. Phys. Lett. 92 (2008), 052109 (052101-052103).

[218] S.-Y. Chang, M.-K. Chen, D.-S. Chen, Multiprincipal-element AlCrTaTiZr-nitride nanocomposite film of extremely high thermal stability as diffusion barrier for Cu metallization, J. Electrochem. Soc. 156 (2009) G37–G42.

[219] M.-H. Tsai, J.-W. Yeh, J.-Y. Gan, Diffusion barrier properties of AlMoNbSiTa-TiVZr high-entropy alloy layer between copper and silicon, Thin Solid Films

516 (2008) 5527–5530.

[220] Y.-F. Kao, S.-K. Chen, J.-H. Sheu, J.-T. Lin, W.-E. Lin, J.-W. Yeh, S.-J. Lin, T.-H. Liou, C.-W. Wang, Hydrogen storage properties of multi-principal-component CoFeMnTi$_x$V$_y$Zr$_z$ alloys, Int. J. Hydrogen Energ 35 (2010) 9046–9059.

[221] I. Kunce, M. Polanski, J. Bystrzycki, Structure and hydrogen storage properties of a high entropy ZrTiVCrFeNi alloy synthesized using Laser Engineered Net Shaping (LENS), Int. J. Hydrogen Energ 38 (2013) 12180–12189.

[222] I. Kunce, M. Polanski, J. Bystrzycki, Microstructure and hydrogen storage properties of a TiZrNbMoV high entropy alloy synthesized using Laser Engineered Net Shaping (LENS), Int. J. Hydrogen Energ 39 (2014) 9904–9910.

[223] C.F. Tsai, P.W. Wu, P. Lin, C.G. Chao, K.Y. Yeh, Sputter deposition of multi-element nanoparticles as electrocatalysts for methanol oxidation, Jpn. J. Appl. Phys. 47 (2008) 5755–5761.

[224] E. Cinar, S. Kocyigit, A. Aytimur, I. Uslu, A. Akdemir, Synthesis, characterization, and thermoelectric properties of electrospun boron-doped barium-stabilized bismuth-cobalt oxide nanoceramics, Metall. Mater. Trans. A 45A (2014) 3929–3937.

[225] T. Nagase, S. Anada, P.D. Rack, J.H. Noh, H. Yasada, H. Mori, et al., MeV electron-irradiation-induced structural change in the BCC phase of Zr-Hf-Nb alloy with an approximately equiatomic ratio, Intermetallics 38 (2013) 70–79.

[226] T. Egami, W. Guo, P.D. Rack, T. Nagase, Irradiation resistance of multicomponent alloys, Metall. Mater. Trans. A 45A (2014) 180–183.

[227] C. Segui, Effects of the interplay between atomic and magnetic order on the properties of metamagnetic Ni-Co-Mn-Ga shape memory alloys, J. Appl. Phys. 115 (2014).

[228] Y.F. Kao, C.I. Hung, S.H. Chang, J.W. Yeh, W.K. Hsu, High entropy alloy mediated growth of graphene, CrystEngComm 16 (2014) 6187–6194.

[229] H.W. Chang, P.K. Huang, J.W. Yeh, A. Davison, C.H. Tsau, C.C. Yang, Influence of substrate bias, deposition temperature and post-deposition annealing on the structure and properties of multi-principal-component (AlCrMoSiTi)N coatings, Surf. Coat. Technol. 202 (2008) 3360–3366.

[230] A.M. Brown, M.F. Ashby, Correlations for diffusion constants, Acta Metall. 28 (1980) 1085–1101.

[231] W.P. Chen, Z.Q. Fu, S.C. Fang, H.Q. Xiao, D.Z. Zhu, Alloying behavior, microstructure and mechanical properties in a FeNiCrCo$_{0.3}$Al$_{0.7}$ high entropy alloy, Mater. Des. 51 (2013) 854–860.

[232] Y. Dong, K.Y. Zhou, Y. Lu, X.X. Gao, T.M. Wang, T.J. Li, Effect of vanadium addition on the microstructure and properties of AlCoCrFeNi high entropy alloy, Mater. Des. 57 (2014) 67–72.

[233] S. Varalakshmi, M. Kamaraj, B.S. Murty, Formation and stability of equiatomic and nonequiatomic nanocrystalline CuNiCoZnAlTi high-entropy alloys by mechanical alloying, Metall. Mater. Trans. A 41A (2010) 2703–2709.

[234] C. Wang, W. Ji, Z.Y. Fu, Mechanical alloying and spark plasma sintering of CoCrFeNiMnAl high-entropy alloy, Adv. Powder Technol. 25 (2014) 1334–1338.

[235] W. Ji, Z. Fu, W. Wang, H. Wang, J. Zhang, Y. Wang, F. Zhang, Mechanical alloying synthesis and spark plasma sintering of CoCrFeNiAl high-entropy alloy, J. Alloys Compd. 589 (2014) 61–66.

[236] S. Fang, W. Chen, Z. Fu, Microstructure and mechanical properties of twinned Al$_{0.5}$CrFeNiCo$_{0.3}$C$_{0.2}$ high entropy alloy processed by mechanical alloying and spark plasma sintering, Mater. Des. 54 (2014) 973–979.

[237] P. Jinhong, P. Ye, Z. Hui, Z. Lu, Microstructure and properties of AlCrFeCuNi$_x$ (0.6<x<1.4) high-entropy alloys, Mater. Sci. Eng. A 534 (2012) 228–233.

[238] X.-W. Qiu, Microstructure and properties of AlCrFeNiCoCu high entropy alloy prepared by powder metallurgy, J. Alloys Compd. 555 (2013) 246–249.

[239] J.-H. Pi, Y. Pan, L. Zhang, H. Zhang, Microstructure and property of AlTiCrFeNiCu high-entropy alloy, J. Alloys Compd. 509 (2011) 5641–5645.

[240] S. Varalakshmi, M. Kamaraj, B.S. Murty, Processing and properties of nanocrystalline CuNiCoZnAlTi high entropy alloys by mechanical alloying, Mater. Sci. Eng. A 527 (2010) 1027–1030.

[241] W. Chen, Z. Fu, S. Fang, Y. Wang, H. Xiao, D. Zhu, Processing, microstructure and properties of Al$_{0.6}$CoNiFeTi$_{0.4}$ high entropy alloy with nanoscale twins, Mater. Sci. Eng. A 565 (2013) 439–444.

[242] C.-Y. Hsu, W.-R. Wang, W.-Y. Tang, S.-K. Chen, J.-W. Yeh, Microstructure and mechanical properties of new AlCo$_x$CrFeMo$_{0.5}$Ni high-entropy alloys, Adv. Eng. Mater. 12 (2010) 44–49.

[243] M.-R. Chen, S.-J. Lin, J.-W. Yeh, S.-K. Chen, Y.-S. Huang, M.-H. Chuang, Effect of vanadium addition on the microstructure, hardness, and wear resistance of Al$_{0.5}$CoCrCuFeNi high-entropy alloy, Metall. Mater. Trans. A 37 (2006) 1363–1369.

[244] S. Liu, M.C. Gao, P.K. Liaw, Y. Zhang, Microstructures and mechanical properties of Al$_x$CrFeNiTi$_{0.25}$ alloys, J. Alloys Compd. 619 (2015) 610–615.

[245] Y.J. Zhou, Y. Zhang, Y.L. Wang, G.L. Chen, Microstructure and compressive properties of multicomponent Al$_x$(TiVCrMnFeCoNiCu)$_{100-x}$ high-entropy alloys, Mater. Sci. Eng. A 454–455 (2007) 260–265.

[246] Z. Fu, W. Chen, S. Fang, D.X. Zhang, H. Xiao, D. Zhu, Alloying behavior and deformation twinning in a CoNiFeCrAl$_{0.6}$Ti$_{0.4}$ high entropy alloy processed by spark plasma sintering, J. Alloys Compd. 553 (2013) 316–323.

[247] W. Ji, W. Wang, H. Wang, J. Zhang, Y. Wang, F. Zhang, Z. Fu, Alloying behavior and novel properties of CoCrFeNiMn high-entropy alloy fabricated by mechanical alloying and spark plasma sintering, Intermetallics 56 (2014) 24–27.

[248] Z. Fu, W. Chen, S. Fang, X. Li, Effect of Cr addition on the alloying behavior, microstructure and mechanical properties of twinned CoFeNiAl$_{0.5}$Ti$_{0.5}$ alloy, Mater. Sci. Eng. A 597 (2014) 204–211.

[249] A. Li, D. Ma, Q. Zheng, Effect of Cr on microstructure and properties of a series of AlTiCr$_x$FeCoNiCu high-entropy alloys, J. Mater. Eng. Perform. 23 (2014) 1197–1203.

[250] Y.X. Zhuang, W.J. Liu, Z.Y. Chen, H.D. Xue, J.C. He, Effect of elemental interaction on microstructure and mechanical properties of FeCoNiCuAl alloys, Mater. Sci. Eng. A 556 (2012) 395–399.

[251] S.G. Ma, Y. Zhang, Effect of Nb addition on the microstructure and properties of AlCoCrFeNi high-entropy alloy, Mater. Sci. Eng. A 532 (2012) 480–486.

[252] Z. Hu, Y. Zhan, G. Zhang, J. She, C. Li, Effect of rare earth Y addition on the microstructure and mechanical properties of high entropy AlCoCrCuNiTi alloys, Mater. Des. 31 (2010) 1599–1602.

[253] Z. Fu, W. Chen, H. Xiao, L. Zhou, D. Zhu, S. Yang, Fabrication and properties of nanocrystalline Co$_{0.5}$FeNiCrTi$_{0.5}$ high entropy alloy by MA-SPS technique, Mater. Des. 44 (2013) 535–539.

[254] H.F. Sheng, M. Gong, L.M. Peng, Microstructural characterization and mechanical properties of an Al$_{0.5}$CoCrFeCuNi high-entropy alloy in as-cast and heat-treated/quenched conditions, Mater. Sci. Eng. A 567 (2013) 14–20.

[255] T.-T. Shun, L.-Y. Chang, M.-H. Shiu, Microstructure and mechanical properties of multiprincipal component CoCrFeNiMo$_x$ alloys, Mater. Charact. 70 (2012) 63–67.

[256] J.M. Zhu, H.F. Zhang, H.M. Fu, A.M. Wang, H. Li, Z.Q. Hu, Microstructures and compressive properties of multicomponent AlCoCrFeNiMo$_x$ alloys, J. Alloys Compd. 497 (2010) 52–56.

[257] T.-T. Shun, L.-Y. Chang, M.-H. Shiu, Microstructures and mechanical properties of multiprincipal component CoCrFeNiTi$_x$ alloys, Mater. Sci. Eng. A 556 (2012) 170–174.

[258] Y.J. Zhou, Y. Zhang, Y.L. Wang, G.L. Chen, Solid solution alloys of AlCoCrFeNiTi$_x$ with excellent room-temperature mechanical properties, Appl. Phys. Lett. 90 (2007) 181904.

[259] F.J. Wang, Y. Zhang, G.L. Chen, H.A. Davies, Tensile and compressive mechanical behavior of a CoCrCuFeNiAl$_{0.5}$ high entropy alloy, Int. J. Mod. Phys. B 23 (2009) 1254–1259.

[260] F. Otto, A. Dlouhy, C. Somsen, H. Bei, G. Eggler, E.P. George, The influences of temperature and microstructure on the tensile properties of a CoCrFeMnNi high-entropy alloy, Acta Mater 61 (2013) 5743–5755.

[261] A.J. Zaddach, R.O. Scattergood, C.C. Koch, Tensile properties of low-stacking fault energy high-entropy alloys, Mat. Sci. Eng. A 636 (2015) 373–378.

[262] H.M. Daoud, A. Manzoni, R. Volkl, N. Wanderka, U. Glatzel, Microstructure and tensile behavior of Al$_8$Co$_{17}$Cr$_{17}$Cu$_8$Fe$_{17}$Ni$_{33}$ (at.%) high-entropy alloy, JOM 65 (2013) 1805–1814.

[263] C. Ng, S. Guo, J. Luan, Q. Wang, J. Lu, S. Shi, C.T. Liu, Phase stability and tensile properties of Co-free Al$_{0.5}$CrCuFeNi$_2$ high-entropy alloys, J. Alloys Compd. 584 (2014) 530–537.

[264] S.G. Ma, S.F. Zhang, J.W. Qiao, Z.H. Wang, M.C. Gao, Z.M. Jiao, H.J. Yang, Y. Zhang, Superior high tensile elongation of a single-crystal CoCrFeNiAl$_{0.3}$ high-entropy alloy by Bridgman solidification, Intermetallics 54 (2014) 104–109.

[265] T.-T. Shun, Y.-C. Du, Microstructure and tensile behaviors of FCC Al$_{0.3}$CoCrFeNi high entropy alloy, J. Alloys Compd. 479 (2009) 157–160.

[266] M.A. Hemphill, T. Yuan, A.M. Wang, J.-W. Yeh, C.-W. Tsai, A. Chuang, P.K. Liaw, Fatigue behavior of Al$_{0.5}$CoCrCuFeNi high entropy alloys, Acta Mater 60 (2012) 5723–5734.

[267] A.V. Kuznetsov, D.G. Shaysultanov, N.D. Stepanov, G.A. Salishchev, O.N. Senkov, Tensile properties of an AlCrCuNiFeCo high-entropy alloy in as-cast and wrought conditions, Mater. Sci. Eng. A 533 (2012) 107–118.

[268] Z. Wu, H. Bei, G.M. Pharr, E.P. George, Temperature dependence of the mechanical properties of equiatomic solid solution alloys with face-centered cubic crystal structures, Acta Mater 81 (2014) 428–441.

[269] N. Stepanov, M. Tikhonovsky, N. Yurchenko, D. Zyabkin, M. Klimova, S. Zherebtsov, A. Efimov, G. Salishchev, Effect of cryo-deformation on structure and properties of CoCrFeNiMn high-entropy alloy, Intermetallics 59 (2015) 8–17.

[270] Y. Wu, W.H. Liu, X.L. Wang, D. Ma, A.D. Stoica, T.G. Nieh, Z.B. He, Z.P. Lu, In-situ neutron diffraction study of deformation behavior of a multi-component high-entropy alloy, Appl. Phys. Lett. 104 (2014).

[271] J.R. Davis, in: Aluminum and Aluminum Alloys, ASM, International, Materials Park, OH USA, 1993.

[272] Ti-5Al-2.5Sn ELI Data Sheet. vol. 2015: RTI, International.

[273] W.H. Liu, Y. Wu, J.Y. He, T.G. Nieh, Z.P. Lu, Grain growth and the Hall-Petch relationship in a high-entropy FeCrNiCoMn alloy, Scr. Mater. 68 (2013) 526–529.

[274] A. Haglund, M. Koehler, D. Catoor, E.P. George, V. Keppens, Polycrystalline elastic moduli of a high-entropy alloy at cryogenic temperatures, Intermetallics 58 (2015) 62–64.

[275] Y. Deng, C.C. Tasan, K.G. Pradeep, H. Springer, A. Kostka, D. Raabe, Design of a twinning-induced plasticity high entropy alloy, Acta Mater. 94 (2015) 124–133.

[276] Z. Wu, H. Bei, Microstructures and mechanical properties of compositionally complex Co-free FeNiMnCr$_{18}$ FCC solid solution alloy, Mat. Sci. Eng. A 640 (2015) 217–224.

[277] A.V. Kuznetsov, D.G. Shaysultanov, N.D. Stepanov, G.A. Salishchev, O.N. Senkov, Superplasticity of AlCoCrCuFeNi high entropy alloy, Mater. Sci.

[278] T.-T. Zuo, S.-B. Ren, P.K. Liaw, Y. Zhang, Processing effects on the magnetic and mechanical properties of FeCoNiAl$_{0.2}$Si$_{0.2}$ high entropy alloy, Int. J. Min. Met. Mater. 20 (2013) 549–555.

[279] H.F. Sheng, L.M. Peng, Microstructure and tensile properties of Al$_{0.5}$CoCr-CuFeNi high-entropy alloy, Appl. Mech. Mater 456 (2014) 494–497.

[280] L. Liu, J.B. Zhu, L. Li, J.C. Li, Q. Jiang, Microstructure and tensile properties of FeMnNiCuCoSn$_x$ high entropy alloys, Mater. Des. 44 (2013) 223–227.

[281] W.H. Liu, J.Y. He, H.L. Huang, H. Wang, Z.P. Lu, C.T. Liu, Effects of Nb additions on the microstructure and mechanical property of CoCrFeNi high-entropy alloys, Intermetallics 60 (2015) 1–8.

[282] C.-Y. Hsu, C.-C. Juan, T.-S. Sheu, S.-K. Chen, J.-W. Yeh, Effect of aluminum content on microstructure and mechanical properties of Al$_x$CoCrFeMo$_{0.5}$Ni high-entropy alloys, JOM 65 (2013) 1840–1847.

[283] H. Zhang, Y. He, Y. Pan, Enhanced hardness and fracture toughness of the laser-solidified FeCoNiCrCuTiMoAlSiB$_{0.5}$ high-entropy alloy by martensite strengthening, Scr. Mater 69 (2013) 342–345.

[284] U. Roy, H. Roy, H. Daoud, U. Glatzel, K.K. Ray, Fracture toughness and fracture micromechanism in a cast AlCoCrCuFeNi high entropy alloy system, Mater. Lett. 132 (2014) 186–189.

[285] O.N. Senkov, J.M. Scott, S.V. Senkova, F. Meisenkothen, D.B. Miracle, C.F. Woodward, Microstructure and elevated temperature properties of a refractory TaNbHfZrTi alloy, J. Mater. Sci. 47 (2012) 4062–4074.

[286] O.N. Senkov, S.V. Senkova, D.B. Miracle, C. Woodward, Mechanical properties of low-density, refractory multi-principal element alloys of the Cr–Nb–Ti–V–Zr system, Mater. Sci. Eng. A 565 (2013) 51–62.

[287] O.N. Senkov, S.L. Semiatin, Microstructure and properties of a refractory high-entropy alloy after cold working, J. Alloys Compd. 649 (2015) 1110–1123.

[288] Z.H. Gan, L.M. Xu, Z.H. Lu, H.H. Zhou, C.H. Song, F. Huang, A novel high-entropy alloy AlMgZnSnPbCuMnNi with low free corrosion potential, Appl. Mech. Mater 327 (2013) 103–107.

[289] Z. Liu, J.M. Zeng, H.H. Zhan, Study on corrosion resistance of high-entropy alloys NiCoCrFeMnCuC in medium acid liquid, Appl. Mech. Mater 117–119 (2012) 1816–1819.

[290] Y.-L. Chou, Y.-C. Wang, J.-W. Yeh, H.-C. Shih, Pitting corrosion of the high-entropy alloy Co$_{1.5}$CrFeNi$_{1.5}$Ti$_{0.5}$Mo$_{0.1}$ in chloride-containing sulphate solutions, Corros. Sci. 52 (2010) 3481–3491.

[291] Y.-L. Chou, J.-W. Yeh, H.-C. Shih, The effect of molybdenum on the corrosion behaviour of the high-entropy alloys Co$_{1.5}$CrFeNi$_{1.5}$Ti$_{0.5}$Mo$_x$ in aqueous environments, Corros. Sci. 52 (2010) 2571–2581.

[292] C.-P. Lee, C.-C. Chang, Y.-Y. Chen, J.-W. Yeh, H.-C. Shih, Effect of the aluminium content of Al$_x$CrFe$_{1.5}$MnNi$_{0.5}$ high-entropy alloys on the corrosion behaviour in aqueous environments, Corros. Sci. 50 (2008) 2053–2060.

[293] Y.-L. Chou, J.-W. Yeh, H.-C. Shih, Pitting corrosion of Co$_{1.5}$CrFeNi$_{1.5}$Ti$_{0.5}$Mo$_{0.1}$ in chloride-containing nitrate solutions, Corrosion 67 (2011).

[294] X.-W. Qiu, Y.-P. Zhang, L. He, C.-G. Liu, Microstructure and corrosion resistance of AlCrFeCuCo high entropy alloy, J. Alloys Compd. 549 (2013) 195–199.

[295] C.-P. Lee, Y.-Y. Chen, C.-Y. Hsu, J.-W. Yeh, H.-C. Shih, The effect of boron on the corrosion resistance of the high entropy alloys Al$_{0.5}$CoCrCuFeNiB$_x$, J. Electrochem. Soc. 154 (2007) C424–C430.

[296] Y.-J. Hsu, W.-C. Chiang, J.-K. Wu, Corrosion behavior of FeCoNiCrCu$_x$ high-entropy alloys in 3.5% sodium chloride solution, Mater. Chem. Phys. 92 (2005) 112–117.

[297] E. Fazakas, J.Q. Wang, V. Zadorozhnyy, D.V. Louzguine-Luzgin, L.K. Varga, Microstructural evolution and corrosion behavior of Al$_{25}$Ti$_{25}$Ga$_{25}$Be$_{25}$ equimolar composition alloy, Mater. Corros. 65 (2014) 691–695.

[298] B. Ren, Z.X. Liu, D.M. Li, L. Shi, B. Cai, M.X. Wang, Corrosion behavior of CuCrFeNiMn high entropy alloy system in 1 M sulfuric acid solution, Mater. Corros. 63 (2012) 828–834.

[299] Y.-Y. Chen, T. Duval, U.-T. Hong, J.-W. Yeh, H.-C. Shih, L.-H. Wang, J.-C. Oung, Corrosion properties of a novel bulk Cu$_{0.5}$NiAlCoCrFeSi glassy alloy in 288 degrees C high-purity water, Mater. Lett. 61 (2007) 2692–2696.

[300] Q.H. Li, T.M. Yue, Z.N. Guo, X. Lin, Microstructure and corrosion properties of AlCoCrFeNi high entropy alloy coatings deposited on AISI 1045 steel by the electrospark process, Metall. Mater. Trans. A 44A (2013) 1767–1778.

[301] V. Soare, D. Mitrica, I. Constantin, G. Popescu, I. Csaki, M. Tarcolea, I. Carcea, The mechanical and corrosion behaviors of as-cast and re-melted AlCrCu-FeMnNi multi-component high-entropy alloy, Metall. Mater. Trans. A 46 (2014) 1468–1473.

[302] O.N. Dogan, B.C. Nielsen, J.A. Hawk, Elevated-temperature corrosion of CoCrCuFeNiAl$_{0.5}$B$_x$ high-entropy alloys in simulated Syngas containing H$_2$S, Oxid. Met. 80 (2013) 177–190.

[303] Y. Yu, F.Q. Xie, T.B. Zhang, H.C. Kou, R. Hu, J.S. Li, Microstructure control and corrosion properties of AlCoCrFeNiTi$_{0.5}$ high-entropy alloy, Rare Metal. Mat. Eng. 41 (2012) 862–866.

[304] Y.-Y. Chen, U.-T. Hong, J.-W. Yeh, H.-C. Shih, Selected corrosion behaviors of a Cu$_{0.5}$NiAlCoCrFeSi bulk glassy alloy in 288 degrees C high-purity water, Scr. Mater 54 (2006) 1997–2001.

[305] C.-P. Lee, Y.-Y. Chen, C.-Y. Hsu, J.-W. Yeh, H.-C. Shih, Enhancing pitting corrosion resistance of Al$_x$CrFe$_{1.5}$MnNi$_{0.5}$ high-entropy alloys by anodic treatment in sulfuric acid, Thin Solid Films 517 (2008) 1301–1305.

[306] C. Huang, Y.Z. Zhang, R. Vilar, J.Y. Shen, Dry sliding wear behavior of laser clad TiVCrAlSi high entropy alloy coatings on Ti-6Al-4V substrate, Mater.

Des. 41 (2012) 338–343.

[307] Z.S. Nong, D.S. Li, J.C. Zhu, H.L. Yu, Z.H. Lai, Effect of aluminum content on microstructure and wear resistance of CuCrFeMnTiAl$_x$ high-entropy alloy, Rare Metal. Mat. Eng. 40 (2011) 550–554.

[308] J.H. Chen, P.N. Chen, C.M. Lin, C.M. Chang, Y.Y. Chang, W. Wu, Microstructure and wear properties of multicomponent alloy cladding formed by gas tungsten arc welding (GTAW), Surf. Coat. Technol. 203 (2009) 3231–3234.

[309] Y.C. Lin, Y.H. Cho, Elucidating the microstructure and wear behavior for multicomponent alloy clad layers by in situ synthesis, Surf. Coat. Technol. 202 (2008) 4666–4672.

[310] C.-Y. Hsu, T.-S. Sheu, J.-W. Yeh, S.-K. Chen, Effect of iron content on wear behavior of AlCoCrFe$_x$Mo$_{0.5}$Ni high-entropy alloys, Wear 268 (2010) 653–659.

[311] J.-M. Wu, S.-J. Lin, J.-W. Yeh, S.-K. Chen, Y.-S. Huang, Adhesive wear behavior of Al$_x$CoCrCuFeNi high-entropy alloys as a function of aluminum content, Wear 261 (2006) 513–519.

[312] J.-C. Jiang, X.-Y. Luo, High temperature oxidation behaviour of AlCuTiFeNiCr high-entropy alloy, Adv. Mat. Res. 652–654 (2013) 1115–1118.

[313] C. Huang, Y. Zhang, J. Shen, R. Vilar, Thermal stability and oxidation resistance of laser clad TiVCrAlSi high entropy alloy coatings on Ti-6Al-4V alloy, Surf. Coat. Technol. 206 (2011) 1389–1395.

[314] J.R. Davis (Ed.), ASM Handbook, tenth ed., ASM, International, Metals Park, OH USA, 1990.

[315] T.-T. Shun, L.-Y. Chang, M.-H. Shiu, Age-hardening of the CoCrFeNiMo$_{0.85}$ high-entropy alloy, Mater. Charact. 81 (2013) 92–96.

[316] T.-T. Shun, C.-H. Hung, C.-F. Lee, The effects of secondary elemental Mo or Ti addition in Al$_{0.3}$CoCrFeNi high-entropy alloy on age hardening at 700 C, J. Alloys Compd. 495 (2010) 55–58.

[317] T.-T. Shun, C.-H. Hung, C.-F. Lee, Formation of ordered/disordered nanoparticles in FCC high entropy alloys, J. Alloys Compd. 493 (2010) 105–109.

[318] T.-T. Shun, Y.-C. Du, Age hardening of the Al$_{0.3}$CoCrFeNiC$_{0.1}$ high entropy alloy, J. Alloys Compd. 478 (2009) 269–272.

[319] L.C. Tsao, C.S. Chen, C.P. Chu, Age hardening reaction of the Al$_{0.3}$Cr-Fe$_{1.5}$MnNi$_{0.5}$ high entropy alloy, Mater. Des. 36 (2012) 854–858.

[320] B. Ren, Z.X. Liu, B. Cai, M.X. Wang, L. Shi, Aging behavior of a CuCr$_2$Fe$_2$NiMn high-entropy alloy, Mater. Des. 33 (2012) 121–126.

[321] C.F. Lee, T.T. Shun, Age hardening of the Al$_{0.5}$CoCrNiTi$_{0.5}$ high-entropy alloy, Metall. Mater. Trans. A 45A (2014) 191–195.

[322] I. Toda-Caraballo, P.E.J. Rivera-Diaz-Del-Castillo, Modelling solid solution hardening in high entropy alloys, Acta Mater 85 (2015) 14–23.

[323] T. Nagase, P.D. Rack, T. Egami, Irradiation damage in multicomponent equimolar alloys and high entropy alloys (HEAs), Microscopy 63 (2014) i22.

[324] C.M. Rost, E. Sachet, T. Borman, A. Moballegh, E.C. Dickey, D. Hou, J.L. Jones, S. Curtarolo, J.-P. Maria, Entropy-stabilized oxides, Nat. Commun. 6 (2015) 8485.

[325] G. Mandigo, D. Freitag, A primer on CMCs, Composites Manufacturing, 2015. http://compositesmanufacturingmagazine.com/2015/02/a-primer-on-ceramic-matrix-composites/.

[326] K. Wood, Ceramic-matrix composites heat up, High-Performance Composites, 2013. http://www.compositesworld.com/articles/ceramic-matrix-composites-heat-up.

[327] C.H. Tsau, Y.H. Chang, Microstructures and Mechanical Properties of TiCrZrNbN$_x$ alloy nitride thin films, Entropy 15 (2013) 5012–5021.

[328] C.-H. Lai, S.-J. Lin, J.-W. Yeh, S.-Y. Chang, Preparation and characterization of AlCrTaTiZr multi-element nitride coatings, Surf. Coat. Technol. 201 (2006) 3275–3280.

[329] C.H. Lin, J.G. Duh, J.W. Yeh, Multi-component nitride coatings derived from Ti-Al-Cr-Si-V target in RF magnetron sputter, Surf. Coat. Technol. 201 (2007) 6304–6308.

[330] W.Y. Tang, J.W. Yeh, Effect of aluminum content on plasma-nitrided Al$_x$CoCrCuFeNi high-entropy alloys, Metall. Mater. Trans. A 40A (2009) 1479–1486.

[331] C.-W. Tsai, S.-W. Lai, K.-H. Cheng, M.-H. Tsai, A. Davison, C.-H. Tsau, J.-W. Yeh, Strong amorphization of high-entropy AlBCrSiTi nitride film, Thin Solid Films 520 (2012) 2613–2618.

[332] R.S. Yu, R.H. Huang, C.M. Lee, F.S. Shieu, Synthesis and characterization of multi-element oxynitride semiconductor film prepared by reactive sputtering deposition, Appl. Surf. Sci. 263 (2012) 58–61.

[333] M. Braic, M. Balaceanu, A. Vladescu, C.N. Zoita, V. Braic, Deposition and characterization of multi-principal-element (CuSiTiYZr)C coatings, Appl. Surf. Sci. 284 (2013) 671–678.

[334] M. Braic, V. Braic, M. Balaceanu, C.N. Zoita, A. Vladescu, E. Grigore, Characteristics of (TiAlCrNbY)C films deposited by reactive magnetron sputtering, Surf. Coat. Technol. 204 (2010) 2010–2014.

[335] H. Duan, Y. Wu, M. Hua, C. Yuan, D. Wang, J. Tu, H. Kou, J. Li, Tribological properties of AlCoCrFeNiCu high-entropy alloy in hydrogen peroxide solution and in oil lubricant, Wear 297 (2013) 1045–1051.

[336] C.H. Lai, K.H. Cheng, S.J. Lin, J.W. Yeh, Mechanical and tribological properties of multi-element (AlCrTaTiZr)N coatings, Surf. Coat. Technol. 202 (2008) 3732–3738.

[337] B. Ren, Z.G. Shen, Z.X. Liu, Structure and mechanical properties of multi-element (AlCrMnMoNiZr)N$_x$ coatings by reactive magnetron sputtering, J. Alloys Compd. 560 (2013) 171–176.

[338] Y. Yu, W.M. Liu, T.B. Zhang, J.S. Li, J. Wang, H.C. Kou, J. Li, Microstructure and tribological properties of AlCoCrFeNiTi$_{0.5}$ high-entropy alloy in hydrogen peroxide solution, Metall. Mater. Trans. A 45A (2014) 201–207.

[339] M. Green, I. Takeuchi, J.R. Hattrick-Simpers, Applications of high throughput (combinatorial) methodologies to electronic, magnetic, optical, and energy-related materials, J. Appl. Phys. 113 (2013) 231101–231153, 231101.

[340] Thermoelectric materials, Wikipedia, 2016. https://en.wikipedia.org/wiki/Thermoelectric_materials.

[341] C. Yu, T.-J. Zhy, R.-Z. Shi, Y. Zhang, X.-B. Zhao, J. He, High-performance half-Heusler thermoelectric materials Hf$_{1-x}$Zr$_x$NiSn$_{1-y}$Sb$_y$ prepared by levitation meling and spark plasma sintering, Acta Mater 57 (2009) 2757–2764.

[342] M. Yin, P. Nash, Standard enthalpies of formation of selected XYZ half-Heusler compounds, J. Chem. Thermodyn. 91 (2015) 1–7.

[343] W. Xie, A. Weidenkaff, X. Tang, Q. Zhang, J. Poon, T.M. Tritt, Recent advances in nanostructured thermoelectric half-Heusler compounds, Nanomaterials 2 (2012) 379–412.

[344] R. Potyrailo, K. Rajan, K. Stoewe, I. Takeuchi, B. Chisholm, H. Lam, Combinatorial and high-throughput screening of materials libraries: review of state of the art, ACS Comb. Sci. 13 (2011) 579–633.

[345] R. Potyrailo, I. Takeuchi, Role of high-throughput characterization tools in combinatorial materials science, Meas. Sci. Technol. 16 (2005) 1–4.

[346] K. Rajan, Combinatorial materials sciences: experimental strategies for accelerated knowledge discovery, Annu. Rev. Mater. Res. 38 (2008) 299–322.

[347] P. McCluskey, J. Vlassak, Combinatorial nanocalorimetry, J. Mater. Res. 25 (2010) 2086–2100.

[348] S. Curtarolo, G.L.W. Hart, M.B. Nardelli, N. Mingo, S. Sanvito, O. Levy, The high-throughput highway to computational materials design, Nat. Mater. 12 (2013) 191–201.

[349] A. Jain, S.P. Ong, G. Hautier, W. Chen, W.D. Richards, S. Dacek, S. Cholia, D. Gunter, D. Skinner, G. Ceder, K.A. Persson, Commentary: the Materials Project: a materials genome approach to accelerating materials innovation, Apl. Mater 1 (2013), 011002–011001, 011011.

[350] G. Ceder, K. Persson, The stuff of dreams, Sci. Am. (2013) 36–40.

[351] C. Colinet, Comparison of enthalpies of formation and enthalpies of mixing in transition metal based alloys, Thermochim. Acta 314 (1998) 229–245.

[352] S. Curtarolo, D. Morgan, G. Ceder, Accuracy of *ab initio* methods in predicting the crystal structures of metals: a review of 80 binary alloys, Comput. Coupling Phase Diagr. Thermochem. 29 (2005) 163–211.